

F. H. Wittmann (Editor)

Materials for Buildings and Structures

EUROMAT 99 – Volume 6



Materials for Buildings and Structures. Edited by F. H. Wittmann
Copyright © 2000 Wiley-VCH Verlag GmbH, Weinheim.
ISBN: 3-527-30125-9

EUROMAT 99 was the biannual meeting of the Federation of European Materials Societies (FEMS) with its 21 member societies across Europe.

The program of the EUROMAT 99 congress was divided into 12 topics. The scientific coordination was managed by topic coordinators. The responsible experts for the individual topics were:

Topic A – Materials for Information Technology

K. Grassie, Philips GmbH, Aachen (D)

Topic B – Materials for Transportation Technology

P. J. Winkler, DaimlerChrysler AG, München (D)

Topic C – Materials for Electrical Power Generation and Energy Conversion

E. Tenckhoff, Siemens AG, Erlangen (D)

Topic D – Materials for Medical Engineering

H. Stallforth, Aesculap AG, Tuttlingen (D)

P. Revell, University College London (UK)

Topic E – Materials for Buildings and Structures

F. H. Wittmann, ETH Zürich (CH)

Topic F1 – Characterization Methods and Procedures

Y. Bréchet, INPG, Grenoble (F)

Topic F2 – Metals

R. Wagner, FZ. Jülich (D)

Topic F3 – Ceramics

G. Müller, Fraunhofer-Inst. f. Silicatforschung ISC, Würzburg (D)

Topic F4 – Polymers

G. Wegner, MPI für Polymerforschung, Mainz (D)

P. J. Lemstra, Univ. of Eindhoven (NL)

Topic F5 – Interface Controlled Materials

M. Rühle, MPI für Metallforschung, Stuttgart (D)

Topic G – Surface Technology

H. Dimigen, Fraunhofer-Inst. f. Schicht- und Oberflächentechnik IST, Braunschweig (D)

Topic H – Nano- and Microtechnology

J. Haußelt, Forschungszentrum Karlsruhe (D)

F. H. Wittmann (Editor)

Materials for Buildings and Structures

EUROMAT 99 – Volume 6



Deutsche Gesellschaft
für Materialkunde e.V.



Weinheim · New York · Chichester
Brisbane · Singapore · Toronto

Editor:
Prof. F. H. Wittmann
ETH Zürich
Institut für Baustoffe, Werkstoffchemie und Korrosion
ETH Hönggerberg, HIF E12
8093 Zürich
Switzerland

This book was carefully produced. Nevertheless, authors, editor and publisher do not warrant the information contained therein to be free of errors. Readers are advised to keep in mind that statements, data, illustrations, procedural details or other items may inadvertently be inaccurate.

Library of Congress Card No. applied for.

A catalogue record for this book is available from the British Library.

Deutsche Bibliothek Cataloguing-in-Publication Data:

A catalogue record for this publication is available from Die Deutsche Bibliothek
ISBN 3-527-30125-9

© WILEY-VCH Verlag GmbH, D-69469 Weinheim (Federal Republic of Germany), 2000

Printed on acid-free and chlorine-free paper.

All rights reserved (including those of translation in other languages). No part of this book may be reproduced in any form – by photoprinting, microfilm, or any other means – nor transmitted or translated into machine language without written permission from the publishers. Registered names, trademarks, etc. used in this book, even when not specifically marked as such, are not to be considered unprotected by law.

Composition: WGV Verlagsgesellschaft mbH, Weinheim
Printing: betz-druck, Darmstadt
Bookbinding: Buchbinderei Osswald, Neustadt/Wstr.
Printed in the Federal Republic of Germany

Preface

Engineering progress essentially depends on the availability and the intelligent use of materials. For many key industry areas, Europe constitutes a premier place for the development of new materials and their applications. EUROMAT 99, the biannual meeting of the Federation of European Materials Societies with its 21 member societies across Europe set out to become the most comprehensive European event to demonstrate the wide range of the interdisciplinary performance of materials.

EUROMAT was essentially focused on applications of materials with high innovation potential. At the same time, fundamental approaches and processing related aspects for unconventional materials were addressed. In the frame of the 12 conference topics, 1650 papers were originally submitted to the 52 symposia. A total of 655 have been selected as oral presentation by the international group of chairpersons and were presented in 161 sessions. Further, the chairpersons have selected 65 renowned experts for keynote lectures in the frame of their symposium. Roughly 700 papers were displayed as posters.

The scope of EUROMAT was truly international. Papers originated from 57 countries. Among them the major industrial countries of the world have contributed considerably to the wealth of the programme. An overwhelming Eastern European contingent shows that there is a strong interest of these countries in international cooperation.

EUROMAT 99 represents a showcase of the competence of the European materials societies. Various European sister societies and federations act as cosponsors of the event. Joining with FEMS, they are about to establish the network MatNet in order to promote and facilitate their communication and cooperation. They have started a dialogue with the European Commission in order to discuss programme goals and priorities for maintaining Europe's global competitiveness. In view of this promising international perspective, the European Community has agreed to sponsor EUROMAT 99 generously for which we are very grateful. EUROMAT 99 was focused to a large extent on the aims of the closing 4th Framework Programme many projects of which were presented.

EUROMAT 99 was hosted by WERKSTOFFWOCHE, a multisociety joint conference project established in Germany in 1996. Among its initiators is the Deutsche Gesellschaft für Materialkunde, one of the founding member societies of FEMS and technical organiser of this year's EUROMAT.

EUROMAT 99 represented an outstanding success. As the President of FEMS, I would hope that it will serve as a model for future meetings, both in terms of organisation and international cooperation. I would like to extend my gratitude to the scientists, chairpersons and coordinators as well as to the various organisations and particularly to the Messe München who have made this success possible.

Dr. Paul Costa

President of the Federation of European Materials Societies

Contents

I. Advanced Concrete Technology

Job Site Experience with Self Compacting Concrete (SCC) and Shrinkage Reduction <i>J. Schlumpf, Sika AG (CH)</i>	3
Mechanisms Governing the Behavior of Fresh Shotcrete: Placement and Stability <i>D. Beaupr, Laval University, Québec (CDN);</i> <i>M. Jolin, S. Mindess, University of British Columbia, Vancouver (CDN)</i>	8
Economic Design and Construction with Structural Lightweight Aggregate Concrete <i>J. P. G. Mijnsbergen, CUR, Gouda (NL);</i> <i>S. Helland, Selmer, Oslo (N);</i> <i>M. Maage, Selmer, Trondheim (N);</i> <i>T. A. Hammer, I. Holand, SINTEF Civil and Environmental Engineering, Trondheim (N);</i> <i>E. L. Sveinsdóttir, The Icelandic Building Research Institute, Reykjavik (IS);</i> <i>K. van Breugel, TU Delft (NL)</i>	18
A New Type of High-performance Lightweight Concrete <i>St. Linsel, H. S. Müller, University of Karlsruhe (D)</i>	23
Shrinkage-Reduced High Performance Concrete <i>P. Schwesinger, G. Sickert, Bauhaus-University Weimar (D)</i>	28
Influence of Specimen Size/Geometry on the Potential For Shrinkage Cracking in Rings <i>S. P. Shah, W. Yang, Northwestern University, Evanston, IL (USA);</i> <i>W. J. Weiss, Purdue University, West Lafayette, IN (USA)</i>	35
Highly Durable Precast Special Concrete <i>P.P. Camanho, M. C. Fernandes, A.A. Fernandes, A.J. M. Ferreira, M. A. V. Figueiredo,</i> <i>Universidade do Porto Rua dos Bragas, Porto Codex (P)</i>	41
Influence of Chemical Admixtures on the Drying Shrinkage of Concrete <i>I. Carol, R. Gettu, M. A. Martín, J. Roncero, Universitat Politècnica de Catalunya,</i> <i>Barcelona (E)</i>	48
II. Fibre Reinforced Cement-Based Materials	
Mechanical Characterisation of Cement Reinforced with Fique Fibers <i>L.E.G. Cambroneró, I. Chacón, A.J. Morañó, J.M. Ruiz Roman, Material Engineering Dept.</i> <i>School of Mines- UPM, Madrid (E)</i>	57
Use of Technical Textiles and Densified Wood for Timber Joints <i>P. Haller, J. Wehsener, Dresden University of Technology (D)</i>	66

Improvement of the Ductility of Concrete Due to the Incorporation of Steel Fibers and its Relation with the Material Toughness <i>B. Barragán, R. de Fatima Zalochi, R. Gettu, M. A. Martín, Universitat Politècnica de Catalunya, Barcelona (E)</i>	72
SIFCON (Slurry Infiltrated Fiber Concrete) Under Dynamic Loading <i>C. Mayrhofer, Fraunhofer Institut für Kurzzeitdynamik, Efringen-Kirchen (D)</i>	78
Size Effect in Compression of High Strength Fibre Reinforced Concrete Cylinders Subjected To Concentric And Eccentric Loads <i>S. Mindess, Department of Civil Engineering, The University of British Columbia, Vancouver (CDN); G. Campione, Department of Structural and Geotechnical Engineering, The University of Palermo (I)</i>	86
III. Fracture Mechanics of Cement-Based Materials	
Micromechanics of Fiber Reinforced Cementitious Composites <i>B.L. Karihaloo, Cardiff School of Engineering, University of Wales Cardiff (GB); J. Wang, Department of Mechanics and Engineering Sciences, Peking University, Beijing (VRC)</i>	95
Fatigue Crack Propagation in Biaxial Compression-Tension <i>J.S. Popovics, Drexel University, Philadelphia, PA (USA); S.P. Shah, K.V. Subramaniam, NSF Center for ACBM, Northwestern University, Evanston, IL (USA)</i>	112
Fractological and Numerical Investigations on Fracture Mechanical Behavior of Concrete <i>V. Mechtcherine, H.S. Müller, University of Karlsruhe (D)</i>	119
Crack Interaction in Concrete <i>C. Shi, B. Sluys, A.G. van Dam, J.G.M. van Mier, Delft University of Technology (NL)</i>	125
A Scale-independent Damage Model for Concrete <i>A: Carpinteri, B. Chiaia, P. Cornetti, Politecnico di Torino (I)</i>	132
Horizontal Wedge Splitting Test Method (HWST) - a New Method for the Fracture Mechanics Testing of Large Samples <i>A. Šajina, IRMA - Institute for Research in Materials and Applications, Ljubljana (SLO); K. Fuchs, H.N. Linsbauer, Vienna University of Technology, Vienna (A)</i>	138
A Near-Field Acoustic Sensor for Rheological Measurements in Both Liquids and Solids: Application to the Cement Setting <i>J. Attal, B. Cros, J.Y. Ferrandis, Laboratoire d'Analyse des Interfaces et de Nanophysique, Université Montpellier 2, Montpellier (F)</i>	144
The Value of the SCB Test for Fracture Testing <i>A.J. den Herder, F. Tolman, Netherlands Pavement Consultants b.v., Utrecht (NL)</i>	149

IV. Transport Phenomena and Durability

The Ion Mobility of Deteriorating Salts in Masonry Materials of Different Moisture Content <i>A. Buchwald, C. Kaps, Bauhaus-Universität Weimar (D)</i>	157
A Percolation Model for Water Sorption in Porous Cementitious Materials <i>H. Böhni, B. Elsener, D. Flückinger, Institute of Materials Chemistry and Corrosion, Swiss Federal Institute of Technology ETH Hönggerberg, Zürich (CH)</i>	163
New Experimental Study Relating Cracking to Water Permeability of Normal Strength Concrete <i>C.-M. Aldea, M. Ghandehari, A. Karr, S.P. Shah, National Science Foundation Center for Science and Technology of Advanced Cement Based Materials, IL (USA)</i> ,.....	170
Micro Ice Lens Formation, Artificial Saturation and Damage During Freeze Thaw Attack <i>M.J. Setzer, University of Essen, Institute of Building Physics and Materials Science IBPM, Essen (D)</i>	175
Chemical Deterioration of Concrete Constructions in Riga <i>U. Cielens, S. Igaune, Y. Setina, I. Vitina, Riga Technical University, Institute of Silicate Materials (LT)</i>	183
Influence of Interfacial Effects on the Determination of Dielectric Properties of Cement Paste <i>M. Alonso, C. Andrade, Institute of Construction Sciences “Eduardo Torroja”, Madrid (E); X. Ramón Nóvoa, Universidade de Vigo, Vigo (E); M. Keddad, H. Takenouti, Université Pierre et Marie Curie, Paris (F)</i>	189
Exploitation of Marble Residues through Material Compund in a Polymer Matrix <i>C. Alonso, L.E. García Cambronero, J.M. Ruiz Prieto, J.M. Ruiz Román, Departamento de Ingeniería de Materiales. E.T.S de Ingenieros de Minas. Universidad Politécnica de Madrid (E); S. Codina Sánchez, F.A. Corpas Iglesias, Departamento de Ingeniería Química, Ambiental y de los Materiales. E.U.P Linares. Universidad de Jaén (E)</i>	198
Permeability of Bound Granular Covers <i>F. Tolman, Netherlands Pavement Consultants, Utrecht (NL); L.J. Ebels, UWP Engineers, Umtata (SA)</i>	202
Gas Permeability, Porosity and Carbonation of Modern Conservation Lime Mortar Mix <i>P. Bartos, J. Hughes, J. Válek, Advanced Concrete and Masonry Centre, University of Paisley, Scotland (GB)</i>	209
Author Index	217
Subject Index	219

I Advanced Concrete Technology

Job Site Experience with Self Compacting Concrete (SCC) and Shrinkage Reduction

Jürg Schlumpf
Sika AG, Switzerland

1 Introduction

In the present paper, the author describes the two following concrete technologies:

- Self Compacting Concrete (SCC)
- Durable shrinkage reduction in cementitious materials.

The main emphasis in this exposé is on the practical experience with these technologies on different job sites. Examples of problems and the ways to approach and solve them, will illustrate the useful and efficient application of these technologies.

In Switzerland, both technologies have been introduced in the market in the years 1998/1999. The projects executed so far, emphasise the importance of these developments.

2 Self Compacting Concrete

SCC (self-compacting concrete) is an extremely flowable, homogeneous and soft concrete with no tendency towards segregation and bleeding.

Its stupendous self-compacting ability allows placing high-quality concrete without any compaction!

2.1 Concrete System SCC

Self-compacting concrete (SCC) opens undreamed-of possibilities for the design of structural elements. Enormous overall performance increase, end of the considerable noise pollution and health risk caused by the vibrators during concrete placement and uniform concrete quality throughout the whole cross-section of the structural element are the key factors for the success of self-compacting concrete.

The elements of successful self-compacting concrete (hereafter called SCC), are the special mix design and advanced concrete admixtures in combination with adapted placement techniques.

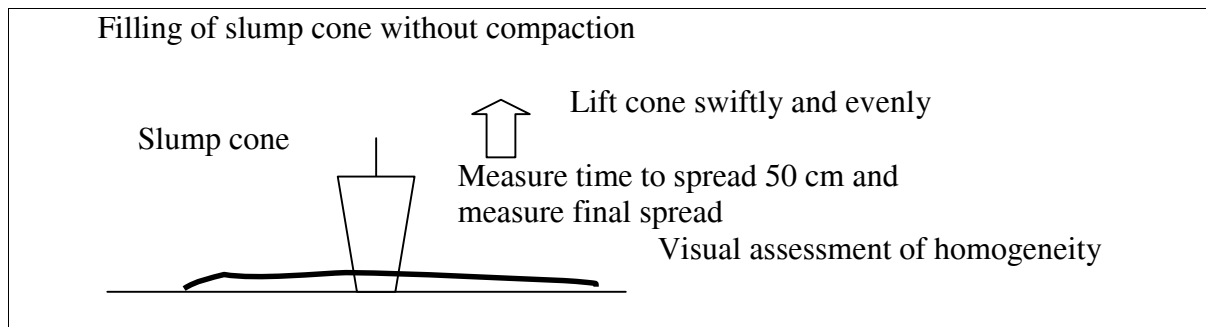


Figure 1: Place slump cone upside down and fill with concrete without compacting. Lift cone swiftly and measure the time the concrete takes to reach a spread of 50 cm. In addition, measure the final spread. All this without any movement of the table!

2.2 Pipe filling Meinrad Lienert-Square

Between Zürich and Thalwil, a 9.4 km long double-track tunnel is driven as part of the Rail 2000 Project of the Swiss Federal Railways SBB.

In the tunnel portal zone around Meinrad Lienert-Square, the overlying ground under the existing buildings is very thin. Protective measures must be taken for the security of these buildings. A pipe shield is therefore driven above the future tunnel from a thrust pit excavated by diaphragm wall method on Meinrad Lienert-Square. 10 pipes between 138 and 150 m long are advanced into the ground by pipe jacking method. The concrete pipes, having an inner diameter of 1,25 m, are pushed over the whole length, starting from the thrust pit.

When the pipes are in place, injections are made in two phases. Massive reinforcement cages are inserted into the pipes.

The pipes are filled with self-compacting concrete SCC. The mix design for the filling of the pipes has been elaborated in collaboration with the ready mix plant and the manufacturer of the concrete admixtures.

The required concrete properties can be *obtained* with the following mix design.

Concrete B 35/25 WD SCC

Aggregate:	0 / 16 mm
Binder:	380 kg/m ³ CEM II / A-L 32.5
Additive:	50 kg/m ³ fly ash
Concrete admixture:	1.70 % Sika ViscoCrete-2 (HBV)

Increased quality insurance measures have been taken during the first concreting stage. Cores have been taken from a first 30 m section, at a flowing distance of 25 m and have been compared with the reference sample taken at the feeding connection. The results obtained show the high degree of consistency of the quality of the concrete.

Strengths:	Before pumping	After pumping distance 120 m and flowing distance of 25 m
Cube 7 days:	35.2 N/mm ² (n= 3)	37.9 N/mm ² (n= 3)
Cube 28 days:	47.2 N/mm ² (n= 3)	44.6 N/mm ² (n= 3)
Cores from the object after 7 days:		34.3 N/mm ² (n= 5)
Cores from the object after 28 days:		46.0 N/mm ² (n= 5)

This mix design allows filling the pipes advanced by jacking at the Meinrad Lienert-Square accurately and with consistent quality to the full satisfaction of the owner and the designing engineers.

2.3 Potable water gallery Lutry

In order to secure water supplies for the future, the township of Lausanne is building a new pumping station in Lutry VD. The project comprises the new pumping station and a 80 m long connection gallery between the excavation pit and the valve chamber of the existing pumping station.

Whereas support during excavation was assured by means of steel fibre reinforced shotcrete B35/25 and steel arches, the lining was to be a 30 cm deep B35/25 concrete layer with inner and outer wire mesh reinforcement. There was no separation between shotcrete and concrete lining.

The concrete was manufactured to the following mix design

- Cement 350 kg/m³ CEM II/A-L 32.5 R
- Additive 75 kg/m³ Fly ash
- Aggregate 0-16mm 52% 0-4mm, 13% 4-8mm, 35% 8-16mm
- HBV* 1.5% SikaViscocrete-2 *High-performance plasticiser

The actual quantity of fines was approximately 520 kg/m³ concrete.

The concrete was supplied to the site by truck mixer and after remixing was pumped through a steel pipe with 100 mm diameter and a maximum length of 120 m up to the point of concreting. The filling was done through a feeding connection in the middle on top of the element.

3 Shrinkage reduction

There are two fundamentally different ways to differentiate the reduction of the shrinkage process:

- **Shrinkage compensation**
Normal shrinkage process compensated by initial volume increase
- **Shrinkage reduction**
Continuous shrinkage reduction from beginning of hardening

The following exclusively deals with shrinkage reduction.

3.1 Concrete System Shrinkage Reduction

Shrinkage reduction of SikaControl-40 is based on physical and chemical effects. Surfactant substances reduce the loss of water in the hardened cement matrix. Special substances reduce in addition the formation of cement phases playing an important role in shrinkage (mainly aluminates and ferrites)

To achieve optimal effect of this shrinkage reduction it has to be planned in combination with the known measures for the improvement of shrinkage characteristics such as water reduction, optimal binder content, correct placement and best possible curing treatment.

3.2. Research Project ETH Zürich

The shrinkage reducing concrete admixture SikaControl-40 was investigated as part of a research project at the Swiss Federal Institute of Technology ETH Zürich. It was shown that, by using this technology, concrete shrinkage could be drastically reduced without any negative side effects on concrete quality.

The main objective was to determine the effects of the shrinkage-reducing admixture on the properties of cementitious materials (concrete and mortar). Mechanical and hydro-mechanical tests were therefore performed on typical cementitious mortars ($W/C = 0,50$) with three different admixture dosages, namely 0 %, 1 % and 2 %.

The above described tests confirm the positive effects of the shrinkage reducing admixture, SikaControl-40, on the shrinkage behaviour of cementitious materials. The final shrinkage values and the hygrometric expansion coefficients are reduced by 30 % (with 1 % admixture by weight of cement, 60 % r.h). At higher humidity levels the effect is consequently lower. Except for a slight reduction of the compressive strength, SikaControl-40 does not affect the mechanical properties of the concrete. This shrinkage-reducing admixture can therefore significantly increase the durability of a structure.

3.3 Birchi Tunnel

For all structures of the new motorway A5 from Solothurn to Biel different quality requirements are specified for the concrete depending on the exposure to be expected.

In specific terms this means for this concrete:

- Max. allowable w/c-ratio 0.42
- Max. allowable shrinkage 0.25 ‰ (tested to ΔS 100/10-60)
- For freeze/thaw/de-icing salt resistant concrete: HIE-FT Test

The optimal mix designs meeting all requirements were elaborated by extensive preliminary testing. All parameters of this concrete had to be taken into account.

The fine-tuning of the mix design with admixtures

To attain the required water reduction and still have excellent workability, Sikament superplasticisers were used. The extremely tough requirements concerning freeze-thaw/de-icing salt resistance were met by using SikaAer air entraining agent. For the assessment of the shrinkage characteristics the method ΔS 100/10-60 of the Solothurn Bureau for National Motorways (BNS) was used.

Shrinkage measure according to method ΔS 100/10-60 of Canton of Solothurn

High performance concrete according to these mix designs shows shrinkage, tested to method BNS ΔS 100/10-60, of about 0.30 ‰ after 60 days. This value can be improved only insignificantly by further water reduction below w/c ratio of 0,4. To achieve the specified shrinkage of ≤ 0.25 ‰, special concrete admixtures are required. The use of SikaControl-40 reduces shrinkage by up to 40% which means reaching values well below the required 0,25‰.

Shrinkage measures to SIA 162/1 Test no 4

Shrinkage measuring method to SIA 162/1 no 4 differs from the method ΔS 100/10-60 by the storage of the test specimen and the zero reading which for SIA is effected after 24 hours and for BNS only after 10 days.

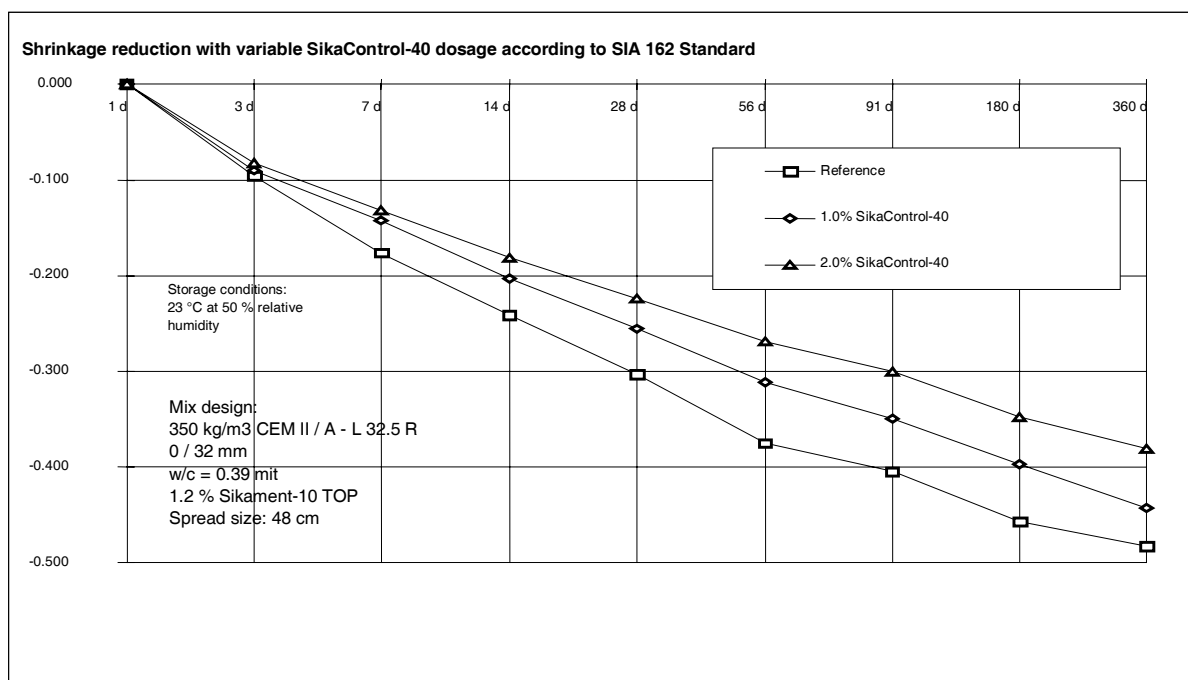


Figure 2: Shrinkage characteristics of: CEM II / A-L 32.5 R 350 kg/m³ / w/c-ratio 0.39

4 Conclusion

From the authors point of view, both of the technologies presented here are significant steps in the development of concrete technology. While self-compacting concrete is offering new and economical problem solutions, shrinkage reduction brings an efficient increase of durability of cementitious materials by reducing shrinkage by about 30 %.

5 References

1. Technische Forschung und Beratung für Zement und Beton
2. TFB, Dr. F. Jacobs; Projekt Frischbetonkonsistenz; 1. Bis 3. Bericht 1997/1998
3. Versuchsstellen Hagerbach AG
4. VSH; SCC Innenring; Versuchsberichte 1998/1999
5. Schweizer. Ingenieur- und Architekten-Verein
6. SIA, Dr. F. Jacobs, Dr. F. Hunkeler, J. Schlumpf Self Compacting Concrete 1999
7. Eidgenössische Technische Hochschule Zürich
8. ETHZ, Prof. Dr. F. H. Wittmann, L. Trausch; Hygromechanisches Verhalten von zementgebundenen Werkstoffen 1999

Mechanisms Governing the Behavior of Fresh Shotcrete: Placement and Stability

Marc Jolin

University of British Columbia, Vancouver, Canada

Denis Beaupr

Laval University, Québec, Canada

Sidney Mindess

University of British Columbia, Vancouver, Canada

1 Introduction

Structural shotcrete for above ground and underground applications as well as shotcrete for structural repairs have been applied using the dry process with success for many years. Its unique pneumatic application procedure is characterized mainly by a certain amount of material loss due to rebound and by the maximum build-up thickness which can be applied in a single pass. To understand and control these two characteristics requires an understanding of the mechanisms involved in the placement of a shotcrete layer. The intent of the present work is to study the fundamental characteristic properties of fresh dry process shotcrete. A discussion of the principles of the dry-mix shotcrete process and a few experimental results related to the basic properties of shotcrete are presented. Two distinct phases in the application process are considered: the placement itself, and the stability of the shotcrete layer immediately after its placement.

2 Research Significance

The main objective of this research project was to investigate the mechanisms involved in the placement and the subsequent stability of a layer of shotcrete applied with the dry process method. The information gathered should be useful to engineers who seek tools and methods to evaluate the properties of fresh dry-mix shotcrete, and to researchers who wish to develop and enhance the dry-mix shotcrete process.

3 The Dry-mix Shotcrete Process

This section deals with the general principles believed to govern the dry process shotcrete. A distinction is made between the stability of the fresh shotcrete layer right after placement, and the placement itself. The objective is to introduce an overview of the “mechanics” of fresh shotcrete.

3.1 Stability

The method of application of dry-mix shotcrete makes it a very exceptional material. Indeed, the consistency of the in-place mixture makes it suitable for both vertical and overhead applications with relatively large build-up thicknesses, without the need for forming. The modeling and characterization of conventional concretes is generally done using rheological concepts, which assume a fluid-like material [1, 2, 3]. However, the relatively stiff consistency of shotcrete means that this material is better characterized using a solid-like behavior approach [4, 5].

A simple but important question that came up early in this research project concerned the identification of the important properties of a fresh shotcrete layer and their measurement. A partial answer is given in Jolin et al. [5], where the research program was mainly oriented toward identifying valid methods for comparing fresh shotcretes, and evaluating basic mechanical properties. To do so, the U.B.C. Penetrometer and the fresh tensile strength apparatus were used. The penetrometer was used to assess the shooting consistency or workability (This property of shotcrete is constantly assessed qualitatively by the nozzleman during shooting, by visual inspection of the surface being shot and right after shooting by poking the surface with his finger), as it has been reported to correlate closely to the water/binder ratio [4, 6]. The fresh tensile strength apparatus, and later the fresh shear strength apparatus, were used to assess other basic mechanical properties. Classical maximum build-up thickness tests (Figure 1) were voluntarily set aside, as they usually do not directly provide information on the fundamental properties (Figure 2). Note that “failure” in this Figure does not necessarily mean fall-out, since simple decohesion will lead to poor in-place quality of the shotcrete.

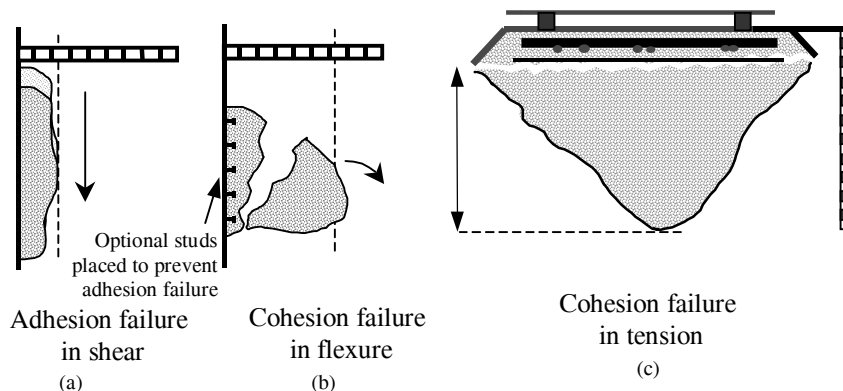


Figure 1. Build-up thickness tests set-ups proposed by Beaupré [7].

It is interesting to note in Figure 2 that the failure mechanisms presented all refer to the quasi-static stress state, thus eliminating the need to know the dynamic properties of the particular material. Indeed the relevant information required to understand the stability of the fresh shotcrete layer in-place only involves the mechanical properties of the material (shear, tensile and compressive strengths). Using the yield criterion concept, a hypothesis concerning the limit of elasticity of a material under any possible combination of stresses, permits one to work only with the stresses at failure (Yield is used here as a synonym of *failure* since yielding of fresh dry-mix shotcrete is considered to be accompanied by large strains that lead to poor in-place shotcrete quality). Neither the stress vs strain relationship nor the stress vs strain rate relationship are required to apply a failure criterion. To be able to characterise fresh

dry-mix shotcrete using a single failure criterion would thus provide the information required to investigate the parameters affecting the stability of a shotcrete layer.

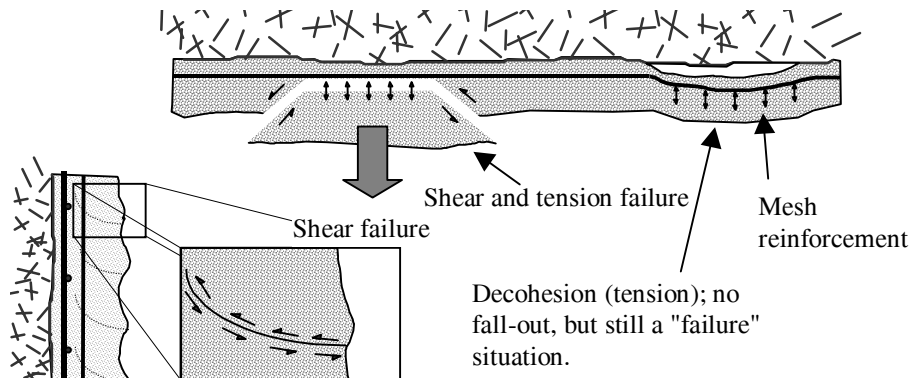


Figure 2. Failure mechanisms involved in build-up thickness situations.

The chosen failure criterion, however, should account for the existence of a tensile strength in the fresh material. Also, since the consistency of fresh shotcrete is close to that of consolidated clay or compacted earth, the common failure criterion applied to soils, the Mohr-Coulomb failure criterion [8, 9], was selected. As shown in Figure 3, this simple criterion acknowledges the existence of two material properties: the angle of internal friction, which represents the interlocking effect of the particles, and the intrinsic cohesion which represents the attraction between the particles (As opposed to the Tresca and Von Mises failure criteria often applied to metals, which considers the existence of only one material property, usually the shear strength). This failure criterion was observed by L'Hermite and Tournon [10] during direct shear tests on fresh concrete.

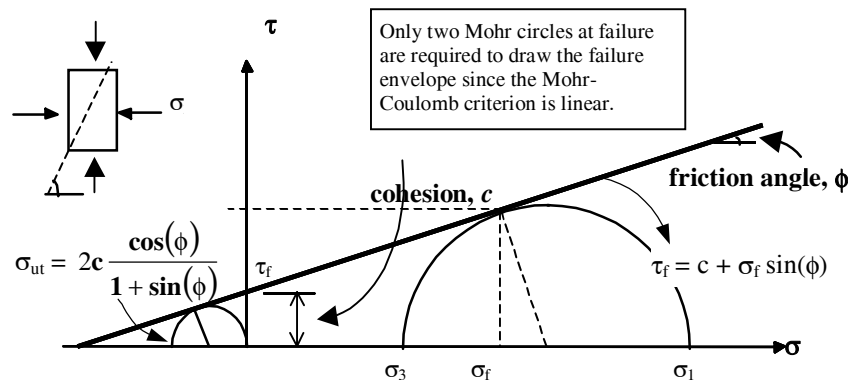


Figure 3. Representation of the Mohr-Coulomb failure envelope.

3.2 Placement

The rebound mechanisms, closely related to the placement phase of dry process shotcrete, have been reported in detail by Armelin [11]. In addition, visual observations combined with the information found in [12, 13] allow us to describe the behavior of an aggregate particle hitting a soft substrate. The various stages reached by a high velocity aggregate particle upon entering the soft shotcrete substrate are shown schematically in Figure 4. When considering the probability of rebound of a given particle, there are three quantities to consider: the kinetic energy of the incoming particle, the dynamic contact stress exhibited by the substrate during the penetrating event, and the work required to debond the particle [4].

First, consider a shotcrete substrate and an incoming spherical aggregate with a given amount of kinetic energy. Once the spherical indenter (aggregate) has transferred all of its kinetic energy into the substrate, it has reached zero velocity at its deepest position; the elastic energy stored in the substrate will then be returned to the indenter, possibly producing rebound, depending upon whether the amount of energy associated with debonding is greater than the elastic energy.

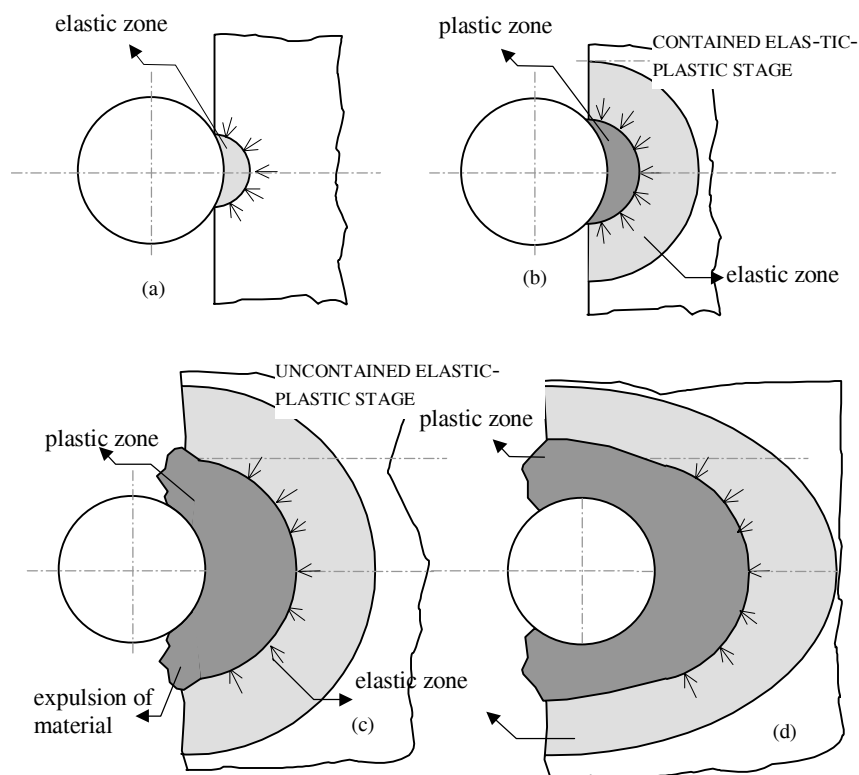


Figure 4. Indentation stages of an aggregate particle entering fresh shotcrete.

Depending on the velocity of the aggregate before the impact and the properties of the substrate, the zero velocity point can be reached at any of the 4 stages sketched in Figure 4. Obviously, the higher the kinetic energy of the aggregate and the lower the dynamic contact stress of the substrate, the deeper the aggregate will penetrate; in turn, a deep penetration will increase the debonding work required to pull out the aggregate, hence decreasing its rebounding probability. On the other hand, a low velocity or a stiff substrate reduces the volume penetrated by the aggregate. In this case, the debonding work is relatively small, due to the small contact area, which generates excessively high rebound values (sketches a and b). Obviously, the dynamic contact stress will vary according to the properties of the substrate onto which shotcrete is applied (hard rock, fresh shotcrete, etc.). This explains why rebound is highest in the first few millimeters of a shooting session and decreases to a constant value thereafter [14].

4 Experimental results – Stability

The stability of a number of shotcrete mixtures was evaluated in the laboratory using two different tests: the fresh tensile strength test and the fresh shear strength test, both described in

detail in [15]. As well, the consistency was evaluated using the U.B.C. Penetrometer [4, 5]. The results presented here are those of for four different mixtures. Three were made of 20% binder, 64% sand and 16% 10 mm crushed stone, and are identified as T10 for the normal portland cement mixture, T10+SF for the one made of normal portland cement and 10% silica fume (replacement by weight of cement) and T30 for the one made with high early strength portland cement. The last mixture, identified as T10@25%, was made of 25% normal portland cement, 60% sand and 15% 10 mm crushed stone. Figure 5 presents the results of both fresh shear strength and fresh tensile strength tests.

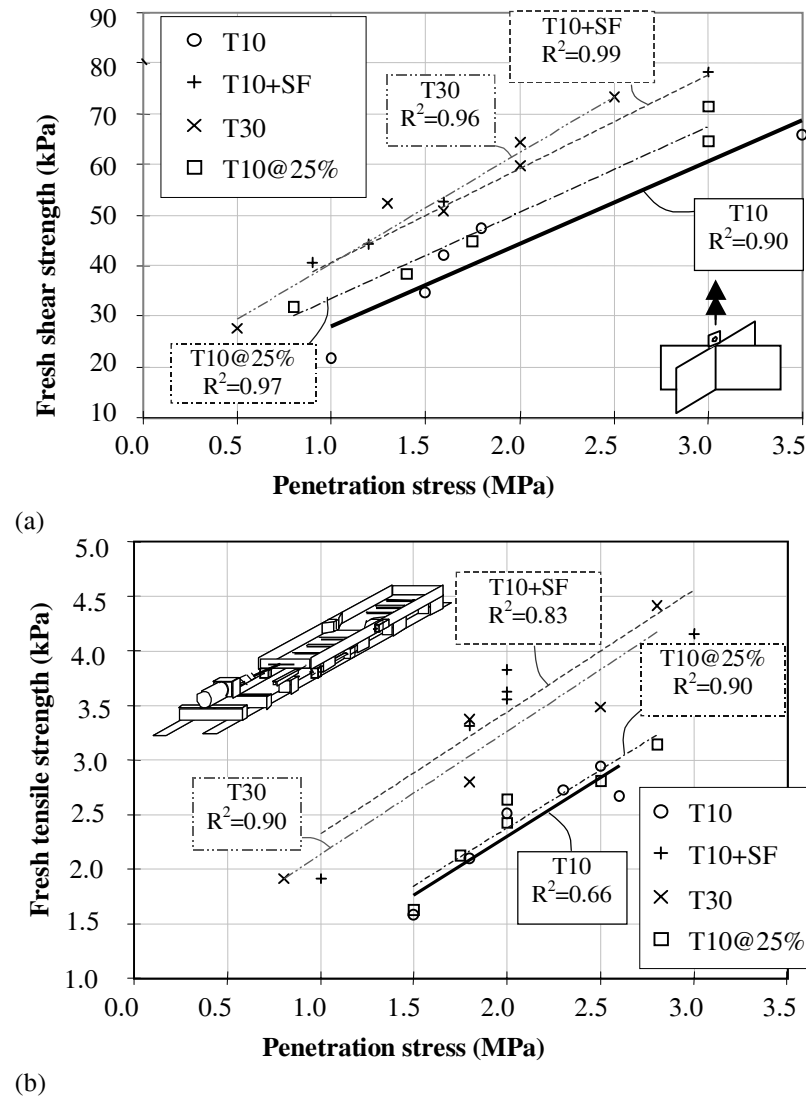


Figure 5. Fresh shear strength (a) and fresh tensile strength (b), as a function of the shooting consistency (i.e. the penetration stress).

Figure 5 shows clearly that, for stability purposes, the use of a silica fume binder or of high early strength portland cement yields better results. As intuitively expected, a stiffer shooting consistency leads to a higher tensile strength of the shotcrete. Moreover, the distinctly different relationships showed in Figure 5 indicate that there are significant differences between the mixtures themselves; they confirm the conclusion of [5], that “the consistency measurement is not sufficient by itself to completely characterize the properties of fresh dry-

mix shotcrete”. This justifies the need for at least a two-parameter yield criterion to characterize fresh shotcrete (Section 3.1).

To pursue the modeling of fresh dry process shotcrete, the angle of friction and the cohesion of the various mixtures were evaluated, using the nomenclature of Figure 3. From the fresh shear strength test (pure shear corresponding directly to the value of the cohesion) and the penetration stress measurement, it is possible to construct one failure envelope for one mixture shot at a given consistency. The mathematical treatment was inspired by [12] and [13], and is fully developed in [15]. The results are presented in Table 1

Table 1. Predicted cohesion and angle of friction using the combination of fresh shear strength and consistency results.

MIX	Consistency	Fresh	Fresh	c	ϕ^*	σ_{ut}^*
		tensile strength (kPa)	shear strength (kPa)			
T10	Dry**	3.4	60.6	60.6	34.4°	64.0
	Normal	2.3	44.3	44.3	33.3°	47.8
	Wet	1.2	28.0	28.0	30.5°	32.0
T10+SF	Dry	4.6	77.8	77.8	31.5°	87.2
	Normal	3.4	59.2	59.2	29.8°	68.6
	Wet	2.3	40.6	40.6	25.6°	51.1
T30	Dry	4.4	84.4	84.4	30.5°	96.5
	Normal	3.3	62.4	62.4	29.1°	73.3
	Wet	2.1	40.5	40.5	25.7°	50.9
T10@25%	Dry	3.4	67.5	67.5	33.1°	73.1
	Normal	2.4	50.5	50.5	31.8°	56.2
	Wet	1.3	33.4	33.4	28.3°	39.9

* σ_{ut} is the predicted ultimate tensile strength using ϕ and c (Figure 3).

** Dry, Normal and Wet, respectively, refer to penetration stress of 3 MPa, 2 MPa and 1 MPa.

The analysis of the ϕ and c values obtained is beyond the scope of this paper; however it is possible to compare the predicted tensile strength and the actual fresh tensile strength measured on shotcrete (Figure 6). The conclusion is that although the Mohr-Coulomb criterion is deficient in predicting the correct value of fresh tensile strength, there is a unique relationship between those two quantities. The discrepancies between the experimental and predicted values are most probably caused by the linear approach of the yield criterion on the tensile portion of the normal stress axis [13] and by the fact that fresh shotcrete is a heterogeneous material, which can lead to stress concentrations, initiating “premature” yield.

5 Experimental results - Placement

The discussion in Section 3.2 points out an important parameter of the fresh shotcrete during the placement phase, the dynamic contact stress (p_d). The dynamic contact stress of different shotcrete substrates was evaluated experimentally by Armelin [11], who validated the following relationship derived using contact mechanics principles [12]:

$$\text{Dynamic contact stress} = \frac{\text{Work of the penetration phase}}{\text{Volume displaced during penetration}} = \frac{W_{\text{PEN}}}{V_{\text{PEN}}} \quad (1)$$

In practice, one needs to know the kinetic energy of a particle when it impacts the fresh shotcrete surface, and the subsequent volume displaced. As described schematically in Figure 7, dropping a sphere from a given height and measuring the diameter of the indentation produced provides the required information.

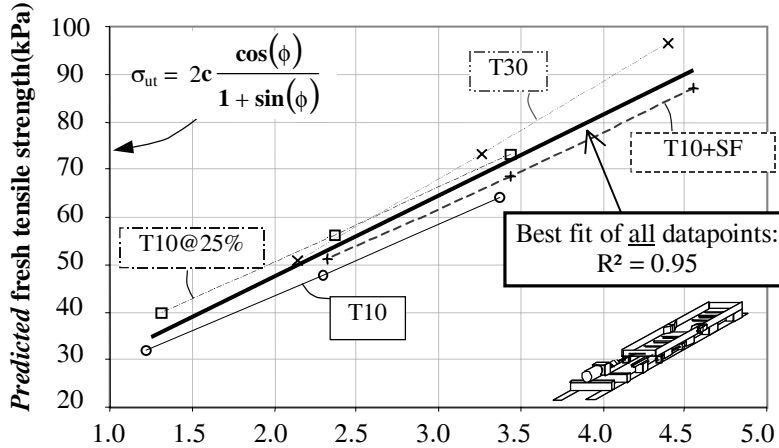


Figure 6. Relationship between the predicted and experimental fresh tensile strength.

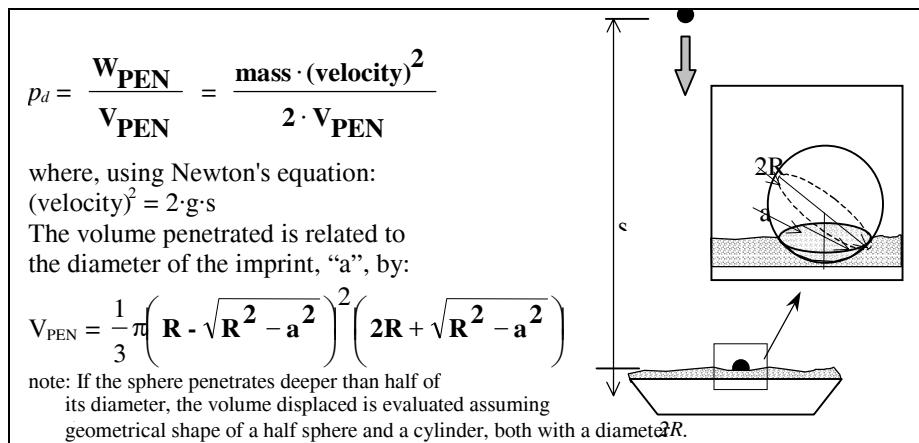


Figure 7. Evaluation of the dynamic contact stress, p_d .

To verify the variations in dynamic contact stress of fresh dry process shotcrete, three mixtures were shot; two as described above, T10 and T10+SF, and a third one, similar to T10+SF, shot with an air-entraining admixture mixed with the shooting water and identified as T10+SF+AEA (This is currently done in some parts of Canada to provide adequate protection against freezing and thawing in aggressive environments. The addition rate is normally of 15 ml of admixture per liter of shooting water). The results, each points being an average of 8 to 10 measurements, are presented in Figure 8.

The most important observation which can be made from Figure 8 is the absence of a unique relationship between the penetration resistance (consistency) and the dynamic contact stress. Instead, there seems to be a proportionality between those two quantities only for a given mix design. The steeper slope of the T10+SF mixture relative to the T10 mixture means that for a given shooting consistency (or penetration stress), the volume penetrated by an aggregate will be larger for the silica fume mixture, hence reducing the rebounding probability. The combination of Figures 5 and 8 confirms, through the evaluation of

fundamental properties, the positive effect of silica fume on both rebound and stability [11, 16, 17].

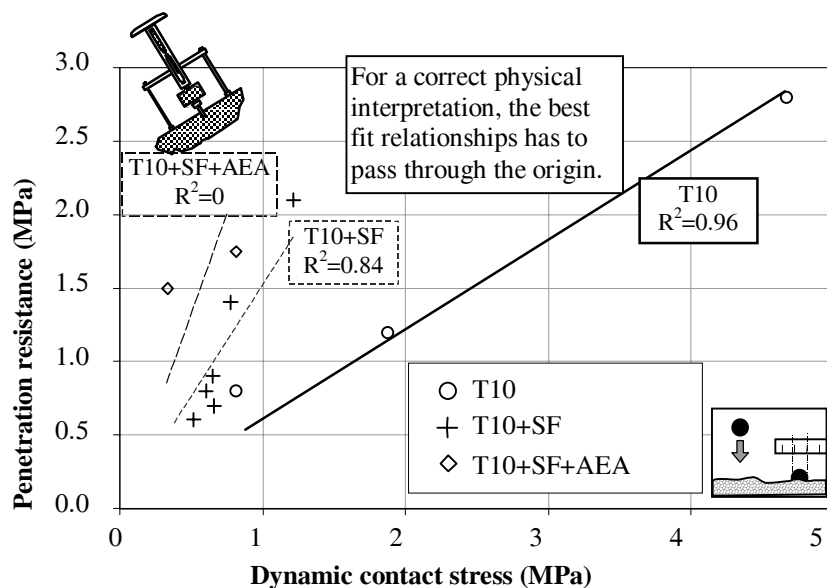


Figure 8. Penetration resistance vs. the average dynamic contact stress.

The two data points obtained for the T10+SF+AEA mixture indicate an even more significant reduction of p_d for a given consistency, thus suggesting lower rebound rates.

The importance of the dynamic contact stress as a fundamental parameter describing fresh dry process shotcrete is highlighted in Figure 9, where experimental values of rebound are plotted against the penetration stress and dynamic contact stress measurements. Although the results of only two mix designs are presented, they seem to indicate a unique relationship between overall rebound and the dynamic contact stress. This is particularly interesting because it suggests that a single parameter, the dynamic contact stress, might be sufficient to predict the overall rebound of any dry process shotcrete mixture (for a given shooting parameter set-up, i.e. air flow, hose diameter, water pressure, etc.).

The relative reduction of dynamic contact stress of the silica fume mixtures is comparable with the associated reduction of plastic viscosity in conventional concretes [2, 18]. Similarly, the air-entraining admixture, by producing a large number of small bubbles, usually decreases the plastic viscosity significantly [2].

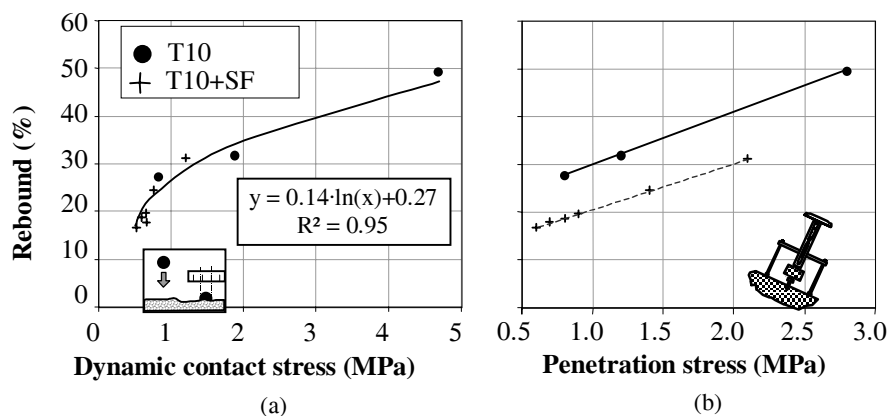


Figure 9. Rebound values as a function of (a) the dynamic contact stress and (b) the penetration stress.

6 Conclusions

The objective of this study was to investigate the placement and the stability of a fresh dry process shotcrete layer. The principal conclusions are:

The investigation of the fresh dry process shotcrete stability showed that this material obeys a yield criterion more complex than that proposed by Mohr-Coulomb. However, the simplicity of the Mohr-Coulomb criterion combined with the linear relationship of Figure 6 validates the approach used.

Replacing part of the cement by silica fume or using finer cement (such as high early strength cement) increases the shear and tensile strengths of the fresh material. In some cases, the fresh tensile strength was increased by almost 50% for a given shooting consistency when compared to the basic mixture (T10).

A very strong effect of silica fume was found on the dynamic contact stress. This is significant since the dynamic contact stress seems directly to affect the overall rebound rate.

The large property changes shown in Figures 5, 8 and 9 with regard to the penetration resistance pertains to the possibility of on-site quality control. The penetration test seems to be particularly suitable for that purpose, since it correlates well for a given mix design. A minimum penetration stress could be set to insure a minimum stability of the shotcrete layer, and a maximum value could be set to limit rebound.

7 Acknowledgements

The authors are grateful to the Natural Sciences and Engineering Research Council of Canada for its financial support of this project through the "Chaire industrielle sur le béton projeté et les réparations en béton" (Industrial Chair on Shotcrete and Concrete Repairs). The members of this Chair are: Ministère des transports du Québec (Quebec's Department of Transportation), Ville de Québec (City of Quebec), Master Builders Technologies Ltd, Sika Canada Inc., Béton Mobile du Québec Inc., King Package Materials and Co., Ciment St-Laurent Inc., and Lafarge Canada Inc.

8 References

1. Beaupré, D., (1994), "Rheology of High Performance Shotcrete", Ph.D. Thesis, Department of Civil Engineering, University of British Columbia, 250 pages.
2. Tattersall, G.H. and Banfill, P.F.G., (1983), "The Rheology of Fresh Concrete", Pitman, London, 1983, 365 pages.
3. Bartos, P., (1992), "Fresh Concrete Properties and Tests", Elsevier, N.Y., 292 pages.
4. Armelin, H. and Banthia, N., (1998), "Mechanics of Aggregate Rebound in Shotcrete", Part I and II, Materials and Structures, RILEM, Vol. 31, No 206, pp. 91-120 and No 207, pp. 195-202.
5. Jolin, M., Beaupré, D., and Mindess, S., (1999), "Tests to characterise properties of fresh dry-mix shotcrete", Cement and Concrete Research, Vol. 29, No 5, pp. 753-760.

6. Prudêncio, L.R., (1993), "Mix Design and Quality Control of Shotcrete", Ph.D. thesis, Departamento de Construcao Civil, Escola Politecnica da Universidade de Sao Paulo, Sao Paulo, Brazil, 1993.
7. Beaupré, D., Mindess, S., and Pigeon, M., (1993), "Rheology of Fresh Shotcrete", RILEM Proceedings #24, Special Concretes: Workability and mixing, Edited by P. Bartos, E&FN Spon, pp. 225-235.
8. Holtz, R.D. and Kovacs, W.D., (1981), "An Introduction to Geotechnical Engineering", Prentice Hall, Englewood Cliffs, New Jersey, 733 pages.
9. Terzaghi, K., Peck, R. B. and Mesri, G., (1996), "Soil Mechanics in Engineering Practice", 3rd ed., John Wiley & Son, USA, 549 pages.
10. Powers, T.C., (1968), "The Properties of Fresh Concrete", John Wiley & Sons, Inc., New York, 664 pages.
11. Armelin, H., Banthia, N, Morgan, D.R. and Steeves, C., (1997), "Rebound in Dry-mix Shotcrete", ACI Concrete International, Vol. 19, No 9, pp. 54-60.
12. Johnson, K.L. (1985) "Contact Mechanics", Cambridge University Press, U.K., 452 pages.
13. Hill, R., (1983), "The Mathematical Theory of Plasticity", Oxford Clarendon Press, UK.
14. Parker, H.W., Fernandez-Delgado, G. and Lorig, L.J., (1976), "A Practical New Approach to Rebound Losses" ACI SP-54, Shotcrete for Ground Support, American Concrete Institute, Detroit, p.149-187.
15. Jolin, M., (1999), "Mechanisms of Placement and Stability of Dry Process Shotcrete", Ph.D. Thesis, Department of Civil Engineering, University of British Columbia, 152 p.
16. Morgan, D.R., (1995), "Special Sprayed Concretes", in Sprayed Concrete: properties, design and application, edited by S.Austin and P.Robins, McGraw-Hill, Inc., 382 pages.
17. Morgan, D.R., (1988), "Dry-Mix Silica Fume Shotcrete in Western Canada", ACI Concrete International, Vol. 10, No 1, p.24-32.
18. Gjörv, O.E., (1992), "High Strength Concrete", Advances in concrete technology, Energy, Mines and Resources, Report MSL 92-6 (R), Canada, 1992, pp. 21-77.

Economic Design and Construction with Structural Lightweight Aggregate Concrete

Tor Arne Hammer

SINTEF Civil and Environmental Engineering, Trondheim

Klaas van Breugel

TU Delft, Delft

Steinar Helland

Selmer, Oslo

Ivar Holand

SINTEF Civil and Environmental Engineering, Trondheim

Magne Maage

Selmer, Trondheim

Jan P. G. Mijnsbergen

CUR, Gouda

Edda Lilja Sveinsdóttir

The Icelandic Building Research Institute, Reykjavik

1 Introduction

1.1 Background

Lightweight aggregate concrete (LWAC) has potential to offer weight reduction without significantly having to compromise the structural properties. Still, however, this material has not realized its potential as a commonly accepted alternative to normal weight concrete (NWC) or other construction materials. Main reasons for this are somewhat higher material and production costs, a common skepticism related to production properties, design/structural performance and durability, and the lack of sufficient and generally valid guidelines, rules and standards. Furthermore, a dependency on local/national conditions as to materials resources has provided specialized guidelines and standards in a way as to limit an all-European and cross-boarder application and trading with the materials. Another motivation to promote LWAC is that the growing shortage on traditional aggregate resources in great parts of Europe, combined with increasing focus on pollution and waste handling, is forcing the building and construction industry to look for alternative solutions that can combine these issues.

1.2 Project Information

Based on this background an European consortium was established in 1995 with the aim to run a project within the framework of the Brite EuRam III program. The baseline is an international state-of-the-art and extensive national research in which the consortium partners have played a key role. The project draws on this present knowledge, co-ordinates, validates and utilizes the results in an extended development towards a more generally applicable, European concept for LWA concrete technology.

The project started in April 1997 and the planned end is April 2000. The total budget is 3 mill. Euro. The consortium covers a broad variety of sectors involved: The coordinator is Selmer (contractor), Norway. The other partners are:

Germany:	Lias-Franken Leichtbaustoffe (LWA manufacturer)
Iceland:	IBRI (research institute), Ice-Consult (consultant)
The Netherlands:	BetonSon (precast industry), CUR (R&D coordinators), Smals (aggregate manufacturer), TU-Delft (university), TU-Eindhoven (university), VASIM (LWA manufacturer).
Norway:	Aker Exclay (LWA manufacturer), NTNU (university), SINTEF, (research institute)
Spain:	Dragados (contractor)
United Kingdom:	Taywood Engineering (contractor)

The consortium has established a close liaison to other bodies like the CEN TC 154 (European standardization for aggregates), CEN TC 104 (Standardization of production of concrete and execution of concrete structures) and CEN TC 250 (Design standard for concrete structures) and fib working group on lightweight concrete (fib is the umbrella organization for some 40 national concrete associations worldwide)

Information on the project is available from the web-site www.sintef.no/bygg/sement/elcon.

1.3 Objective

The overall objective is to develop a reliable and cost effective design and construction methodology for structural concrete with LWA of natural aggregates (i.e. pumice) as well as artificial aggregates, the latter manufactured from natural materials (i.e. expanded clay) or industrial waste (i.e. flyash). One part objective is to be innovative in the development/improvement of materials, methods and elements/components that can open for new and un-exploited applications. Another part objective is to improve international standards and guidelines.

The project aims at all structural LWAC from "low strength" (10 - 15 MPa) to "high strength" (60 - 80 MPa), and densities ranging from 800 to 2200 kg/m³.

The project is organized in five technical tasks that are presented in the following.

2 Task 1: Baseline Report on Technology and Material Development

In Task 1 a summary and evaluation was made of different types of existing information on LWAC. The work was split up in two parts. In the first part an short historical overview is given of the evolution of LWA and LWAC. This overview, in which emphasis was on the situation in Germany, Iceland, UK, The Netherlands, Belgium, France, Norway and Spain, is followed by a compilation of clauses in existing codes and standards dealing with LWA and LWAC. In these compilation codes which are in use in Austria, Italy, Japan and the USA were considered. The codes were compared with each other with respect to a number to topics, viz. materials properties, modelling of LWAC, data for prestressing, rules for structural analysis, clauses for different limit states, durability, detailing, fire resistance, execution, quality control and concrete technology. The aim of the work in this part of task 1 was to check these codes for omissions and inconsistencies, which might cause a threshold for using LWAC in practice.

The results of this work have been laid down in a report that ends with a list of white spot in the codes.

The second part of Task 1 focuses on the materials properties in more detail. The report covering this part of Task 1 starts with an explanation of the major differences between LWAC and NWC. Concretes with both natural LWA and manufactured LWA are considered. Differences are observed in all stages of the lifetime of the concrete, i.e. the stage of mixing, execution, pouring, hydration, strength and stiffness, creep and relaxation, response on thermal loads, permeability and durability, to mention at least a number of them. The reason for a different behaviour of NWC and LWAC goes back to the porous nature of the LWA and the water present in the aggregate. Different types of aggregate with different pore size distributions behave differently. Some LWAC's require special care during execution. Particularly the pumpability of some LWAC's is a point of concern. Another aspect of special interest concerns the ductility and brittleness of LWAC. Fire and freeze-thaw resistance of LWAC is compared with that of NWC. Experimental data on creep and shrinkage of LWAC appeared to be scarce. Data on materials properties of high strength LWAC is very limited. The report, with up to hundred pages, ends with a list of white spots and list of references. Both reports of Task 1 are available on the web-site if EuroLightCon.

3 Task 2: Lightweight Aggregates

One objective is to identify and evaluate new and unexploited sources of raw materials for LWA production, that can offer a combination of environmental and technical issues, i.e. utilizing waste/secondary materials in a production of aggregates that can meet the relevant requirements for structural use. These materials are classified in three groups: Spoil, silt and fly ash. The health risks (e.g. regarding leaching of possible toxic substances), chemical stability and manufacturing resources and investments have been evaluated. Test production of these materials has taken place.

Another objective is to use the impact of the project to ensure that the classification system and evaluation system being drafted by the TC-154 group on LWA will cover all types of LWA for structural LWA- concrete.

4 Task 3: Lightweight Aggregate Concrete Production

The objectives of Task 3 have been to: 1) Develop a mix design method with a particular focus on production properties, standard compliance requirement like density, strength, durability and costs. The method will be based on a set of characteristic properties of the constituents determined by both existing and new methods. 2) To evaluate test methods for LWA in the fresh state, and develop new methods if necessary. 3) Develop a Quality Assurance procedure for LWA concrete production, transport, placing and compaction, especially when it is different from normal density concrete.

The mix design approach is primarily based on a particle-matrix model developed for NDA concrete under Brite EuRam project 5480. However, the particle system has to be paid particular attention due to the fact that LWA has a very high porosity. Both light weight,

normal density and recycled LWA are included in the program. The mix design method is based on optimizing both mechanical properties as well as production properties including stability and pumpability. Procedures will be established for the characterization and control of central mix properties, such as the effective water/binder ratio, segregation and workability.

Test methods both for constituents as input parameters to the mix design method and test methods for fresh concrete normally used for ND concrete, will be evaluated. Aggregate parameters like grading curves and void volume seems to be important for the mix design mode. The matrix is well characterised by the flow properties developed in the Brite EuRam project 5480. In fresh state, special attention will be paid on methods for documenting workability, air content, stability and effective water/binder ratio. A new method, for documenting stability in fresh LWA concrete is developed based on different densities as a result of segregation.

The part on Quality Assurance will include a combination of requirements on light weight aggregates, handling of aggregates as well as mixing procedures, transport, placing and compaction. This will be a technical guideline how to fulfil the requirements on aggregates and fresh and hardened concrete properties. Special concern will be given to the different procedures that have to be used when the LWA is prewetted or when remixing is necessary. The guideline will be compatible to the European CEN standards prEN 13055-1 (Light-weight aggregates), prEN 206 (Production of concrete) and prENV 13670-1 (Execution of concrete structures).

5 Task 4: Lightweight Aggregate Concrete Properties

On the basis of the state-of-the-art report on materials properties compiled under Task 1, a number of experimental and theoretical studies has been formulated. The research should fill up some of the white spots formulated in Task 1. This materials research, which is partly still underway, focuses on the properties of mixtures with a low water/binder ratio, i.e. high strength LWAC (HSLWAC), and mixture made with natural LWA. Two partners had performed experimental studies on the deformational behaviour at early ages of low water/binder ratio concrete. The autogenous shrinkage and swelling for different mixtures was determined experimentally and compared with NWC. Also creep and long term strength of HSLWAC is investigated. Optimisation studies were performed, aiming at high strength at minimum costs, i.e. minimum cement content. The mechanical properties of LWAC made with different types of natural LWA have been investigated and compared with data given in codes.

Although literature indicates that on the average the durability of LWAC is good, it was decided still to perform a number of durability studies. Emphasis was on the performance of LWAC with low water/binder ratios under simulated or real environmental conditions. Different mixtures, made with different LWA and different binders, were tested on their resistance against chloride penetration. Results obtained so far confirm that LWAC does not perform worse than NWC, in spite of the fact that the porosity of LWAC is much higher than that of NWC. The reason for this is, most likely, that the chloride penetration depth is mainly determined by the quality of the paste and to a minor extent by the porosity of the aggregate. Moreover, the good bond between matrix and LWA results in a dense interfacial zone between these two components. This improves the diffusions resistance of the LWAC.

Besides laboratory studies also the performance of real LWAC structures is tested. For about fifteen projects were selected, in service for up to thirty years. Carbonation depths and chloride profiles are determined on cores drilled from the structures.

6 Task 5: Lightweight Aggregate Concrete Structures

The objectives of Task 5 are divided on four sub-tasks: 1) To develop design criteria and design rules for lightweight aggregate concrete structures with special emphasis on high performance structures utilizing LWA concrete with high strengths relative to the strength and density of the aggregates. 2) To identify and develop new and under-exploited applications for LWAC and combinations of LWAC and normal density concrete, including application of fibres. 3) To identify and prepare the necessary additional requirements, documentation and procedures for the LWAC production and construction (quality assurance). 4) To prepare requirements and procedures for recycling of crushed LWAC.

As examples of detailed activities under the various sub-tasks are mentioned: Design rules for strength and deformation of LWAC, valid for a large number of different LWAs, are needed. Design rules rely upon mechanical properties, which at present mainly are described by empirical formulae with two parameters: strength and density. The objective of the activity is to formulate a composite model as a convenient tool for the description of the interaction between aggregates and matrix. In particular it is necessary to understand and describe quantitatively the low long-term strength of LWAC that has been reported in various research projects. All rules shall be formulated as suggested modifications of clauses in ENV 1992-1-4: 1994 and/or supplements to CEB-FIP Model Code 90.

Case studies documenting experience from LWAC structures built so far and comparisons with structures built with normalweight concrete are compiled. The compilation will be based on a close cooperation with fib and published as a fib Bulletin. Promotion and distribution of the report will be undertaken by fib. The publication will contain about 30-40 two-page presentations. fib Task Group 8.1 will discuss a first draft at the fib Symposium in Prague October 99. The final text will be subject to approval by the two bodies, and the bulletin will appear early in 2000.

Properties of concrete with recycled LWA will be compared with those of concrete with recycled normalweight aggregates. The influence of recycled LWA on mix design will be studied in Task 3, whereas the influence on strength development, shrinkage, modulus of elasticity and freeze/thaw-resistance is done in Task 4. The data from Task 4 will be fundamental for the work on design rules in Task 5.

A New Type of High-performance Lightweight Concrete

Harald S. Müller and Stefan Linsel
University of Karlsruhe, Germany

1 Abstract

Some few unfavourable technical properties of structural lightweight concrete being mainly connected with its production, consistency and transportation have been overcome by the development of a new technology, where the lightweight aggregate particles are coated with a thin cementitious layer by the application of a special coating technology. Besides the effect of making the aggregates impermeable against water, also a significant increase of the strength of the aggregate particles is obtained. Experimental results on properties of fresh and hardened lightweight concrete made with coated aggregates show that both workability and strength are considerably improved. It is shown that this new type of high-performance lightweight concrete may be produced having a compressive strength higher than 90 MPa while the unit weight remains below 2000 kg/m³.

2 Introduction

Structural lightweight concrete combines a low density with a considerably high compressive strength. Despite of this advantage compared to the properties of ordinary structural concrete the use of lightweight concrete is limited which is to some extent due to the difficulties being connected with its production, consistency and transportation. These problems result from the open porosity of the mineral lightweight aggregate particles which may lead to a pronounced absorption of the mixing water. The related reduction of the effective water content of the cement paste in the concrete mix affects primarily the workability of the fresh concrete but also strength and durability of the hardened concrete. In order to fix the total amount of mixing water or the effective water-cement ratio, the lightweight aggregates must be wetted. Among the procedures recommended, the use of pre-wetted saturated aggregates represents the most usual one [1]. Even then the pumping of lightweight concrete, which is advantageous for economic reasons, frequently fails [2]. In addition some negative effects on the behaviour of hardened lightweight concrete are accompanied by using saturated aggregates. These problems can be overcome by using lightweight aggregates having a dense and impermeable surface. This may be achieved by coating the porous mineral aggregate particles by a thin cementitious layer, which yields also an increase of the strength of the aggregates [3]. The application of coated lightweight aggregates leads to the production of a new type of high-performance lightweight concrete.

3 Technology of coating lightweight aggregate particles

A specific high-efficiency mixer has to be used to coat the porous, mineral lightweight aggregate particles with a thin cementitious layer. The coating process starts with the mixer being filled with dry, preferably coarser fractions of lightweight aggregates before a well-defined amount of cement paste slurry having an optimised composition is added. Through the agglomeration process within the mixer the lightweight aggregates are uniformly coated with a thin but dense layer of cement paste. The isolation of the individual grains is achieved by a dosed powdering of the aggregate particles with a bonding agent at the end of the agglomeration process. Figure 1 shows the sectional view of a lightweight aggregate particle coated with a thin cementitious layer by means of the new coating technology.

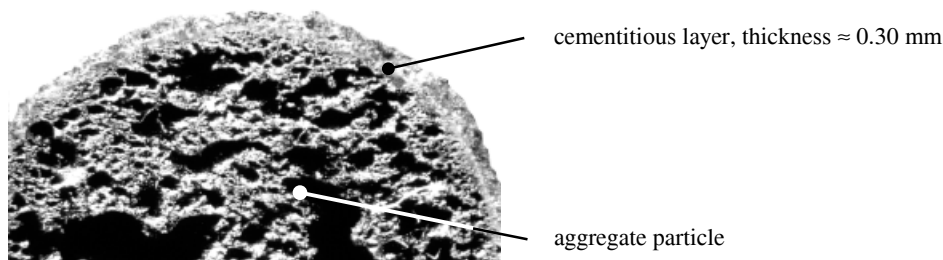


Figure 1. Coated lightweight aggregate particle of the type Liapor F4, grain size approx. 5 mm

The water-cement ratio of the cement paste slurry may be fixed to approx. 0.36 for different kinds of expanded clay aggregates. The addition of silica fume as well as a small quantity of plasticizer to the mix have been found to be favourable both with respect to obtain a dense hardened cement paste structure of the layer and to facilitate the coating process. The thickness of the cementitious layer is approx. 0.25 to 0.35 mm, depending on the kind of lightweight aggregates. The amount of cement to coat 0.1 m³ of lightweight aggregate particles ranges between 35 and 45 kg. Further details may be found in [3].

4 Properties of coated lightweight aggregates

The water absorption of uncoated and coated lightweight aggregates are compared to each other in Figure 2. The obtained results clearly indicate that the coating considerably reduces the water absorption of the aggregates both for 30 minutes of water storage as well as for the applied storage under water at a pressure of 50 bar. This effect holds true both for rather porous (Liapor F4) and denser (Liapor F8) lightweight aggregates.

The observed reduction of the water absorption under a high water pressure is a basic requirement in view of a successful pumping of the fresh lightweight concrete. Two large scale pumping tests with common concrete pumps have been already successfully conducted using a lightweight concrete of the strength class LC 45/50 made with coated aggregates.

The coating leads to an increase of the unit weight of the lightweight aggregates which is the more pronounced the higher the porosity, i.e. the lower the unit weight of the aggregates. The increase of the unit weight by coating Liapor F4 is approx. 45 %, whereas the increase for an aggregate grain having a higher unit weight, such as Liapor F8, is approx. 18 %. However, the coating also produces a remarkable gain in strength of the grains, leading to a significant increase of the strength/density ratio of the concrete [3].

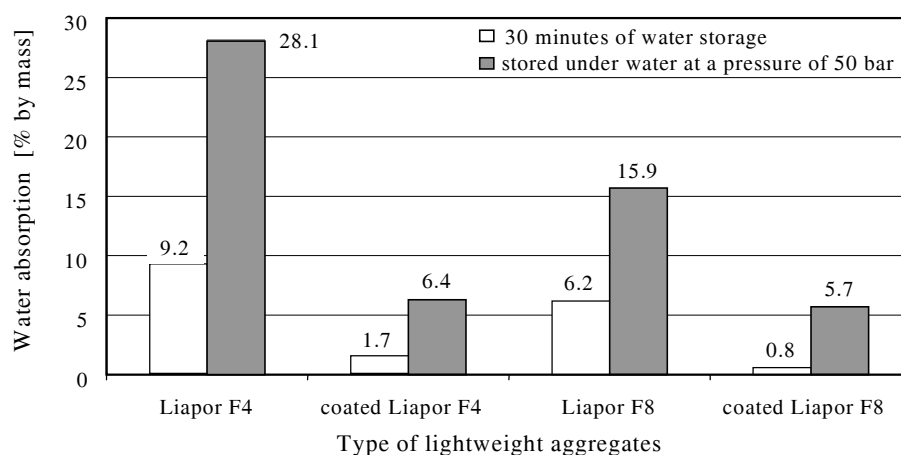


Figure 2. Water absorption of two types of coated and uncoated lightweight aggregates at 30 minutes of water storage or subjected to a water pressure of 50 bar, respectively

5 Composition and properties of high-performance lightweight concrete

Within a research program being underway, various mixes for high-performance lightweight concretes using coated lightweight aggregates have been developed. The main objective consisted in obtaining an optimum strength/density ratio for a well-workable and pumpable lightweight concrete which also complies with economical requirements. Table 1 summarizes the composition of two lightweight concretes of the strength classes LC 45/50 and LC 70/77 having a unit weight of 1.56 and 1.96 kg/dm³, respectively.

Table 1. Main constituents and composition of two high-performance lightweight concretes

constituents and composition			lightweight concrete	
			LC 45/50	LC 70/77
cement	CEM I 42.5 R	kg/m ³	450	450
water	natural	kg/m ³	133	92
addition	microsilica-slurry	kg/m ³	68	68
water-cement ratio		—	0.38	0.33
aggregates	natural sand	kg/m ³	130	555
	lightweight sand	kg/m ³	340	-
	gravel	kg/m ³	-	140
	coated Liapor	kg/m ³	550	710

The production process of the lightweight concretes made with coated aggregates complies completely with the procedure being well-known for ordinary normal-weight concrete. The addition of low quantities of a plasticizer and a retarder ensures a sufficient workability over a period of more than 2 hours without any re-mixing of the concrete. Figure 3 illustrates changes of the consistency of the fresh concrete measured by means of the flow table test immediately, 60 and 120 minutes after mixing.

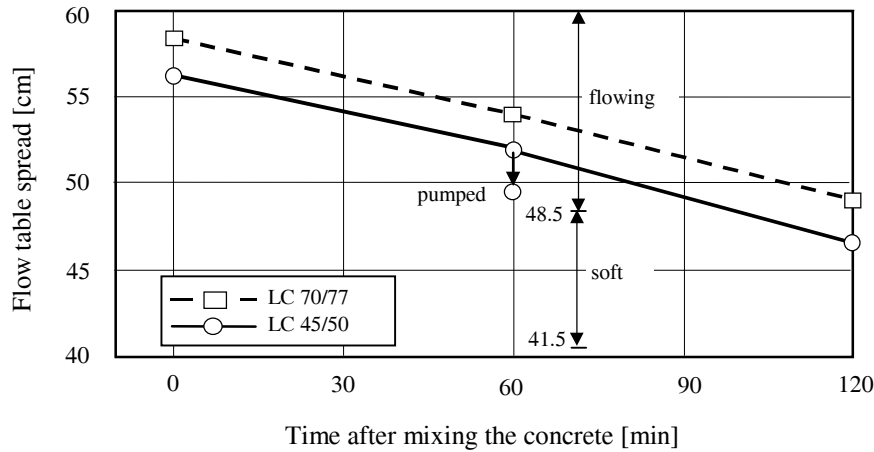


Figure 3. Consistency of fresh lightweight concretes made with coated aggregates, determined immediately, 60 and 120 minutes after mixing

The values of the flow table spread of approx. 45 cm and higher at a time of 120 minutes after mixing indicate a good workability. Even after pumping the lightweight concrete only a minor decrease of the workability has been observed. The use of microsilica proved to be a sufficient measure to reduce the tendency of segregation by increasing the cohesiveness of the concrete mixes.

In limiting the cement content of the lightweight concretes to a value of 450 kg/m³, a critical rise in temperature due to the heat of hydration is avoided, even for the lightweight concrete LC 70/77 which undergoes a very rapid strength development (see Table 2).

Compressive strength values of both structural lightweight concretes are indicated in Table 2. It may be seen that the lightweight concrete LC 70/77 reaches a compressive strength of 77.2 MPa already at an age of 2 days which corresponds to approx. 83 % of the strength at an age of 28 days. The development of the compressive strength is obviously less pronounced than it is known from normal-weight concrete. The reason is, that the strength of the cement mortar matrix in the high-strength lightweight concrete exceeds already at an early age the strength of the lightweight aggregates. Consequently, a further gain in the strength of the matrix is only accompanied by a minor increase of the concrete strength.

The modulus of elasticity at an age of 28 days has been found to be 19320 MPa for the LC 45/50 and 30940 MPa for the LC 70/77, indicating reasonably low elastic deformations under load.

Table 2. Compressive strength of structural lightweight concretes

age of concrete [days]		2	7	28
compressive strength [MPa]	LC 45/50	–	58.9	63.5
	LC 70/77	77.2	83.3	93.1 ¹⁾

¹⁾ determined at an age of 30 days

Finally, it should be noted that the ratio of the compressive strength to the density of hardened lightweight concrete made with coated lightweight aggregates is significantly higher than the corresponding value of a comparable lightweight aggregate concrete made with uncoated aggregates [3].

6 Conclusions and outlook

A new technology to coat mineral lightweight aggregates with a thin and dense cementitious layer has been developed. This layer prevents the absorption of the mixing water by the aggregates even in the case of the application of a water pressure. Consequently, the use of coated lightweight aggregates in structural lightweight concrete ensures a sufficient workability of the fresh concrete mix over a long period, and pumping of this type of lightweight concrete proved to be possible without any problems. By the application of coated lightweight aggregates also a significant increase of the compressive strength and of the strength/density ratio of the concrete is achieved. Hence, this new type of high-performance lightweight concrete allows interesting applications for the construction industry. In co-operation with partners from industry, university and authorities the developed concrete will be applied in a pilot project for the construction of a prestressed concrete bridge.

7 References

1. S. Helland, M. Maage: "Strength Loss in Un-remixed LWA-Concrete". International Symposium on Structural Lightweight Aggregate Concrete, Proceedings, Sandefjord, Norway, 20.-24. June 1995.
2. M. Sandvik, T. A. Hammer: "The Development and Use of High Performance Lightweight Aggregate Concrete in Norway". International Symposium on Structural Lightweight Aggregate Concrete, Proceedings, Sandefjord, Norway, 20.-24. June 1995.
3. H. S. Müller, S. Linsel, H. Garrecht: "Zementgebundene Umhüllung von Blähton-leichtzuschlägen zur Verbesserung der Eigenschaften von frischem und erhärtetem Konstruktionsleichtbeton". Research Report, Institute of Concrete Structures and Building Materials, University of Karlsruhe, to be published in 1999.

8 Acknowledgement

The research on the development of the coating technology for lightweight aggregates and the investigations on the development and properties of high-performance lightweight concretes have been supported by the companies Lias-Franken Leichtbaustoffe GmbH & Co. KG Hal-lerndorf and Lias Leichtbaustoffe GmbH & Co. KG Tuningen, Bilfinger + Berger Bauaktiengesellschaft and by the Federal Minister of Economy. Their financial contributions are gratefully acknowledged.

Shrinkage-Reduced High Performance Concrete

Peter Schwesinger and Günter Sickert
Bauhaus-University Weimar

1 Introduction

Even though there are numerous research projects on high performance normal weight concrete (HPC) only little is known on the long-term behaviour of those concrete whose dense aggregates content is partly (HPLWAC) or completely (HPLC) replaced by lightweight aggregates. In this cases the interaction of a high performance matrix and the water stored in the pore system of the LWA and their influences on creep and especially on shrinkage were of particularly interest. In pursuance of this aim a comparison between high performance concrete without and with LWA - both in the same range of strength - was needed. Besides this the influence of sealed and unsealed specimen surfaces has been investigated. The deformation measurements for shrinkage were started at an age of 20 ... 28 h; the early age shrinkage was not observed.

2 Mix Composition and Characteristics

2.1 Water Absorption

The properties of concrete depends both on the properties of the individual components and their compatibility. The aggregate type has to satisfy a high strength/density potential. At the present stage the upper limit of lightweight high performance concrete is margined to the compressive strength of the aggregate. By using Liapor 9.5 a high density lightweight aggregate in 4 - 8 mm fraction and a unit loose weight of 950 kg/m^3 , concrete with a 75 - 85 MPa compressive strength can be produced realistically also with respect to practical needs.

This LWA consists of expanded clay with a spherical geometry and a pore volume of approximately 55 %. According to manufacturers data the crushing resistance is 168,8 kN /1/. One major advantage of the LWA is the development of a pozzolanic reaction between the LWA and the cementitious paste. Because of the porous structure lightweight aggregates have a considerable water absorption potential. One of the problems arising was to know the exact absorption rate while mixing the concrete. So this rate has been measured by store oven dried (24 h at $105 \text{ }^\circ\text{C}$) LWA in fresh water. The test results are presented in Fig. 1.

Dry LWA hardly ever becomes completely saturated when used in concrete admixtures. Consequently the absorption rate of the aggregate in concrete has to be less than in free water. Nevertheless the knowledge of the exact absorption rate in fresh concrete is indispensable for realise an aimed effective water/binder-ratio. Furthermore the absorption rate depends on kind, size and initial moisture content of the aggregate, real w/b-ratio and consistence of the fresh concrete. A material-volume model has been developed to obtain the real rate of water

absorption in fresh concrete. For concrete investigated here the absorption rate after 25 minutes reached values between 5,6 and 6,0 mass-%.

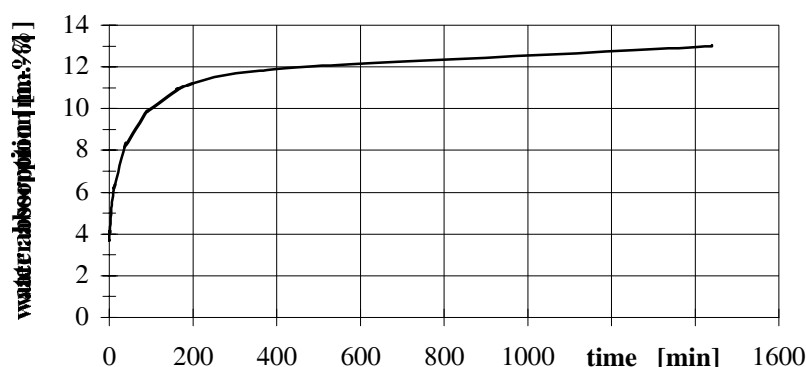


Figure 1: Free water absorption of dried Liapor 9,5 when soaked in pure water

2.2 Mix Composition of the Concrete

To get information on the influence of the LWA on the time dependent properties, different aspects has to be taken into account. The concrete without and with different contents of LWA should have nearly identical compressive strengths. Their effective w/b-ratio should be similar. As a consequence 5 different concrete mixes were com-posed. The Mix 1 without any LWA is the reference concrete for both the concrete with comparable compressive strength and the concrete with identical effective w/b-ratio.

The moisture-related condition of the LWA, dry, pre-soaked or any intermediate state, is of major interest: Using dry LWA will have a negative influence on the workability of concrete whereas using pre-soaked LWA will complicate the evaluation of the exact effective w/b-ratio /2/. Therefore the LWA has been moisturised with 1/3 of the mixing water for about 45 seconds prior to adding the cement. On this way the concrete mixtures as shown in Table 1 were realised.

To achieve the required slump, superplasticizer had to be added while mixing and therefore the target value of the effective w/b-ratio could not be obtained in all cases. The exact ratio-values of all designed concrete mixtures can be taken from Table 2. The LWA volume in relation to the total concrete volume increases obviously by a decrease of concrete density. While the LWA volume for Mix 2 and Mix 3 is 31%, it is 54 respectively 49% for Mix 4 and Mix 5.

Table 2: Mix design of HPLC, HPLWAC and HPC

Components	Concrete					Unit	
	Mix 1	Mix 2	Mix 3	Mix 4	Mix 5		
Cement: CEM 42,5 R	452	463	450	462	474	kg/m ³	
Mikrosilica (SF)	45,2	46,3	45	46,2	47,4	kg/m ³	
Superplasticizer (SP)	13,9	16,4	13,3	10,3	6,7	kg/m ³	
Aggregates total (agg _{tot})	1746	1441	1435	1256	1143	kg/m ³	
Sand	0,125/0,25	96	101	100	100	91	kg/m ³
	0,25/0,5	148	130	129	126	114	kg/m ³
	0,5/1	140	144	143	138	126	kg/m ³
	1 / 2	166	144	143			kg/m ³
Gravel	2/4	253	216	215			kg/m ³
	4/8	384					kg/m ³
	8/16	559	187	187			kg/m ³
Liapor 9,5	4/8		519	517	892	812	kg/m ³
LWA Volume		313	312	538	489		dm ³ /m ³
Water total (w _{tot})		145	136	144	131	192	kg/m ³
Water absorbed by LWA (w _{abs})			31	31	70	45	kg/m ³
effect. Water (w _{eff}) = (w _{tot}) - (w _{abs})		145	105	113	61	147	kg/m ³

Table 3: Ratio values of the different concrete mixtures

Ratio	Concrete					Unit
	Mix 1	Mix 2	Mix 3	Mix 4	Mix 5	
w _{tot} /c	0,32	0,36	0,39	0,44	0,50	kg/kg
w _{eff} /c	0,32	0,29	0,32	0,28	0,40	kg/kg
(w _{eff} +SP)/(c+SF) = eff.	0,32	0,30	0,32	0,28	0,38	kg/kg
w/b						
SF/c	0,1	0,1	0,1	0,1	0,1	kg/kg
SP/c	0,031	0,036	0,030	0,022	0,014	kg/kg
agg _{tot} /c	3,87	3,11	3,19	2,72	2,41	kg/kg
w _{abs} /LWA	-	0,059	0,060	0,079*)	0,056	kg/kg

*) This value seems to indicate a measuring error

2.3 Fresh and Hardened Concrete Properties

A further aim of the pre-investigations was to determine the influence of the lightweight aggregate on the mechanical properties. The compressive strength was measured at 28 days (cubes 150 mm and cylinders d = 150 mm, h = 300 mm). The values were randomised to cube strength (200 mm cube) according to DIN 1048, Part 5. The modulus of elasticity was measured at sealed and drying cylinders (d = 103 mm, h = 500 mm) to gain information on the drying effect on the modulus of elasticity. These cylinders which correspond to the size of the specimen used for the creep and shrinkage tests were also taken to measure the compressive strength $f_{ck,cyl 103,500}$ to determine the exact load level for the creep tests.

Table 4: Concrete density and mechanical properties at concrete age of 28 d

Concrete property	Concrete		Unit			
	Mix 1	Mix 2	Mix 3	Mix 4	Mix 5	
slump (15 min)	50	49	53	39	39	cm
air content	2,1	2,0	2,2	1,9	1,8	Vol.-%
fresh concrete density	2,40	2,13	2,12	1,98	1,91	kg/dm ³
oven dry concrete density	2,32	2,01	2,00	1,82	1,78	kg/dm ³
compress. strength: $f_{ck,cube\ 200mm}$ measured on cubes 150 mm	105	96	90	86	80	N/mm ²
compress. strength: $f_{ck,cube\ 200mm}$ at cyl. d=150; h=300 mm	107	101	100	78	78	N/mm ²
modulus of elasticity: E_c cylinder d=103; h=500 mm:	40400	31900	31500	25800	24200	N/mm ²
compress. strength (sealed) $f_{ck,cyl}$	89	88	81	86	84	N/mm ²
compress. strength (drying) $f_{ck,cyl}$	87	84	85	86	80	N/mm ²
modulus of elasticity (sealed) E_c	40200	31800	33900	30500	29500	N/mm ²
modulus of elasticity (drying) E_c	34600	30600	28500	26300	20900	N/mm ²

3 Test Program

3.1 Test Equipment

The creep tests were realised by using a servo-hydraulic loading device developed for static and dynamic short and long-term investigations. This equipment allows besides others a very fast and precise loading rate /3/. For the registration of all measurands a computerised multiple-point measurement unit UPM 100 was used.

3.2 Time and Environment Related Conditions

A minimum of at least 3 parallel samples for each mixture and each test parameter were casted. For compaction a vibrating table was used; the samples were demoulded after 24 hours. After that the samples were either stored at 20°C and 65% r.H. or sealed completely to investigate basic and drying creep/shrinkage separately. The commencement of the shrinkage measurements varied between 20 and 28 hours after casting. The minimum duration of these measurements was 210 days. The creep specimen were loaded at 28 days and the test duration was 98 days at a loading degree of 35-40% related to the cylinder strength $f_{ck,cyl\ 103,500}$. Afterwards creep recovery was observed for at least another 84 days.

4 Test Results

4.1 Creep and Creep recovery

The characteristic values of creep and creep recovery were investigated. Even though the creep deformation of the different concrete varies only in a small range the creep coefficient for HPLWAC and HPLC is reduced by approximately 15% due to diversified elastic

properties. Both the basic creep coefficient and the basic creep are almost equal for all HPCs using LWA independent of the applied amount of LWA. Although there is a certain amount of drying creep of HPC with LWA, the drying creep coefficient is basically not influenced by the application of LWA. Therefore the creep coefficient of HPLWAC and HPLC is independent of the storage conditions of the specimen (Figure 3). The amount of drying creep is primarily influenced by the matrix, a specific dependence of LWA can not be determined.

The total creep coefficient of HPLWAC and HPLC is reduced by approximately 15-20% compared to HPCs without LWA. This positive impact is a result of the reduced difference of the modulus of elasticity of the mortar and the LWA which leads to an improved stress redistribution. This improved feature prevents the development of peak stresses and therefore reduces irreversible deformation components. A specific influence of the amount of lightweight aggregates on total creep can not be ascertained and therefore it can be stated that there is only a minor influence of aggregates. The total creep depends basically on the mortar content and the effective w/b-ratio.

Finally can be stated, that the use of lightweight aggregates leads to an increased creep recovery of concrete. The above mentioned adjustment of the modulus of elasticity of mortar and aggregate and the resulting improved stress distribution cause a reduction of irreversible creep. As a consequence LWA improves the relaxation of concrete. Whereas the creep recovery of HPC seems to approach an ultimate value it is not finalised for HPLWAC and HPLC even after a cycle of 125 days. A definite influence of the amount of applied LWA can not be determined by analysing the test results.

4.2 Shrinkage

The characteristic values of shrinkage investigations are presented in Figures 2 and 3 showing the amounts of autogenous shrinkage and drying shrinkage separately. Selected shrinkage test will be continued until reaching a steady state condition.

The internal water reservoir of the LWA has a great influence on the shrinkage behaviour of the investigated concrete. The pre-moistured LWA caused a stable swelling at all sealed specimen which still occurred even now after nearly two years (Figure 2). The results show also that the higher the LWA content the higher is the swelling of concrete.

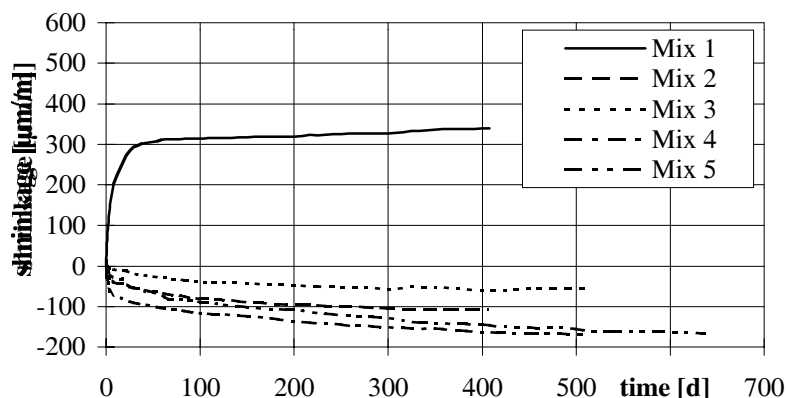


Figure 2: Autogenous shrinkage (sealed specimen) of HPC, HPLWAC and HPLC

The drying shrinkage is also strongly influenced by the use of LWA (Figure 3). Normal HPC shows distinctive drying shrinkage only at very early age. Approximately 70% of the

total 450 day drying shrinkage has occurred by an age of 30 days. On the other hand the drying shrinkage of HPCs with LWA develops constantly over a long period of time and is significantly larger than the drying shrinkage of concrete without LWA. During the investigated period there was no sign of an approximation to a steady state value.

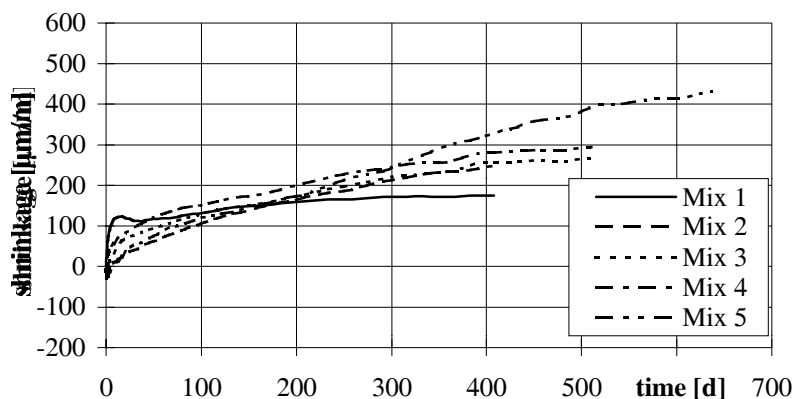


Figure 3: Drying shrinkage of HPC, HPLWAC and HPLC

The summation of drying and autogenous shrinkage is determined as total shrinkage. For the low density HPC it is significantly lower than that of normal density HPC, but its development is increasing over time and the ultimate value is up to now unidentified. The time dependent deformation at the very early age has great influence on the total shrinkage. Due to the available testing equipment the first measured data were obtained after demoulding at the age of approximately 24 hours. Therefore any shrinkage deformations does not include the early age deformation part.

5 Concluding Remarks

From the test results the following conclusions can be drawn.: The lightweight aggregate Liapor 9,5 can be used for a reliable production of HPLWACs and HPLCs due to its spherical shape and the relatively dense outer shell. The water absorption of the analysed LWA is approximately 6,0 mass-% during a mean mixing and compaction time. The LWA demonstrates a high density/strength potential; a concrete with a dry density of $1,8 \text{ kg/dm}^3$ and a compressive strength of 100 N/mm^2 was able to be produced under laboratory conditions. A LWA content of around 30 % reduces the modulus of elasticity at equal compressive strength by 25 %. The internal moisture conditions were able to reduce or eliminate autogenous shrinkage, whereas the drying shrinkage was reduced drastically due to the same reason.

Total creep deformation is basically influenced by the matrix properties and less by the use of LWA. Creep recovery of high performance concrete using LWA is higher than of HPC without LWA and takes place even after a observed period of 125 days.

Further research is needed to clarify the reasons of swelling of the sealed specimen of HPLWAC and HPLC. To get an overall understanding of the autogenous shrinkage the time dependent properties of the concrete at the very early age have to be investigated [4]. Therefore shrinkage measurements immediate at casting are essential. On this basis it seems to be possible to develop a shrinkage reduced high performance concrete.

6 References

1. EuroLightCon: "Light Weight Aggregates Datasheets". European Union - Brite EuRam III, Document BE96 - 3942/MG/R1a, September 1998
2. Punkki, J.; Gjorv, O.E.: "Effect of Aggregate Absorption on Properties of High Strength Lightweight Concrete". Proceedings of the International Symposium on Structural Lightweight Aggregate Concrete, Sandefjord 1995, Norwegian Concrete Association, Oslo, 1995
3. Schwesinger, P.; Sickert, G.; Ehlert, G.: "Zum Übergangskriechen von hochfestem Beton". Advances in Building Material Science - Festschrift Wittmann, Aedificatio Publishers, Freiburg, 1996
4. Takada, K.; van Breugel, K.; Koenders, E.A.B.; Kaptijn, N.: "Experimental Evaluation of Autogenous Shrinkage of Lightweight Aggregate Concrete". Autoshrink '98, Proceedings of the International Workshop on Autogenous Shrinkage of Concrete, June 13-14, 1998, Hiroshima, Japan, JCI, 1998

Influence of Specimen Size/Geometry on the Potential For Shrinkage Cracking in Rings

W. Jason Weiss^a, Wei Yang^b, and Surendra P. Shah^b

^aPurdue University, West Lafayette, IN USA

^bNorthwestern University, Evanston, IL USA

1 Abstract

Early-age cracking can occur in concrete when drying, autogenous, or thermal shrinkage is prevented by the surrounding structure. While the potential for early-age shrinkage cracking is influenced by many factors including the magnitude of shrinkage, rate of shrinkage, stress relaxation, degree of structural restraint, and age-dependent material property development; this paper highlights a recent investigation which has illustrated that shrinkage cracking is also influenced by the size/geometry of the structure. A series of experiments were conducted using three different ring size specimens to illustrate this fact. The rings have the same inner diameter and drying surface to volume ratio but different wall thickness. Despite having the same residual strain (and similar residual stress), the experiments showed that the age at which concrete cracks varies with specimen size. This paper highlights how a fracture mechanics based solution can be used to describe the size/geometry dependent early-age cracking behavior of concrete. The stress development is simulated by considering that concrete behaves as an aging, linear, visco-elastic material. A non-linear fracture mechanics failure criterion is used to determine the time and geometry dependent tensile strength. Finally, the developed stress and size/geometry/age dependent strength are used to predict the age of cracking. The theoretical simulations were found to compare reasonably with the experimental observations.

2 Experimental Observations

Two concrete mixtures are described in this paper, a normal strength concrete (plain) and a normal strength concrete with a shrinkage-reducing admixture (SRA). Both mixtures consisted of 65% aggregate by volume with equal components of coarse (9 mm) and fine (3 mm) aggregate with a liquid to binder ratio (approximately water-to-cement ratio) of 0.5. The first mixture (plain) was a conventional composition while the second mixture (SRA) had 4% of the water replaced with a glycol-based shrinkage-reducing admixture (SRA). After mixing, the concrete was placed in the forms, rodded, finished with a steel trowel, placed under a plastic sheet to prevent moisture loss, and maintained at 30°C for 24 hrs. The specimens were demolded at an age of 24 hrs and placed in a 30°C, 40% RH environment for the remainder of the experiment.

Age-dependent fracture and compressive properties were also measured in accordance with the procedures outlined in the RILEM recommendations (1), ASTM C-39, and C-469 (2)

using three specimens at each age. Figure 1 summarizes the average age-dependent mechanical properties from these mixtures. It can be seen that the mechanical behavior of the plain and SRA mixtures is similar.

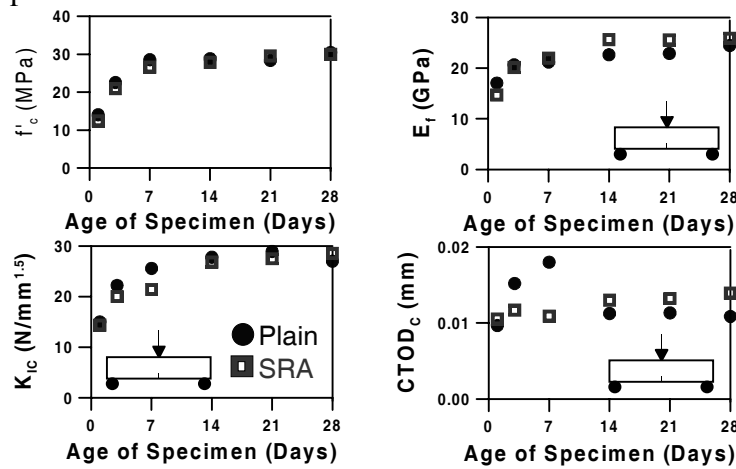
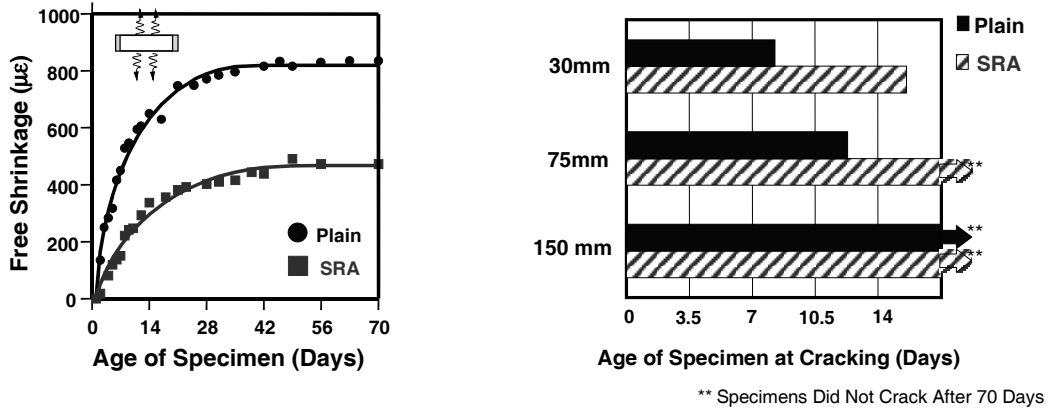


Figure 1. Age Dependent Material Property Development for the Plain and SRA Mixtures (a) Compressive Strength, (b) Elastic Modulus, (c) Critical Stress Intensity Factor, and (d) Critical Crack Tip Opening Displacement

Free shrinkage (ϵ_{SH}) was measured using three $30 \times 100 \times 400$ mm³ prisms that were permitted to dry only from the top and bottom surface (100×400 mm²; note that the volume to surface ratio is identical to that of the rings) of the specimens using the procedure outlined in ASTM C-341 (2). Figure 2a illustrates that the free shrinkage measured on the concrete containing the shrinkage-reducing admixture (SRA) resulted in a substantial reduction in free shrinkage at both early and later ages, which is consistent with previous findings (3). For further details on the testing procedures used in this investigation, the reader is referred to the literature (4,5).

A total of nine ring specimens were cast for each mixture. Each ring specimen consists of a concrete annulus that was cast around a solid steel cylindrical plate with a radius of 150 mm. Three different wall thicknesses were selected for the concrete rings, 30, 75, and 150 mm to produce specimens with a ratio of the outer radius to inner radius (R_O/R_I) of approximately 1.25, 1.50, and 2.00. The depth of the rings was relatively short (30 mm) to minimize the influence of moisture gradients. The top and bottom surfaces of the ring were permitted to dry freely while the outer circumference of the ring was sealed to prevent moisture loss using a rubberized silicon coating which was applied immediately after demolding. It should be noted that by allowing uniform moisture loss from the top and bottom surfaces, uniform shrinkage strains are introduced in the radial direction. The ring specimens were monitored every 12 hours for the development of visible cracks and the average age at which cracking was observed in the three specimens is noted in Figure 2b. It can be seen that as the wall thickness of the ring increases, the potential for cracking is reduced even though the specimens exhibit identical free shrinkage. The smallest plain concrete rings cracked on average at approximately 8 days, whereas the medium sized ring cracked at an average of 10.67 days, and the largest ring had not cracked when the testing was stopped at 70 days. In addition, the use of the shrinkage-reducing admixture (SRA) can be seen to delay or prevent cracking in all the rings.



a)

b)

Figure 2. (a) Free Shrinkage Measured on a 30 mm x 100 mm Section Sealed on the Sides and (b) Average Age of Cracking For Rings with Different Wall Thickness

3 Theoretical Prediction of Cracking Potential

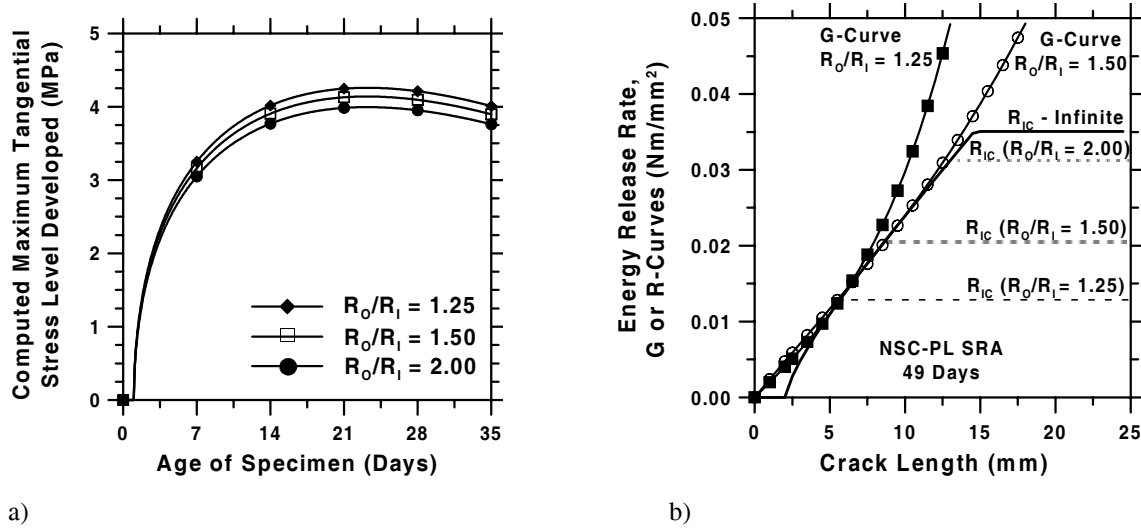
Cracking resistance, like other material properties, develops slowly over time and can be linked with the degree of hydration in cementitious systems. In addition to the slow development of material properties, the residual stresses that develop are also time-dependent since shrinkage (i.e., moisture loss) typically takes place over a long period of time (i.e., months to years). The residual stress that develops in concrete as a result of restraint can not be computed directly by multiplying the free shrinkage by the elastic modulus (i.e., Hooke's Law) since the concrete is sensitive to stress relaxation (creep), resulting in a significant reduction of overall specimen stresses, especially at early-ages. The residual stress that develops in a thick wall ring specimen over time can be written in terms of the radial (σ_r) and circumferential (σ_θ) component using the following equations:

$$\sigma_\theta = \int_0^t A(\xi) \left(1 + \frac{R_o^2}{r^2} \right) d\xi, \quad \sigma_r = \int_0^t A(\xi) \left(1 - \frac{R_o^2}{r^2} \right) d\xi \quad (1)$$

in which R_o represents the outer radius, r represents the radial coordinate, and $A(\xi)$ represents a time constant of integration which can be obtained by solving the integral equation (2) which satisfies the condition that zero displacement is permitted at the internal boundary.

$$\int_0^t [C(t, \xi)] \left[(1 - \nu) + (1 + \nu) \frac{R_o^2}{R_i^2} \right] A(\xi) d\xi + \varepsilon_{SH}(t) = 0 \quad (2)$$

where R_i denotes the inner radius, ν is Poisson's ratio, ε_{SH} is the free shrinkage as described in Figure 2a, and $C(t, \xi)$ is the creep compliance (in this work $C(t, \xi)$ is taken as that described by Muller (6)). Using this approach and combining the age dependent material properties (Figure 1) the maximum tensile stress (circumferential $\sigma_{\theta-R_i}$ at $r = R_i$) that develops in the plain concrete rings can be determined as illustrated in Figure 3a.



a) b)
Figure 3. (a) Influence of on Time and Size on the Maximum Tensile Stress Development Plain Mixture and (b) the R-Curve Approach for Predicting Failure

Once the level of residual stress is determined, an appropriate failure criterion can be applied to assess whether the ring can be expected to crack. The failure criterion used in this model relates the fracture resistance (R-Curve) of a material to the energy consumed in propagating (driving) a crack (G-Curve). The material is thought to reach its peak load (failure) when the energy rates are equal ($G=R$), as are their derivatives ($dG/da=dR/da$) implying the G-Curve is at the outer edge of the stable failure region.

The R-Curve envelope (infinite SEN specimen) is shown as the solid line whereas the dashed lines denote the point where the resistance becomes constant for various size specimens. The resistance curve (R-Curve) used in this investigation is based on the derivation of Ouyang and Shah (7) in which a geometry dependent R-Curve can be represented by the following relationship

$$R = \beta\psi(a - a_0)^{d_2} \quad (3)$$

where a is the crack length, a_0 is the initial crack length (assumed to be 2mm), and β , ψ , and d_2 can be determined from the experimentally measured stress intensity factor, critical crack tip opening displacement, and elastic modulus (Figure 1). Further details describing the R-Curve (7) and how it is used in this approach are available in literature (6).

The G-Curve represents the energy that is available to cause the crack to grow (i.e., drive the crack). The G-Curves for two different size specimens are shown in Figure 3b (lines with the symbols). It can be seen that as the size of the specimen increases (R_0/R_1 changes from 1.25 to 1.5) the G-Curve becomes flatter and eventually approaches a straight line approximately by the time $R_0/R_1 = 2.0$. This is important because it signifies that a larger value of the G-Curve would be necessary to cause it to come in contact with the R-Curve, especially as the crack length grows.

Mathematically the G-Curve is written using the classical fracture definition that describes the energy that is supplied to propagate the crack (G-Curve) as,

$$G = \frac{(\sigma\sqrt{\pi a}f(a/w))^2}{E} \quad (4)$$

in which E is the elastic modulus, σ is the maximum tensile stress level (in this case circumferential stress at the inner radius $\sigma_{\theta-RI}$), a is the crack length, and $(f(a/w))$ is the geometry correction factor. This geometry factor is unity in the case of an infinite body with

an internal crack and 1.12 in the case of semi-infinite specimen with an edge crack. In this work, the expressions for the geometry factor were obtained from Wu and Carlsson (8) as listed below.

$$\begin{aligned} f(a/w)_{1.25} &= 1.12 - 0.0887(a/w) + 3.8572(a/w)^2 - 0.0006(a/w)^3 - 0.7679(a/w)^4 \\ f(a/w)_{1.50} &= 1.12 - 0.6648(a/w) + 5.3858(a/w)^2 - 6.7727(a/w)^3 + 3.6573(a/w)^4 \\ f(a/w)_{2.00} &= 1.12 - 1.5692(a/w) + 5.5320(a/w)^2 - 7.8713(a/w)^3 + 4.5378(a/w)^4 \end{aligned} \quad (5)$$

The critical resistance stress level (size dependent tensile strength), $\sigma_{\theta-R_I}$, was calculated for various ages of drying using age-dependent material properties (Figure 1) with the R-Curve approach. This was done by incrementally increasing the stress level until the failure criterion is met ($G=R$ and $dG/da=dR/da$). It can be seen that as the specimen becomes larger, (increasing R_O/R_I) the specimen becomes more resistive to cracking (i.e. the tensile strength increases). This is significant in that it differs from a maximum strength based approach in which a unique tensile strength exists that is independent of specimen size. It should be noted that as the R_O/R_I increases beyond the value of approximately two (for these mixtures), the cracking resistance approaches the theoretical uni-axial tensile strength of concrete as reported by Jenq and Shah (9).

Figure 4 shows the age of cracking for plain concrete that is defined as the age when the residual stress that develops due to restraint is equal to the strength predicted using the fracture approach. It should be noted that while the fracture approach predicts a slightly earlier age of cracking the general trend is relatively similar to the behavior observed in the experiments (i.e., size/geometry dependence) whereas the tensile strength prediction would predict a more similar age of cracking for all the mixtures. The degree to which the geometry dependence exists is dependent on the material composition and a reduction in brittleness corresponds with stronger size/geometry dependence.

4 Summary and Conclusions

In conclusion, this paper has illustrated that an ultimate strength criterion may be inappropriate to accurately predict the potential for restrained shrinkage cracking. Experimental results were presented which showed that the age at which shrinkage cracking occurs can be influenced by the specimen dimensions. Residual stress development was calculated by considering concrete as an aging, linear, visco-elastic cylinder in which shrinkage induced displacements are prohibited at the inner radius. A non-linear elastic fracture mechanics theory was utilized to illustrate that the age at which shrinkage cracking occurs in restrained concrete is size, geometry, and material dependent. A favorable correlation was observed between the theoretically predicted age of cracking and the experimentally observed age of cracking.

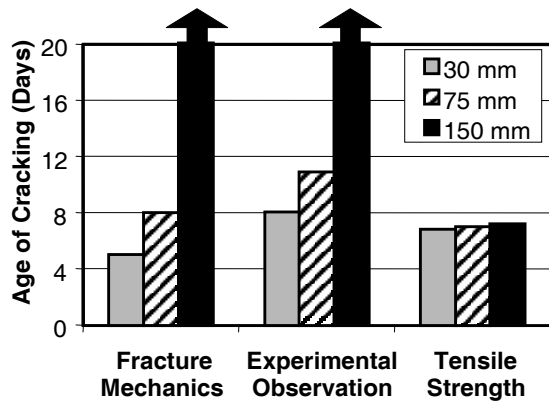


Figure 4. Age of Cracking Predicted Using the Fracture Mechanics Approach Compared With Experimental Observation

5 References

1. RILEM Committee on Fracture Mechanics of Concrete - Test Methods, RILEM Materials and Structures, 1991, 23, 138, 457-460
2. ASTM Annual Book of ASTM Standards, Vol. 4.02, © 1994
3. Shah, S. P., Karaguler, M.E., and Sarigaphuti, M. ACI Materials Journal, 1992 89, 3, 88-90
4. Weiss, W. J., Yang, W., and Shah, S. P., ASCE Journal of Engineering Mechanics, 1998, 124, 7, 765-774
5. Weiss, W. J., Yang, W., and Shah, S. P., Accepted ASCE Journal of Engineering Mechanics, In press
6. Müller, H. S., 1992, ACI SP 135-1, 1-19
7. Ouyang, C., and Shah, S. P., Journal of the American Ceramics Society, 1991, 74, 11, 2831-2836
8. Wu, X. R., and Carlsson, A. J., Pergamon Press, Oxford England, © 1991
9. Jenq, Y. S., and Shah, S. P., ASCE Journal of Engineering Mechanics, 1985, 111, 10

The Authors gratefully acknowledge the Support of the National Science Foundation Center for Advanced Cement-Based Materials and Grace Construction Co. – Conn.

Highly Durable Precast Special Concrete

A.J. M. Ferreira, P.P. Camanho, M. Cristina Fernandes, M. A. V. Figueiredo, A.A. Fernandes
Instituto de Engenharia Mecânica e Gestão Industrial, Faculdade de Engenharia da Universidade do Porto
Rua dos Bragas, 4050-123 Porto Codex, PORTUGAL

Abstract

Polymer concrete is a relatively new concrete with a resin binder. These concretes aim to produce high-performance structures with high mechanical and corrosion-resistance properties. In this paper the results of three-point bending tests are discussed. The Taguchi method was applied, to plan the experimental programme and identify possible correlations and interactions among the mechanical behaviour controlling parameters.

1 Introduction

Polymer concrete is a relatively new kind of concrete where a resin system binds together natural aggregates, such as silica sand. It is produced by mixing a liquid thermoset resin with inorganic aggregates (such as gravel, sand and fly ash). Initiators and promoters are added to the resin prior to its mixing with the inorganic aggregates to initiate the curing reaction. Polymer concrete therefore consists of well-graded inorganic aggregates bonded together by a resin binder instead of the water and cement binder typically used in normal cement concrete [1]. Typical resins used are polyester, epoxy or methacrylate thermoset resins. The most common type of binder utilized in polymer concrete is unsaturated polyester because of its good properties and relatively low cost.

The advantages of polymer concrete are its very good strength, very good durability (e.g., freeze-thaw, acid, and abrasion resistance), very low permeability, and very fast curing time (polymer concrete cures in a few minutes or hours while portland cement concrete cures in a few days or weeks). The use of polymer concrete materials is growing very rapidly in many structural precast applications such as utility components (e.g., drains for acid wastes, underground vaults and junction boxes, sewer pipes, power line transmission poles), transportation-related components (e.g., median barriers, bridge panels, railroad ties), and building panels [2].

The good strength and durability properties of polymer concrete allow the production of high quality precast components with very thin cross sections and low cover depths (in reinforced concrete), thus reducing dead loads in structures and minimizing transportation and erection costs. The very fast cure time of polymer concrete enables the rapid and efficient use of forms and other production facilities and confers to the structures higher resistance to large stresses due to transportation and erection operations.

Like portland cement concrete, polymer concrete has relatively low tensile strength compared to its compressive strength. Therefore, sudden and brittle failures occur in planes where tensile stresses exceed the tensile strength of the material. Reinforcing steel or FRP (fiber reinforced plastic) rods are therefore added in tensile zones of polymer concrete to increase its strength capacity, ductility and toughness [3-6]. The objective of this paper is to report an experimental programme on polymer concrete, designed using Taguchi method [7-11].

2 Experimental Set-up

The samples were produced in prismatic shapes: 16x4x4cm for bending tests (figure 1).

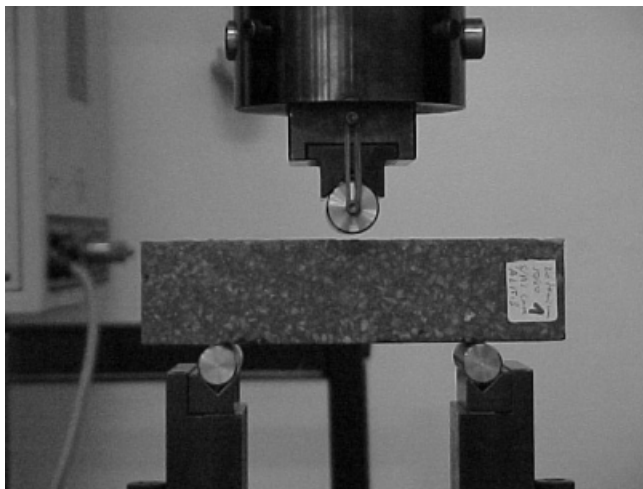


Figure 1 – Prismatic samples tested in three-point bending

The experimental plan was prepared according to Taguchi method [7-11]. Five fabrication factors at two levels were chosen. The number of potential combinations, for this case would be costly. The Taguchi method reduces the number of tests to be performed, by the use of pre-set orthogonal arrays, without the loss of relevant information. Interactions among factors can be identified through the application of this method. Table 1 illustrates factors and levels selected. Table 2 shows the experimental plan devised.

Table 1 – Factors and levels (% in weight)

	FACTORS				
	Type of resin	Additives	Resin content	Type of sand	Post-cure
Level 1	Polyester	No	17%	Clean sand	No
Level 2	Epoxy	25%	20%	Foundry sand	Yes

The selected array was L16 [7-11]. This array has 16 lines, corresponding to 16 tests performed. This array allows the evaluation of major effects of the factors on performance and the interaction between factors.

For each combination of factors, indicated in table 2 , three tests were performed in a total of 48 tests.

Table 2 – Experimental plan, L16 (2^{15})

Test	Resin	Charge	% resin	Type of sand	post-cure
1	Polyester	No	17%	Clean	no
2	Polyester	No	17%	Foundry	yes
3	Polyester	No	20%	Clean	yes
4	Polyester	No	20%	Foundry	no
5	Polyester	25%	17%	Clean	yes
6	Polyester	25%	17%	Foundry	no
7	Polyester	25%	20%	Clean	no
8	Polyester	25%	20%	Foundry	yes
9	Epoxy	No	17%	Clean	yes
10	Epoxy	No	17%	Foundry	no
11	Epoxy	No	20%	Clean	no
12	Epoxy	No	20%	Foundry	yes
13	Epoxy	25%	17%	Clean	no
14	Epoxy	25%	17%	Foundry	yes
15	Epoxy	25%	20%	Clean	yes
16	Epoxy	25%	20%	Foundry	no

Table 3 – Main results for three-point bending tests

Test	Max Load [N]	Flexural Strength [MPa]	Flexural toughness [N.mm]
2	2467.4	5.8	730.3
9	4240.4	9.9	1301.6
1	4273.2	10.0	1427.5
11	4356.3	10.2	2274.0
4	5182.2	12.1	1581.7
3	5491.5	12.9	1780.4
7	6323.6	14.8	1828.9
13	7050.0	16.5	1656.7
12	7229.8	16.9	4329.0
10	7881.1	18.5	2522.4
5	10335.9	24.2	2750.0
15	12052.3	28.2	3818.1
6	14406.6	33.8	5018.8
8	14689.4	34.4	4707.4
16	17439.7	40.9	6511.3
14	17893.3	41.9	6888.2

3 Results and discussion.Conclusions

Figure 2 displays a typical load-displacement curve resulting from the flexural test of polymer concrete beams.

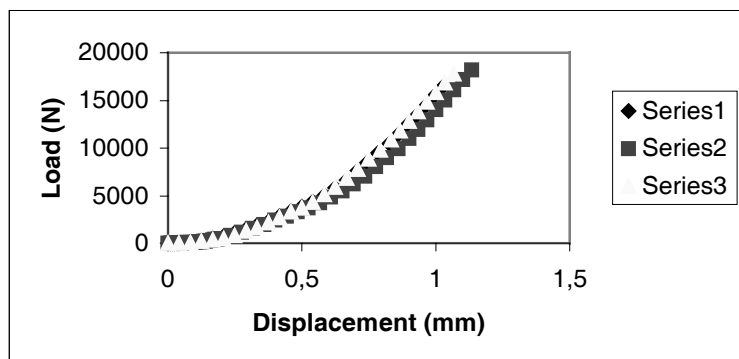


Figure 2 – A typical load-displacement curve for polymer concrete beams under flexural tests

The results indicated in table 3, represent the average responses of the tests carried out (three tests for each combination), measured by three different parameters: maximum load, flexural strength and flexural toughness.

Table 4 – Main results of the ANOVA

Factors:	DF	Max. Load		Flexural Strength		Flexural Toughness	
		P-Value	% Contrib.(P)	P-Value	% Contrib.(P)	P-Value	% Contrib.(P)
Type of Resin	1	0.0001	3.58	0.0001	3.56	0.0001	9.31
% of Charge	1	0.0001	56.82	0.0001	56.80	0.0001	31.29
% Resin	1	0.0589	0.21	0.0577	0.22	0.0034	1.97
Type of Sand	1	0.0001	17.75	0.0001	17.77	0.0001	25.12
Post-cure	1	0.0015	0.84	0.0015	0.84	0.0208	1.07
Type of Resin * % of Charge	1	0.2762	0.02	0.2779	0.02	0.8149	0.21
Type of Resin * % Resin	1	0.0865	0.16	0.0837	0.17	0.0031	2.02
Type of Resin * Type of Sand	1	0.0001	2.44	0.0001	2.44	0.0001	4.91
Type of Resin * Post-cure	1	0.3869	0.02	0.3905	0.02	0.0296	0.91
% of Charge * % Resin	1	0.2397	0.03	0.2379	0.03	0.0226	1.03
% of Charge * Type of Sand	1	0.0001	9.53	0.0001	9.50	0.0001	11.91
% of Charge * Post-cure	1	0.0001	2.28	0.0001	2.28	0.0584	0.62
% Resin * Type of Sand	1	0.8420	0.07	0.8461	0.07	0.6800	0.18
% Resin * Post-cure	1	0.0318	0.31	0.0324	0.30	0.3377	0.01
Type of Sand * Post-cure	1	0.0001	2.57	0.0001	2.59	0.3215	0.00
Residual	32		3.37		3.39		9.44
Total	47		100.00		100.00		100.00

A statistical analysis (ANOVA) of the results was performed in order to evaluate the effects of the main factors and identify potential interactions between factors.

Table 4 shows the results of the ANOVA analysis: 5% significance tests were carried out. The contributions of the different factors to the response total variance are illustrated.

The study of table 4 shows that the main contributing factors to behaviour of the polymer concrete as measured by different response parameters are as follows: Strength: charge (56.8%), type of sand (17.8%) and type of resin (3.6%). A significant interaction between charge and type of sand was observed (9.5%)

Toughness: charge (31.3%), type of sand (25.1%) and type of resin (9.3%). An interaction charge/type of sand was also identified (11.9%).

Figures 3 to 5 illustrate the main effects and interactions of the controlling factors.

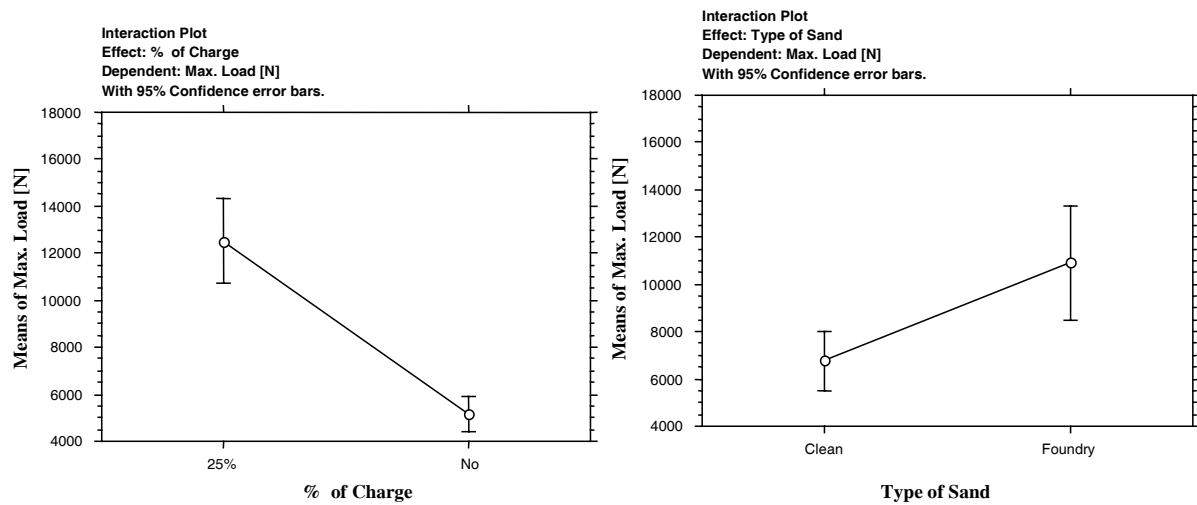


Figure 3 –Effects of the % of charge and type of sand on maximum load

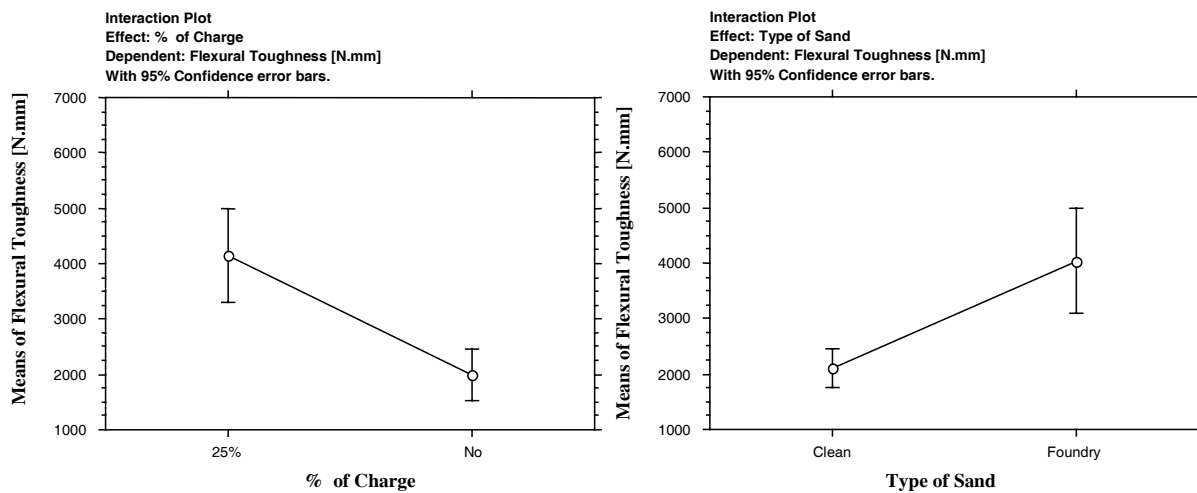


Figure 4 –Effects of the % of charge and type of sand on flexural toughness

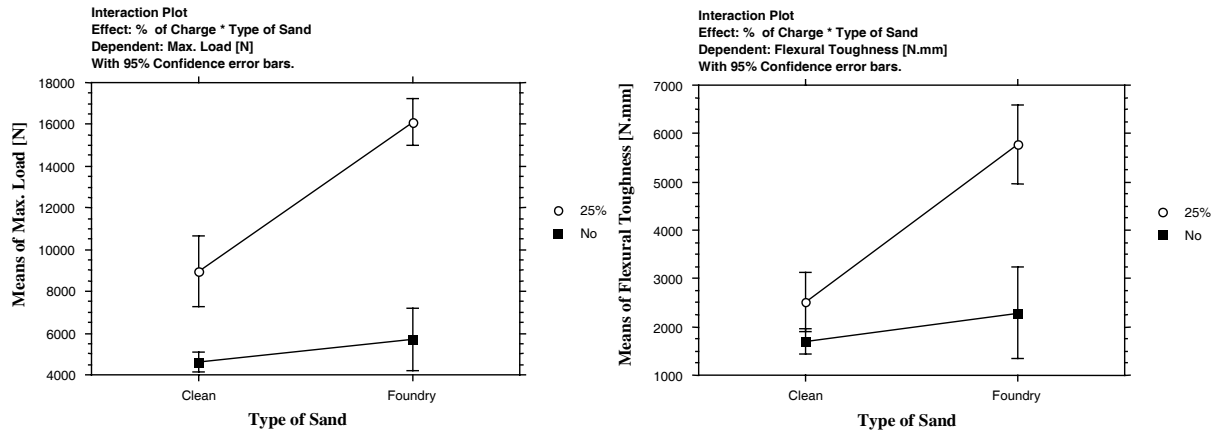


Figure 5 – Interaction of the type of sand/% of resin on maximum load and flexural toughness

The analysis of the results show that:

- epoxy concrete has higher strength and flexural toughness strength and than polyester concrete
- the % of charge (calcium carbonate) is the variable that affects the most the mechanical properties. This charge is added to resin, prior to mixing
- The type of sand also influences significantly the mechanical properties of both epoxy and polyester concrete
- Post-curing increases mechanical properties of both epoxy and polyester concrete. However, such influence is smaller than % of charge
- A significant interaction was identified between the % charge and sand type as far as strength and toughness is concerned
- The effects of type and percentage of resin are small compared with other factors leading to the conclusion that the use of cheaper resins might be cost effective

4 Acknowledgement

The support of Fundação para a Ciência e Tecnologia under project PRAXIS/C/ECM/12277/1998, “*Desenvolvimento de novos betões poliméricos*”, is gratefully acknowledged.

5 References

1. ACI Committee 548, Guide for the use of polymers in concrete (ACI 548, IR-86), American Concrete Institute, Detroit, 1986
2. J. Dikeou, Precast polymer concrete in the United States, Proceedings of the Fifth International Congress of Polymers in Concrete, Brighton, England, 1987, pp. 251-256
3. K. S. Rebeiz and D. W. Fowler, Flexural strength of reinforced polymer concrete made with recycled plastic waste, ACI Structural Journal, 1996, pp. 524-530
4. K. S. Rebeiz, S. P. Serhal, D. W. Fowler, Recommended design procedure in shear for steel-reinforced polymer concrete, ACI Structural Journal, 1993, pp. 562-567

5. J. T. San José and J. L. Ramirez, FRP bars in the bending behaviour of the polymer concrete, IRF International Conference, Porto, 1999
6. J. T. San José and J. L. Ramirez, Pure bending in polymer reinforced concrete-Design guidelines for polyester polymer concrete, Proceedings of Arquimacom, 98, Bordeaux, France, 1998
7. P. P. Camanho, R. M. Guedes, A. J. M. Ferreira and A. A. Fernandes, Flexural behaviour of polymer mortar, IRF International Conference, Porto, 1999
8. G. Taguchi, System of experimental design, Unipub/ASI, 1987
9. G. Taguchi and S. Konishi, taguchi methods, orthogonal arrays and linear graphs, American Supplier Institute, 1987
10. Figueiredo, M., Fernandes, A.A., O Método de Taguchi no planeamento e análise de operações de soldadura, Ingenium, 2ª Serie, nº11, Agosto-Setembro, 1996, pp 79-85
11. P. Ross, Taguchi techniques for quality engineering-loss function, orthogonal experiences, parameter and tolerance design, McGraw-Hill, 1988

Influence of Chemical Admixtures on the Drying Shrinkage of Concrete

Ravindra Gettu, Joana Roncero, Ignacio Carol and Miguel A. Martín
Universitat Politècnica de Catalunya, Barcelona, Spain

1 Introduction

The incorporation of chemical admixtures in concrete is common practice, especially in high performance concretes. These admixtures are designed to have specific effects on certain properties of the concrete, and are expected to have little or no negative effects on other aspects. One such admixture is the superplasticizer that is added to concrete in order to increase its workability in the fresh state, eliminating the need for increasing the water content. The effects of superplasticizers on the long-term properties of the hardened concrete have been studied to a very limited extent (1, 2), and not much data is available on their effects on creep and shrinkage. In the present work, the influence of two different types of superplasticizers on the shrinkage of mortars is studied, along with another product belonging to an emerging class of chemical admixtures that are shrinkage reducing admixtures (SRAs). Work reported in the literature (3, 4) on concretes with SRAs clearly demonstrates the decrease in the drying shrinkage and a reduction in restrained shrinkage crack widths. The influence of an SRA, which also has a plasticizing effect in the fresh state, has been analyzed in the present work, especially in terms of the shrinkage of concrete under drying conditions.

2 Effects of Superplasticizer Type on the Shrinkage of Cement Mortar

2.1 Materials

Cement mortars with the same base composition (denoted as Ref) and different admixture incorporations were studied: two mortars with different superplasticizers (melamine and copolymer based), one with the melamine superplasticizer and an SRA, which also has a plasticizing effect, and another with the melamine superplasticizer and silica fume. A CEM I 52.5R cement, crushed limestone sand with a grain size range of 0-5 mm, and a polypropylene glycol based SRA were used. The water/cement and sand/cement ratios were 0.4 and 2, respectively. All the mortars with admixtures were designed to be flowable, requiring little or no compaction during casting. The mortars and the admixtures used are specified in Table 1, along with some of the properties obtained. The superplasticizer dosages are given as the solid superplasticizer/cement ratio, by weight, with the water content being accounted for in the water/cement ratio. The SRA and silica fume dosages are also expressed with reference to the cement content, by weight.

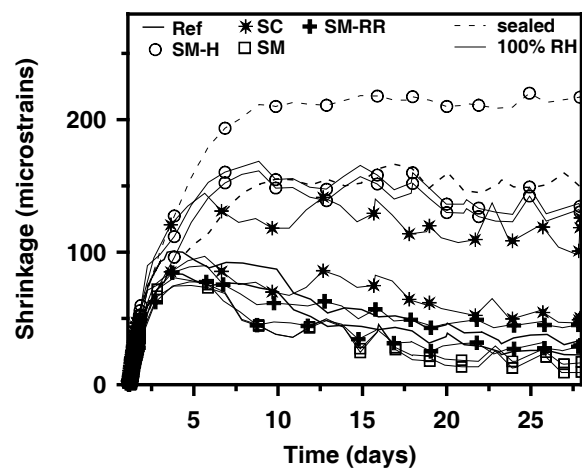
Table 1. Characteristics of the mortars

Mortar	Superplasticizer type and dosage	SRA dosage	Silica fume dosage	Jolting table spread (cm)	90-day cylinder compressive strength (MPa)
REF	none	--	--	16	68
SM	melamine sulfonic acid based, 1%	--	--	> 35	74
SC	polycarboxylic acid based, 0.1%	--	--	> 35	65
SM-RR	melamine sulfonic acid based, 0.5%	1.5%	--	22	64
SM-H	melamine sulfonic acid based, 2%	--	5%	19	82

2.2 Experimental Details and Test Results

Tests were performed on 150×300 mm cylinders with 100 mm long extensometers, based on strain gages in the full-bridge configuration, embedded at the center. Measurements of the strain were initiated immediately after casting and the reference value was taken to be that observed at 24 hours, at which age the specimens were demolded. Thereafter, the specimens were subjected to one of the following three conditions: sealed, at 100% relative humidity, and at 100% r.h. for 28 days and later at 50% r.h. (drying conditions). The ambient temperature was maintained at 20°C.

The results (each curve is an average of 2 specimens) obtained for the mortars are shown in Figure 1 for the curing period of 28 days. All specimens exhibit shrinkage during first few days, which can be attributed to thermal contraction and autogenous shrinkage. As seen in the figure, the specimens at 100% r.h. experience swelling; this continues even after 150 days. The sealed specimens are stable after about 15 days, before which the mortar with silica fume (SM-H) experiences significant autogenous shrinkage. The increments in strains during the drying period, in the specimens cured at 100% r.h. for 28 days, are shown in Figure 2 as the drying shrinkage, over a period of 120 days. The mortars with superplasticizers exhibit slightly higher drying shrinkage than the reference mortar, while the mortars with silica fume and SRA perform much better.

**Figure 1.** Strains during the first 28 days

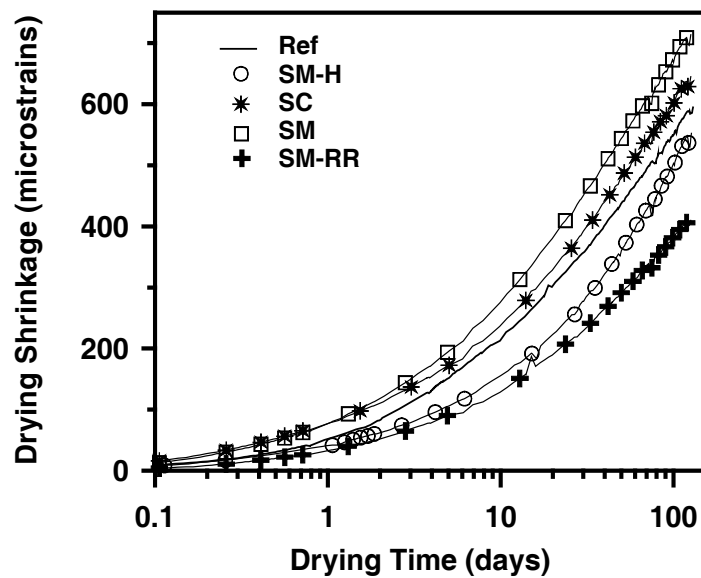


Figure 2. Shrinkage strains under drying conditions

3 Effect of SRA Dosage on the Shrinkage of Concrete

3.1 Materials

As seen in the tests of mortars, the SRA is effective in reducing the drying shrinkage. This is further studied through shrinkage measurements on concretes over one year, with the objective of providing long-term data, which is not readily available in the literature. The base (reference) concrete used in the study was designed to have a 28-day characteristic compressive strength of 35 MPa (along with a high pumpability). The materials used in the concretes were: Cement of type CEM I 52.5 R, crushed limestone sands with grain size ranges of 0-2 mm and 0-5 mm, crushed limestone gravels with grain size ranges of 5-12 mm and 12-20 mm, a naphthalene-based superplasticizer and a polypropylene glycol based SRA. A water/cement ratio of 0.45, and SRA dosages (expressed as admixture/cement ratios, by weight) of 1.5 and 2% were considered.

Since the incorporation of the SRA led to an increase in the workability of the concrete, the superplasticizer content was modified in each concrete to yield a slump of about 17 cm. The compositions of the concretes are given in Table 2, along with their basic properties.

For each concrete, cylinders of 150×300 mm were cast for the shrinkage tests and for determining the compressive strength at 28 days. A 100 mm long embedment strain gage was placed at the center of each of the specimens used in the shrinkage tests.

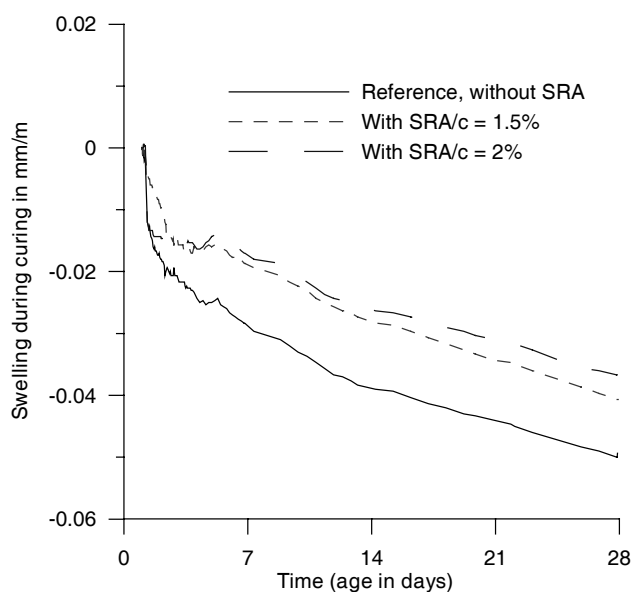
Table 2. Compositions and properties of the concretes

Property	HG-00	HG-15	HG-20
Composition (per m ³)			
Cement CEM I 52.5 R	325 kg	325 kg	325 kg
0-2 mm sand	250 kg	250 kg	250 kg
0-5 mm sand	740 kg	740 kg	740 kg
5-12 mm gravel	200 kg	200 kg	200 kg
12-20 mm gravel	725 kg	725 kg	725 kg
superplasticizer/cement ratio	0.69%	0.40%	0.33%
SRA/cement ratio	0	1.5%	2%
28-day compressive strength	45.0 MPa	42.8 MPa	39.8 MPa

The results of the compression tests indicate a slight decrease in strength with the incorporation of the SRA, with a drop of about 5% for SRA/c = 1.5% and of about 12% for SRA/c = 2%, confirming the trends observed by other researchers (4).

3.2 Experimental Details and Test Results

The measurements of shrinkage were begun immediately after casting. All the specimens were demolded after 24 hours and submerged in lime-saturated water, until the age of 28 days. The age of 24 hours, just after demolding, was taken as the reference point for the shrinkage measurements. After 28 days, the specimens were subjected to drying at a temperature of 20°C and 50% r.h. The evolutions of the average deformations during the period of curing are shown in Figure 3. As expected, all three concretes experience some swelling under water. More importantly, the swelling appears to be slightly lower in the concretes with SRA.

**Figure 3.** Swelling during under-water curing

In the curves shown in Figure 4 for drying conditions, it can be observed that the absolute shrinkage in the concretes with SRA is significantly lower than the base concrete. Note that the drying shrinkage curves do not begin from zero values of strain at the start of drying but retain the strains observed at the end of the curing period. After 1 year, the absolute value of the shrinkage in both the concretes with SRA (HG-15 and HG-20) is about 50% of that of the base concrete. However, after about 50 days, the curve of the base concrete exhibits a decreasing slope while no such tendency can be identified in the concretes with SRA. This implies that the reduction in the value of ultimate shrinkage (corresponding to infinity) due to the SRA could be lower than that determined after 1 year of drying, under the present test conditions.

Interestingly, the final trends of the concretes with SRA/c = 1.5% and 2% are practically identical, implying that there is no significant benefit of the higher dosage of SRA for under-water curing.

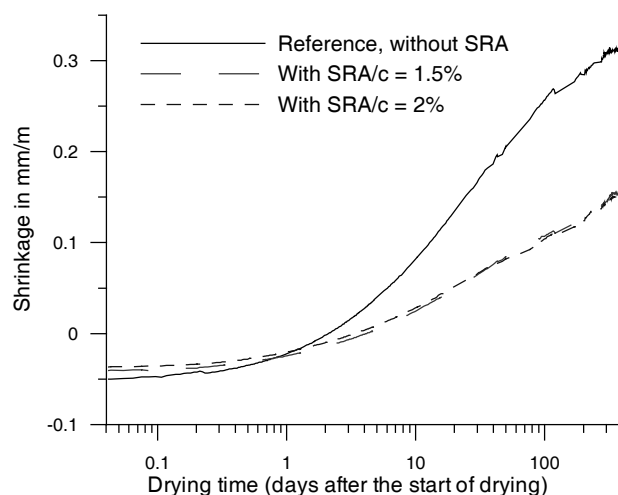


Figure 4. Evolution of drying shrinkage strains

4 Conclusions

Measurements on cement mortars show that superplasticizers may lead to an increase in the drying shrinkage strains, which can, however, be compensated incorporating silica fume. On the other hand, the addition of a shrinkage reducing admixture reduces drying shrinkage considerably. A 50% reduction in the absolute strains in concrete after one year of drying is obtained with 1.5% of the admixture. The influence of chemical admixtures on drying shrinkage of concrete can be significant and is worth further study.

5 Acknowledgements

Partial funding was provided by Spanish DGES Research Grant PB95-0500 and CICYT Research Grant MAT96-0967. The work on concretes with the SRA was supported by GRACE, S.A. through a Technology Transfer agreement with the UPC. Materials used here

were donated by Bettor MBT, Cementos Molins, Ferroatlantica and GRACE. The tests were performed at the Structural Technology Laboratory of the UPC.

6 References

1. R.K. Dhir, A.W.F. Yap, Magazine of Concr. Res. 1983, 35(125), 214-228.
2. J.J. Brooks, Concrete Intl. 1999, 21(4), 35-38.
3. S.P. Shah, M.E. Karaguler, M. Sarigaphuti, ACI Mater. J. 1992, 89(3), 289-295.
4. K.J. Folliard, N.S. Berke, N.S., Cem. Concr. Res. 1997, 27(9), 1357-1364.

II Fibre Reinforced Cement-Based Materials

Mechanical Characterization of Cement Reinforced with Figue Fibers

A.J.Moraño/ L.E.G.Cambronero/ I.Chacón/ J.M.Ruiz Roman

Material Engineering Dept. School of Mines- UPM, Ríos Rosas 21, 28003 Madrid- Spain

Abstract

Low ductility, flexural resistance and impact resistance is a characteristic of cement mortars and concrete. This limits the application of these ceramics materials when dynamic loads are present. Then, fiber addition is one way to increase these properties, especially ductility.

In this work, natural fibers from a plant known as "fique" are used as reinforcement since they are cheap and non toxic, although their durability and resistance is low. Different fiber lengths were used (1 cm to 3 cm), with a final content of 2% to 6% in weight of fiber. Several procedures for mixing based on Standard UNE-EN 196-1 was used in order to get a well homogenization of fibers into the mortar.

Besides flexural strength and compression strength (according UNE-EN 196-1 Standard), a parameter of toughness according with UNE 83-510-89 was obtained. This parameter allows evaluating the improvement of toughness after fiber addition.

1 Introduction

Fiber reinforced composite materials are not new materials. Natural fibers with clay can be read on Bible [1]. Materials evolution allowed the substitution of vegetal fibers of low strength and durability by materials with higher hardness and durability like mineral fibers (asbestos), glass fibers, plastics or iron alloys fibers. However they are very expensive materials if they have to be used by people with low rent belonged to Iberoamerican countries. Besides, some areas of these countries are under the risk of earthquakes and building materials for small houses have to be higher toughness.

Cement is the most common material for building. However its toughness is low and it is difficult to be tested. When, fiber is added to cement can modify this property. Thus, two standards have been applied to study the toughness of fiber reinforced cement: UNE-EN 196-1 [2] and UNE 83-510-89 [3]. The first one allows the mechanical characterization of cements, it is also are easy procedure of fiber reinforced cement mortar preparation and the second one (a national standard) is applied to fiber reinforced concrete in order to determine a defined "toughness index", but in this work this standard was applied for mortars. This new procedure to research and development cement reinforced by natural fibers is proposed.

2 Experimental Procedure

2.1 Raw materials

A cement type: CEM IV 32,5 was used within standardized sand deionized water was needed to prepare the mortars according to UNE-EN 196-1. Vegetal fibers from the fique were used. These fibers have a tensile strength close to 200 MPa and an elongation between 4%-6% [4]. Fibers were cut between 1 to 3 cm and several quantities were added (2% to 4% in weight of total mortar). In all cases, fibers were water saturated before adding to the mixture in order to avoid any water losses of the mortar.

2.2 Materials preparation

Following the UNE-EN 196-1 Standard, fibers were added to the mixture of water, sand and cement. Only the shovel had to be modified due to the higher viscosity of mixture when fiber is added [5][6]. Any fiber segregation or size relation on fiber clearing mixing was force.

Samples were cured seven and 28 days before testing. According with UNE-EN 196-1, flexural and compression test were carried out on these samples.

2.3 Toughness index

According with UNE 83-510-89 standard, this index is obtained (Figure 1) through the expression:

$$I_{30} = \frac{\text{AREA (O'ACD)}}{\text{AREA (O'AB)}}$$

After testing, the curve load/displacement was analyzed in order to get the areas of this expression.

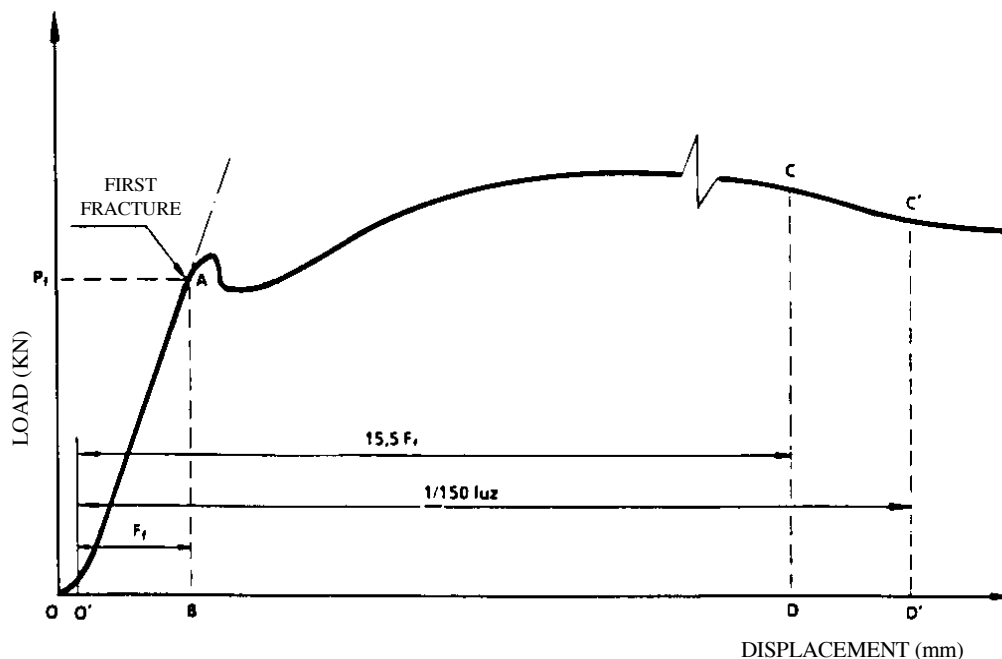


Figure 1. Drawing of curve load-displacement

3.1 Results and Discussion

Mechanical properties are on table 1. It can be seen that fiber addition decreases the strength [7]. Also when length of fiber is increased, the strengths are improved.

When fiber content and length is increased, toughness index is improved (Table 2) (Figure 2). This could be justified since mechanical friction between fibers and cement matrix is increased. Also lower toughness index is obtained when strength is increased after 28 days (Figure 3, figure 4, figure 5, figure 6, figure 7 and figure 8).

Concerning toughness, fiber addition allows an improvement of this property since fibers make more difficult the crack propagation. However fibers are only mechanically fixed and are pulled out without any fracture (Figure 9). Then, there is not any good chemical bonding between fiber and matrix [1] (Figure 10). This decreases the efficiency of the fiber on the cement composite.

Table 1. Design of mortars and Strength mechanics

DESIGN	FIBER		FLEXION (N/mm ²)		COMPRESSION (N/mm ²)	
	% WEIGHT	LENGTH (cm)	7 DAYS	28 DAYS	7 DAYS	28 DAYS
PATT.	0,0	---	8,8	13,30	45,84	53,70
1	2,0	1,0	6,14	9,15	28,47	32,97
2	4,0	1,0	3,04	5,74	13,57	17,11
3	6,0	1,0	1,99	4,69	6,44	13,83
4	2,0	3,0	5,62	10,11	33,33	36,14
5	4,0	3,0	5,19	6,24	22,76	21,32

Table 2. Toughness index

DESIGN	I ₃₀ (7 DAYS)	I ₃₀ (28 DAYS)
PATT.	2,52	2,02
1	14,03	7,04
2	25,84	22,20
3	39,47	18,64
4	13,43	11,04
5	27,96	26,37

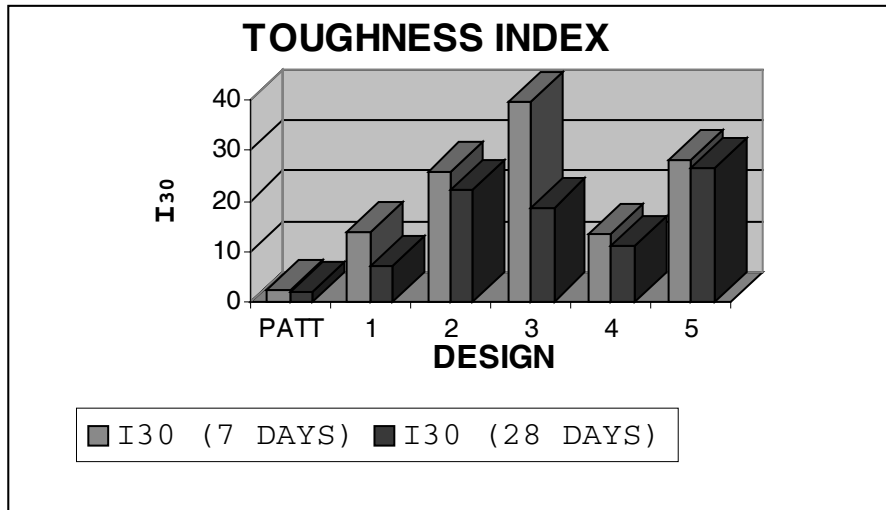


Figure 2. Toughness index evolution

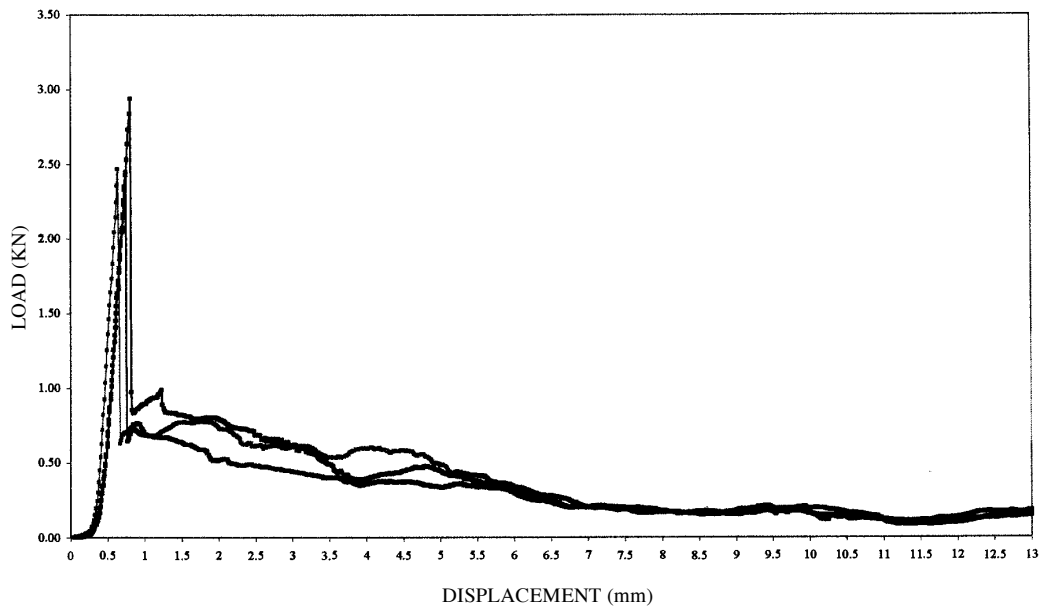


Figure 3. Curve load/displacement of design n° 1 (2% fiber, 1 cm). Tested after 7 days.

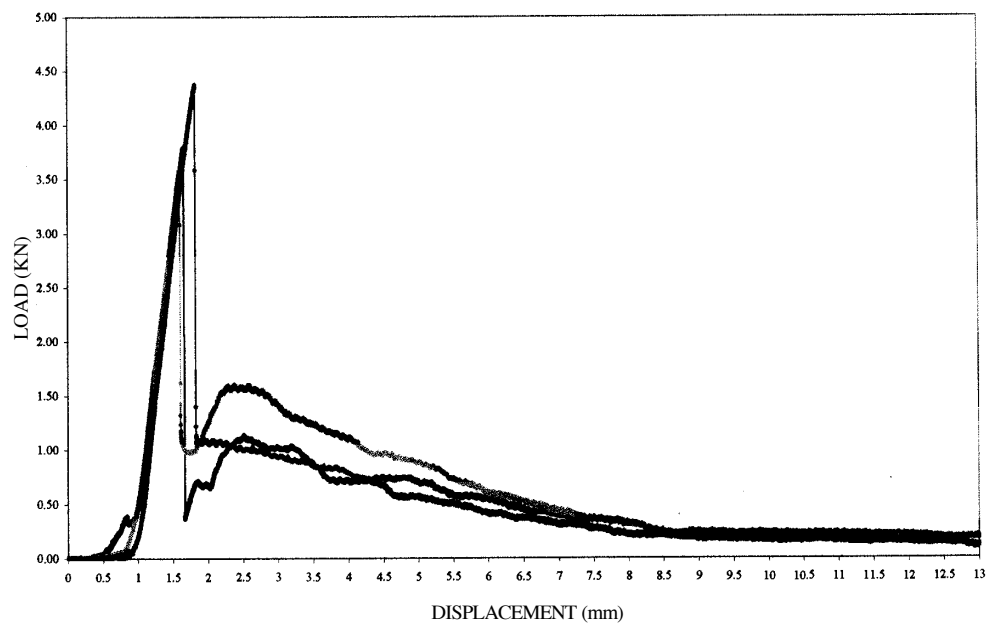


Figure 4. Curve load/displacement of design n° 1 (2% fiber, 1 cm). Tested after 28 days.

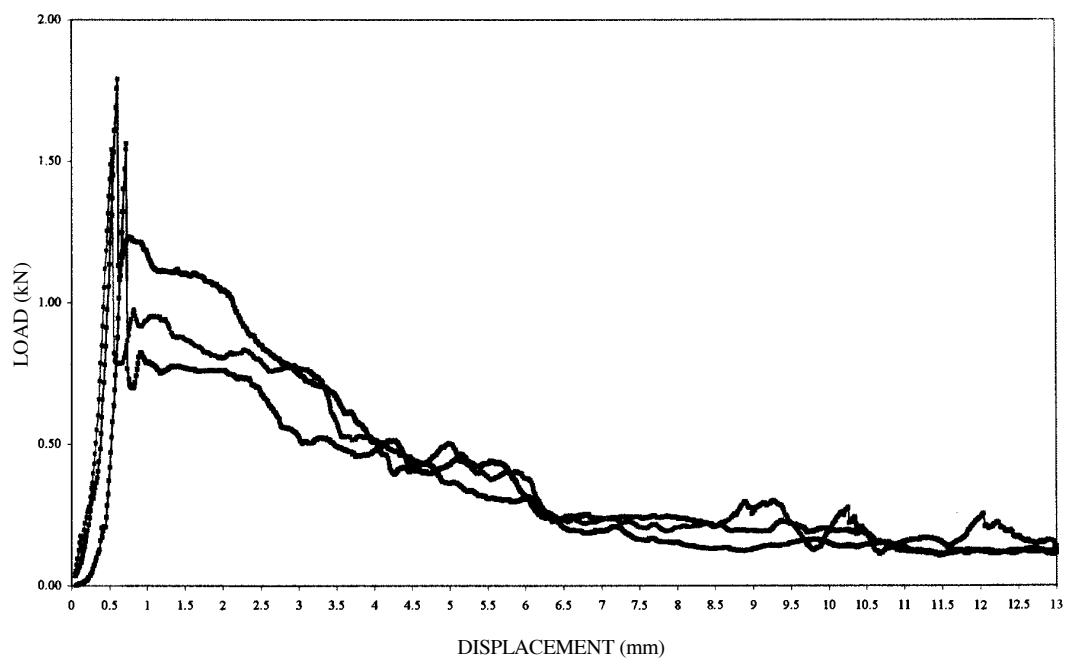


Figure 5. Curve load/displacement of design n° 2 (4% fiber, 1 cm). Tested after 7 days.

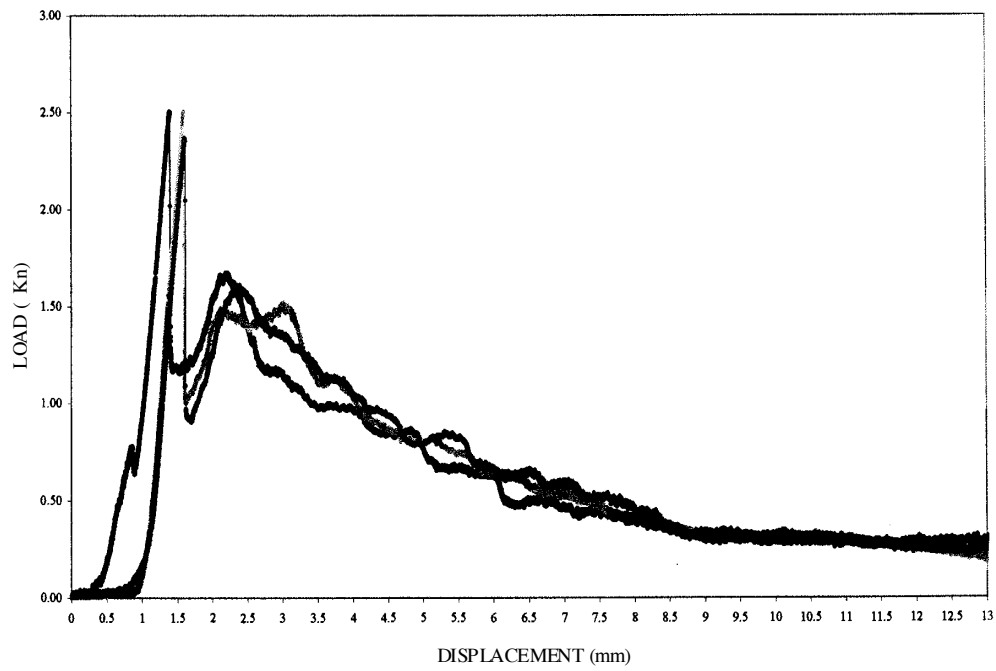


Figure 6. Curve load/displacement of design n° 2 (4% fiber, 1 cm). Tested after 28 days.

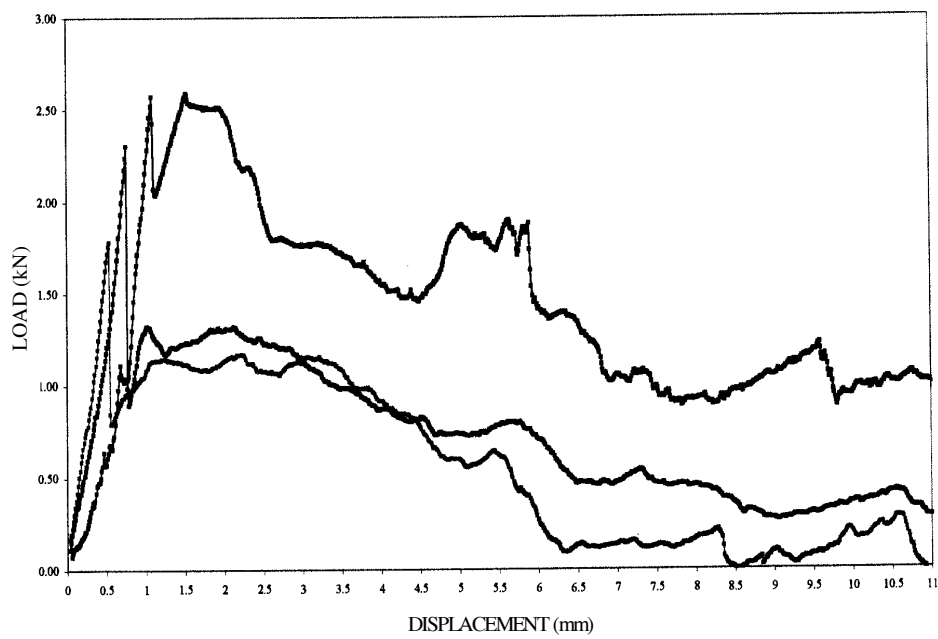


Figure 7. Curve load/displacement of design n° 5 (4% fiber, 3cm). Tested after 7 days.

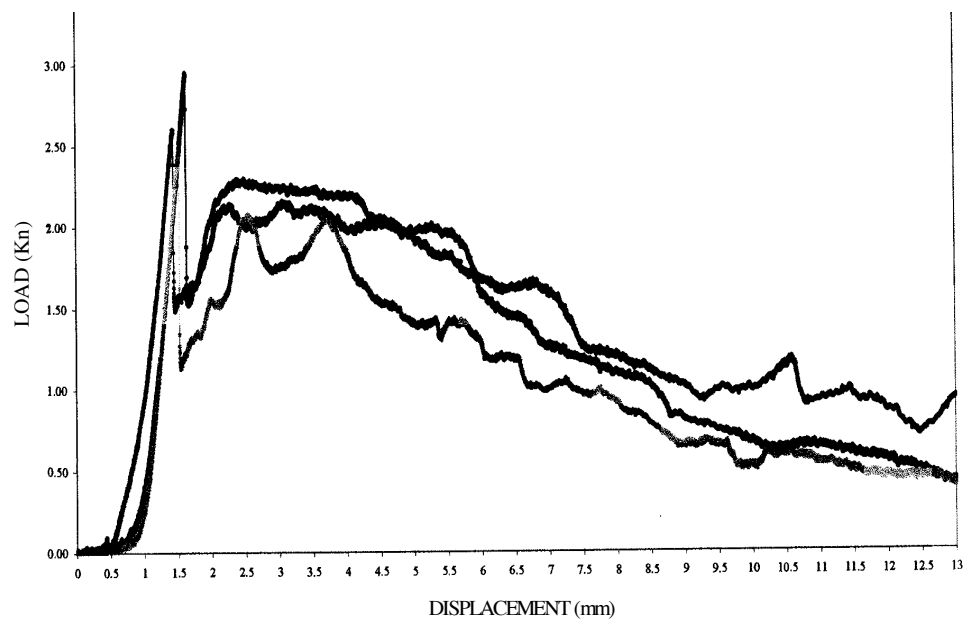


Figure 8. Curve load/displacement of design n° 5 (4% fiber, 1 cm). Tested after 28 days.

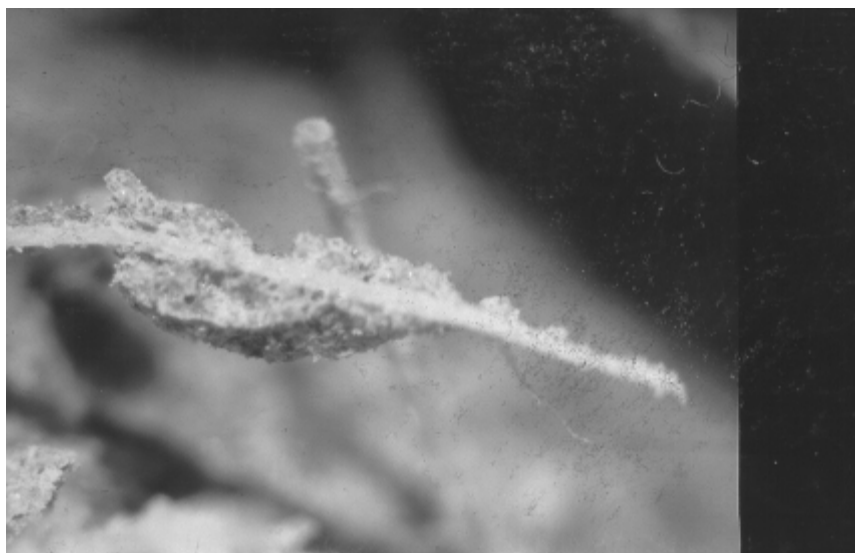


Figure 9. Photography of fracture

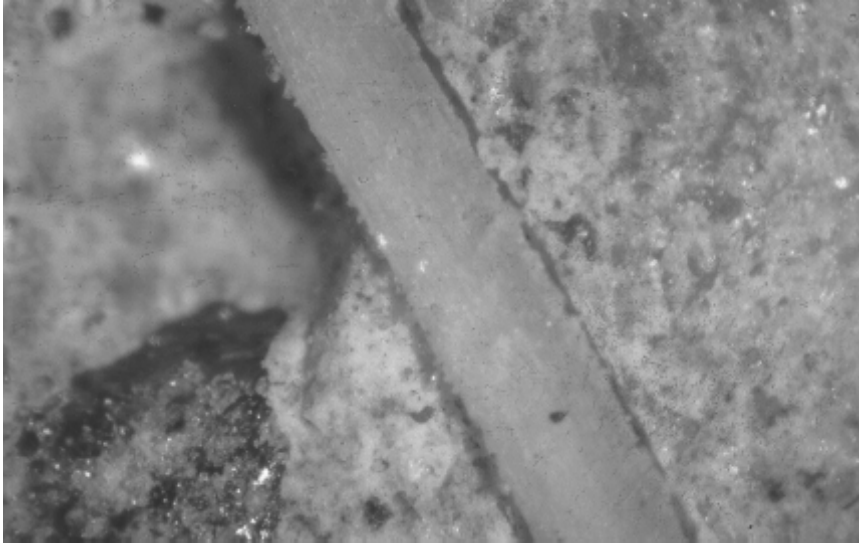


Figure 10. Photography of fracture

4 Conclusions

- Fique fibers allow increasing the toughness index of cement mortars obtained following UNE-EN 196-1 standard.
- Fibers have to be cut and water saturated before addition to cement mortar.
- When fiber length is increased, strength (both flexural and compression) is decreased.
- Also toughness increased when fibers are longer.
- Besides toughness is improved when the fiber content is increased.
- UNE-EN 196-1 standard has shown its feasibility to prepare cement mortars with fiber reinforcement.

5 Acknowledgment

We want to give thanks to LOEMCO by its help on materials preparation and testing, IECA by the cement supply and ICI by the project VIII.5 of CYTED program.

6 References

1. Delvasto Arjona, Silvio. 1998. Departamento de Ingeniería Mecánica y de Materiales, E.T.S.I. Industriales, Universidad Politécnica de Valencia, España.
2. UNE-EN 196-1 (1996). CEN-AENOR.
3. UNE 83-510-89. (1989). AENOR
4. P. Gañan, i. Mondragón. VI Reunion de Materiales p.332, 22-24 June 1999, San Sebastian, Spain.

5. Cambrero, L.E.G. y Moraño Rodríguez, A.J. 1996. (Departamento de Ingeniería de Materiales E.T.S.I. Minas, Universidad Politécnica de Madrid). II Reunión de Miembros del Proyecto de Precompetitividad VIII.5 del CYTED. Monterrey, Méjico.
6. Cambrero, L.E.G. y Moraño Rodríguez, A.J. 1998. (Departamento de Ingeniería de Materiales E.T.S.I. Minas, Universidad Politécnica de Madrid). Curso Internacional de Materiales Compuestos Fibrorreforzados. IV Reunión Proyecto de Precompetitividad VII.% del CYTED. Santiago de Cali, Colombia.
7. Swamy, R.N. 1988. (Department of Mechanical Engineering, University of Sheffield, UK). Concrete Technology and Design.

Use of Technical Textiles and Densified Wood for Timber Joints

Peer Haller, Jörg Wehsener

Dresden University of Technology, Faculty of Civil Engineering

1 Introduction

Joints in timber engineering transfer load mostly by means of slotted steel plates attached to the timber cross section by means of dowel-type fasteners. Load is transferred and distributed via these steel plates what avoids dangerous transverse and shear stresses in the wood. This technique also avoids cross-sectional variations as occur in joints used in carpentry or those with laterally fixed side members.

The occurring shear and cleavage stresses below the fasteners are a major drawback encountered by low strength properties of the fibrous material wood. Therefore timber-steel-compounds exploit the load carrying capacity of the timber cross section only to some extent (about 10 - 20%) and tend to brittle failure if the wood fails without prior plasticization of the metal fasteners. So plastic design methods as e. g. with semi-rigid joints in steel construction cannot be applied [1].

The load carrying behaviour of timber joints with regard to rigidity, load capacity and ductility can essentially be improved by reinforcement. This requires an increase of transverse and shear strength of the wood by means as described in [2].

Technical textiles prove to be very promising and universally applicable. Especially transverse and shear strength of wood can be improved very effectively by the application of textile structures with adhesives. Common technical textiles are reasonable in price, can be draped and varied in almost every way concerning their weight, kind of fibre and structure [3].

Glass-fibre reinforcement with commercial fabrics does not much improve embedding strength and rigidity but essentially improves ductility [5]. The embedding behaviour of wood decisively depends on its density [6] so that the use of hard wood or densified soft wood [7] results in a further improvement of load carrying behaviour. Textile structures and densified wood present two techniques that produce very stiff, strong and ductile joints.

State of the art

According to the objectives timber elements can be reinforced by textiles in two different ways.

On the one hand the timber element is reinforced by means of pultruded laminates glued to it parallel to the grain. Thus e. g. flexural rigidity and strength of beams are increased what is applied with great success in wooden buildings rehabilitation. In this case mainly stiff high-strength carbon and aramide fibres are used. The especially good mechanical properties of laminated wood have to be considered together with small cross section of a thin carbon laminate so that its ultimate load and tensile strength are approximately equivalent.

On the other hand commercial fabrics of different weight can be glued on the wet or dry surface producing the composite directly on the wood. This method is applied in boat,

propeller and timber construction [9]. This does not primarily aim at improving the longitudinal strength of the wood but its transverse and shear strength as well as the protection against environment and weather.

Objectives

In this study two experimental series were carried out. In the first part the embedding characteristics according to DIN EN 383 were investigated for solid wood, textile reinforcement and densified wood.

In the second part the load carrying behavior of a shear joint is investigated for different design parameters.

At present the authors intent the use of straight forward textile technology that allows an orientation of the fibre according to the local stress state and the shape of the construction element.

2 Material and Methods

2.1 Material

The samples were made of spruce boards (2000 x 135 x 40 mm) of grade GK II according to [DIN 1052]. Prior to the tests these boards were industrially dried and a part of them was densified in a heating press to 50 % of the initial cross section. These boards - normal and densified - were connected by means of finger joints and glue laminated. For the shear specimens the densified part of the laminates was shifted by 100 mm respectively (fig. 1b) what resulted in a conical connecting area with a higher density. As an adhesive there was used a formaldehyde-free polyurethane glue (manufacturer Collano: Purbond HB 110). Table 1 contains the mean values of moisture content and density before and after densification.

Moreover, samples were made of commercial laminated wood of grade GK II which serve as a reference.

Table 1 Density and wood moisture of spruce laminates used

Materials	Density [kg/m^3]	Moisture [%]
laminated wood, GK II	370 ... 430	10 ... 14
spruce laminate before densification and after densification (to 50%)	450 ... 480 880 ... 980	14 ... 16 6 ... 8

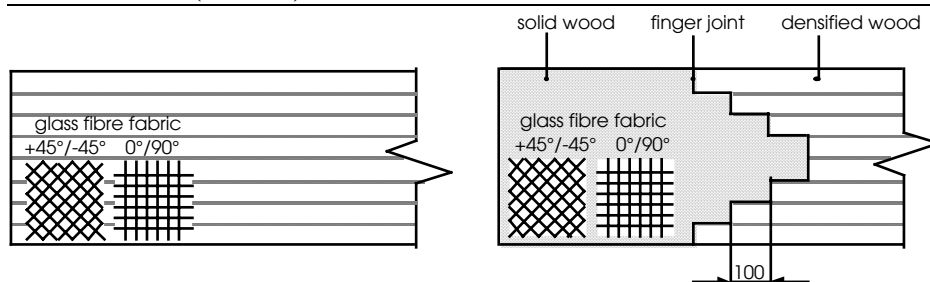


Figure 1a) GF-reinforced / solid wood

Figure 1b) GF-reinforced / 50% densified

2.2 Making of Samples

Densification

The laminates were densified in three steps: heating up, densification and recooling. During the first phase the laminates were heated up by the panels of the press using a low contact pressure of 0.2 to 0.3 MPa. The solid wood heating was calculated with an assumed value of 1 to 2 mm/min. After the temperature in the centre of the sample had reached 140 °C the densification process started. With a further heating to 150 °C pressure was continually increased to 2.5 MPa. In order to prevent excessive drying there was chosen a relatively high closing speed of 1 mm/min. After the densification process of about 40 minutes the recooling of the wood samples to 60 °C began, which lasted approximately as long as the heating.

Lamination

The timber components were reinforced by glass-fibre fabrics of type E and a weight of 200 g/m². Previously an adhesive activator (manufacturer: Vosschemie; G4 - primer) was applied to enhance bonding strength. From 0 to 4 layers were applied manually using a two-component epoxy resin (manufacturer: Vosschemie; LN-1 Epoxy A + B). The „wet method“ was used [8], where the adhesive is spread on the timber surface and the fabric is pressed on it without prior impregnation. Using epoxy resin avoids an additional surface pressure. For complete hardening the components had been stored in ambient climate for 10 days. Rigidity and characteristic values of the fabric and the adhesive are presented in the following table.

Table 2 Material values according to [7]

Characteristic values	Glass fibre Type E	Epoxy resin	Composite
Young-modulus [MPa]	73000	3700	25 ... 30000
Density [kg/m ³]	2600	1040 (hardener) 1150 (resin)	approx. 2000
Bending strength [MPa]		123	
Compression strength [MPa]		130	
Tensile strength [MPa]	2400		150... 200

3 Tests and test results

Test set-up: single dowel

The specimens (320 x 120 x 40 mm) were reinforced on both sides by means of glass fibre fabric. Testing was carried out 10 days after the manufacturing. The dowel diameter was 22mm with an end distance about of 5d. Figure 3 shows how much the embedding strength for tension load is increased and that brittle failure is avoided [table 3].

Table 3 Comparison of different types timber joints (single dowel, \varnothing 22mm)

Specimen	Species	Reinforcement [Angle]	Layer	Densification [%]	Load [N/mm ²]	Ratio
1	spruce	0	0	0	28,6	1,00
2	oak	0	0	0	36,9	1,29
3	spruce	0° / 90°	2	0	38,6	1,35
4	oak	+45° / -45°	2	0	63,0	2,20
5	spruce	0	0	50	80,8	2,82
6	spruce	+45° / -45°	2	50	89,3	3,12
7	spruce	0° / 90°	4	50	99,6	3,48
8	spruce	+45° / -45°	4	50	103,0	3,60

The investigation of the embedding characteristics from two species and reinforcements showed a proportional increase of the failure load with respect to density. The load bearing capacity of densified reinforced spruce was 3,5 times higher than unreinforced solid spruce. At the same time a considerable increase of embedding stiffness and ductility was achieved.

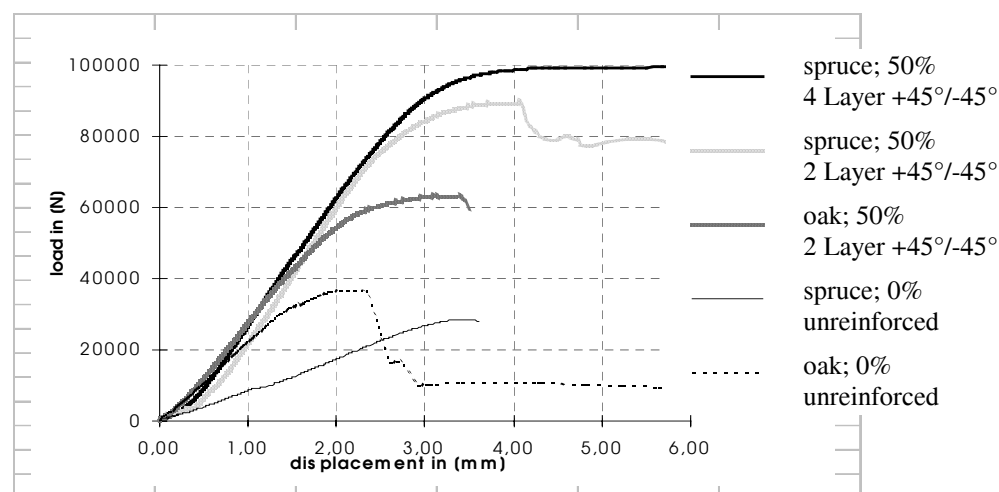


Figure 3 Embedding characteristics of a single dowel for different species and design parameters

Test set-up: dowel connection under shear force

The load carrying behavior of the shear connection was tested according to EN 26981. Geometry of the sample and the test set up are shown in fig. 4. Four shear connections using different design of the assembly zone have been investigated [see also Fig. 1]. Further results of connections subjected to tension parallel to grain and bending were presented in [4]. The reinforced densified joint was much stiffer and stronger than the other samples, however it behave more brittle due to the debonding and rupture of the reinforcement.

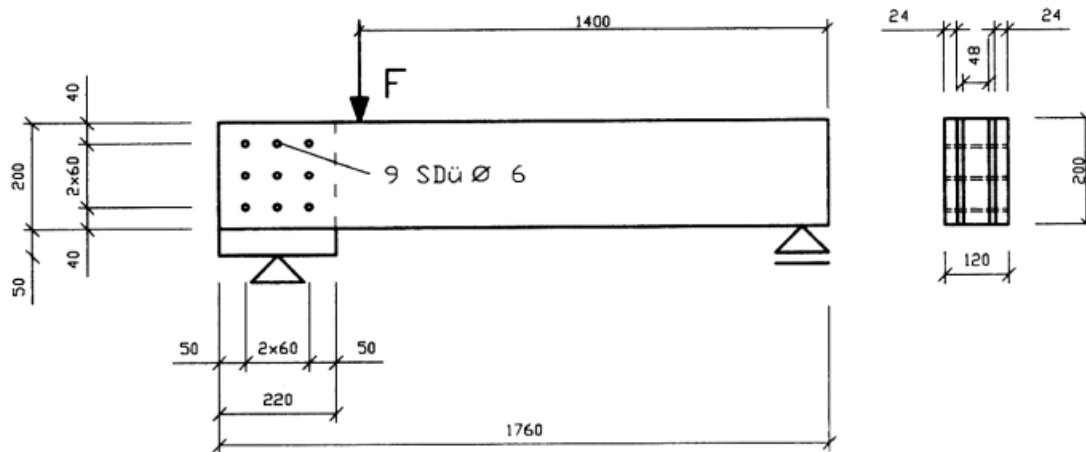


Figure 4: Shear specimen

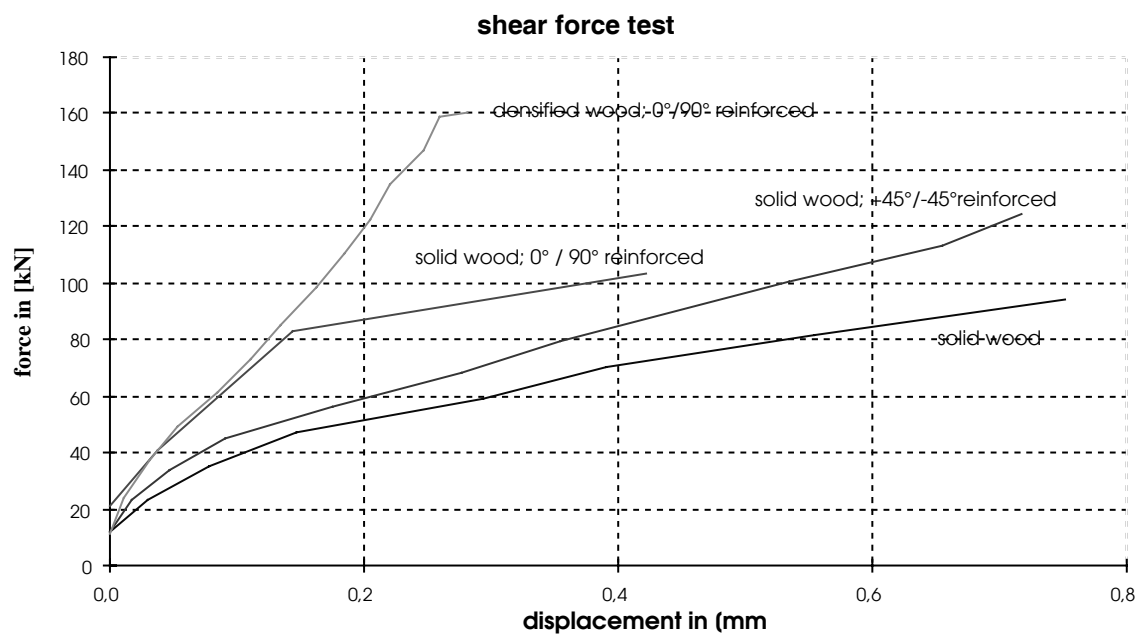


Figure 5 Load - slip - relationship of shear load

Table 4 Summary of test results (geometry 1760 x 120 x 200 mm)

Specimen	Reinforcement [Angle]	Layer	Densification [%]	Failure load [kN]	Ratio	Deformation [mm]
1	0	0	0	92,2	1,00	0,7
2	0° / 90°	2	0	103,4	1,12	0,4
3	+45° / - 45°	2	0	124,0	1,35	0,7
4	0° / 90°	2	50	160,5	1,73	0,3

4 Conclusion

The experimental study on glassfibre reinforced and densified timber joints has shown that the load carrying capacity was increased up to two times. Apart from the ultimate load,

stiffness and ductility are improved considerably so that construction elements could be prevented from sudden failure. The structural use of densified wood arise questions about the bonding strength of the wood textile composite. Particularly, the connection of densified and undensified boards which was done in this study by means of finger joints present a weak point and must be improved.

In order to fully benefit from new technical textiles, more especially from those having an optimal fibre orientation regarding the stress state a thorough understanding of the mechanical behavior of the wood-textile-composite is required.

5 Literature

1. P. Haller [ed.], COST C1 - Final Report of Working Group „Timber Joints“, Semi-rigid timber joints - structural behavior, modelling and new technologies, Dresden, 1998
2. P. Haller, Progress in the development and modelling of timber joints, Proceedings, 5th World Conference of Timber Engineering, Montreux, Switzerland, 1998, Vol. 1, 337-344
3. P. Offermann, G. Franzke, K. Hörsting, B. Wulfhorst; New types of textile abrics for fiber composites, SAMPE Journal, Covina/USA, 29 (1993) 1, 7-11
4. P. Haller, J. Wehsener, Use of technical textiles and densified wood for timber joints, Proceedings, 1th RILEM Symposium on Timber Engineering, Stockholm, Schweden, 1999, 717 - 726
5. P. Haller, J. Wehsener, C.J Chen; Development of joints by compressed wood and glassfibre reinforcement, Proceedings, Final Conference Report, COST C1, Control of the semi rigid behaviour of connections in civil engineering, Liege, Belgium, 1998
6. J. Ehlbeck, H. Werner; Tragfähigkeit von Laubholzverbindungen mit stabför migen Verbindungsmitteln, Forschungsbericht, Universität Karlsruhe 1992
7. P. Haller, C.J. Chen, J. Natterer; Experimental study of glass fibre reinfor-ced and densified timber joints, Proceedings, International Wood Engineering Conference, New Orleans, Louisiana, USA, 1996
8. Gougeon Brothers, Moderner Holzbootsbau, Verlag H. von der Linden, Wessel, Germany, 1998
9. C. J. Chen; Study of mechanical behaviors and optimization of fiber glass reinforced timber joints; Dissertation; EPF-Lausanne, Schweiz, 1999

Improvement of the ductility of concrete due to the incorporation of steel fibers and its relation with the material toughness

Bryan Barragán, Rosangela de Fatima Zalochi, Ravindra Gettu and Miguel A. Martín
Universitat Politècnica de Catalunya, Barcelona, Spain

1 Introduction

The incorporation of steel fibers in concrete is a rational way of reducing its brittleness and increasing its toughness through mechanisms such as crack-arrest and fiber-bridging, which leads to less catastrophic failure and higher post-cracking load-carrying capacity. This is of particular interest in structural failures that are dominated by sudden crack propagation, such as in tension and shear or diagonal tension. In this respect, there is a need for the development of a fundamental understanding that could be achieved through small-scale testing to obtain parameters that could then be utilized in large-scale fiber reinforced concrete structural elements.

In the present study, results of tests performed on normal and high strength concrete, with and without steel fibers, using notched beams and prisms under direct shear, are reported. The improvement in the ductility is characterized through parameters defined in terms of the load versus crack opening response of the bending test. Similar, parameters are obtained from the load-slip response in the shear tests.

2 Test Program

2.1 Materials

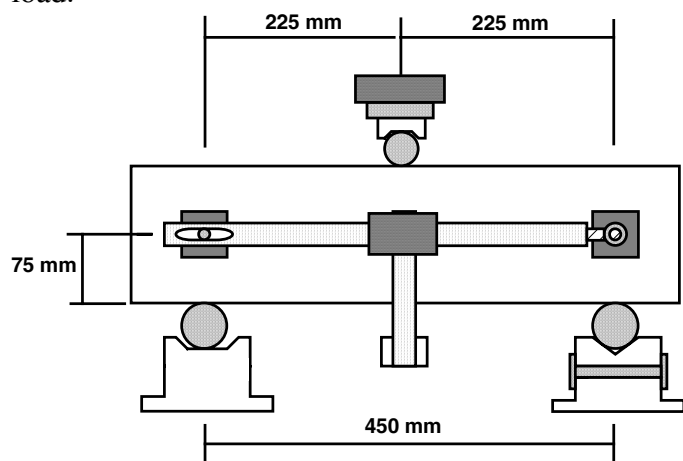
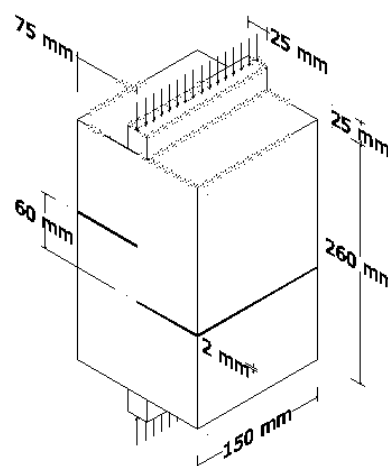
Two classes of concrete were studied: a normal strength concrete (NSC) designed for a characteristic strength of 35 MPa (denominated C35) and a high strength concrete (HSC) designed for 70 MPa (C70). In each of these base (reference) concretes, two dosages of hooked steel fibers, 20 and 40 kg/m³, were incorporated: in the NSC, a low carbon fiber with a length of 60 mm and diameter of 0.75 mm, and in the HSC, a high carbon fiber with a length of 30mm and a diameter of 0.38 mm. The characteristics of the concrete are given in Table 1, where f_c is the 28-day cylinder compressive strength and E is the modulus of elasticity in compression.

Table 1. Characteristics of the concrete

Concrete	Fiber dosage (kg/m ³)	slump (cm)	f_c (MPa)	E (GPa)
C35/00	0	15	40.2	30.0
C35/20	20	14	38.9	31.8
C35/40	40	11	38.3	31.8
C70/00	0	20	77.7	36.6
C70/20	20	13	76.5	37.2
C70/40	40	5	77.8	38.9

2.2 Experimental Details

In addition to the cylinders for the compression tests, 150×150×600 mm prisms were cast for each concrete. Before testing them at the age of about 40 days, a 25 mm long notch was cut at mid-length. The flexural test was performed in the configuration shown in Figure 1, under crack opening (CMOD) control in a servohydraulic testing machine and the deflection was recorded at midspan. After this, a specimen with the geometry shown in Figure 2 was cut for direct shear push-off tests, similar to those of Barr (6), Swamy (9), Balaguru and Dipsia (1), and Valle and Buyukozturk (2). These tests were performed under piston displacement control and the vertical displacement (nominal slip) was recorded, along with the applied load.

**Figure 1.** Flexural test configuration**Figure 2.** Shear test configuration

3 Test Results

3.1 Flexure

The typical load-deflection and load-CMOD curves are shown in Figure 3. In all the cases, the increase in post-peak load carrying capacity due to the fibers is appreciable, with a drop after the peak followed by a plateau or hardening-type behavior.

The toughness of fiber concretes can be defined in terms of the area under the load-deflection, as is normally done with unnotched specimens (3) and has been recently extended to notched specimens (4). In the present study, the area under the curve is used as a toughness

measure, as in the Belgian NBN B 15-238 standard. The values B_n equal to the area up to the deflection limit of span/ n , for $n = 600, 300$ and 150 , are given in Table 2. It can be seen that the toughness increases with the deflection limit, fiber content and concrete strength.

Since the deflection measurement is not straightforward and the deflection limits are arbitrary (3), the definition of toughness measures based on the load-CMOD curve has been proposed (3-5). Such definitions can be made in terms of CMOD limits based on allowable crack widths. Accordingly, B_w^C equal to the area under the load-CMOD curve up to the CMOD-value w , for $w = 0.5, 1.0$ and 2.0 mm, are given in Table 2.

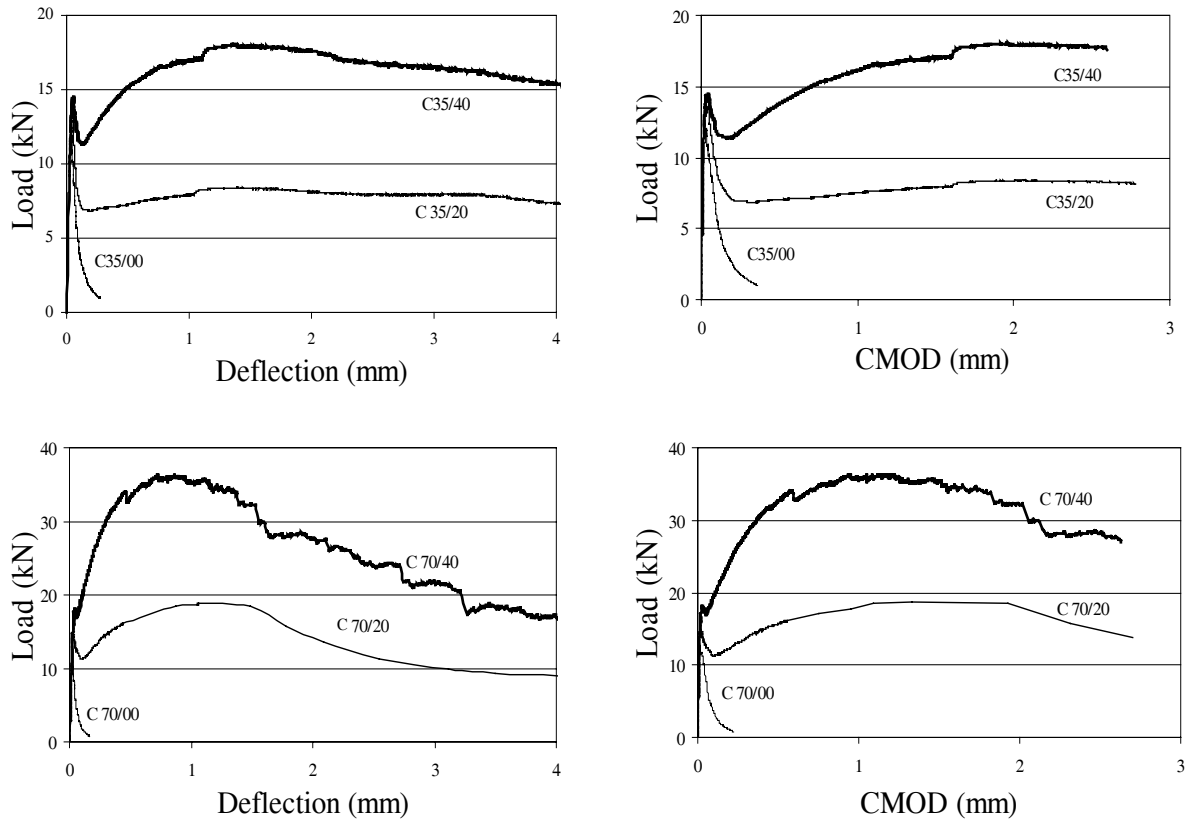


Figure 3. Load-deflection and load-CMOD response for NSC and HSC.

Table 2. Flexural toughness

Concrete	Area under load-deflection curve (kN-mm)			Area under load-CMOD curve (kN-mm)			Equivalent flexural strength (MPa)		
	B_{600}	B_{300}	B_{150}	$B_{0.5}^C$	$B_{1.0}^C$	$B_{2.0}^C$	$f_{0.5}^C$	$f_{1.0}^C$	$f_{2.0}^C$
C35/20	5.5	11.5	23.8	3.8	7.3	15.2	2.1	2.1	2.2
C35/40	9.6	21.7	46.0	5.9	12.9	29.0	3.4	3.7	4.2
C70/20	11.8	26.5	48.4	6.9	15.9	35.5	3.8	4.4	4.8
C70/40	29.2	64.1	82.5	10.2	24.4	53.5	5.6	6.7	7.3

Using the areas under the load-CMOD curves, equivalent flexural strengths $f_w^C = 1.5B_w^C S/w bh^2$ (where span $S = 450$ mm, width, $b = 150$ mm, ligament depth, $h = 125$ mm and $w =$ CMOD limit), have also been calculated and reported in Table 2. As a reference, the average CMOD-value at the first peak is 0.025 mm.

It can be seen that the areas under the curves reflect the increase in toughness with fiber content and deformation limit. More importantly, the equivalent flexural strengths increase with crack width and with significant values, for crack widths up to 2 mm.

3.2 Shear

Typical stress-slip curves obtained in the direct shear tests for the different concretes are shown in Figure 4. The maximum loads are used to obtain the shear strength (τ_u), reported in Table 3, as done by Walraven (8), and Balaguru and Dipsia (1) Extending the definition of flexural toughness, as proposed by Barr (6,7) and Valle and Büyüköztürk (2), parameters B^D_s equal to the area under the load-slip curve in the direct shear test up to the slip-value s , have been determined for $s = 0.25, 0.5$ and 1.0 mm, and presented in Table 3. Furthermore, equivalent shear strengths $f^S_s = B^D_s/sA$ (where the ligament area, $A = 93.8 \text{ cm}^2$ and $s = \text{slip limit}$) are also reported in the same table. As a reference, the average slip-value at the first peak is 0.15 mm.

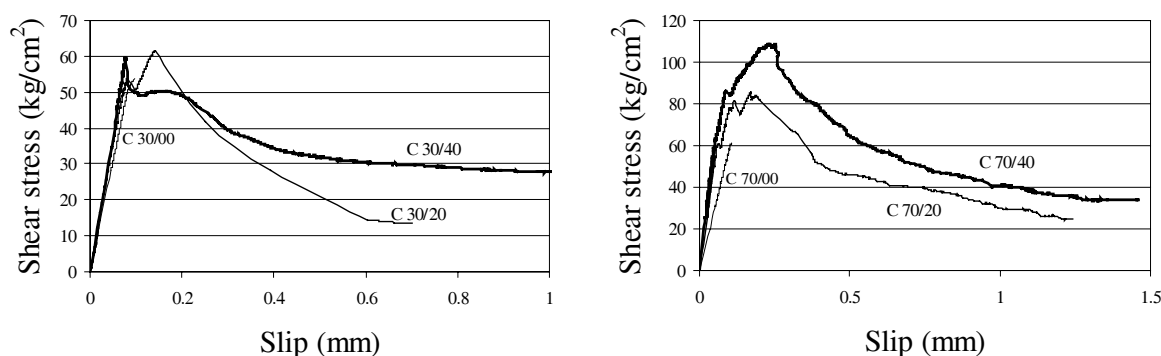


Figure 4. Stress-slip response for NSC and HSC

Table 3. Results of direct shear (push-off tests)

Concrete	τ_u (MPa)	Area under load-slip curve (kN-mm)			Equivalent shear strength (MPa)		
		$B^D_{0.25}$	$B^D_{0.5}$	$B^D_{1.0}$	$f^S_{0.25}$	$f^S_{0.5}$	$f^S_{1.0}$
35/00	5.3	-	-	-	-	-	-
35/20	6.2	10.5	18.6	33.2	4.6	3.9	3.6
35/40	5.9	10.3	18.2	31.2	4.4	3.9	3.3
70/00	5.4	-	-	-	-	-	-
70/20	8.0	14.3	25.4	40.2	6.4	5.6	4.4
70/40	10.5	16.5	32.0	59.9	7.1	7.0	6.5

The data indicate that the shear strength increases with the incorporation of fibers and a significant toughening effect is observed in the fiber concretes after the maximum load, reflecting the absence of a sudden drop in load-carrying capacity that is associated with the shear failure of plain concrete. The gradual decrease in the equivalent shear strength reflects the softening response in the post-peak regime.

3.4 Discussion

Both the flexural and shear tests reflect the toughening effect of the fibers in the normal and high strength concretes. The use of notched beams instead of the conventional unnotched specimens facilitates the stable control of the test, using the crack opening, and provides a direct means of defining toughness parameters based on crack width limits. Furthermore, equivalent (post-peak) flexural strengths that are convenient for structural design can be obtained.

In the shear tests, an increase in pre-peak deformation and strength is observed due to the incorporation of the fibers, as opposed to the matrix-dominated pre-peak behavior in flexure. Moreover, the toughness parameters and equivalent shear strengths reflect the absence of a sudden drop in the post-peak load-carrying capacity. However, the softening response leads to a decrease in equivalent shear strength with an increase in slip, unlike the increasing equivalent flexural strengths due to the post-peak hardening-type response of the beams.

4 Conclusions

Significant improvements in the ductility of concrete during failure are achieved through the incorporation of steel fibers, in both normal and high strength concretes. Tests of notched specimens subjected to flexure and shear demonstrate the energy dissipation capacity of the fiber concretes in the post-cracking regime. Using the load versus crack opening curve in flexure and the load versus slip curve in shear, toughness parameters and equivalent (post-peak) strengths have been determined.

5 Acknowledgements

The present study was partially supported by the Spanish CICYT grant MAT96-0967 to the UPC. The doctoral studies of B.Barragán and R.Zalochi at the UPC are funded by CONICET (Argentina) and FAPESP (Brazil), respectively. Travel funding from the School of Civil Engineering (ETSECCPB-UPC) is gratefully appreciated.

6 References

1. P. Balaguru, M.G. Dipsia, *ACI Mater. J.* 1993, 90, 399-405.
2. M. Valle, O. Büyüköztürk, *ACI Mater. J.* 1993, 90, 122-133.
3. V. S. Gopalaratnam, R. Gettu, *Cement & Concrete Composites.* 1995, 17, 239-254.
4. H. Saldivar Moguel, *Flexural Toughness Characterization of Steel Fiber Reinforced Concrete – Study of Experimental Methodologies and Size Effects*, Doctoral Thesis. Universitat Politècnica de Catalunya, Barcelona, Spain, 1999.
5. D. Jamet, R. Gettu, V.S. Gopalaratnam, A. Aguado in *Testing of Fiber Reinforced Concrete*, American Concrete Institute, Detroit, USA, 1995, 23-39.

6. B. Barr in Fiber Reinforced Concrete, Properties and Applications (Ed.: S.P. Shah and G. B. Batson), American Concrete Institute, Detroit, USA, 1987, 27-53.
7. F. Benaiche, B. Barr in Fiber Reinforced Cement and Concretes: Recent Developments (Ed.: R.N. Swamy and B. Barr) Elsevier Applied Science, London, England, 1989, 411-419.
8. J. Walraven, J. Stroband, in High Performance Concrete. Proceedings ACI International Conference, Singapore (Ed.: V.M. Malhotra) American Concrete Institute, Detroit, USA, 1994, 311-330.
9. R. Swamy, R. Jones, T. Chiam in Fiber Reinforced Concrete, Properties and Applications (Ed.: S.P. Shah and G.B. Batson), American Concrete Institute, Detroit, USA, 1987, 565-593.

SIFCON (Slurry Infiltrated Fiber Concrete) Under Dynamic Loading

Christoph Mayrhofer

Fraunhofer Institut für Kurzzzeitdynamik, Ernst-Mach-Institut, Efringen-Kirchen, Germany

Abstract

The response of „reinforced SIFCON“-slabs under static and dynamic loading conditions was experimentally investigated. The bending capacity was determined and ISO-damage curves in p-J-diagrams were calculated. The bending capacity as well as the energy absorption capacity proved to be much higher compared to normally reinforced concrete. The increasing brittle behavior of reinforced concrete slabs with increasing reinforcement was not observed with reinforced SIFCON. As a result reinforced SIFCON can be used favorably to design highly dynamically loaded structures.

1 Introduction

To improve the response of structures to highly dynamic loading it is important to use a material with large working capacity. SIFCON has high toughness and ductility. In connection with reinforcing steel bars, the so called „reinforced SIFCON“ additionally has strong bending capacity.

Reinforced SIFCON slabs (2,0-0,6-0,1 m³) were subjected to static load and dynamic load in a shock tube. The behavior of the reinforced SIFCON was judged in comparison to normally reinforced concrete by its bending capacity under flexural stress. More detailed results are given in the references [1], [2] and [3].

2 Experimental set-up

The tests under high dynamic loading conditions were done in a shock tube (Fig. 1) in the reflected mode. A typical load function is shown in Fig. 2.

The shock-tube arrangement is about 50 [m] long, the diameter of the test section is 2,4 [m]. The tube is air-driven. Blast waves with peak reflected over-pressure from 10 [kN/m²] to 300 [kN/m²] and positive duration from 10 [ms] to seconds are possible.

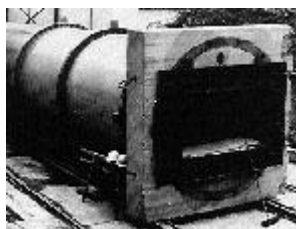
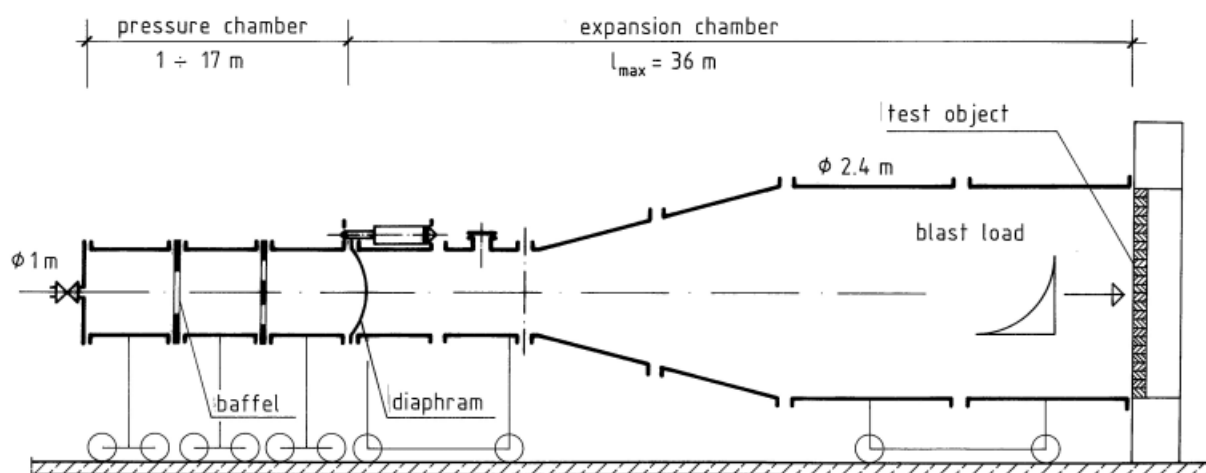


Figure 1. Shock tube

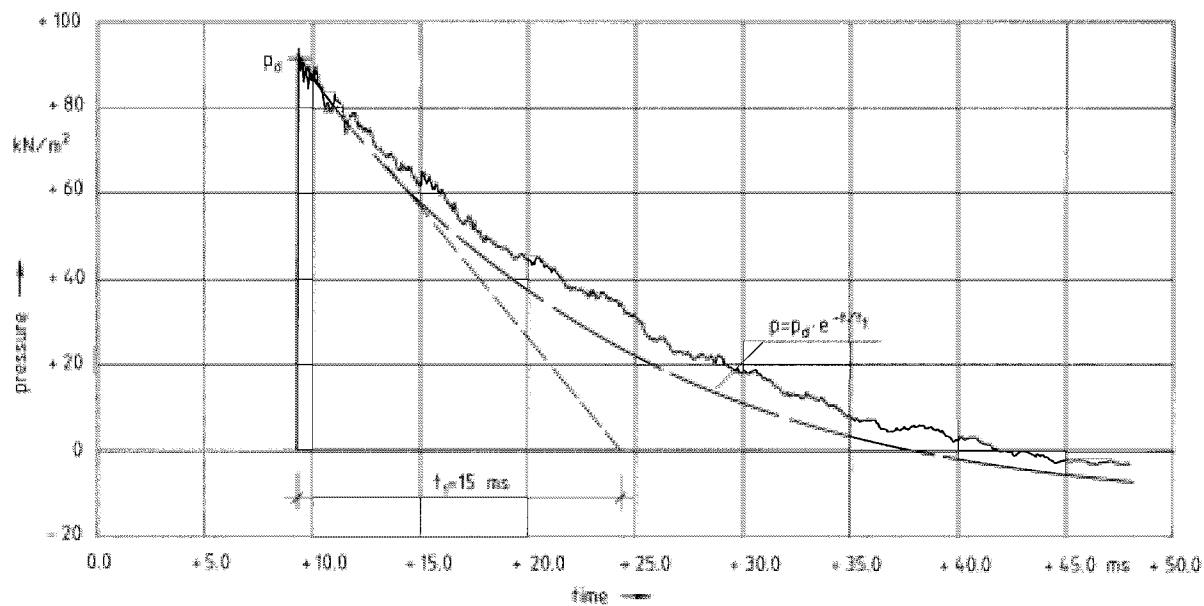


Figure 2. Load-time function

3 Results

The material behavior of SIFCON is influenced by the fiber volume (V_f), the ratio of the fiber length to the fiber diameter (l_f/d_f) and the fiber shape (OL, M, ZL). The relative effect of the fiber volume is reduced for SIFCON, the fiber shape and the relationship of the fiber length to

the diameter dominate [1]. The material strength under bending conditions and compression is displayed in Fig. 3. A typical stress-strain relation between SIFCON and plain concrete is demonstrated in Fig. 4. In Fig. 5 is the energy absorption of SIFCON in comparison to fiber concrete, plain concrete and plain cement represented. For the investigated fiber types (OL, M, ZL) and certain slurry mixes, described in [1], the compressive stress of SIFCON is about four times of the bending tensile stress.

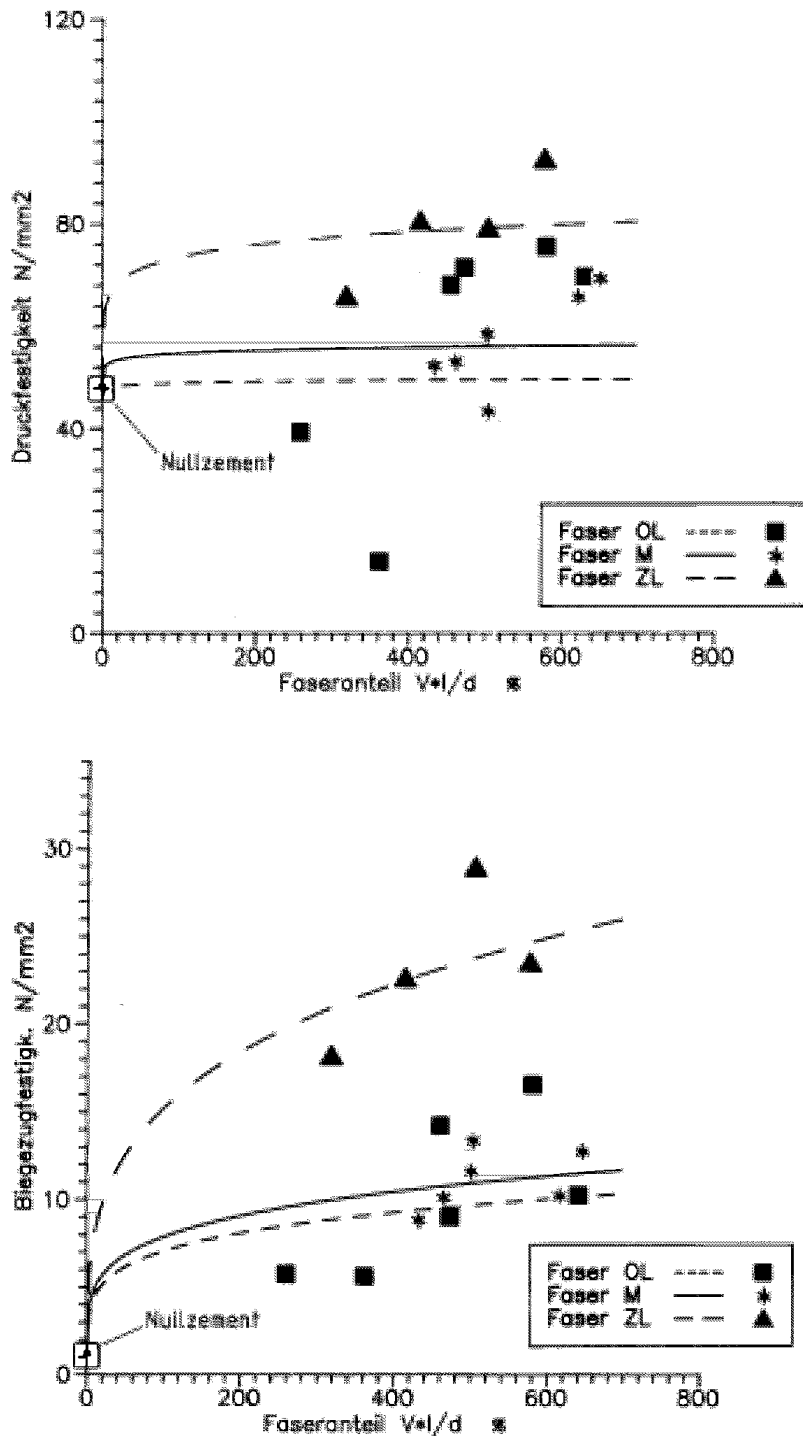


Figure 3. Material strength of SIFCON

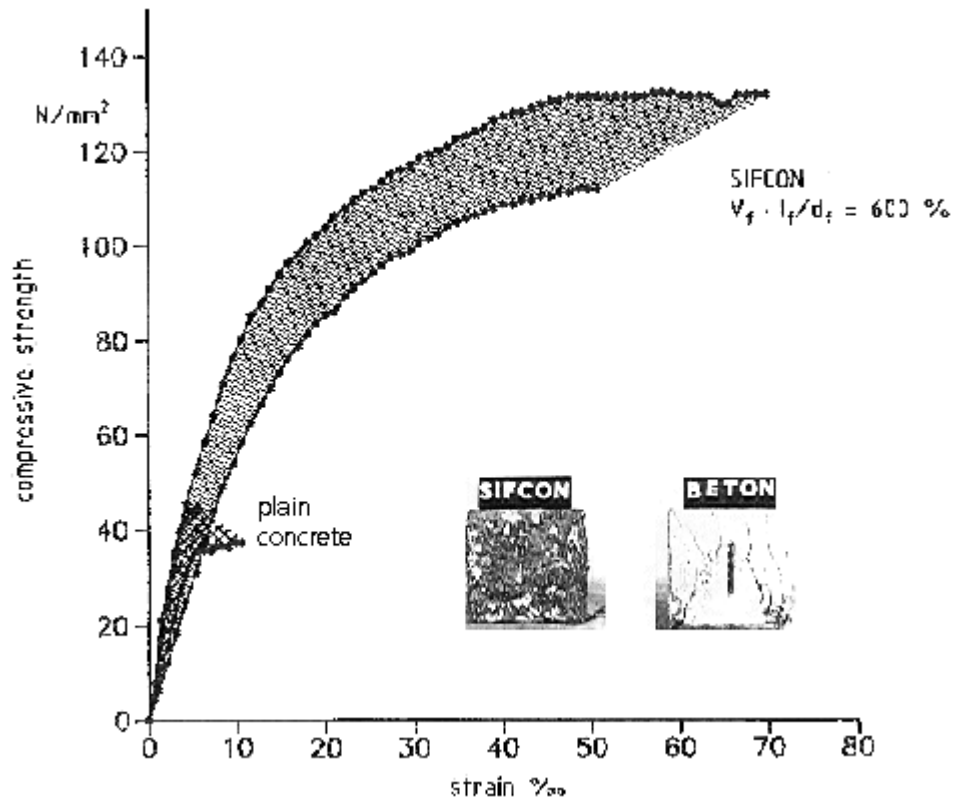


Figure 4. Stress-strain behavior of SIFCON and concrete

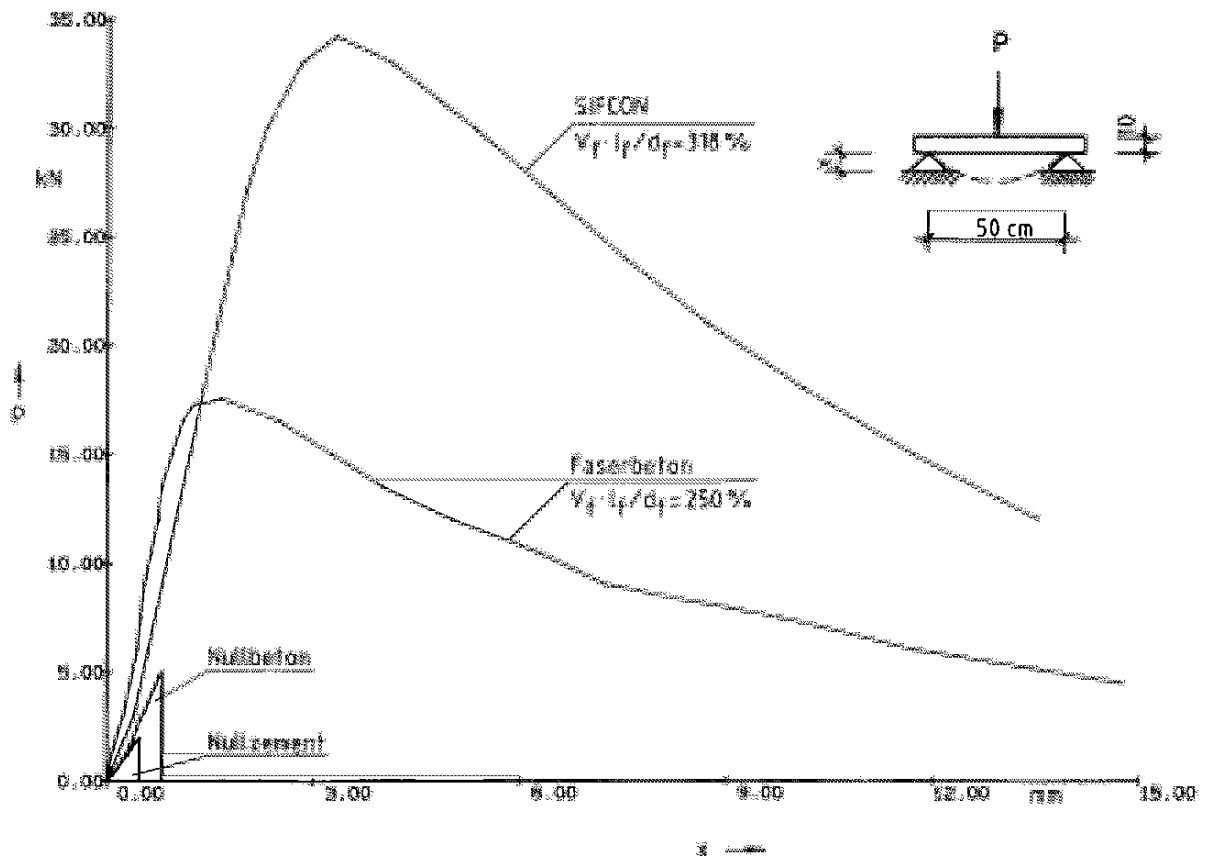


Figure 5. Energy absorption of fiber reinforced concrete and plain concrete

3.1 Static behavior of reinforced SIFCON

The experiment clearly point out the enhancement of the bending capacity of reinforced SIFCON compared to conventional reinforced concrete (Fig. 6). The enhancement depends on the amount of reinforcing steel bars (μ) and the material strength (σ_e , β_s , β_b , σ_{BZ}^s).

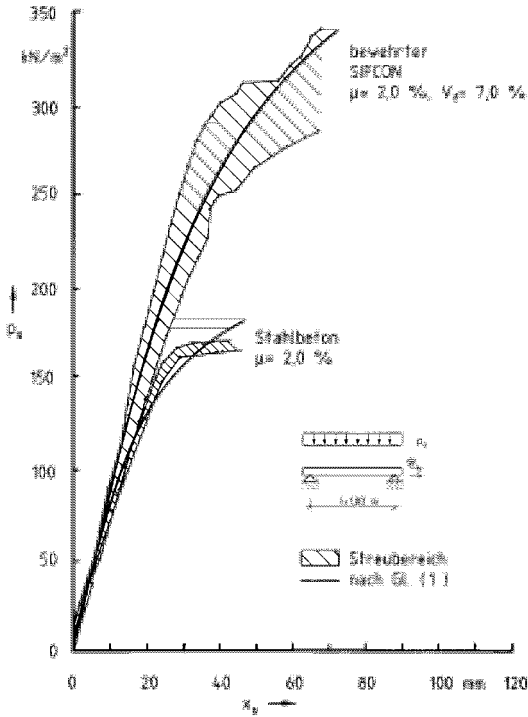


Figure 6. Static response of reinforced SIFCON and reinforced concrete

Of interest is that independent of μ , with reinforced SIFCON the ductility was not changed. For low and high reinforcement ($\mu = 0,6 \%$, $\mu = 2,0 \%$) the same ductility was achieved ($x_{failure} = 2,5 \cdot x_{elastic}$). This is not the case with reinforced concrete (high μ , low ductility).

For the calculation of the static response the bending moment of reinforced SIFCON was determined by the formula

$$M_i^s = b \cdot h^2 \cdot \beta_s \left[\frac{\alpha'}{2} + \bar{\mu}_s - \frac{(\alpha' + \bar{\mu}_s)^2}{2(1 + \alpha')} \right] \quad (1)$$

with $\alpha' = \bar{\sigma}_{BZ}^s / \beta_s$, b = width and h = effective depth. Because $\beta_s = 4 \cdot \sigma_{BZ}^s$, α' becomes a constant value of $\alpha' = 0,1$. In Fig. 7 the enhancement of the bending moment of reinforced SIFCON M^s to reinforced concrete M^b vs. a normalized reinforcement $\bar{\mu}_s = \mu \cdot \sigma_e / \beta_s$ is presented for different ratios of the compressive strength of concrete to SIFCON $\gamma' = \beta_b / \beta_s$. For low reinforcement $\bar{\mu}_s$ the effectively factor of reinforced SIFCON is twice as high as of reinforced concrete. This factor is even greater by an extreme high $\bar{\mu}_s$ and a low value of γ' (γ' is low for large β_s and small β_b).

On the other hand: If the same response of reinforced concrete and reinforced SIFCON is required the amount of steel bars in reinforced SIFCON can be reduced. This result was illustrated in Fig. 8 for a certain value of the compression strength ratio of $\gamma' = 0,38$ and for instance of a given normalized bending moment of $m^b = m^s = 0,15$. A reduction of $\bar{\mu}_s$ of a magnitude nearly 2 was obtained. This problem deals with an economical point of views.

3.2 Dynamic behavior of reinforced SIFCON

The judgement of the dynamic behavior was based on the experimental load-deflection curve, which can be approximated by the function

$$p_s = p_o \cdot \frac{2}{\pi} \cdot \arctan\left(\frac{\pi \cdot x_s \cdot c_o}{2 \cdot p_o}\right). \quad (2)$$

The theoretical approach of a one-degree-of-freedom system normalized ISO-damage curves were developed ([2], [3]). The nonlinear resistance function (Fig. 7) causes a field of curves with multiples of the $1/\lambda$ criterion. In the normalized situation $1/\lambda$ stands for the elastic deflection. From the experimental results a failure criterion of $2,5/\lambda$ was detected. In Fig. 9 are the normalized curves transferred for the given slab size ($2,0 \cdot 0,6 \cdot 0,1 \text{ m}^3$) in a non normalized manner. Now it's possible to assess the effects of the peak pressure and the impulse for the breaking of the slab. Points above the boundary line indicate that the slab will be destroyed whereas points in the lower region imply an intact construction. In the boundary domain of the quasi-static and the impulsive loading the magnitude is given in Fig. 10. The load bearing capacity in the quasi-static area (long load duration t_1) of reinforced SIFCON is nearly twice as high as than for normally reinforced concrete.

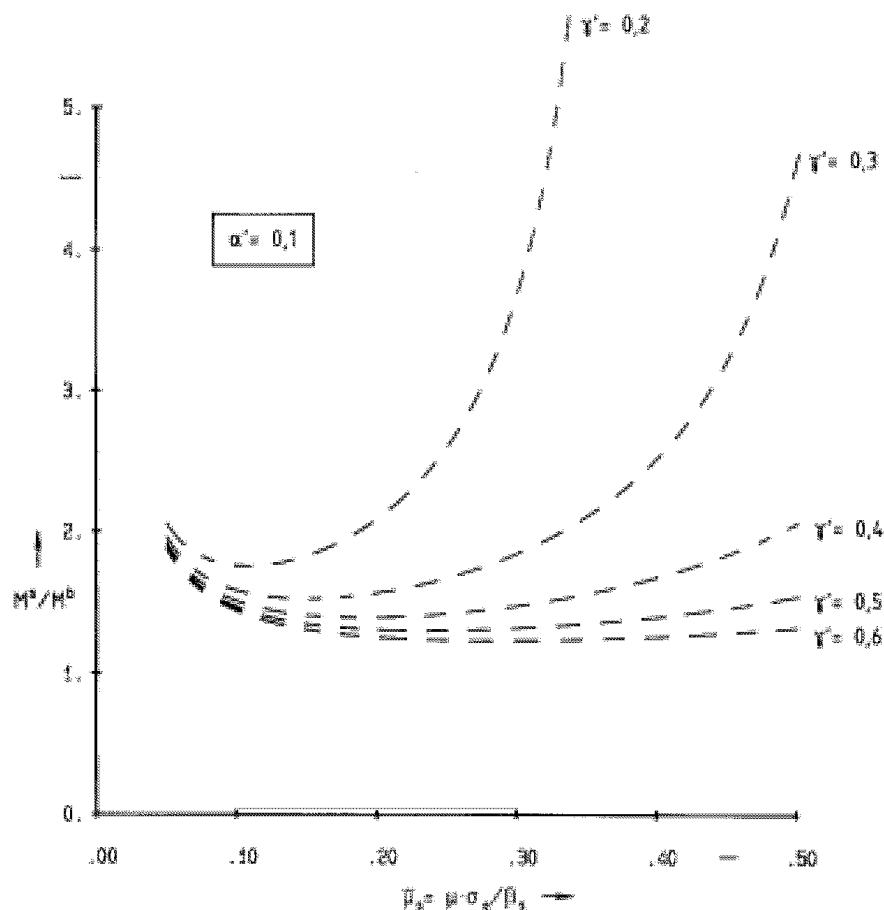


Figure 7. Enhancement of bending moment of reinforced SIFCON

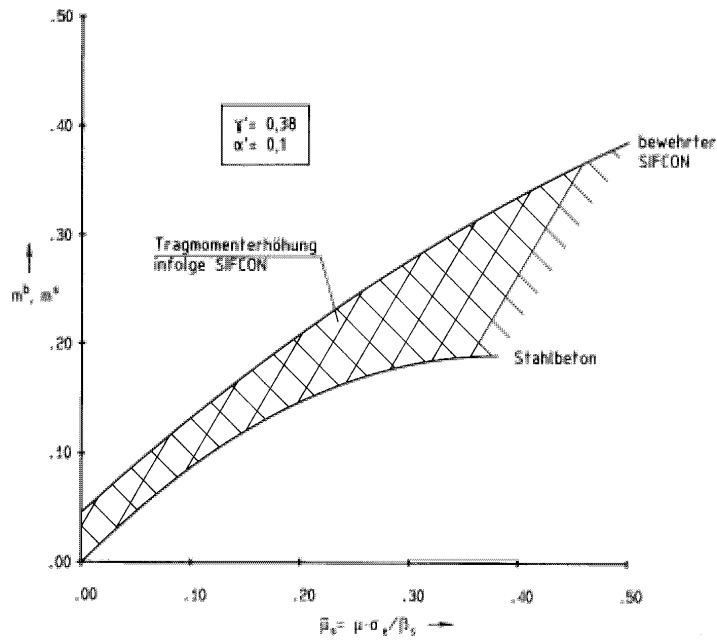


Figure 8. Flexure capacity of reinforced SIFCON and reinforced concrete

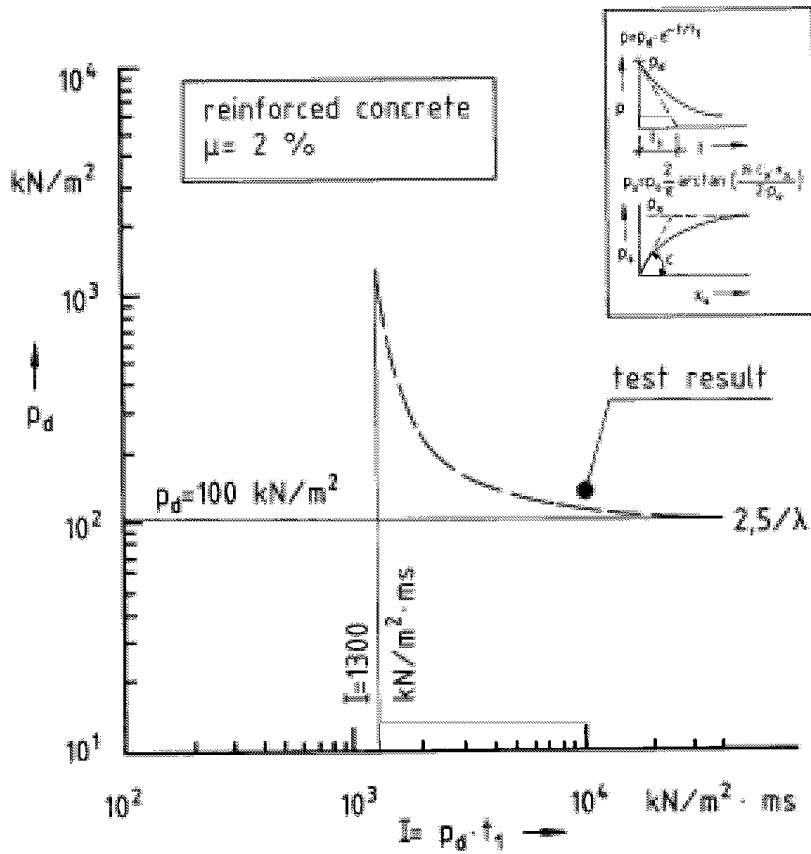


Figure 9. a) ISO-damage curves of reinforced SIFCON and reinforced concrete

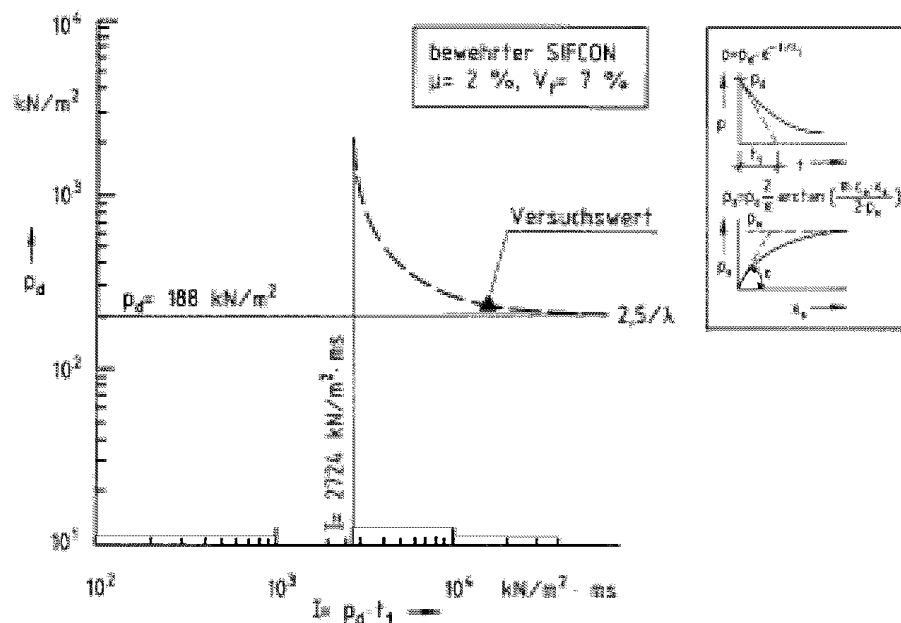


Figure 9. b) ISO-damage curves of reinforced SIFCON and reinforced concrete

4 Conclusions

- The load bearing capacity of reinforced SIFCON is drastically enhanced in static as well as in dynamic response compared to normally reinforced concrete.
- In contrast to normally reinforced concrete no brittle behavior was observed with strongly reinforced SIFCON.
- The breaking of reinforced SIFCON was reached at the maximum deflection of 2,5 times of the elastic deflection.
- To reach the same bending capacity as conventional reinforced slabs the depth of the slab or the amount of steel can be reduced for reinforced SIFCON.
- Compact reinforced composites like „reinforced SIFCON“ are favorable for dynamic loading, to suppress scabbing effects and to design plastic hinges.

5 References

1. Mayrhofer, Chr.: SIFCON und spezielle Faserbetone für extreme dynamische Beanspruchungen, E 17/90, Ernst-Mach-Institut, Freiburg i. Br., Dez. 1990
2. Mayrhofer, Chr.: Tragverhalten von SIFCON-Platten bei Druckstoßbelastung, E 12/92, Ernst-Mach-Institut, Freiburg i. Br., Nov. 1992
3. Mayrhofer, Chr.: Tragverhalten druckstoßbeanspruchter SIFCON-Platten mit zusätzlicher Baustahlbewehrung, E 7/93, Ernst-Mach-Institut, Freiburg i. Br., Aug. 1993

Size Effect in Compression of High Strength Fibre Reinforced Concrete Cylinders Subjected To Concentric And Eccentric Loads

Giuseppe Campione^a and Sidney Mindess^b

^a Department of Structural and Geotechnical Engineering, The University of Palermo, Italy.

^b Department of Civil Engineering, The University of British Columbia, Vancouver, Canada.

1 Abstract

Tests results obtained as a part of a study of size-effects on the compressive behavior of axially and eccentrically loaded plain and fibre reinforced concrete members are presented. The specimens were geometrically similar, having circular cross-sections with diameters of 60 and 100 mm, and varying in length from 120 to 400 mm. Several types of fibres (steel and synthetic) were added to the high strength matrices at a constant volume percentage of 2 % to evaluate their influence on the behavior of the material and on the size effect. It was observed that for all types of specimens the failure loads exhibited a size effect. The nominal stress at maximum load decreased as the size of the specimens or the eccentricity of the external load increased, but the post peak behavior and the mode of failure of the specimens were not much affected by the specimen size when high volume fractions of fibres were utilized.

2 Introduction




Most current design codes, which are based on limit state theory and justified by theory of plasticity, do not take into account size effects. In quasi-brittle materials, including concrete and rock, the observed load-deformation diagrams of members subjected to tension or compression are characterized by post-peak strain softening, which is due to the progressive development of damage in the form of microcracks which, after localization, lead to the final failure¹. For this reason the description of the behavior of concrete is incorrect in terms of plasticity, and thus a size effect is observed. Recent developments in fracture mechanics have shown that the size effects which are observed in the failure of concrete structures are due to the concrete rather than the steel; this is true not only when the concrete fails in tension, (diagonal shear, bar pull-out, torsion, etc), but also when the concrete fails in compression, except when there are confining pressures that greatly exceed the uniaxial compression strength²⁻⁴. Recent studies⁵⁻⁷ have shown that by adding sufficient quantities of randomly distributed short fibers of appropriate geometries to the matrices it is possible to improve the behavior of plain concrete and conventionally reinforced concrete in terms of both ductility and residual strength, especially in the case of high strength concrete. The active confinement due to the fibers because of their pull-out resistance ensures ductile behavior, reducing the quantity of lateral steel reinforcement required and thus reducing the size effect. Our aim here was to investigate the size effect in specimens having different aspect ratios, made of high

strength concrete reinforced with randomly distributed fibres. The influence of different types of fibres on the reduction in nominal strength due to the size effect, and also the effect of eccentric loading on the reduction in strength of the specimens is discussed. Only small reductions were observed in the apparent ductility and residual strength with increasing size of specimens, showing the effectiveness of using fibres to mitigate the brittle nature of high strength concrete.

3 Experimental Program

High strength matrices containing different types of fibres were cast to investigate the influence of specimen size on compressive behavior. The HSC mix designs previously investigated by the authors⁵ yielded 28-day compressive strengths of 70 MPa, measured on 100x200 mm cylinders, and had 3.61 MPa direct tensile strengths. The fibers, utilized at volume percentages of 2 %, were straight polyolefin and carbon fibres , crimped steel fibers and hooked steel fibers; the properties of the fibres are given in Table 1.

Table 1. Types and properties of the fibres

Type of fibre	Shape	Equivalent diameter d_f [mm]	Length L_f [mm]	Tensile strength f'_t [MPa]	Elastic modulus [MPa]
Polyolefin		0.80	30	375	12000
Crimped steel		1.00	35	1115	207000
Carbon		0.78	20	800	100000
Hooked steel		0.50	35	1115	207000

Several series of three cylindrical specimens each were cast for the different mixes (plain concrete and fiber reinforced concrete) and sizes investigated. The dimensions of the specimens tested were 60x120, 100x200, 150x300 and 100x400 mm. Figure 1 shows the test setup used to apply both the concentric and eccentric loads. It consists of two stiff metal rings placed separately on the top and on the bottom of the cylindrical specimens: concentrically, as in Figure 1 a) and eccentrically as in Figure 1 b). The eccentricity “e” of the axial load was 20 mm, corresponding to $e/D=0.2$, where D is the specimen diameter. The cylindrical specimens were tested in compression using an open loop machine with a maximum load capacity of 160 kN. To obtain the complete load versus deflection curves, a slow rate of loading of 0.3 MPa / s was employed. The axial deformations were measured using three LVDT’s which were mounted on the steel platen of the compressive machine with a gauge length equal to the entire length of the specimens.

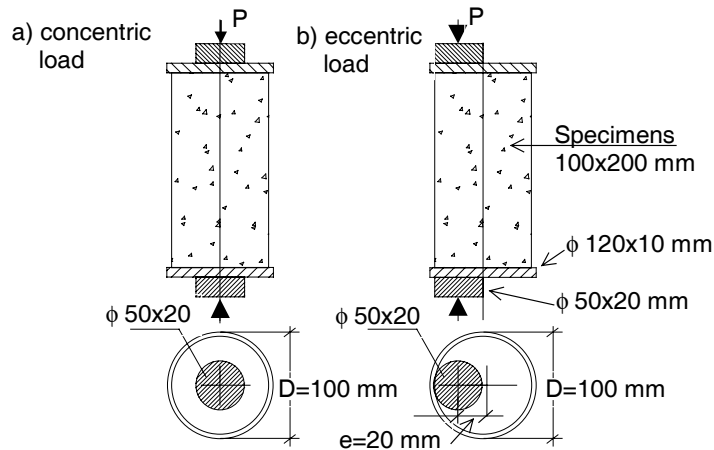


Figure 1. Test set-up

4 Experimental Results

In Figure 2 the nominal stress-strain curves are given for the different sized specimens of plain concrete.

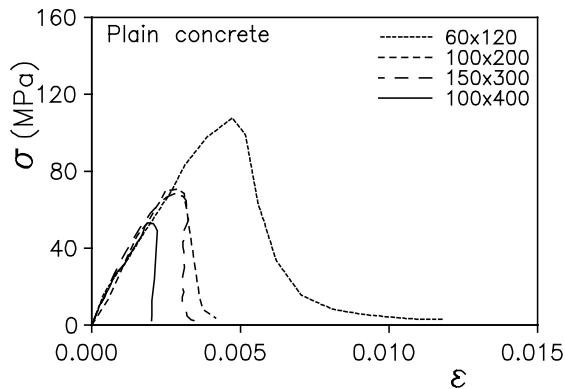


Figure 2. Stress-strain curves for HSC specimens in compression

The curves shown are the average values for three specimens tested for each series. The stresses refer to the initial transverse cross section, and the strains are evaluated on a gauge length equal to the entire length of the specimen. It is interesting to observe that with an increase in the size or the slenderness of the specimens (100×400 mm), the HSC exhibits a more brittle behavior and the size effect becomes more evident in terms of strength. Typical results of tests on HSC containing 2% by volume of steel or polyolefin fibres are shown in Figures 3, 4 and 5. In the case of FRC too, a size effect was observed in terms of both strength and strain.

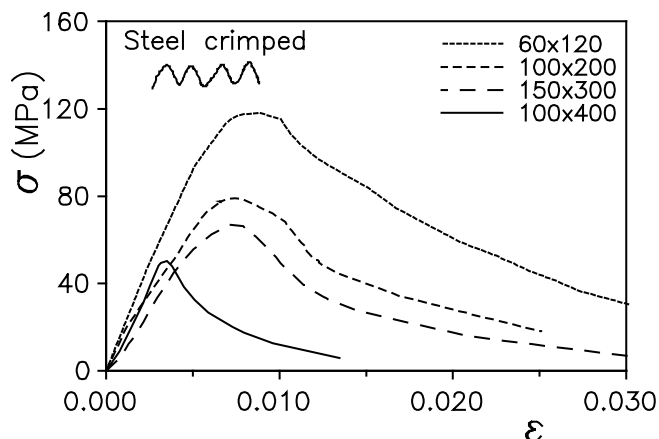


Figure 3. Stress-strain curves for HSC with crimped steel fibres at 2 % by volume

For FRC with steel fibers, either crimped or hooked (fibers with high modulus of elasticity and tensile strength), greater residual strength and absorbed energy were observed than with polyolefin fibers (fibers with low mechanical properties) or plain concrete.

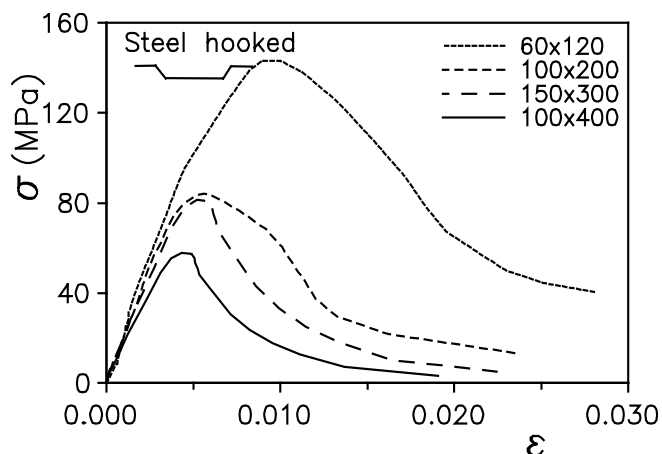


Figure 4. Stress-strain curves for HSC with hooked steel fibres at 2 % by volume

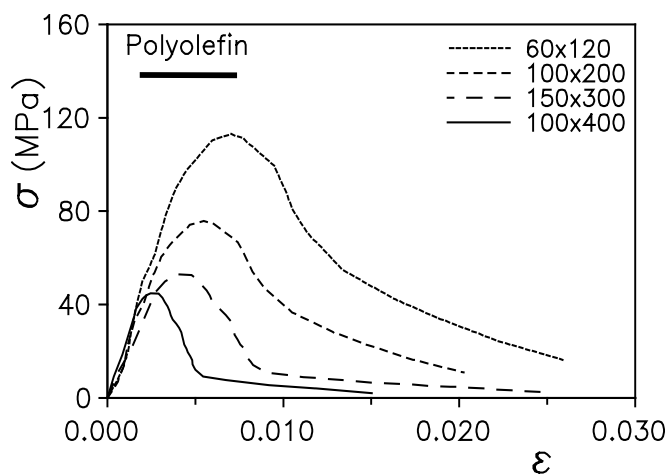


Figure 5. Stress-strain curves for HSC with polyolefin fibres at 2 % by volume

Figure. 6 shows that the shear mode of failure characteristic of ductile materials such as FRC containing high volume fractions of fibres appears to be the same for the specimens of different sizes.



Figure 6. Mode of failure of cylinders of different sizes containing 2% by volume of hooked steel fibres

Figure 7 presents the stress-strain curves for FRC with the different types of fibres obtained on 100x200 mm specimens loaded concentrically (case (a)) and eccentrically (case (b)). The effect of the eccentric load is a reduction in the load bearing capacity of the specimens particularly for plain concrete and FRC with polyolefin fibres. In the case of steel fibres, due to the higher tensile strength of the composite both in the precracking and post-cracking stages a smaller reduction in maximum and residual strengths was observed.

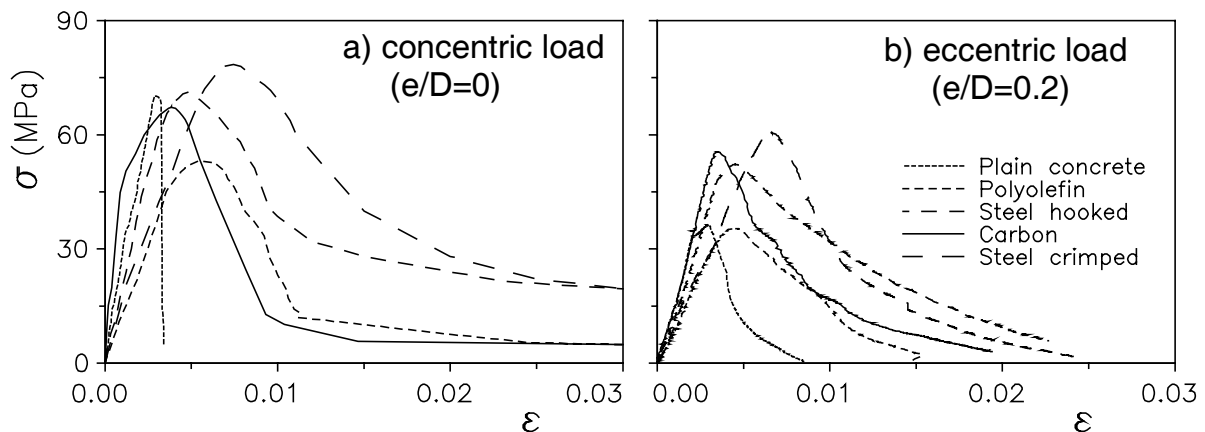


Figure 7. Effect of eccentric loading on the behavior of FRC cylinders (100x200 mm) containing 2% fibres.

Table 2 gives the values of compressive strength, splitting tensile strength, modulus of elasticity and modulus of rupture for plain concrete and for FRC

Table 2. 28-day strength results for FRC with 2% fibres

Type	Shape	Compressive strength [MPa]	Modulus of elasticity [MPa]	Modulus of Rupture [MPa]	Splitting tensile strength [MPa]
Plain concrete	/	70.23	33427	7.80	3.21
Polyolefin	————	53.02	33331	7.34	3.40
Crimped steel	~~~~~	78.48	34111	11.05	5.73
Carbon	————	67.31	36576	10.07	4.45
Hooked steel	—┐—┐—┐—┐—	71.14	39107	11.37	7.67

5 Conclusions

The results show that for both plain concrete and FRC made with high strength matrices, a reduction in nominal strength with an increase in the size of the specimens occurs. However, only a small reduction in apparent ductility was observed in the case of FRC. A ductile mode of failure was observed for all specimen sizes. The results also show a reduction in nominal strength due to eccentricity loading, which is smaller for FRC due to the higher tensile strength of the FRC compared to that of plain concrete.

6 References

1. Z.P.Bazant, Size effect in blunt fracture: concrete, rock, metal, *J.Engng Mech. ASCE* **110** (1984) 518-535.
2. Z.P.Bazant and Y.W.Kwon, Failure of slender and stocky reinforced concrete columns: tests of size effect. *Materials and Structures*, **27** (1994) 79-90.
3. B.I.G.Barr, H.F.Abusiaf and S. Sener, Size effect and fracture energy studies using compact compression specimens. *Materials and Structures*, **31**, January-February (1998) 36-41.
4. B.I.G.Barr, H.F.Abusiaf and S. Sener, Size-effect in unreinforced concrete columns *Magazine of Concrete Research*, **51** 1 (1999) 3-11.
5. G. Campione, S. Mindess, and G. Zingone, Compressive stress-strain behavior of normal and high-strength carbon fiber concrete reinforced with steel spirals. *ACI Mater. Journal* **96** 1 pp 27-35 (1999).
6. G.Campione, S.Mindess, and G.Zingone, Failure mode in compression of fibre reinforced concrete cylinders with spiral steel reinforcement. *Fifth International Symposium on Brittle Matrix Composites*, Warsaw, Poland, 13-15 October, (1997) 123-132.
7. G. Campione, and S. Mindess, Compressive toughness characterization of normal and high strength fiber concrete reinforced with steel spirals, in *Structural Applications of Fiber Reinforced Concrete*, SP-182 (1999), American Concrete Institute, 141-161.

III Fracture Mechanics of Cement-Based Materials

MICROMECHANICS OF FIBER-REINFORCED CEMENTITIOUS COMPOSITES

B L Karihaloo

Cardiff School of Engineering, University of Wales Cardiff, Queen's Buildings,
P. O. Box 686, Cardiff CF2 3TB, UK

J Wang

Department of Mechanics and Engineering Science, Peking University, Beijing 100871,
P. R. China

Abstract The strain hardening and tension softening response of short fiber-reinforced cementitious composites under unidirectional tensile/flexural loading is modelled using concepts from fracture and damage mechanics. The tensile strain hardening in these composites is due to the formation of microcracks which are however prevented from coalescing by the bridging action of the fibers. The density of microcracks increases with increasing tensile/flexural loading until it reaches a saturation level at the tensile load carrying capacity of the composite. Thereafter the fibers progressively debond from the elastic matrix and the deformation begins to localise in the eventual fracture plane, first as unconnected cracks and later as a connected through crack subjected to the residual frictional bridging action by the fibers.

1 Introduction

Figure 1 shows the typical load-deformation response of two types of fiber-reinforced concrete (FRC) to tensile/flexural loading. The deformation is generally expressed in terms of strain up to the peak load (point 2) and through crack opening displacement thereafter. The responses of the two FRCs have both similarities and differences. Thus, both exhibit linear elastic behaviour up to 1, strain hardening behaviour between 1 and 2, tension softening due to localisation of damage in the form of unconnected crack fragments between 2 and 3, and continued tension softening due to localisation of damage in the form of a through crack until complete rupture. The differences in the tensile load carrying capacity, the extent of strain hardening and the energy absorption capacity (the area under the load-deformation curve) reflect the differences in the microstructure of the two types of FRC and in the bonding between the steel fibers and the surrounding cementitious matrix.

The transition from linear elastic to strain hardening behaviour (point 1) is governed by the tensile strength of the cementitious matrix but is mostly unaffected by the fiber parameters (i.e. fiber aspect ratio, volume fraction and bond strength). The tensile strain hardening response (region 1 to 2) is known to be a result of the bridging action of fibers on microcracks which prevents their growth and coalescence (Mobasher *et al.*, 1990; Tjiptobroto and Hansen, 1993). The density of the microcracks increases with increasing tensile/flexural loading until it reaches a saturation level (point 2). The extent of strain hardening is determined by both the microstructure of the cementitious matrix and the volume fraction and the bond strength of the fiber.

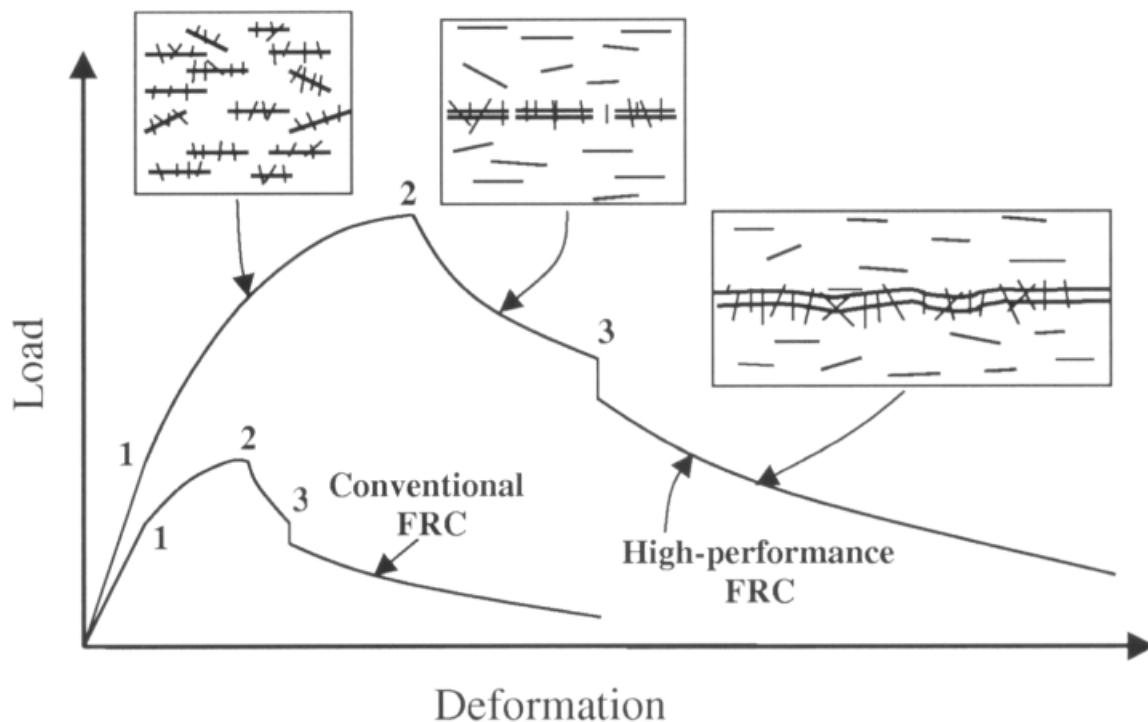


Figure 1 Complete pre- and post-peak tensile response of two short fiber reinforced cementitious composites.

When the strain hardening capacity has been exhausted (i.e. the tensile/flexural strength of the composite has been reached), some of the fibers begin to debond from the matrix, resulting in the localisation of deformation along the eventual failure plane. The localisation manifests itself in the opening of cracks along this plane, but without their actual coalescence. The strain level away from this localised zone usually decreases first and then remains almost unchanged. The increased deformation is due to the progressive debonding of the fiber under decreased applied loading which results in the opening of fragmented cracks and their growth (region between 2 and 3).

The fraction of fibers that remains elastically bonded to the matrix progressively decreases from 2 to 3 until at 3 all the fibers debond, resulting in an instantaneous drop in the residual load carrying capacity and in the coalescence of crack fragments to form a through crack (Ortiz, 1988). Thereafter, the residual tensile carrying capacity is

determined entirely by the frictional contact between the fibers and the matrix until the fibers are completely pulled out of the matrix, and failure occurs. It is the aim of this paper to develop a micromechanical model that describes the above strain hardening and tension softening response of FRC and highlights the role of microstructural parameters of the matrix and fibers in the different responses of the two types of FRC. The paper is organised as follows. Section 2 is devoted to the bridging action of fibers on microcracks and to quantifying the force applied on the crack faces as a function of the volume fraction, aspect ratio and the bond strength of fiber. Section 3 then describes the mechanism of strain hardening by considering an ideal situation in which an elastic matrix contains a doubly periodic array of identical cracks which are subjected to the bridging force of fibers. A model for the evolution of damage, i.e. increase in the microcrack density, under increasing tensile/flexural loading is introduced in order to give a complete description of the strain hardening range from 1 to 2. Section 4 develops a micromechanical model for the initial post-peak response from 2 to 3 when the localised zone of deformation consists of unconnected fiber-bridged crack segments and combines it with an existing model for a through crack subjected to the residual frictional bridging force exerted by the fibers. Section 4 also applies this micromechanical approach to two types of FRC and shows how it is capable of predicting their complete load-deformation response.

2 Bridging Action of Fibers

The bridging action of a single fiber is usually established from a pull-out test (Naaman and Shah, 1976; Balaguru and Shah, 1992) and expressed in terms of the elongation of the fiber or the mouth opening of an artificial crack, δ , and the shear stress τ along the matrix-fiber interface (Figure 2). Alternatively, δ is expressed in terms of the equivalent crack opening of an effective crack $\bar{\delta}$ when the transition is made from a single to a multiple fiber situation, as shown in Figure 3. The distribution of bridging stresses along the effective crack $p(v_t)$ is taken to conform with the slip-weakening behaviour exhibited by steel fibers (Figure 2). τ_v is the average adhesive bond strength, τ_g the frictional bond strength, δ^s the elongation (or crack mouth opening) in a single-fiber pull out test. The corresponding quantities for multiple fiber situation are τ_v^* , τ_g^* and δ . δ_0^s (δ_0) are the respective crack openings at initiation of a single (multiple) pull-out (Figure 4). The corresponding effective quantities are identified by an overbar. Note that $\bar{\delta} = 2\bar{v}_t$ (Figure 3), such that slip initiates when $\delta_0 = 2\bar{v}_{cr}$ (Figure 2). It is clear from Figure 2 that a single fiber oriented along the direction of tension exerts a higher bridging force than does a collection of fibers randomly criss-crossing a crack. However, the crack opening is smaller in the latter case.

There are several approaches to estimating the force exerted by the fibers based on the concepts of strength (Banthia and Yan, 1996), fracture mechanics (Balaguru and

Shah, 1992; Karihaloo, 1995; Stang *et al.*, 1990), and the so-called mismatch-strain (Hsueh, 1006). It can be shown (Lange-Kornbak and Karihaloo, 1997) that

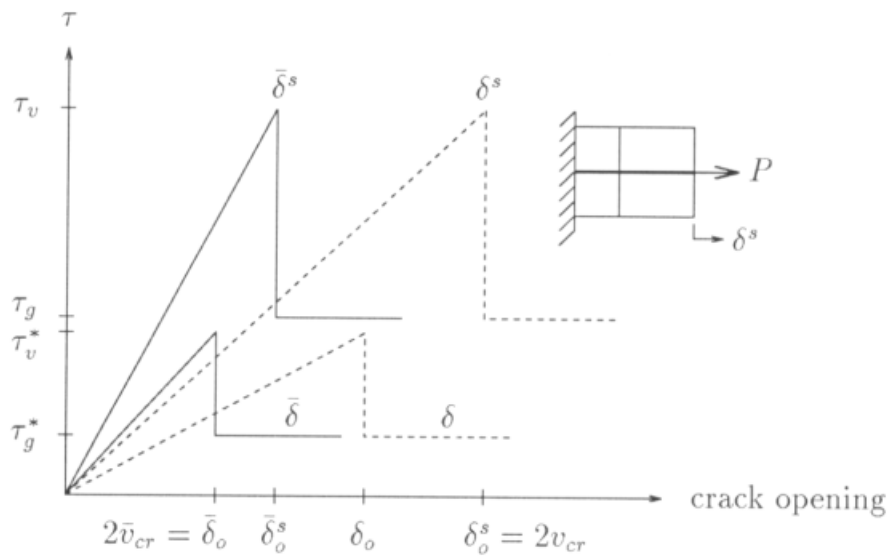


Figure 2 Idealised interfacial matrix-fiber shear stress (τ) vs. crack mouth opening (elongation of fiber) (δ) or effective crack opening. $\bar{\delta}$ (τ) relationship for single-fiber (superscript s) and multiple fiber pull-out.

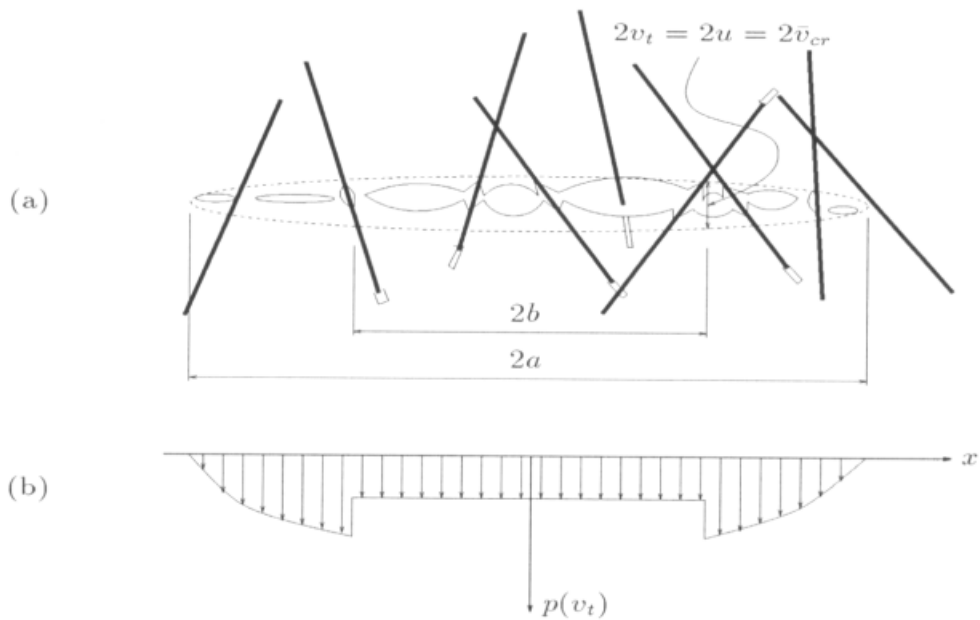


Figure 3 (a) Effective crack (dashed line) and physical 'crack' of fiber-reinforced material with (b) distribution of bridging stress $p(v_t)$ prior to coalescence of cracks.

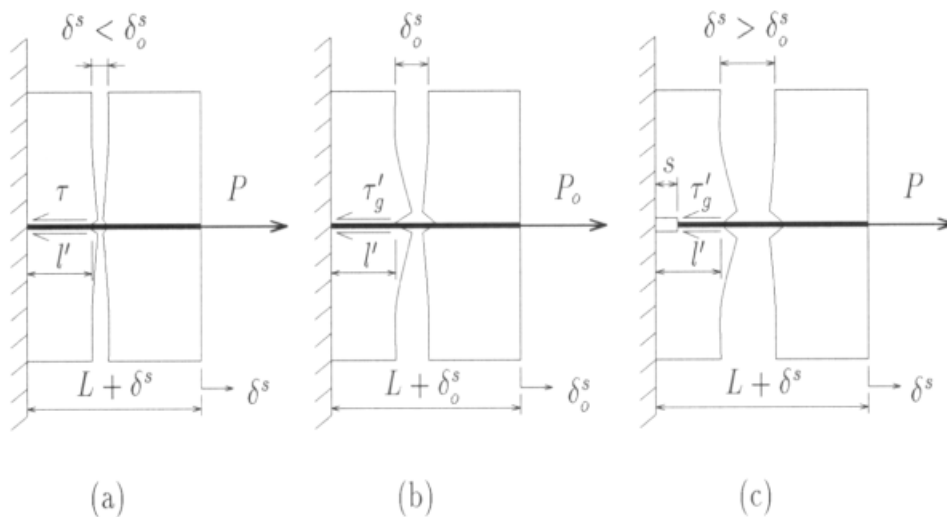


Figure 4 Single-fiber pull-out (a) prior to slip, (b) at onset of slip, and (c) during slip.

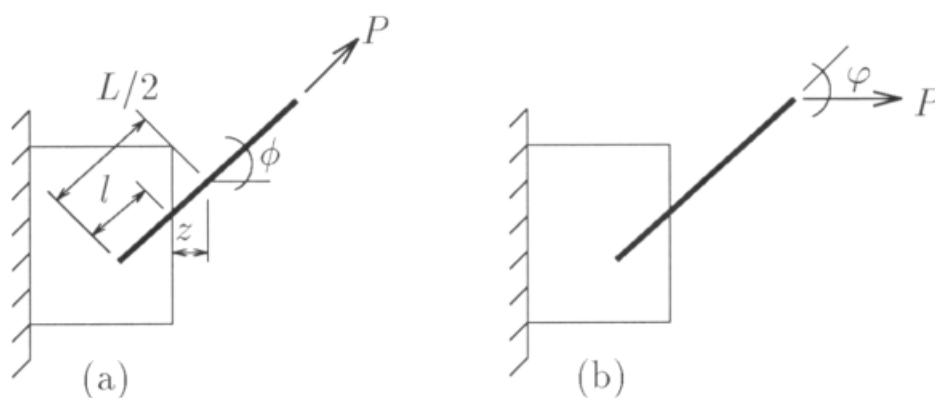


Figure 5 (a) Single-fiber pull-out without snubbing ($\phi=0$) and (b) with snubbing ($\phi \neq 0$, $\phi=\phi$).

$$\begin{aligned}
p(v_t) &\approx 2V_f \frac{\tau_v}{\tau_g} E_f \frac{h}{L} v_t; & v_t < \bar{v}_{cr} \\
&\approx \frac{1}{2} V_f \tau_g \frac{L}{d} h \frac{\bar{v}_{cr}}{v_{cr}}; & v_t \geq \bar{v}_{cr}
\end{aligned} \tag{1}$$

where E_f is the modulus of elasticity of the fiber, and h is the so-called snubbing factor to account for the fiber dowel action when it is acted upon by a force which is not directed along its length (Figure 5). It is defined by

$$h = \frac{2}{4 + f^2} \left(e^{f\pi/2} + 1 \right) \tag{2}$$

where f is the snubbing friction coefficient (Li *et al.*, 1991). $v_t(x)$ denotes the local half-opening of the effective crack (Figure 2) which will be simply designated $v(x)$ in the following. It is clear from (1) that

$$\begin{aligned}
p(v) &\approx k v; & v < \bar{v}_{cr} \\
&\approx C; & v \geq \bar{v}_{cr}
\end{aligned} \tag{3}$$

The bridging stiffness k of the elastic adhesive bond is directly proportional to V_f , τ_v , E_f and h and inversely proportional to L and τ_g . On the other hand, the constant frictional bridging stress C is directly proportional to τ_g and L . Thus, a compromise has to be made in the length of the fiber L and its frictional pull-out resistance τ_g in order to produce an FRC which has both extensive strain hardening behaviour and a high energy absorption capacity, because as we shall see later a high k ensures an extended strain hardening range, whereas a high C ensures an extended tail of the tension softening response. The compromise can also be secured by using a mix of short and long fibers in the same FRC.

3 Pre-Peak Strain Hardening

As mentioned above, the tensile strain hardening in FRC is due to the formation of microcracks which are however prevented from coalescence by the bridging action of fibers. Moreover, as the applied tensile/flexural loading is increased, more and more microcracks are formed until their density reaches a saturation level when the composite is no longer able to withstand additional tension.

In a real FRC the microcracks are of varying lengths and are randomly distributed. From a mathematical point of view it is an extremely difficult, if not impossible, task to investigate a random distribution of bridged microcracks of arbitrary lengths. We therefore consider a configuration in which all microcracks are oriented normal to the applied tension. Such a configuration leads to the maximum reduction in the stiffness in the direction of the applied tension. In a real FRC, the reduction in the stiffness will be

much lower, because all microcracks are unlikely to be oriented in the most unfavourable direction (i.e. normal to the applied tension). We assume further that the microcracks are of equal length and are distributed in a doubly-periodic array (Figure 6). The mathematical problem therefore is to solve an infinite, isotropic elastic solid containing a doubly-periodic array of bridged cracks. The solid is subjected to a uniform remote stress σ normal to the cracks. The crack faces are subjected to a normal bridging traction imposed by the fibers which is proportional to the crack opening (3). By symmetry, the bridging traction has the same distribution along all cracks. Note that in the strain hardening range (1 to 2 in Figure 1) the fibers are fully bonded to the matrix, i.e. $v < \bar{v}_{cr}$ in (3).

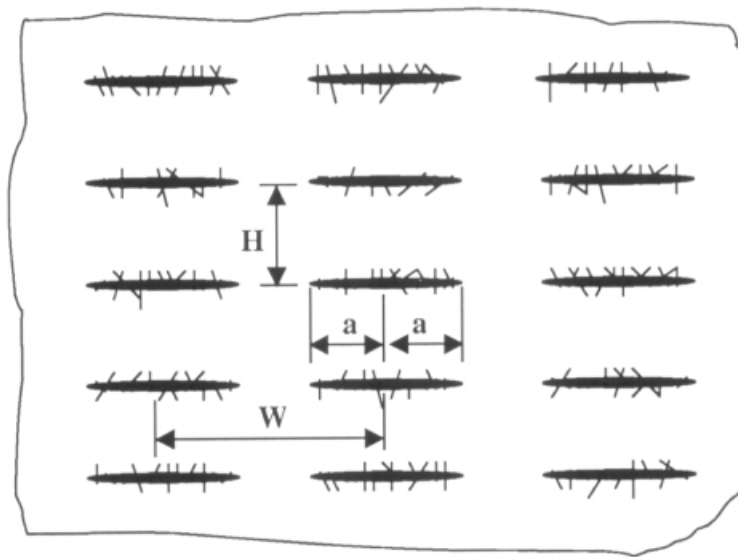


Figure 6 A doubly periodic array of bridged cracks.

This problem is solved by decomposing it into an infinite sequence of subsidiary problems in each of which only one row of collinear cracks is considered. This superposition procedure was first proposed by Karihaloo *et al.* (1996) (see also Karihaloo and Wang, 1997a). By this procedure and the formalism of pseudo-traction (Horii and Nemat-Nasser, 1985; Hu *et al.*, 1994), the traction consistency condition on each crack in a subsidiary problem can be written as

$$\sigma^p(x) - 2 \sum_{j=1}^{\infty} \int_0^a K_{\sigma}(x, x^j) \sigma^p(x^j) dx^j + p(x) = \sigma, \quad x, x^j \in [0, +a) \quad (4)$$

where $\sigma^p(x)$ ($x \in [0, +a)$) are the unknown pseudo-tractions on the faces of each crack, and the kernel $K_{\sigma}(x, x^j)$ represents the stress at x induced by a set of unit crack surface tractions at x^j in sub-problem j (Figure 7). The crack opening displacement is determined solely by the pseudo-tractions $\sigma^p(x^i)$ on the crack in sub-problem i

$$v(x) = \int_0^a K_v(x, x^i) \sigma^p(x^i) dx^i, \quad x, x^i \in [0, +a) \quad (5)$$

where the kernel $K_v(x, x^i)$ represents the crack opening displacement at x induced by a set of concentrated unit loads at x^i . Both kernels can be obtained in a closed form from the results in the handbook by Tada *et al.* (1985).

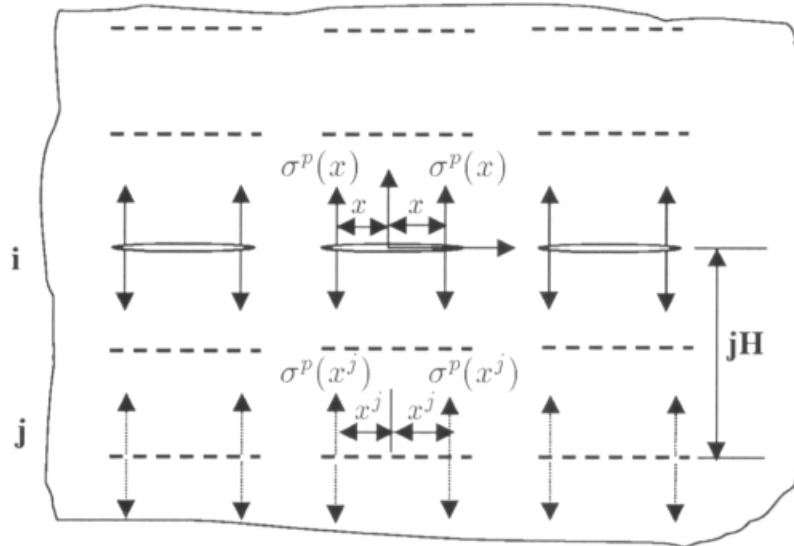


Figure 7 Decomposition of the original problem and the calculation of crack interaction.

Substitution of (5) into (3), and of the latter into (4) results in an integral equation for the unknown pseudo-traction. The kernel $K_\sigma(x, x^j)$ is not singular, provided $H > 0$, and it decays exponentially when j tends to infinity. The kernel $K_v(x, x^i)$ has an integrable logarithmic singularity at $x = x^i$ which can be easily handled by regularisation. The integral equation was solved accurately using Gauss-Legendre quadrature by Karihaloo *et al.* (1996) (see also Karihaloo and Wang (1997b)). After solving $\sigma^p(x)$ the crack opening displacement is easily calculated from (5). The influence of bridging stiffness k on the normalised crack opening of a quadrant of a crack in the array is shown in Figure 8. The non-dimensional bridging stiffness $c = 2(1-\nu^2)ak/E$, and the geometry of the array is described by $W/a = 2.5$ and $H/a = 2.0$. Here, E is Young's modulus of the matrix. The information on how the bridged cracks open under increasing imposed tension σ is needed to quantify the decrease in the stiffness of the composite, using the incremental constitutive relations for a cracked body (Horii and Nemat-Nasser, 1983)

$$\Delta \varepsilon_{ij} = D_{ijkl} \Delta \sigma_{kl} + \frac{1}{V} \int_S \frac{1}{2} ([v_i] n_j + [v_j] n_i) dS \quad (6)$$

where $[v_j]=v_j^+-v_j^-$ denotes the displacement jump across the crack with unit normal vector n_i ; D_{ijkl} is the elastic compliance tensor of the uncracked matrix, and the integration is carried over the crack surface S contained in a representative volume V of the composite. In the model being studied, the stiffness decreases the most in the direction of application of tension, and it is the tangent modulus of the composite in that direction that is of most interest here. It should however be noted that the composite is no longer a macroscopically isotropic medium but an orthotropic one. Application of (6) to the incremental stress and strain in the loading direction gives the instantaneous tangent modulus E_y in that direction

$$\frac{E_y(\sigma)}{E} = \left[1 + \frac{8a^2}{WH} \int_0^1 v^*(t) dt \right]^{-1} \quad (7)$$

where

$$v_t^*(t) = \frac{v(t)E}{2\sigma a}; \quad t \in [0,1] \quad (8)$$

E is the plane stress Young's modulus of the uncracked matrix in the direction of loading. Under plane strain, E is replaced with $E/(1-\nu^2)$. The variation of $v^*(t)$ is shown in Figure 8 under plane strain conditions. The plane stress non-dimensional bridging stiffness is simply

$$c=2ak/E \quad (9)$$

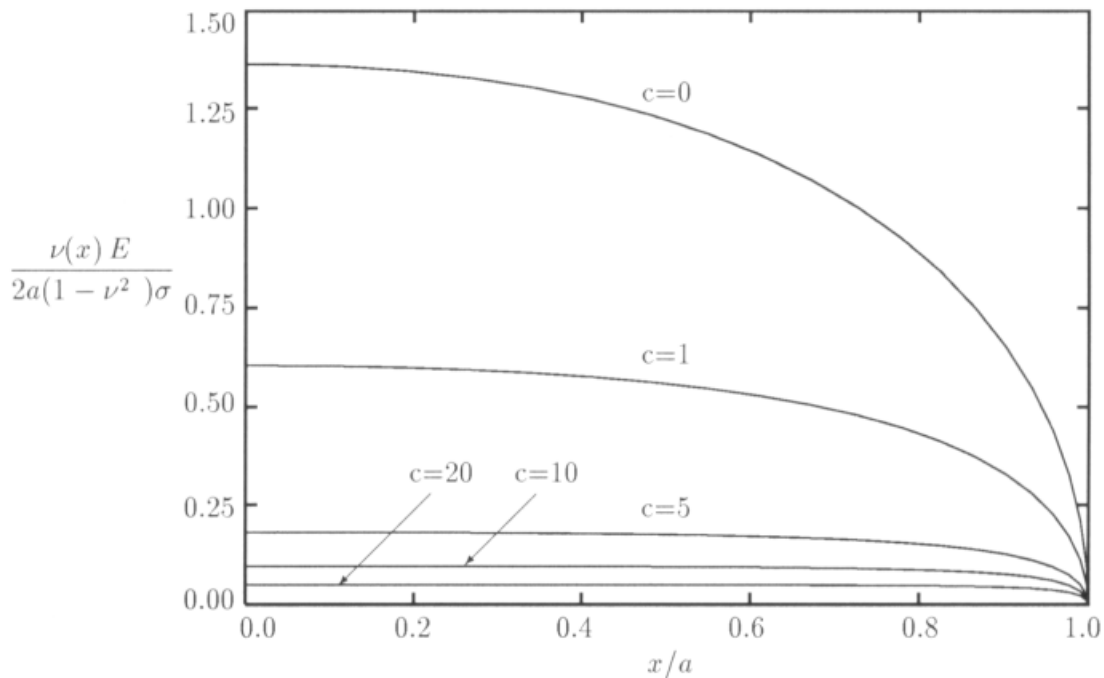


Figure 8 Influence of bridging stiffness on crack opening displacement.

The dependence of the instantaneous tangent modulus on the normalised bridging stiffness (9) may be judged from Figure 9. Finally, to study the variation of the tangent modulus with increasing applied tension when additional microcracks are formed, it is necessary to postulate a microcrack evolution law. Karihaloo and Wang (1997b) have postulated the following two-dimensional linear evolution law based on experimental evidence

$$\frac{\sigma}{\sigma_{mc}} = 1 + \frac{\left(\frac{WH}{a^2}\right)_s [\sigma_s / \sigma_{mc} - 1]}{\frac{WH}{a^2}} \quad (10)$$

where σ_{mc} is the stress level at the initiation of cracks, and the subscript s denotes the value of the corresponding quantity at the saturation of microcracking. The initiation value σ_{mc} may be equated to the tensile strength of the matrix σ_m , whereas the saturation value σ_s will represent the ultimate tensile capacity of the composite σ_c . Rigorous estimates of σ_m and σ_c based on the principles of fracture mechanics may be found in Lange-Kornbak and Karihaloo (1997). They showed in particular that the rigorous estimate of σ_c is in close agreement with the rule of mixtures

$$\sigma_c = \alpha \sigma_m (1 - V_f) + \beta \tau_v V_f \frac{L}{d} \quad (11)$$

The empirical constants α and β in (11) are to be ascertained from tests. However, in order to retrieve σ_m when $V_f=0$, α is usually set equal to 1, whereas for randomly distributed short fibers, Aveston *et al.* (1971) have proposed $\beta=0.5$. Lange-Kornbak and Karihaloo (1997) also showed that σ_m depends on the water to cement ratio, and the maximum size and Young's modulus of the aggregates in the concrete matrix.

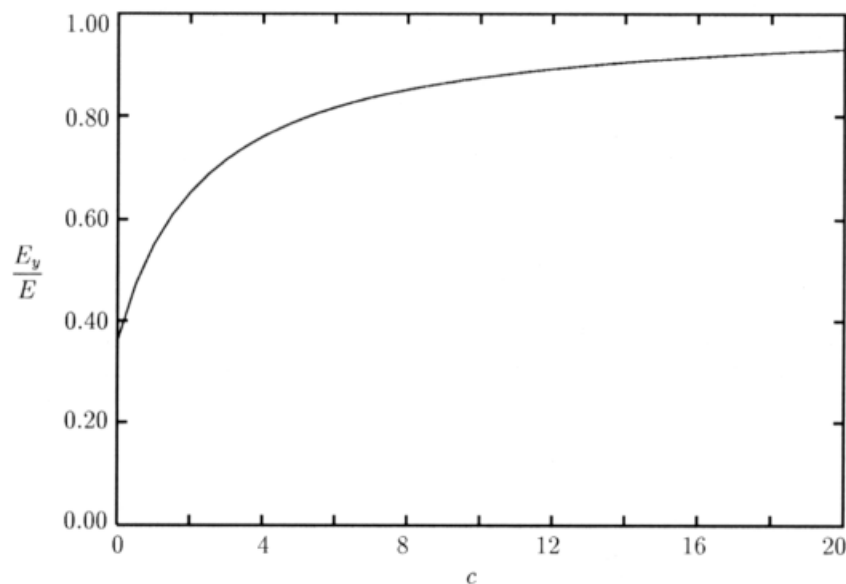


Figure 9 Influence of bridging stiffness on normalised instantaneous tangent modulus.

Once $\sigma_m (\equiv \sigma_{mc})$ and $\sigma_c (\equiv \sigma_s)$ have been properly estimated, the variation of tangent modulus with the applied stress during the evolution of microcracks can be determined from (7) and (10). The stress-strain relation past the initiation stress level σ_{mc} can be obtained incrementally via

$$\Delta \varepsilon = \Delta \sigma / E_y(\sigma) \quad (12)$$

$$\frac{\Delta \varepsilon}{\varepsilon_{mc}} = \frac{\Delta \sigma}{\sigma_{mc}} / \frac{E_y(\sigma)}{E} \quad (13)$$

where Δ denotes a small increment.

To conclude this Section, we note that Wang *et al.* (1999) have provided a closed-form asymptotic expression for E_y/E

$$\frac{E_y}{E} = \left[1 - \eta \frac{4W}{\pi H} \ln \left(\cos \frac{\pi a}{W} \right) \right]^{-1} \quad (14)$$

where

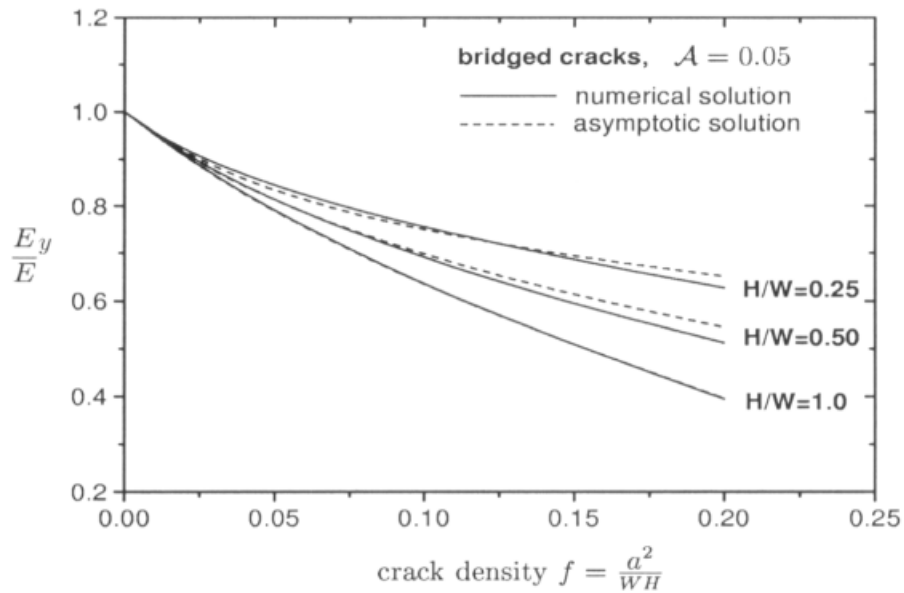
$$\eta = \left\{ 1 + 4 \sin^2 \frac{\pi a}{W} e^{-2 \frac{H}{W} \pi} \left[\frac{1}{1 - e^{-2 \frac{H}{W} \pi}} + \frac{2 \frac{H}{W} \pi}{\left(1 - e^{-2 \frac{H}{W} \pi} \right)^2} - \frac{c}{2\pi} \left(\frac{W}{a} \right)^2 \right] \right\}^{-1} \quad (15)$$

They have compared the asymptotic expression (14) with the numerical solution and have shown that it is very accurate for low to moderate levels of microcracking and for a wide range of bridging stiffness c (9). Typical comparisons for two values of $A = c/(2\pi)$ are shown in Figure 10.

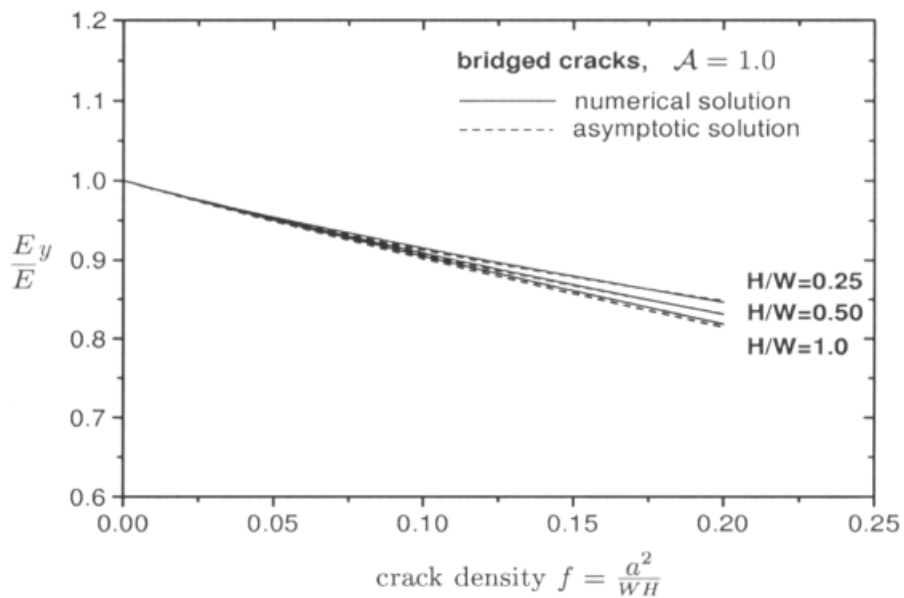
4 Post-Peak Tension Softening

At the peak load (i.e. when $\sigma = \sigma_c$) the strain hardening capacity of the composite is exhausted and some of the fibers begin losing their adhesion to the matrix. The microcracks that are bridged by these fibers begin to open more widely than the others, so that the deformation begins to increase while the load carrying capacity of the composite drops. Initially only a few microcracks, which are still unconnected, experience large opening while the others actually are less strained. The deformation is mostly due to the former which localises along the eventual fracture plane. The location

of this plane of localised deformation is determined by the variations in the microcrack lengths and the bridging forces. Thus, it is likely that the eventual failure plane will form where there are longer microcracks or where there are fewer fibers owing to their uneven distribution. In fact, Karihaloo and Wang (1998) have demonstrated this by considering an array of bridged cracks containing a finite number of collinear rows of cracks in which the cracks in one row is different from the other rows.



(a)



(b)

Figure 10 Variation of normalised modulus with crack density for bridged cracks with $\mathcal{A}=0.05$ (a) and $\mathcal{A}=1.0$ (b).

In the doubly-symmetric array of identical bridged cracks under consideration here, localisation can take place in any one of the collinear rows. What is important for the present purposes is that the initial part of tension softening (from 2 to 3 in Figure 1) is a result of the progressive growth of the discrete cracks in the localisation zone into the unbroken material. In this range, the fibers are progressively pulled out beginning from the centre of each crack where the opening is the largest, so that the crack can grow towards its neighbours. Eventually, when the neighbouring cracks have linked up, a through crack forms which is under the action of the residual frictional fiber bridging force (Figure 11).

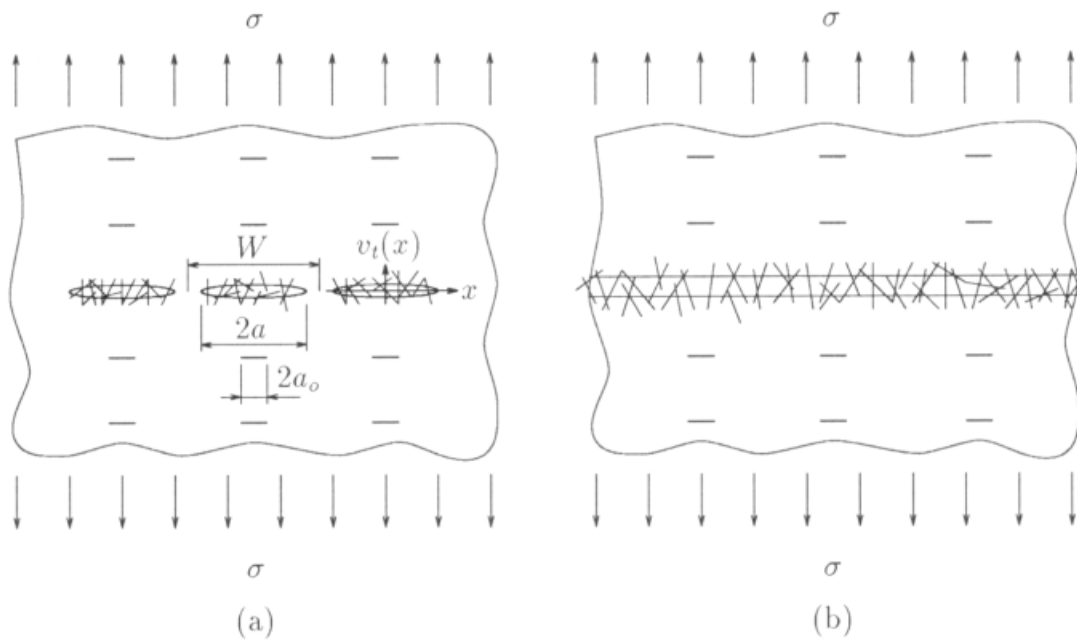


Figure 11 (a) Crack configuration prior to coalescence of cracks and (b) after coalescence of cracks during tension softening of fiber-reinforced quasi-brittle materials.

In the initial part (Figure 11a), each crack is subjected to a fiber bridging force as shown in Figure 3. The cracks will begin to grow into the unbroken material when the following two dynamic conditions for crack growth are simultaneously met

$$\begin{aligned} K_I(\sigma, a; b) &= \overline{K}_{Ic} \\ v(\sigma, a; b) &= \overline{v}_{cr} \end{aligned} \quad (16)$$

where $v(\sigma, a; b)$ is the crack opening at $x=b$ and σ denotes the reduced tensile carrying capacity. At the onset of tension softening $b=0$, so that (8) can be used to calculate the average critical crack opening \overline{v}_{cr} . The effective fracture toughness of the composite \overline{K}_{Ic} is related to its ultimate tensile carrying capacity (11), i.e. the tensile stress at the onset of tension softening and the half-crack length a_0

$$K_{Ic} = \Gamma_0 \sqrt{\pi a_0} \sigma_c \quad (17)$$

The geometrical factor Γ_0 for the row of elastically bridged cracks at the onset of tension softening depends on a_0/W and is calculated using the same numerical procedure as for the doubly-periodic array but with the distance of vertical separation H set equal to a very large value ($H \rightarrow +\infty$).

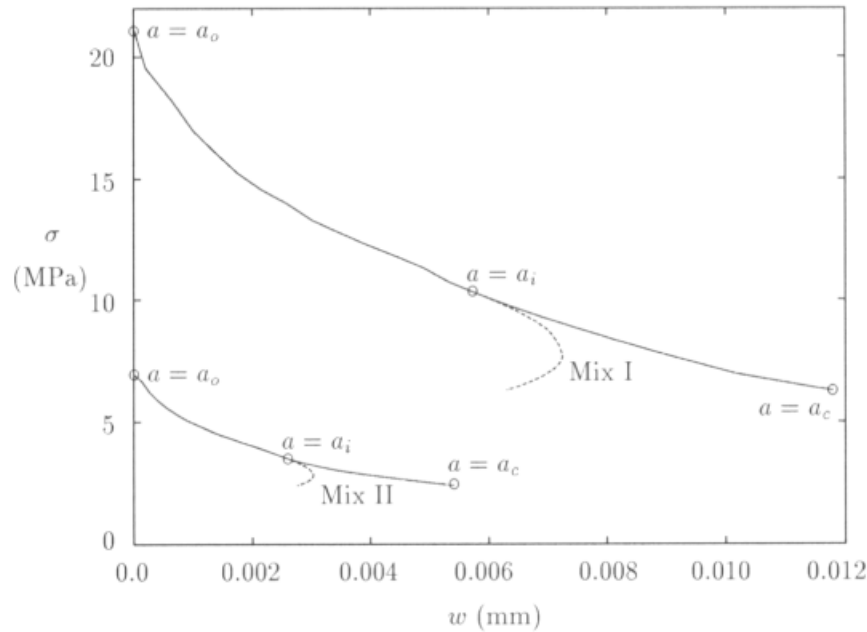


Figure 12 Initial tension softening curves of high-performance (mix I) and conventional (mix II) fiber-reinforced cement composites according to the multiple-crack model (dashed) and the modified multiple-crack model (solid). The onset of tension softening, onset of instability, and instant of coalescence of cracks are indicated by the corresponding half-crack length a_0 , a_i and a_c , respectively.

From (16) and (17) it is now possible to determine the reduced tensile carrying capacity σ and the length of the central portion of the crack b over which the fibers exert closure force due to friction only. To complete the description of the initial part of the tension softening process it remains to determine the average inelastic crack opening along the localised damage band, given by

$$w \equiv \langle v \rangle = \frac{1}{W} \left[\int_{-a}^{+a} [v_t] dt - \int_{-a_0}^{+a_0} [v_e] dt \right] \quad (18)$$

where $[v_t]$ is the total opening of the crack faces, and $[v_e]$ is the elastic (recoverable) opening of the crack faces. Note that over the unbroken ligaments, $|x| = (W/2) - a$, $[v_t] = 0$.

Figure 12 shows the initial tension softening response for two composite mixes whose micromechanical material parameters are shown in Table 1. Mix I is a cement-silica-based high performance mix (HPFRC), while mix II is based on a conventional high-strength cement binder (CFRC). In the initial part of tension softening regime, the

growth of fragmented bridged cracks takes place at a constant fracture toughness K_{Ic} . However, it is known, that when the tips of coplanar cracks are very close to each other (Melin, 1983) an instability sets in, whereby w decreases with decreasing σ . This phenomenon has not been observed in real materials, in which it appears that closely-spaced coplanar cracks do not grow towards each other but rather avoid each other by deviating from their plane. As a result, there is decrease in K_I , or what is the same, an apparent increase in the fracture toughness K_{Ic} . This increase in K_{Ic} is manifested through a change in the sign of curvature $\frac{\partial^2 \sigma}{\partial w^2}$ of (σ, w) diagram when $a=a_i$ (Figure 12). Beyond $a>a_i$, K_{Ic} is allowed to increase incrementally such that the instability is avoided, i.e. $\frac{\partial^2 \sigma}{\partial w^2}$ is allowed to maintain the same sign, until $a=a_c$, when only a few fibers along the discontinuous crack segments remain elastically bonded to the matrix, i.e. at $a=a_c$, $b \approx a$. Hence, an instantaneous drop in the stress can be anticipated when the crack fragments link up to form a through crack (Figure 11b). The situation here is akin to the pull-out of a single fiber (Figure 2).

Table 1 Material Parameters

Parameter Material	E E (GPa)	σ_m (MPa)	ν	τ_v (MPa)	τ_g (MPa)	L (mm)	d (mm)
HPFRC	40	10	0.2	9.0	5.0	20	0.4
CFRC	40	3	0.2	3.0	2.5	20	0.4

Once the through crack has formed the frictional bridging force exerted by the fibers is constant (3). Li (1992) has shown that the tension softening relation in this regime is

$$\sigma(w) \approx V_f \tau_g \frac{\bar{v}_{cr}}{v_{cr}} \frac{L}{d} \frac{h}{2} \left(1 - \frac{4}{L} w + \frac{4}{L^2} w^2 \right) \quad (19)$$

such that the residual tensile carrying capacity drops to nothing when $w=L/2$, i.e. the crack opening displacement equals half the largest fiber embedment length.

Figure 13 shows the bridging traction-total crack opening relationship with $V_f=0.0$ and $E_f=210$ GPa. Note that $f=0.9$ for mix I and $f=0.75$ for mix II (Li, 1992). Also, at large crack opening $v_{cr} \approx \bar{v}_{cr}$.

The above strain hardening and tension softening relations are now used to predict the complete pre-peak and post-peak tensile response of the high-performance short fiber-reinforced cementitious composite (HPFRC). Figure 14 shows the complete pre- and post-peak curves for the mix. The values of W and a_0 are assumed to be 50 mm and 4.5 mm, respectively. The predicted response is in very good agreement with the typical load-elongation response of this material.

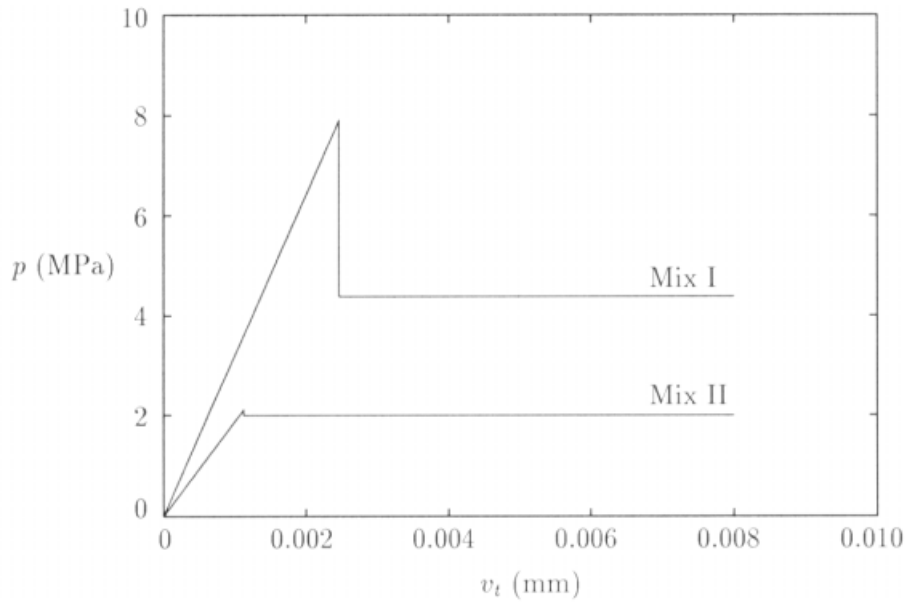


Figure 13 Bridging stress-total crack opening relationship for mixes I and II with $a_0=4.5$ mm

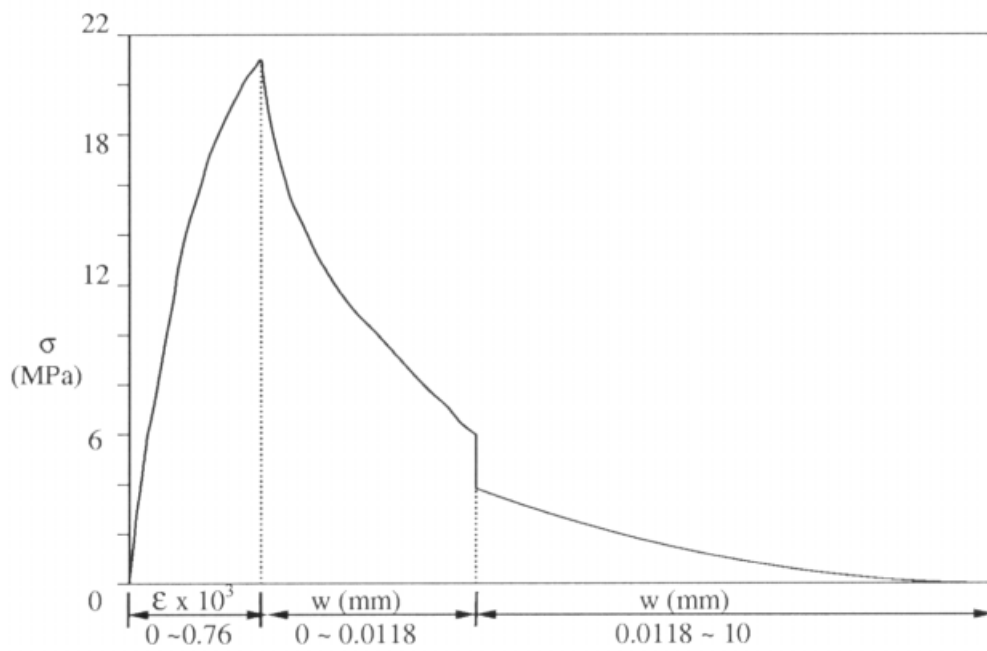


Figure 14 Complete pre-peak and post-peak tensile curve of high-performance short fiber-reinforced cementitious composites (HPFRC). The pre-peak regime is expressed in terms of a stress-strain relation, and the post-peak regime is expressed in terms of the relation between stress and crack opening displacement w , following eqns (18) and (19).

Acknowledgements

Financial support of the Royal Society to JW is gratefully acknowledged.

References

1. J. Aveston, G. A. Cooper, A. Kelly, *The Property of Fiber Composites*. Proc. NPL, IPC Science and Technology Press Ltd., Guilford, UK, 1971, 15—26.
2. P. N. Balaguru, S. P. Shah, *Fiber-Reinforced Cement Composites*, McGraw-Hill, New York, 1992.
3. N. Bathia, C. Yan, *Cement & Concrete Research*, 1996, 26, 657—662.
4. H. Horii, S. Nemat-Nasser, *J. Mech. Phys. Solids*, 1983, 31, 155—171.
5. H. Horii, S. Nemat-Nasser, *Int. J. Solids Structures*, 1985, 21, 731—745.
6. C.-H. Hsueh, *Acta Mater.*, 1996, 44, 2211—2216.
7. K. X. Hu, A. Chandra, Y. Huang, *Int. J. Solids Structures*, 1994, 31, 599—611.
8. B. L. Karihaloo, *Fracture Mechanics and Structural Concrete*, Addison Wesley Longman, UK, 1995.
9. B. L. Karihaloo, J. Wang, M. Grzybowski, *J. Mech. Phys. Solids*, 1996, 44, 1565—1586.
10. B. L. Karihaloo, J. Wang, *J. Mech. Mater.*, 1997a, 26, 209—212.
11. B. L. Karihaloo, J. Wang, *J. Computational Mech.*, 1997b, 19, 453—462.
12. B. L. Karihaloo, J. Wang, *Material Instabilities in Solids* (eds.: R. de Borst and E. van der Giessen), John Wiley & Sons, New York, 1998, 323—337.
13. D. Lange-Kornbak, B. L. Karihaloo, *Cement & Concrete Composites*, 1997, 19, 315—328.
14. V. C. Li, Y. Wang, S. Backer, *J. Mech. Phys. Solids*, 1991, 39, 607—625.
15. V. C. Li, *J. Mater. Civil Eng.*, 1992, 4, 41—57.
16. S. Melin, *Int. J. Fract. Mech.*, 1983, 13, 641—654.
17. B. Mobasher, H. Stang, S. P. Shah, *Cement & Concrete Research*, 1990, 20, 665—676.
18. A. E. Naaman, S. P. Shah, *ASCE J. Struct. Div.*, 1976, 102, 1537—1548.
19. M. Ortiz, *Int. J. Solids Structures*, 1988, 24, 231—250.
20. H. Stang, Z. Li, S. P. Shah, *ASCE J. Eng. Mech.*, 1990, 116, 2136—2150.
21. H. Tada, P. C. Paris, G. R. Irwin, *The Stress Analysis of Cracks Handbook*, Paris Productions, Inc., St. Louis, Missouri.
22. P. Tjiptobroto, W. Hansen, *ACI Mater. J.*, 1993, 90, 16—25.
23. J. Wang, J. Fang, B. L. Karihaloo, *Int. J. Solids Structures*, 1999 (in press).

Fatigue Crack Propagation in Biaxial Compression-Tension

Kolluru V. Subramaniam¹, John S. Popovics², and Surendra P. Shah¹

¹NSF Center for ACBM, Northwestern University, Evanston, IL 620208

²Drexel University, Philadelphia, PA 19104

Abstract

Rigid airport pavement structures are subjected to high-amplitude cyclic stresses resulting from passing heavy aircraft. It is of interest to model the response of plain portland cement concrete to such loading. There is a need to develop more accurate fatigue-based material models for concrete for implementation in mechanistic pavement design procedures. In this work, the uniaxial tension and biaxial compression-tension fatigue responses of concrete are investigated. The experimental results from the quasi-static and low cycle fatigue tests are presented. The damage mechanism owing to quasi-static loading is identified and the evolution of damage with repeated loading is monitored. The damage evolution in fatigue is shown to follow an S-shaped trend. The rate of damage accumulation is however shown to be a two-stage process. The fatigue failure of concrete is shown to be a local phenomenon like the failure in quasi-static loading, wherein the failure of the specimen is caused owing to crack propagation. The crack length at fatigue failure is shown to be predicted by the quasi-static failure envelope. Finally, a fracture-based fatigue failure criterion in terms of the quasi-static response is presented.

1 Introduction

The long term mechanical behavior of portland cement concrete subjected to cyclic fatigue loading is an important factor in the design and analysis of pavement structures; the stiffness of the concrete pavement degrades with continued fatigue loading and the overall pavement response (concrete pavement and the subgrade) depends on the stiffness of the top layer. This provides the motivation for this study. In a pavement structure, the applied wheel load is resisted by the plate bending action of the concrete slab and the subgrade reaction. The critical stress-state in the concrete slab corresponds to a biaxial combination of tensile and compressive stresses; the bending action of plate results in in-plane tensile stresses at the bottom of the slab and the subgrade reaction results in compressive stresses in a direction orthogonal to the tensile stresses. The in-plane tensile stresses are normally larger in magnitude than the out-of-plane compressive stress. A thorough experimental investigation to characterize the material response in a particular region of the compression-tension space where the magnitude of the principal tensile stress is larger than the magnitude of the principal compressive stress is conducted in this study. This region of the biaxial stress space is referred to as the tensile-compression-tension (t-C-T) region in this paper.

In the experimental program two different test configurations (Figure 1) were used. Concrete beam specimens were subjected to three-point bending to obtain the uniaxial tensile material properties. The experimental setup for applying biaxial t-C-T stresses consisted of applying torsional loading to hollow cylindrical concrete specimens. Torsion introduces a state of pure shear stress in the material which, when resolved in terms of principal stresses corresponds to a biaxial state of stress wherein the two principal stresses are equal in magnitude but of opposite signs. The two stress states investigated correspond to the boundaries of the t-C-T region.

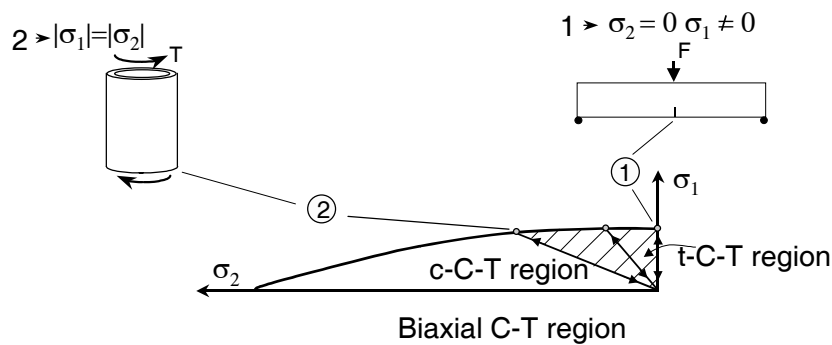


Figure 1: Schematic representation of the test configurations in the biaxial t-C-T stress-state.

2 Experimental Results

2.1 Flexure

Experimental program consisted of loading notched concrete beams in a three-point bending configuration. A displacement gage mounted at the bottom surface of the beam at the mouth of the notch monitors the crack mouth opening displacement (CMOD) throughout the loading procedure. The displacement registered by the CMOD gage is used as the feedback signal, wherein the CMOD is increased at a constant rate. A typical quasi-static test response obtained using this procedure exhibits softening response owing to propagation of a single crack emanating from the notch tip. The quasi-static response may be visualized as a failure envelope curve in terms of crack length, where each point in the post-peak is an equilibrium point representing the maximum load that can be supported for that given crack length. An estimation of crack length can be obtained by unloading the specimen from the static envelope curve. A typical quasi-static cyclic response obtained by unloading the specimen at different points in the post-peak part of the load response and then reloading is shown in Figure 2(a). There is a progressive decrease in structural stiffness due to crack propagation evidenced by the decrease in the slope of the loading-unloading curves in the post-peak. The effective crack length at different points in the post-peak can now be estimated from the structural stiffness using the principles of LEFM. The non-linear response of the material in front of the crack tip is modeled using the effective crack concept, wherein the actual crack is represented in terms of an equivalent effective crack embedded in an elastic material matrix that gives the same compliance as the actual crack. Details of this procedure are provided in Reference 1.

The value of K_I in the post-peak for different specimens tested in quasi-static cyclic loading is shown in Figure 2(b). The X-axis of these graphs corresponds to the load in the post-peak

as a percentage of the peak load. It can be seen that the value of K_I remains constant throughout the entire post peak. The critical value of K_I (K_{IC}) corresponding to the peak load obtained using this procedure has been previously shown to be a material parameter [RILEM 1991]. This analysis shows that the stress intensity factor during crack growth in the post peak part of the quasi-static response stays constant and is equal to K_{IC} . An average value of $40 \text{ N/mm}^{3/2}$ is obtained for K_{IC} . The crack growth along the quasi-static post-peak envelope can hence be characterized by the fracture condition

$$K_I = K_{IC} \quad (1)$$

Low cycle flexural fatigue tests were performed at four different load ranges. In all the tests load was applied between two-fixed load levels in a sinusoidal waveform at a frequency of 2 Hz. All fatigue tests were performed in load control. The lower limit of the load cycle was kept fixed at 5% of the average quasi-static peak load and four different upper load levels corresponding to 95%, 89%, 83% and 74% of the average quasi-static peak load were used. Figure 2(c) shows a typical flexural fatigue response of a beam specimen. The flexural stiffness represents the secant stiffness computed between the minimum and maximum load levels. The damage evolution in concrete during flexural fatigue, in terms of the measured stiffness, follows an S – shaped trend. Similar responses were obtained for all four-load ranges tested.

The change in crack length for the same specimen was computed from the observed change in stiffness using the procedure described earlier. The rate of crack growth as a function of crack length for the same specimen is shown in Figure 2(d). The rate of crack growth follows a two-stage process; a deceleration stage followed by an acceleration stage up to failure. In the deceleration stage there is a decrease in the rate of fatigue crack growth with an increase in crack length. In the acceleration stage the rate of fatigue crack growth increases continuously. There is a distinctive bend-over point marking the crack length where the rate of crack growth changes from deceleration to acceleration. The bend-over point occurs at the same crack length as the inflection point in the observed fatigue stiffness plot.

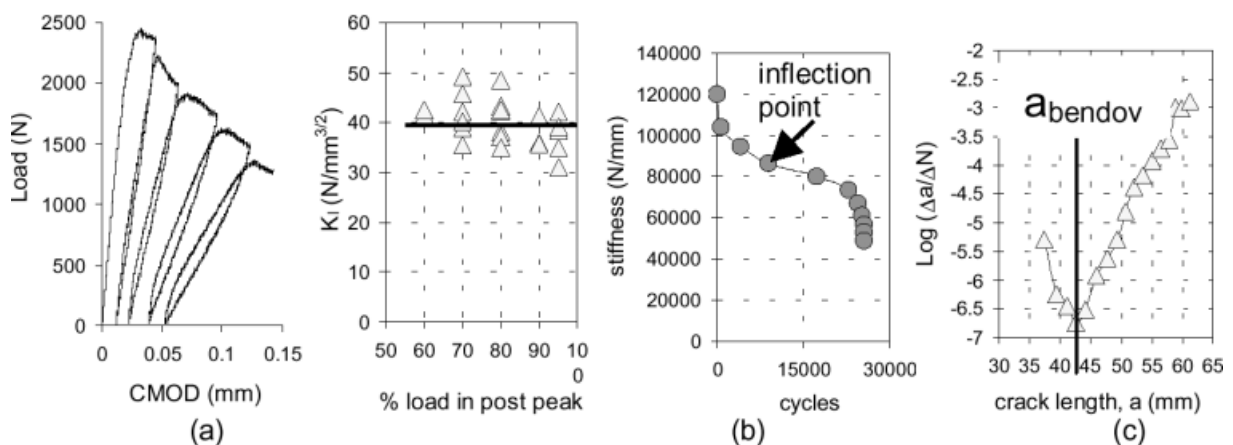


Figure 2: (a) Typical quasi-static response, and (b) K_I measured in the post-peak of the load response, (c) change in stiffness with number of fatigue cycles (d) Rate of fatigue crack growth.

2.2 Torsion

In this section results from torsional tests performed with a closed-loop test system on hollow concrete cylinders are presented. Hollow concrete cylinders that are reinforced at the ends are used in this study. The response of concrete specimens subjected to torsion was obtained

using specially designed test equipment. The axial deformation and rotation of the gage region were monitored throughout a test. The complete load-deformation response of unnotched concrete specimens subjected to torsion is difficult to obtain because of test instabilities. The test instability is a result of snapback in the post-peak part of the torque-twist response of these specimens [2,3]. Inspection of a specimen after failure revealed a single crack inclined approximately 45 degree with respect to the horizontal. The crack surface was normal to the observed crack on the outer surface and was planar. A test signal that is a combination of torque and gage rotation was used and was demonstrated to give improved control by eliminating the test instability. Details about instrumentation, test setup, the nature and control of the instability are given in References 2 and 3.

An indirect estimate of the damage associated with crack growth can be obtained from a quasi-static cyclic test. A typical cyclic response of the specimen obtained using the combined signal is shown in Figure 3. The decrease in the rotational stiffness of the specimen during the load cycles can be attributed to the propagation of an effective crack. Closed form solutions for the relationship between the decrease in rotational stiffness of the hollow cylinder and the crack length are not available. A numerical analysis was performed to predict the crack length from the stiffness measurements. Details of the analysis are provided in Reference 3. In the analysis it was implicitly assumed that the decrease in rotational stiffness is a result of the propagation of a single crack that is inclined at 45 degrees with respect to one of the axes. By matching the decrease in compliance predicted by the numerical analysis with experimental values an estimate of crack length is obtained. Using the results of the numerical analysis it was shown that Equation 1 can be used to predict crack growth in the post-peak under torsional loading.

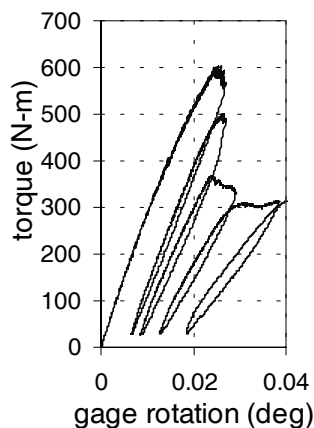


Figure 3: Typical cyclic response in torsion.

Constant amplitude fatigue tests were conducted in torsion at three different load ranges up to failure. In all the tests the lower torque limit in a torque cycle was kept fixed at 5% of the average quasi-static peak torque and three different upper torque limits corresponding to 75%, 85% and 95% of the average quasi-static peak torque were used. The trends in fatigue crack growth were similar to those observed in flexure, wherein, the fatigue crack growth showed an S-shaped trend. The rate of fatigue crack growth exhibited a distinctive two-phase response corresponding with deceleration and acceleration. The crack length at the bendover point where the rate of fatigue crack growth changes from deceleration to acceleration corresponds with the inflection point in the observed fatigue crack growth curve.

2.3 Fatigue Crack Growth

There is little agreement regarding the failure criterion for concrete subjected to fatigue loading. The deflections at failure for plain concrete have been shown to be significantly higher than the corresponding deflections in the post-peak part of the quasi-static monotonic response [Hordijk 1991; Shah and Chandra 1970]. Therefore, a failure criterion based on quasi-static deflections may not be suitable for plain concrete subjected to fatigue. A comparison of the effective crack lengths at fatigue failure and those in the post peak part of the quasi-static response, for specimens tested in flexure, is shown in Figure 4(a). The hollow symbols represent the crack length obtained from quasi-static cyclic tests. Each solid symbol in the graph represents a specimen tested in fatigue with one of the four load levels; different symbols represent different load ranges. The crack lengths at fatigue failure compare favorably with the crack lengths at the corresponding load in the quasi-static post-peak part response. Similar comparison was also obtained for specimens tested in torsion. This suggests that the crack length at fatigue failure can be obtained from the quasi-static response. Hence the quasi-static response acts like an envelope to the fatigue response when framed in terms of effective crack length. Further, this suggests that a fracture based failure criterion that is obtained from quasi-static response, Equation 1, can be used for concrete subjected to fatigue loading.

A comparison of the critical crack length at the peak load of the quasi-static response (a_{crit}) and the crack length at the bend-over point, where the rate of crack growth changes from deceleration to acceleration ($a_{bendover}$) is shown in Figure 4(b) for flexure specimens. Each point on the graph corresponds to one specimen tested in fatigue. The X-axis corresponds to the maximum applied load in a fatigue-load cycle as a percentage of the average maximum quasi-static monotonic peak load. The Y-axis of the graph is the ratio of $a_{bendover}$ to the average a_{crit} obtained by testing six specimens under cyclic quasi-static loading. From the figure it can be seen that $a_{bendover}$ in the fatigue response at load ranges used in this study is the same magnitude as a_{crit} of the quasi-static monotonic response. Similar comparison was also obtained from torsion specimens. Hence, $a_{bendover}$ in low-cycle, constant-amplitude fatigue can be predicted from a_{crit} that is obtained from the quasi-static response.

The results obtained so far can be represented schematically as shown in Figure 4(c). The quasi-static and the fatigue responses are plotted in the load–effective crack length space in the top part of the figure while the bottom part of the figure shows the fatigue crack growth with number of cycles of loading. Referring to the top part of the figure, the origin, O' , is located at the initial notch length a_0 . As the load is increased there is no crack growth till a certain load is reached (point O). The region OB represents stable crack growth in the quasi-static monotonic response up to peak load. After peak load, there is a decrease in the load with an increase in crack length (region BD). The fatigue response, which exhibits crack growth due to repeated loading between two fixed load levels, is also shown schematically by line AC in the figure. From the previous analysis, it has been demonstrated that the quasi-static response acts as the failure envelope to the fatigue response when framed in terms of crack length. Point A represents the crack length in the first cycle of fatigue loading and point C represents the crack length at fatigue failure. The post peak part of the monotonic response (region BD in Figure 4(c) can be predicted using the failure condition, $K_I = K_{IC}$, given in Equation (1). Using the failure envelope concept in terms of effective crack length, the same conditions also applies to fatigue failure.

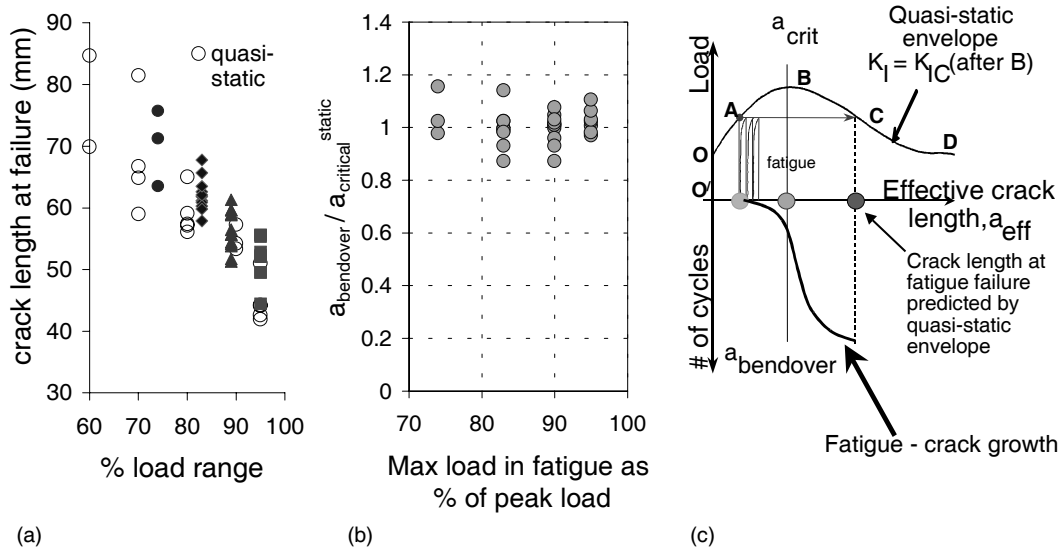


Figure 4: (a) Comparison of crack lengths at fatigue failure and at the corresponding load in the quasi-static post-peak in flexure, (b) Comparison of crack lengths at inflection point in fatigue response and at the quasi-static peak load, (c) Schematic representation of crack growth under fatigue and quasi-static loading.

3 Conclusions

Based on the results presented in this paper, the following conclusions can be drawn:

- Crack growth in the post-peak part of the quasi-static response in the tensile part of the biaxial compression tension (t-C-T) region is predicted by $K_I = K_{IC}$.
- The crack length at fatigue failure in the t-C-T region is predicted by the quasi-static load response. Fatigue failure in the t-C-T region can be predicted using $K_I = K_{IC}$.
- The fatigue crack growth in the t-C-T region exhibits an S-shaped response with an inflection point.
- The rate of fatigue crack growth in the t-C-T region shows a two-phase response; the crack growth rate decelerates initially up a_{bendover} and then accelerates up to failure. The crack length, a_{bendover} , corresponds to the observed inflection point in the fatigue crack growth response.
- The crack length corresponding to the peak load in the quasi-static response predicts the crack length at the inflection point in the fatigue crack growth.

4 References

1. RILEM Committee on Fracture Mechanics of Concrete - Test Methods, *Materials and Structures*, vol. 23, No. 138, 1991, 457-460.
2. Subramaniam K.V., Popovics, J.S., and Shah, S.P., "Testing Concrete in Torsion: Instability Analysis and Experiments," *J of Eng. Mech.*, (ASCE), Vol. 124, No. 11, 1998, 1258-1268.
3. Subramaniam K.V., "Fatigue of Concrete Subjected to Biaxial Loading in the Tension Region," Ph.D. Dissertation, Northwestern University, 1999

4. Hordijk, D.A., "Local Approach to Fatigue of Concrete," Ph.D. dissertation, Delft University, 1991.
5. Shah, S.P., and Chandra, S., "Fracture of Concrete Subjected to Cyclic and Sustained Loading," *J. of American Concrete Institute*, Vol. 67, No. 9, 1970, 816-825.

Fractological and Numerical Investigations on Fracture Mechanical Behavior of Concrete

Viktor Mechtcherine, Harald S. Müller
University of Karlsruhe

1 Introduction

In recent years fracture surfaces became an object of intensive research for better understanding of the phenomena of crack formation and propagation in concrete. In order to quantify the condition of fracture surfaces, different measurement techniques and calculation algorithms are applied. As a result of these different approaches, the obtained values of roughness and fractal dimension of concrete fracture surfaces scatter in a very wide range.

In this study a verification method was developed to estimate the reliability of the values derived from fractological measurements. Further, this method was applied for the generation of FE-meshes for a numerical analysis of concrete failure.

2 Fractological investigations

In the fractological part of this study the fracture surfaces obtained from uniaxial tension tests on high strength concrete and normal strength concrete [1] were investigated using the projected fringes technique [2]. The compressive strength of the concretes was 93 MPa and 44 MPa, respectively.

Figure 1 shows images of typical concrete fracture surfaces computed from the measured data. In the case of the high strength concrete the trans-aggregate fracture dominates, whereas the fracture process in the normal strength concrete is governed by the failure of the aggregate-cement paste bond.

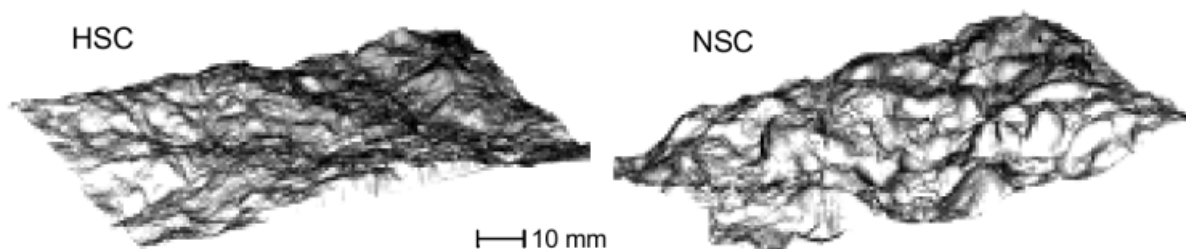


Figure 1. Typical contours of concrete fracture surfaces

From the data of optical measurements the roughness and the fractal dimension of the fracture surfaces were determined in order to quantify their condition. The roughness R_S was calculated as the surface area measured with a mesh size of 0.16 mm and divided by the projected area. The fractal dimension was defined by the grid scaling method [2].

Table 1. Roughness and fractal dimension of concrete fracture surfaces

Concrete	Roughness R_S	Fractal dim. D_S
HSC	1.167 (0.008)	2.029 (0.001)
NSC	1.323 (0.04)	2.052 (0.003)

Standard deviations are given in parentheses.

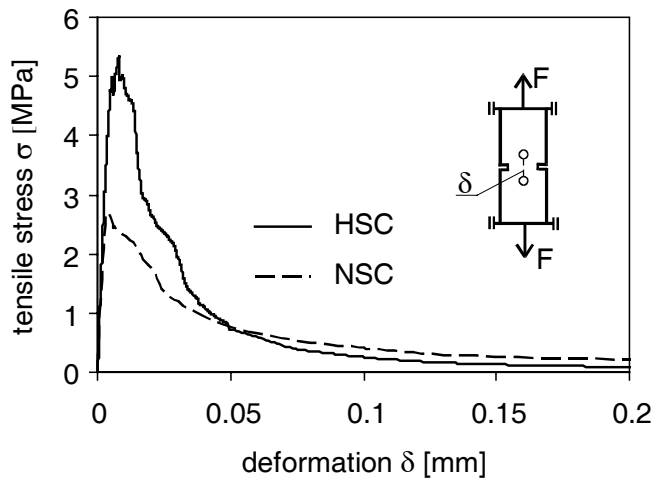
**Figure 2.** Influence of the concrete strength on the shape of the σ - δ -relation

Table 1 gives the results of the calculations. The roughness and the fractal dimension of the fracture surface increase with decreasing strength of concrete.

Further, the condition of the fracture surface was correlated to the fracture behavior of the concretes. Figure 2 shows the influence of the concrete strength on the shape of the stress-deformation relation obtained from uniaxial tension tests [1]. For deformations larger than approx. 50 μm the σ - δ -relation of the normal strength concrete is above the corresponding curve of the high strength concrete. This indicates a lower energy consumption in the case of the high strength concrete at this stage of crack development.

The condition of the fracture surfaces gives an explanation for this phenomenon: the higher roughness and the higher fractal dimension of the fracture surfaces of the normal strength concrete indicate a pronounced interlocking of the crack surfaces, which provides a better transfer of the tensile stresses across the crack.

3 Generation of fracture surfaces

As it has been shown in the previous section the derivation of the D_S -values enables a quantitative comparison between different fracture surfaces. However, the obtained absolute values of the fractal dimension have to be verified in view of the fact that very controversial information can be found in the literature where values of the fractal dimension up to $D_S = 2.6$ are given for fracture surfaces of the concrete [3].

For the verification of the derived D_S -values artificial fracture surfaces having a pre-defined fractal dimension were generated and compared with the real fracture surfaces. For the gen-

eration of the artificial fracture surfaces the midpoint displacement method was applied, which had been initially developed for the simulation of Brownian motion [4].

Figure 3 shows schematically the first four steps in applying the one-dimensional version of the midpoint displacement method. In the first step a straight line is generated, whose one end has a zero altitude while the other end is defined as a sample of a Gaussian random variable with a mean value of zero and unit variance σ^2 . In the next step the midpoint between these two end points is calculated and displaced by a random variable A_1 with a mean value of zero and variance $(\Delta_1)^2$. Further, new midpoints between the neighboring points are considered and displaced by a random value A_2 , which is in average smaller than the displacements in the former steps.

The procedure can be continued until the desired resolution is achieved. The variances of the displacement variables are calculated using eq. 1, where n is the step number and H is the Hurst exponent depending on the chosen fractal dimension:

$$\Delta_n^2 = \frac{\sigma^2}{(2^n)^{2H}}(1 - 2^{-2H-2}) \quad (1)$$

where $H = 2 - D_L$ and D_L = fractal dimension of a line, i.e. the crack profile.

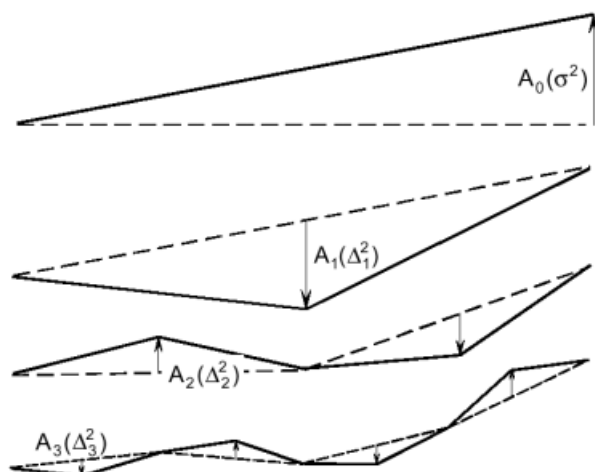


Figure 3. Principle of the midpoint displacement method

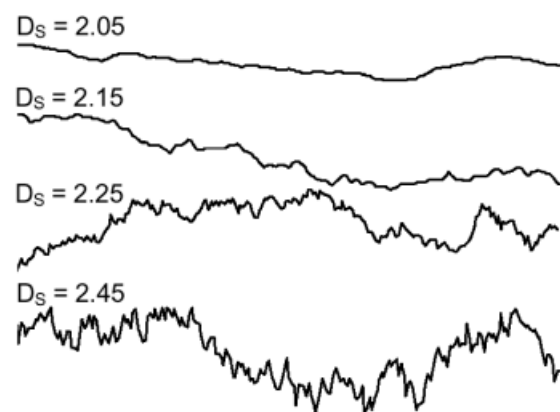


Figure 4. Typical crack profiles of generated fracture surfaces

A similar procedure was applied for the generation of fracture surfaces. In this case for the calculation of the altitude of each midpoint four neighboring points in a quadratic lattice were used. The displacement variances $(\Delta_1)^2$ were derived using eq. 2 governed by the fractal dimension of a surface D_S . Details may be found in [5].

$$\Delta_n^2 = \sigma^2 (\frac{1}{2})^{n(3-D_S)} \quad (2)$$

Figure 4 shows typical crack profiles obtained from the fracture surfaces generated using different fractal dimensions. The profile taken from the artificial surface with a fractal dimension $D_S = 2.05$, which approximately corresponds to the values obtained by the authors in the fractological investigations, looks rather similar to those optically measured for the high strength concrete. The crack profiles having a considerably higher fractal dimension appear less realistic. Generally, it can be concluded that the experimentally derived D_S -values being higher than approx. 2.15 can most likely be traced back to some measurement errors or to the application of an unsuitable evaluation method rather than to the real condition of fracture surfaces.

The midpoint displacement method seems to be quite good for the generation of fracture surfaces with dominating aggregate failure, which is typical for high strength concrete or lightweight aggregate concrete. To simulate the fracture surfaces of ordinary concretes the generated surfaces have to be accomplished by some portion of unbroken aggregates.

For this purpose the “crater and hill”-method was developed on the basis of a similar technique applied for the generation of “moon landscapes” [6]. In this method first a point on a generated fracture surface is randomly chosen. Figure 5 shows a corresponding crack profile as a sectional view of the surface in the x-z-plane. In the next step this point is displaced up or down, again randomly. From now on the displaced point serves as the center of an ellipsoid with random radii r_x , r_y and r_z which are linked to the minimum and maximum aggregate size. In the following step the z-coordinates of the concerned lattice points are redefined to reproduce the shape of a “crater” or a “hill”, depending on the position of the ellipsoid center with respect to the surface plane. The procedure has to be repeated so many times until the surface is provided with the desired amount of unbroken aggregates.

Figure 6 shows an artificial surface with a high content of unbroken aggregates.

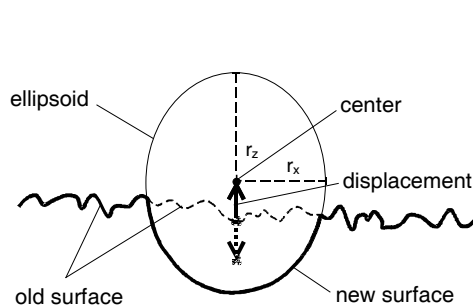


Figure 5. “Crater and hill”-method



Figure 6. Example of an artificial surface with unbroken aggregates

4 Numerical analysis

The generation of fracture surfaces or crack profiles is a powerful tool for a comprehensive analysis of different physical and mechanical phenomena with regard to concrete cracking [6]. In this study the artificial fracture surfaces were used for modelling the mesh in a FE-analysis in order to investigate the transmission of stresses across discrete cracks in concretes with and without aggregate failure.

First a profile of a generated surface with “complete aggregate failure” was selected (Figure 7, left). After having added some “craters” and “hills” to the surface a new profile of the same section was chosen again (Figure 7, right). Then both profiles were discretized using interface elements. Finally, the properties of the concrete components, i.e. mortar, coarse aggregate and bond were assigned to the corresponding finite elements. For this purpose both discretized profiles were compared. The common elements represented the mortar matrix. Other elements were considered to belong to the aggregates in the case of the first profile and to the bond zone in the case of the second profile (Figure 7, below).

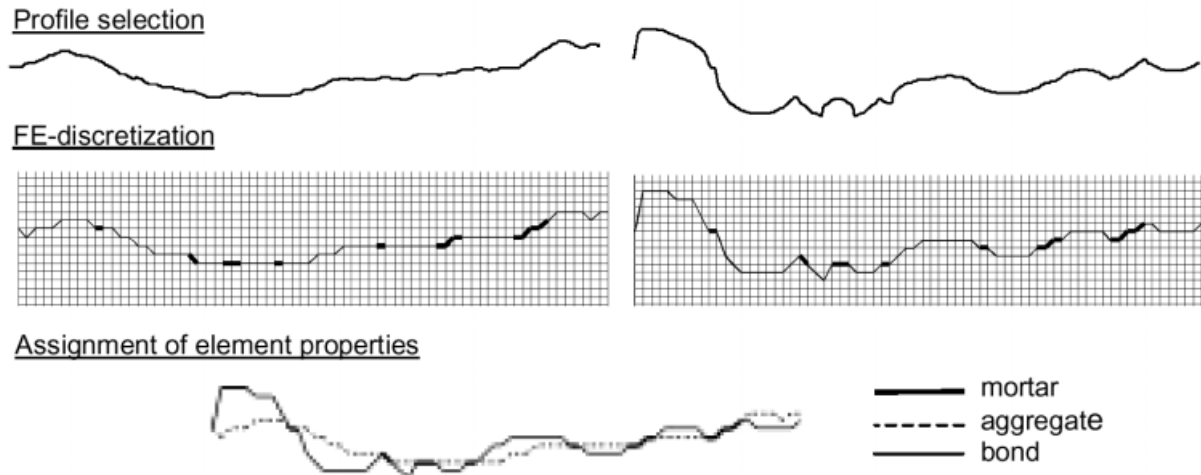


Figure 7. Application of crack profiles in FE-analysis

In the first series of calculations exactly the same fracture mechanical properties, i.e. tensile strength f_t and fracture energy G_F were assigned to all elements, see Table 2, models 1a and 2a. As a result, exclusively the effect of the crack geometry could be studied. In the analysis a linear stress-crack opening relation was assumed. The comparison of the calculated σ - δ -relations shows that the model with unbroken aggregates provided a better stress transfer across the crack than the model with aggregate failure, see Figure 8.

The difference becomes much more evident if more realistic values of the tensile strength and the fracture energy for the concrete components are used, see Table 2. In this calculation series model 1b was considered to represent high strength concrete and model 2b normal strength concrete, respectively. As a result, the obtained σ - δ -relations for both concretes showed a very good agreement with the corresponding curves from the experiments for a small as well as for a large crack opening, compare Figures 2 and 8 (right).

Table 2. Input parameters for the components of the concrete fracture surfaces

Input parameter	E_0 [GPa]	$f_{t,mortar}$ [MPa]	$G_{F,mortar}$ [N/m]	$f_{t,agg}$ [MPa]	$G_{F,agg}$ [N/m]	$f_{t,bond}$ [MPa]	$G_{F,bond}$ [N/m]
model 1a	35	4	60	4	60	-	-
model 2a	35	4	60	-	-	4	60
model 1b, "HSC"	45	7	70	7	100	-	-
model 2b, "NSC"	35	6	60	-	-	2	60

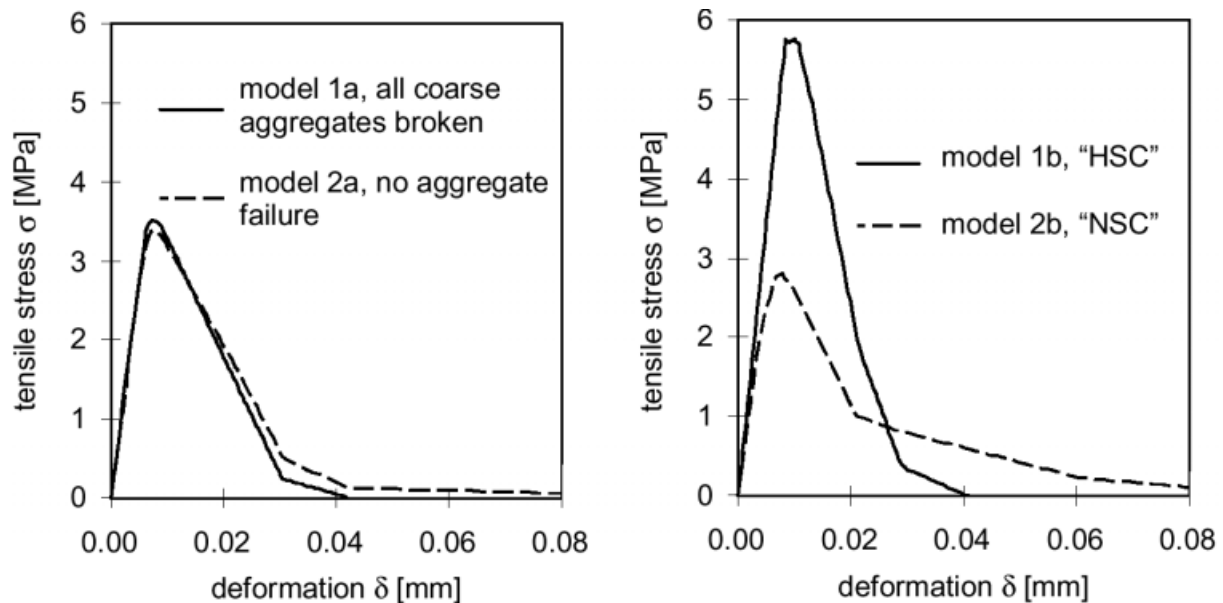


Figure 8. Effect of the crack profile geometry (left) and of the properties of the components of failure surface (right) on the shape of the calculated stress-deformation relations

5 Summary and conclusions

From the results of this investigation the following conclusions can be drawn:

- The lower values of the roughness and the fractal dimension of fracture surfaces obtained for the high strength concrete correspond to a steeper descending branch of the σ - δ -relation and to a lower energy consumption at larger crack widths.
- The midpoint displacement method can be used to generate fracture surfaces with predefined fractal dimensions. In addition, the “crater and hill”-method provides a simple tool to accomplish the generated surfaces by “unbroken aggregates”.
- The generation of fracture surfaces can be applied for the verification of the results of fractological investigations as well as for the FE-analysis of mechanisms of the stress transfer over discrete cracks.

6 References

1. V. Mechtcherine, H. S. Müller, in *Brittle Matrix Composites* (Ed.: A. M. Brand, V. C. Li, I. H. Marshall), Woodhead Publishing Ltd/Cambridge - Bigraf/Warshaw, 1997, 231-240.
2. V. Mechtcherine, H. Garrecht, H. K. Hilsdorf, in *Fracture Mechanics of Concrete Structures* (Ed.: F. H. Wittmann), AEDIFICATIO Publishers, 1995, 719-728.
3. M. Issa, A. M. Hammad, *Cement and Concrete Research*, 1994, 24, 325-334.
4. H.-O. Peitgen, D. Saupe, *The Science of Fractal Images*, Springer-Verlag, New York, 1988.
5. V. Mechtcherine, *Fracture Mechanical, Fractological and Numerical Investigations on Concretes*, Doctoral thesis in preparation, University of Karlsruhe, 1999.
6. R. Scholl, O. Pfeiffer, *Natur als fraktale Grafik*, Markt&Technik Verlag, 1991.

Crack Interaction in Concrete

Chunxia Shi, Arie G. van Dam, Jan G.M. van Mier, Bert Sluys
Delft University of Technology

1 Abstract

This paper describes a series of uniaxial tensile tests on two different concretes. Cracks were triggered by edge notches which had an off-set in the direction of the load. The load was applied in deformation control. The crack formation and development were accurately monitored. The results show the influence of notch displacement and grain size on the crack pattern and fracture energy. Some preliminary numerical lattice simulations have been carried out for the comparison with the experimental results.

2 Introduction

Two cracks that approach each other rarely connect head-on. This phenomena causes softening and aggregate interlock on a macro scale, which are considered to be responsible for size effects in strength and ductility of structural elements.

In a perfect homogeneous material, two adjacent cracks often curl around each other instead of just connecting. This can be easily explained from the stress trajectories in the material between the crack tips. However, many materials are heterogeneous, which introduces a randomness that strongly complicates matters.

A research program is being carried out to qualify and quantify the phenomena of overlapping interactive crack growth. As part of this, 56 tensile tests were performed of concrete specimens with shifted double edge notches. A preliminary numerical simulation with a lattice model is carried out and a comparison is made with the experimental results. In this paper, the specimens and materials are presented in section 2. Experimental results and outcome of the simulation are given in section 3 and 4.

3 Specimen preparation and test set-up

The double-edge-notched specimen used in this study is shown in Figure 1. The width of the specimen is chosen such that the expected crack area between the two notches could be fully covered with a long distance microscope. The notches have been translated in vertical direction with respect to each other. The vertical distances between the two notches are 0, 5, 10 and 15 mm, respectively, symmetric with respect to the horizontal center axis of the specimen.

Two types of materials are used to make the specimens: 8 mm concrete and 2 mm mortar. The 8 mm concrete specimens are sawed from spare cubes that were cast two and half years

ago for other experiments. They are made from ordinary Portland Cement (CEM I 52.5) and river gravel of 8 mm maximum size. The 2 mm mortar specimens are made of white Portland Cement (Blanc BEL P40) and sand with a maximum size of 2 mm. The weight proportions of water, cement and aggregate are 0.5 : 1 : 4.82 and 0.5 : 1 : 4.04 for the 8 mm concrete and 2 mm mortar, respectively, see also [1]. 24 hours after casting, the cubes were demoulded and put in a wet room of 20 °C and 95% RH. The specimens and the notches are sawn from the cubes a few days before testing. The 8 mm concrete specimens are tested at ages over 900 days. The 2 mm mortar specimens are tested at ages of 50 to 70 days.

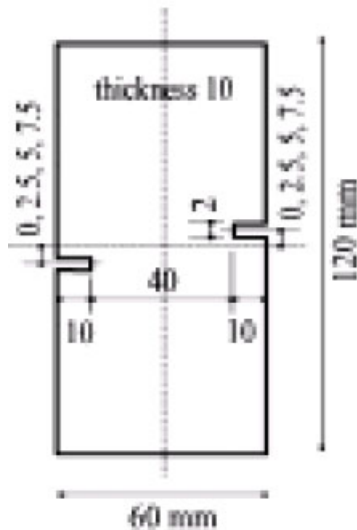


Figure 1. Specimen dimensions

All tensile tests are conducted in a 10 KN servo-controlled hydraulic test machine (INSTRON 8874). A specimen was glued directly to the loading platens. Four LVDTs were used for measuring the deformation in the middle area of a specimen during loading, with two on front and two on rear face of the specimen. The LVDTs are placed immediately at the left and right edge of the specimen in order not to interfere the viewing area of the microscope. The vertical measuring range of LVDTs is 30 mm. The average value of these four LVDTs is used as control signal in the load process. All tests were performed with deformation control at a rate of 0.04 $\mu\text{m/s}$.

A long-distance remotely controlled optical microscope, Questar (QM100 MK-III), combined with a black and white CCD camera is employed in order to trace the crack initiation, propagation and interaction in detail. The technical description of Questar remote measuring system can be found in [2].

4 Experimental results

As an example, Figure 2 shows cracking at different load stages, as well as the related load-deformation diagram. The specimen used in this test has a 10 mm notch distance (or notch off-set) and is made of 2 mm mortar. The crack patterns in Figure 2(a-d), are assembled from a large number of individual images.

The crack patterns are shown at different deformation levels w (13 μm , 25 μm , 100 μm and 200 μm). When the load reaches its peak, the first crack (1) starts from the right-hand notch. In other tests, cracking also started from left-hand notches due to the heterogeneity of the material. In the load-deformation diagram the curve shows a sharp drop while the crack propagates towards the opposite side. Shortly after the first crack, a second crack (2) develops at the left-hand notch. With increasing deformation, both cracks propagate continuously and become wider. In most tests, the two cracks show an attraction towards each other when the tips have a larger separation. However, in some tests, the two crack tips seem to repel each other when they become closer (this phenomenon is also shown in literature [3]). While in some tests the two cracks just grow to meet each other. In this example, the first crack propagates continuously and forms a main path. The second crack grows slowly towards the first crack until the test is stopped.

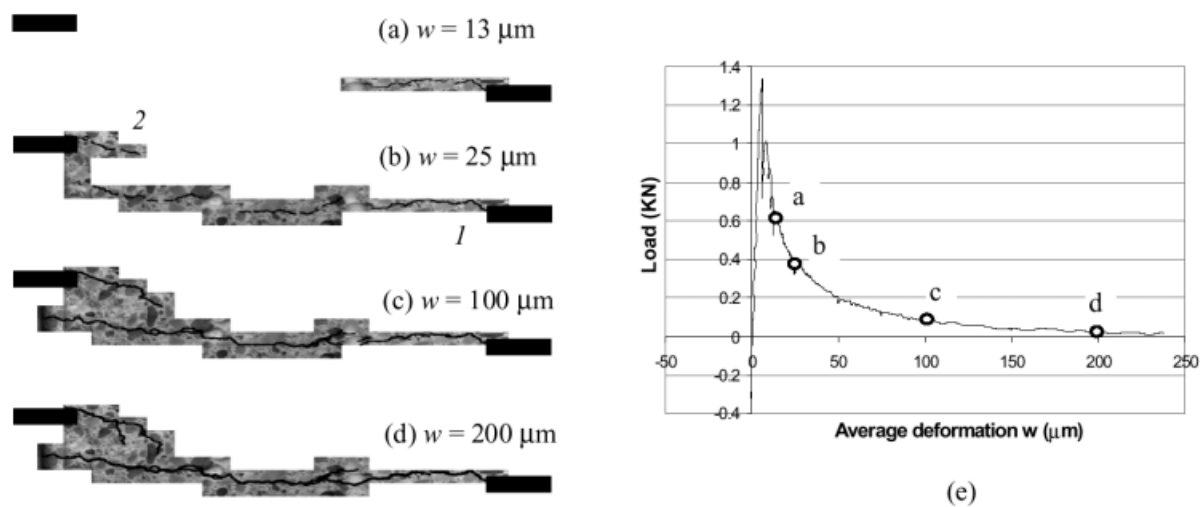


Figure 2. Crack patterns at different load stages (a-d) and the load-deformation diagram (e)

Figure 3 shows representative load-deformation diagrams for both materials and each notch off-set. Comparing the results of the two materials, it was noted that the average peak stress of 8 mm concrete is larger than that of 2 mm. The load-deformation curves show that, generally, also the fracture energy of the 8 mm concrete is larger than that of the 2 mm mortar. This possibly results from the stronger interlock introduced by the larger grains.

For the 2 mm mortar, the variation in the load-deformation curves is small. Specimens with a larger notch distance require more energy to fracture. For large deformations ($>150 \mu\text{m}$) the differences between the curves become negligibly smaller. For the 8 mm concrete, the curves for different notch off-sets show more variation than for the 2 mm mortar. Remarkable differences occur in the tails of the curves of this material.

Some final crack patterns of successful tests are assembled in Figure 4 for each notch off-set, for both the 2 mm mortar and the 8 mm concrete.

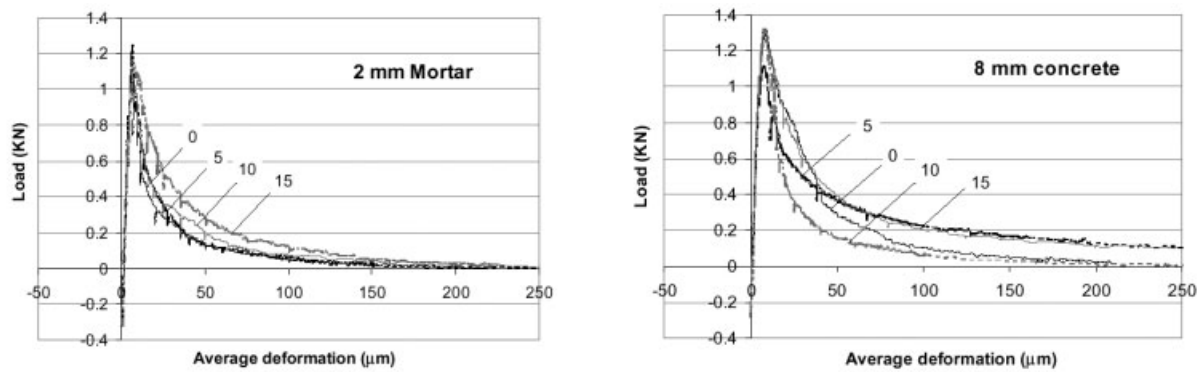


Figure 3. Load-deformation curves for 2 mm mortar and 8 mm concrete with notch off-sets 0, 5, 10 and 15 mm

Most crack paths in the 2 mm mortar are less curved than those in the 8 mm concrete. This might be related directly to the aggregate size. When the notch off-set increases to 15 mm, the crack patterns are more variable for both materials. The interaction between the cracks becomes weaker.

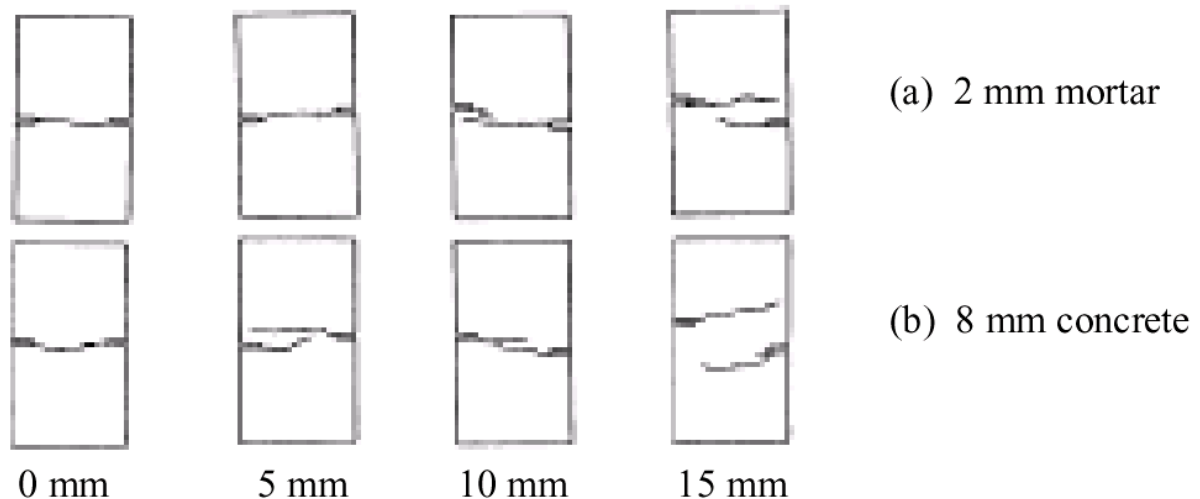


Figure 4: Typical final crack patterns of 2 mm mortar and 8 mm concrete

It was observed that large pores could have a significant effect on the crack path. The effect might be as large as that of large aggregates. Sometimes, they even induced unstable crack propagation and caused sudden specimen failure.

5 Preliminary lattice simulation

The Delft lattice model developed by Schlangen and Van Mier [4] has proven to be an efficient tool to simulate fracture process in concrete. In this model, concrete is schematized as a network of two-node beams. Normally, three main phases (aggregate, matrix and bond zone) are considered. The heterogeneity of concrete is introduced by mapping different material properties on different lattice beam elements. In lattice analysis, the fracture process is simulated by removing the element with the biggest stress/strength ratio in each loading step from the lattice structure.

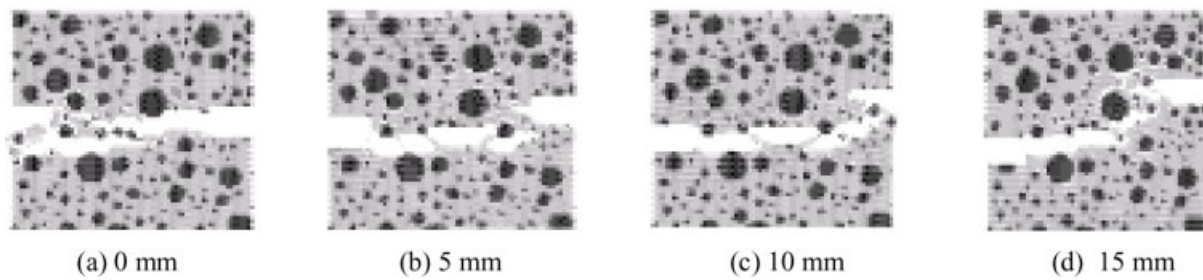


Figure 5. Crack patterns for 4 types of notch off-set

In this study, lattice simulations have been carried out of specimens with the same dimension as used in the experiments. The specimen is modeled with regular triangle lattices in the area where the cracks are expected, while the rest of the area is modeled with 4-noded quadrilateral continuum elements. The length of a lattice element is set to 1 mm. The aggregate sizes vary between 2 mm and 8 mm. The volume ratio of aggregates $P_k = 0.7$. The material and geometrical parameters, i.e. tensile strength f_t , Young's modulus E and Poisson's ratio ν , are determined according to refs. [2][5]: $f_{ta} = 10$ MPa, $f_{tm} = 5$ MPa and $f_{tb} = 1.7$ MPa, where the subscripts a , m and b denote aggregate, matrix and bond respectively. The elastic properties E_a , E_m , E_b are calibrated in order to match the stiffness of continuum and lattice regions: the values are $E_a = 66.429$ MPa and $E_m = E_b = 22.143$ Mpa. $\nu = 0.16$.

The computations are carried out with the FEM code DIANA 7.1. All four cases of notch off-set are simulated. For the case of 15 mm notch off-set, three types of aggregate structure are adopted. In that case $f_{tb} = 1.25$ MPa. Some of the results are presented in Figures 5, 6 and 7.

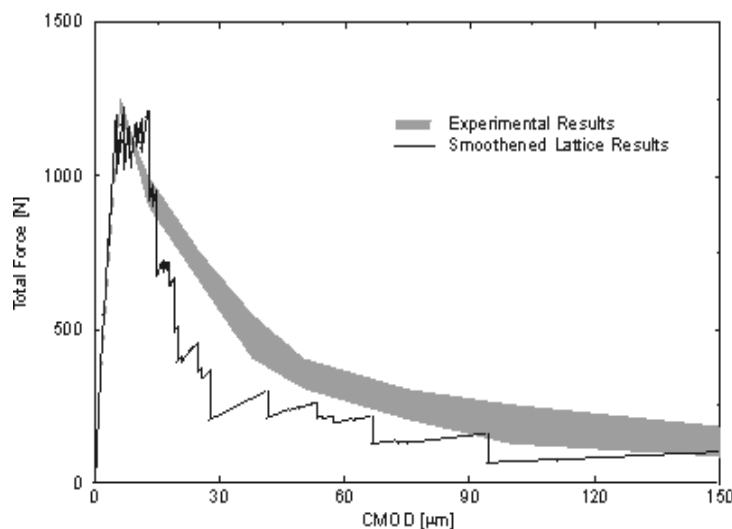
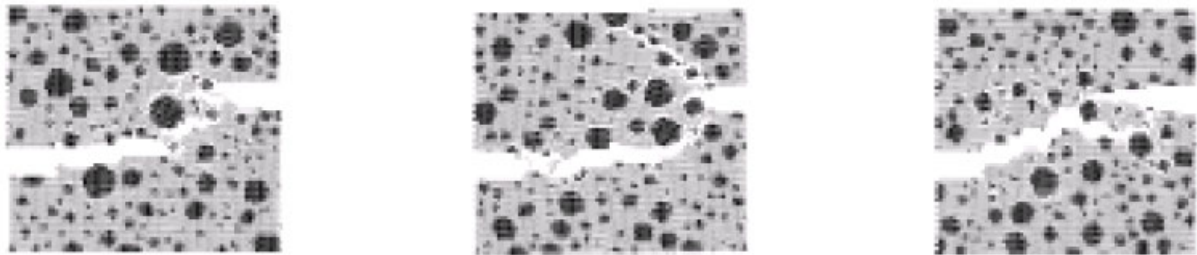


Figure 6. Comparison of lattice and experimental results

Figure 5 gives the calculated crack patterns for the four types of notch off-set. With increasing load, discrete micro-cracks start in the center area by debonding of the aggregates and matrix. At some stage, cracks form from two notches and propagate to the opposite side. In general, one crack grows much faster than the other. It seems that these two cracks attract each other when the tips are further apart, whereas they repel each other when the tips are closer, which is also observed in some experiments.

Figure 6 gives the load-deformation diagram obtained from the lattice simulation and the experiments. The lattice result is more brittle than the experimental one, as observed before [4][5].



(a) Aggregate structure 1 (b) Aggregate structure 2 (c) Aggregate structure 3
Figure 7. Crack patterns of 15mm notch off-set specimen with 3 types of aggregate structure

For 15 mm notch off-set, computations are made with three types of aggregate structures. The results reported in Figure 7 show that crack pattern is aggregate dependent and displays arbitrary characteristics for different aggregate structure. This was also observed in the experiments on 8 mm concrete.

6 Conclusions

Interaction of cracks is observed in double-edge-notched concrete specimens with a different notch off-set. Both the concrete heterogeneity and the notch off-set have a significant effect on the crack growth. Crack coalescence (small off-set and fine grained material) and crack repulsion (large off-set and coarse grained material) have been observed. In the latter case, the variability in cracking is found to be larger. Crack growth was monitored in detail with a long distance microscope. Preliminary analyses with a simple lattice model confirm the observation.

The results explain how structural elements benefit from a material with large aggregates. Large aggregates widen a crack band, increase fracture energy, and hence they improve strength and ductility of an element.

7 Acknowledgements

The authors wish to express appreciation to Mr. A. Elgersma for his expert help during the experimental program. This research was sponsored through a grant from PPM (Priority Program Materials Research, project 96PPM127) and STW (the Dutch Technology Foundation).

8 References

- [1] D. A. Hordijk, Local Approach to Fatigue of Concrete. PhD thesis, Delft University of Technology, 1992, p. 210.

- [2] A. H. J. M. Vervuurt, Interface Fracture in Concrete. PhD thesis, Delft University of Technology, 1997, p. 164
- [3] J. G. M. Van Mier, Fracture Process of Concrete. CRC Press, Boca, Raton, Florida, 1997, p.448.
- [4] E. Schlangen, J. G. M. Van Mier, Cem. Conc. Comp. 1992,14, 105–118.
- [5] E. Schlangen, Experimental and Numerical Analysis of Fracture Process in Concrete. PhD thesis, Delft University of Technology, 1993, p.121

A Scale-independent Damage Model for Concrete

Alberto Carpinteri, Bernardino Chiaia, Pietro Cornetti
Politecnico di Torino

1 Introduction

The behavior of concrete is well described by the cohesive crack model [1]. Accordingly, the material is characterized by a stress-strain relationship (σ - ϵ), valid for the undamaged zones, and by a stress-crack opening displacement relationship (σ - w , the cohesive law), describing how the stress decreases from its maximum value σ_u to zero as the distance between the crack lips increases from zero to the critical displacement w_c . The area below the cohesive law represents the energy Γ_F spent to create the unit crack surface.

The cohesive crack model is able to simulate tests where high stress gradients are present, i.e. tests on pre-notched specimens. Particularly, the model captures the ductile-brittle transition occurring by increasing the size of the structure. On the other hand, relevant scale effects are encountered also in uniaxial tensile tests on dog-bone shaped specimens [2] [3] [4], where much smaller stress gradients are present. In this case, size effects, which should be ascribed to material rather than to stress-intensification, can not be predicted by the cohesive model.

In this paper, a scale independent damage model is proposed which overcomes the drawbacks of the original cohesive model, assuming that damage occurs in a *fractal band*. The fractal nature of the damage process allows us to explain the size effects on the tensile strength, the fracture energy and the critical displacement and, particularly, the rising tail of the cohesive law observed in [4]. New fractal quantities will be introduced, in terms of which a fractal cohesive law can be defined which is universal, i.e. a material property.

2 Mechanics in the damaged band

2.1 Fractal tensile strength

Recent experimental results about concrete porous microstructure and the evidence of size effects on its strength led us to believe that a consistent modeling of damage in concrete can be achieved by assuming that the rarefied resisting sections in correspondence of the critical load can be represented by stochastic lacunar fractal sets with dimension $2-d_\sigma$ ($d_\sigma \geq 0$). From fractal geometry, we know that the area of lacunar sets is scale-dependent and tends to zero as the resolution increases. Finite measures can be obtained only with non integer (fractal) dimensions.

For the sake of simplicity, let us describe the specimen cross-section with the Sierpinski carpet built on the square of side b (fig. 1a). The fractal dimension of this domain is 1.893 ($d_\sigma = 0.107$). Hence, the maximum force is given by the product of the Hausdorff measure $A^* = b^{2-d_\sigma}$ of the Sierpinski carpet times the *fractal tensile strength* σ_u^* [5]:

$$F = \sigma_u A_0 = \sigma_u^* A^*, \quad (1)$$

where σ_u^* presents the anomalous physical dimensions $[F][L]^{-(2-d_\sigma)}$. The fractal tensile strength is the true material constant, i.e., it is scale-invariant. Since $A_0 = b^2$ and $A^* = b^{2-d_\sigma}$, from eq. (1) we obtain the scaling law for the tensile strength:

$$\ln \sigma_u = \ln \sigma_u^* - d_\sigma \ln b, \quad (2)$$

which implies linear scaling in the bilogarithmic diagram, with slope equal to $-d_\sigma$ (fig. 1b). Eq. (2) represents the negative size effect on tensile strength, experimentally revealed by several authors. Experimental and theoretical results allow us to affirm that d_σ can vary between the lower limit 0 – canonical dimensions of σ_u^* and absence of size effect on tensile strength – and the upper limit 1/2 – σ_u^* with the dimensions of a stress intensity factor and maximum size effect on tensile strength (as in the case of LEFM).

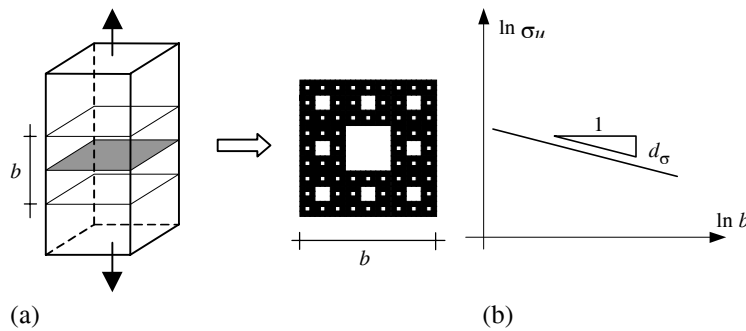


Figure 1. Lacunarity of the cross-section in the damaged band and scaling of the tensile strength.

2.2 Fractal critical strain

Turning now our attention from a single cross-section to the whole damage zone, it can be noticed that damage is not localized onto a single section but is spread over a finite band where damage distribution presents fractal patterns. This hypothesis is not a simple abstraction in material science. For instance, in some metals, the so-called slip-lines develop with typical fractal patterns [6]. Fractal crack networks develop also in dry earth or in old paintings under tensile stresses due to shrinkage.

As representative of the damaged band, consider now the simplest structure, a bar subjected to tension, where, at the maximum load, dilation strain tends to concentrate into different softening regions, while the rest of the body undergoes elastic unloading. If, for the sake of simplicity, we assume that strain is localized onto cross-sections whose projection on the longitudinal axis is given by the Cantor set, the displacement function at rupture can be represented by a *devil's staircase* graph (fig. 2a). In the singularity points, the strain defined in the classical manner is meaningless as it tends to diverge even if the displacement discontinuities are finite. On the other hand, an original definition of fractal strain acting upon lacunar domains was introduced by Cornetti [7]. Let $1 - d_\varepsilon = 0.6391$ be, for instance, the fractal dimension of the lacunar projection of the damaged sections ($d_\varepsilon \geq 0$). According to the fractal measure of the damage line projection, the total elongation of the band at rupture must be given by the product of the Hausdorff measure b^{1-d_ε} of the Cantor set times the *fractal critical strain* ε_c^* :

$$w_c = \varepsilon_c b = \varepsilon_c^* b^{1-d_\varepsilon}, \quad (3)$$

where ε_c^* has the anomalous physical dimension $[L]^{d_\varepsilon}$. The fractal critical strain is the true material constant, i.e., it is the only scale-invariant parameter governing the kinematics of the fractal band. Hence, the scaling law for the critical displacement is:

$$\ln w_c = \ln \varepsilon_c^* + (1-d_\varepsilon) \ln b, \quad (4)$$

implying linear scaling in the bilogarithmic diagram, with slope equal to $1-d_\varepsilon$ (fig. 2b).

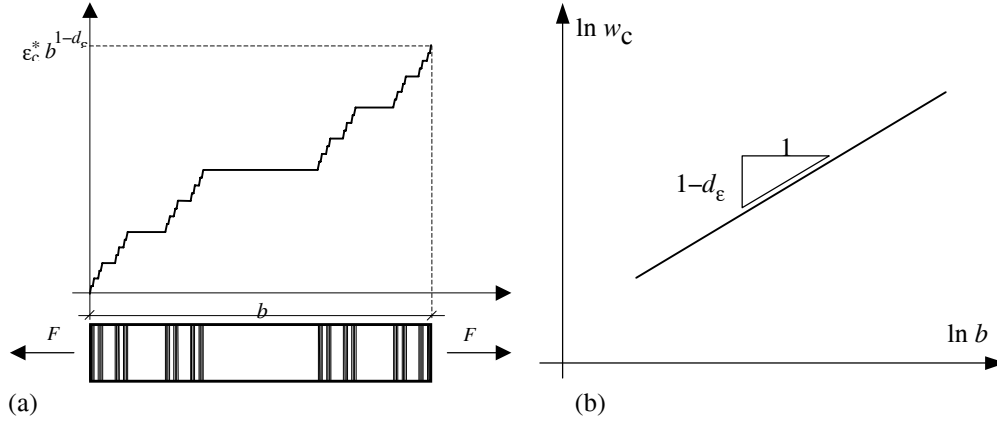


Figure 2. Fractal strain localization in the damaged band and scaling of the critical displacement.

The fractional exponent d_ε is intimately related to the degree of disorder in the mesoscopic damage process. When d_ε varies, the kinematical controlling parameter ε_c^* moves from the critical strain $\varepsilon_c - [L]^0$ to the critical crack opening displacement $w_c - [L]^1$. Therefore, when $d_\varepsilon = 0$ (diffused damage, ductile behavior), one obtains the classical response, i.e. collapse governed by the canonical critical strain ε_c , independently of the bar length. In this case, continuum damage mechanics holds, and the critical displacement w_c is subjected to the maximum scaling effect ($w_c \sim b$). On the other hand, when $d_\varepsilon = 1$ (localization of damage onto a single section, i.e. very brittle behavior) fracture mechanics holds and the collapse is governed by the critical displacement w_c , which is size-independent as in the cohesive model.

2.3 Fractal fracture energy; universal limits to disorder

Several experimental investigations have shown that the fracture energy Γ_F increases with the size of the specimen. This behavior can be explained by assuming that, after the peak load, energy is dissipated inside the damage band, i.e. over the infinite lacunar sections where softening takes place (fig. 3a). Generalizing eqs (2) and (4) to the whole softening regime, we get $\sigma = \sigma^* b^{-d_\sigma}$ and $w = \varepsilon^* b^{1-d_\varepsilon}$. These relationships can be seen as changes of variables and applied to the integral defining the fracture energy:

$$\Gamma_F = \int_0^{w_c} \sigma dw = b^{1-d_\varepsilon-d_\sigma} \int_0^{\varepsilon_c^*} \sigma^* d\varepsilon^* = \Gamma_F^* b^{1-d_\varepsilon-d_\sigma}. \quad (5)$$

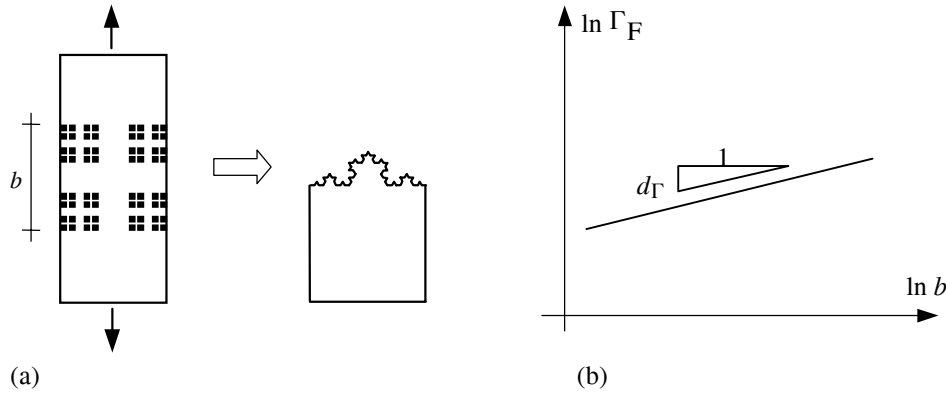


Figure 3. Energy dissipation in the damaged band and scaling of the fracture energy.

Eq. (5) highlights the effect of the structural size on the fracture energy (fig. 3b). On the other hand, since (fig. 3a) the damage process takes place on a domain A^* with a dimension $2+d_\Gamma$ larger than 2 ($d_\Gamma \geq 0$), we can also say that the total energy expenditure W is equal to [5]:

$$W = \Gamma_F A_0 = \Gamma_F^* A^*, \quad (6)$$

where Γ_F^* is called the *fractal fracture energy*, possessing the anomalous physical dimensions $[\text{FL}][\text{L}]^{-(2+d_\Gamma)}$ and, as well as σ_u^* and ε_c^* , it is scale-independent. Since $A^* = b^{2+d_\Gamma}$, the value of d_Γ is linked to the values of d_σ and d_ε according to:

$$d_\sigma + d_\varepsilon + d_\Gamma = 1, \quad (7)$$

where all the exponents are positive. While d_ε can get all the values inside the interval $[0,1]$, d_σ and d_Γ seem to be comprised between 0 and $1/2$ (brownian disorder). Equation (7) states a clear restriction to the maximum degree of disorder, confirming that the sum of d_σ and d_Γ is always lower than 1, as previously asserted, through dimensional arguments, by Carpinteri [5].

3 Scale-independent cohesive law and experimental results

It is interesting to note how, from eq. (5), the fractal fracture energy Γ_F^* can be obtained as the area below the softening fractal stress-strain diagram (fig. 4b). During the softening regime, i.e. when dissipation occurs, σ^* decreases from the maximum value σ_u^* to 0, while ε^* grows from 0 to ε_c^* . In the meantime, the non-damaged parts of the bar undergo elastic unloading (fig. 4a). We call the σ^* - ε^* diagram the *fractal or scale-independent cohesive law* (fig. 4b). Contrarily to the classical cohesive law, which is experimentally sensitive to the structural size, this curve is an exclusive property of the material since it is able to capture the fractal nature of the damage process.

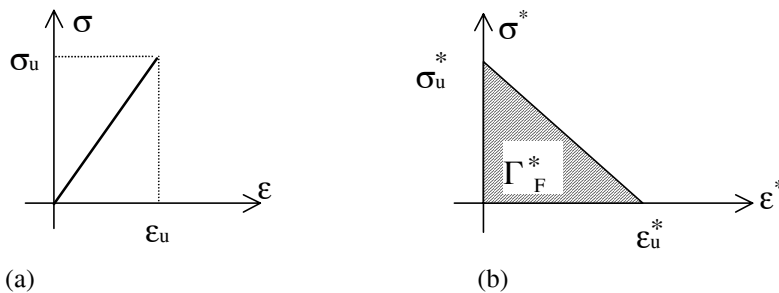


Figure 4. Scale-independent cohesive crack model.

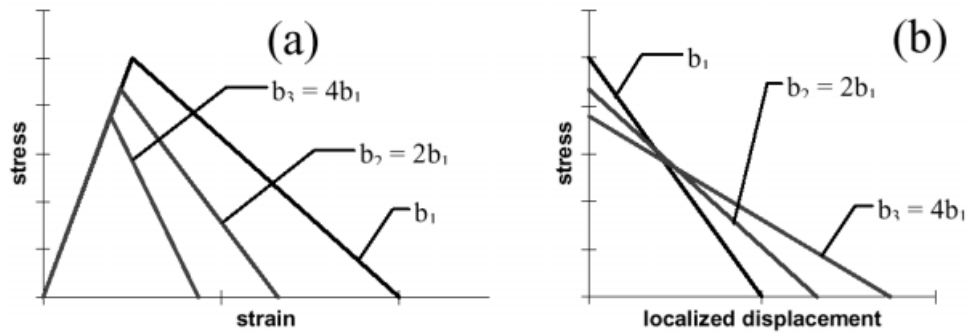


Figure 5. Implications of the fractal cohesive law on the σ - ε and σ - w diagrams.

Recently, van Mier & van Vliet [4] accurately performed tensile tests on dog-bone shaped specimens over a wide scale range (1:32). They plotted the cohesive law for specimens of different sizes and found that, *increasing the specimen size, the peak of the curve decreases whereas the tail rises*. More in detail, w_c increases more rapidly than σ_u decreases, since, in the meantime, an increase of the area below the cohesive law, i.e. of the fracture energy, is observed. Thus, the fractal model consistently confirms the experimental trends of σ_u , Γ_F , w_c .

In order to highlight the implications of the proposed model onto the classical constitutive laws, we can assume linearity for both σ - ε and σ^* - ε^* diagrams (fig. 4). Consider now three specimens, made by the same material, presenting a ligament size respectively equal to b_1 , $b_2 = 2b_1$, $b_3 = 4b_1$, and a band thickness proportional to the ligament. If w_{c1} , ε_{c1} , σ_{u1} are the parameters of the first specimen, the σ - ε and σ - w relationships can be plotted (fig. 5) for the three specimens, assuming, for instance, that $d_\sigma = 0.2$ and $d_\varepsilon = 0.6$ (hence $d_\Gamma = 0.2$). In the σ - ε diagram (fig. 5a), a more brittle behavior is observed as the size increases. The cohesive law is represented by three different curves (fig. 5b), one for each specimen, whereas for the fractal cohesive model the curve is unique. Note that the tensile strength decreases, while the fracture energy and the critical displacement increase, thus justifying the rising tails observed in [4].

The model has been applied eventually to some tensile data obtained by Carpinteri & Ferro [2][3] under fixed boundary conditions. They interpreted the size effect on the ultimate stress and on the fracture energy by means of fractals. Fitting the experimental results, they found the values $d_\sigma = 0.14$ and $d_\Gamma = 0.38$. Some of the σ - ε and the σ - w diagrams are reported in fig. 6, where w is the displacement localized in the damage band, obtained by subtracting, from the total one, the displacement due to elastic and inelastic pre-peak deformation. Note that the trends correspond to the theoretical curves in fig. 5. Last but not least, eq. (7) yields $d_\varepsilon = 0.48$, so that the fractal cohesive laws can be represented in fig. 7. As expected, all the curves related to the single sizes tend to merge in a unique, scale-independent cohesive law.

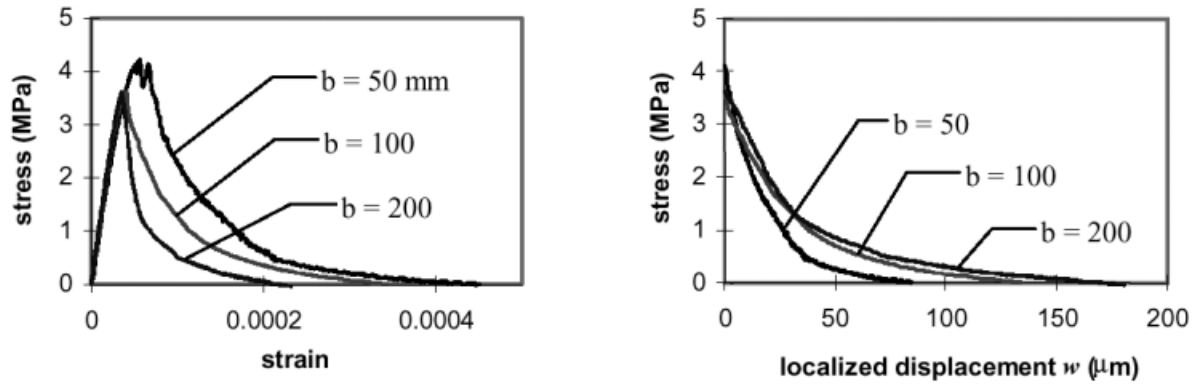


Figure 6. Stress vs. strain and cohesive laws for dog-bone specimens [2][3].

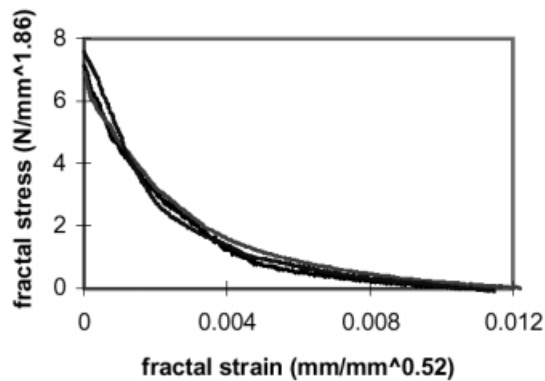


Figure 7. Fractal cohesive law for the specimens tested by Carpinteri & Ferro [3].

4 References

- [1] A. Hillerborg, M. Modeer, P.E. Petersson, *Cem. & Con. Res.* 1976, 6, 773-782.
- [2] A. Carpinteri, G. Ferro, *Materials and Structures* 1994, 28, 563-571.
- [3] A. Carpinteri, G. Ferro, *Materials and Structures* 1998, 31, 303-309.
- [4] J.G.M. Van Mier, M.R.A. Van Vliet, *Proc. of FRAMCOS-3* 1998, 3, 1923-1936.
- [5] A. Carpinteri, *Mechanics of Materials* 1994, 18, 89-101.
- [6] T. Kleiser, M. Bocek, *Zeitschrift fur Metallkunde* 1986, 77, 582-587.
- [7] P. Cornetti, Phd Thesis, Politecnico di Torino, 1998.

Horizontal Wedge Splitting Test Method (HWST) - a New Method for the Fracture Mechanics Testing of Large Samples

Herbert N. Linsbauer

Vienna University of Technology, Vienna, Austria

Aljoša Šajna

IRMA - Institute for Research in Materials and Applications, Ljubljana, Slovenia

Karl Fuchs

Vienna University of Technology, Vienna, Austria

1 Introduction

The principles and methods of fracture mechanics, besides their utmost importance in the field of metallic and ceramic materials, have also become powerful tools for the investigation of cracking in structural elements and structures of concrete on the one hand and for material optimization to reduce cracking on the other. Especially non-reinforced (plain) concrete structures such as dams and lock walls are very sensitive to cracking due to the special character of mass concrete. Mass concrete in the juvenile state generates high temperatures and thus increases thermal stress related cracking during the hydration process. Yet it also is quite vulnerable to tensile stresses after setting.

The theories of linear and nonlinear fracture mechanics in the case of concrete materials seem to be fully developed in the sense that the physical process of cracking has been well understood and mathematically simulated. The main problem in terms of a practical application however is the formulation of an adequate fracture criterion which is directly tied to the knowledge of a *realistic* materials parameter. This is of particular difficulty in the testing of mass concrete [1] where the size of the aggregates can often be up to 120 mm and across, requiring sample dimensions of 1 m and more to achieve homogeneous behavior as is given in the structure. Usual size effect models therefore must fail when using conventional testing sample dimensions.

There are two possibilities to overcome this problematic. One is to develop a procedure adapted for testing mass concrete with small samples as is given by the wet-screening method [2,3]. The other is to test adequate sized samples with a special testing equipment.

This paper presents a method for fracture mechanics testing of large samples of concrete which can easily be used in the laboratory and on the construction site.

2 Problem outline

The main problem for the testing of large samples of (mass) concrete may be seen in the determination of *realistic* fracture mechanics parameters, which is a basic demand in Linear Elastic Fracture Mechanics (LEFM). Test results of large samples also serve as calibration

parameters for the testing methods using small samples and as a grade of the efficiency of *size effect models*.

The most common methods of investigating fracture mechanics material parameters for concrete are the three point bending test (3PB) recommended by RILEM [4] and the wedge splitting test (WST) originally developed at the Vienna University of Technology [5,6]. These methods require testing machines with stiff frames, which in the case of testing of large samples, are available only in laboratories with a special equipment.

The objective of the project was to develop a new method for testing large samples with the least possible effort which would be suitable both in the laboratory and in situ.

3 Horizontal wedge splitting test method (HWST)

The basic idea of the HWST is a horizontal arrangement of the cone-shaped loading device (Fig.1), thereby avoiding a very large, stiff and hardly portable loading frame and minimizing friction effects usually resulting from the vertical to horizontal load conversion in the conventional wedge splitting test method.

The new loading device consists of two rigid steel blocks, two gabled sliding plates, two wedges, one force measuring beam equipped with strain gages and a drive axle. The force measuring device is connected to both the sliding plate and the load transfer block, acting as a four-point bending beam. On each side of the beam (tension and compression side) two strain gauges are mounted to form a Wheatstone's bridge.

The splitting force is activated by two wedges facing horizontally within the groove of the testing sample which are pulled together by a hand or a machine driven axle (with a screw threaded rod) acting through holes in the wedges. Like the axle, one wedge hole has a screw thread. The second wedge can be moved freely on the axle. As the loading device is assembled and placed into the groove of the specimen, the wedges are in perfect contact with the gabled gliding plates. When the axle is turned both wedges slide from the outside to the inside of the specimen, thereby inducing horizontal forces to the upper edge of the groove and subsequently causing a starter notch opening. The acting force is measured through the deformation of the previously calibrated four point bending beam. The calibration has to be carried out according to the usual standards in measuring technique under all aspects of loading - unloading cycles, etc.. An advantage of this testing system compared to an also horizontal applied splitting loading device [7] may be seen in the practical use without special load transferring adaptations and testing equipment.

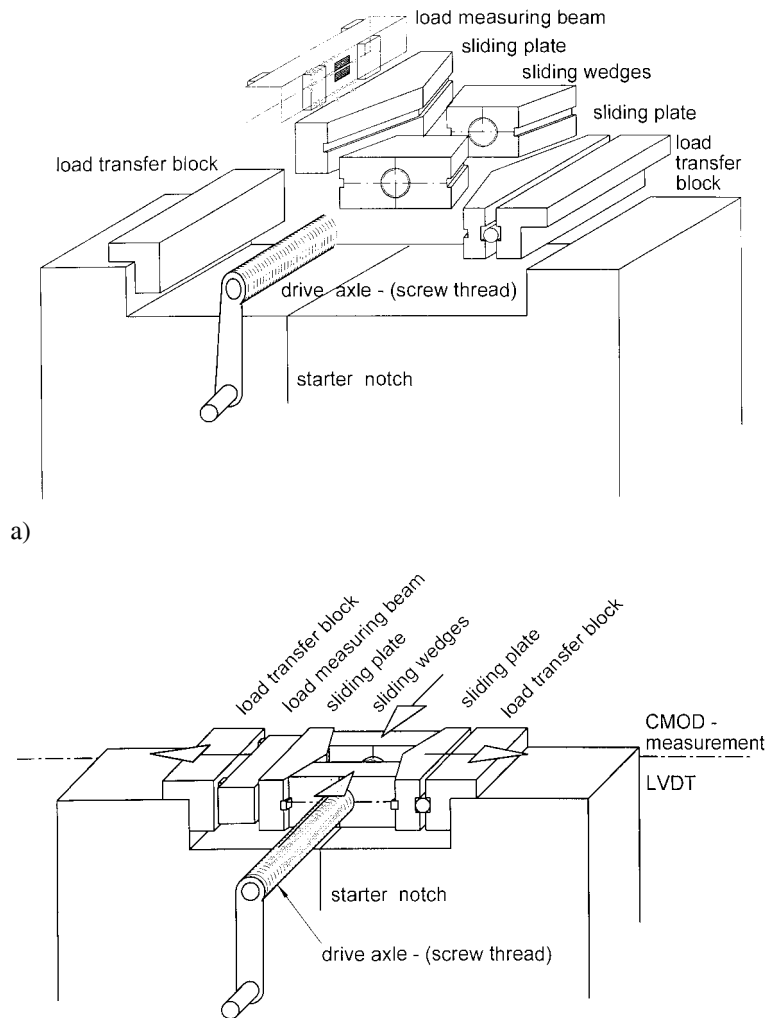


Figure 1. Principle of the new Horizontal Wedge Splitting Test (WST) a) specified; b) assembled

4 Comparative tests

The HWST-method was developed for the testing of large samples of mass (dam) concrete (Fig. 2).

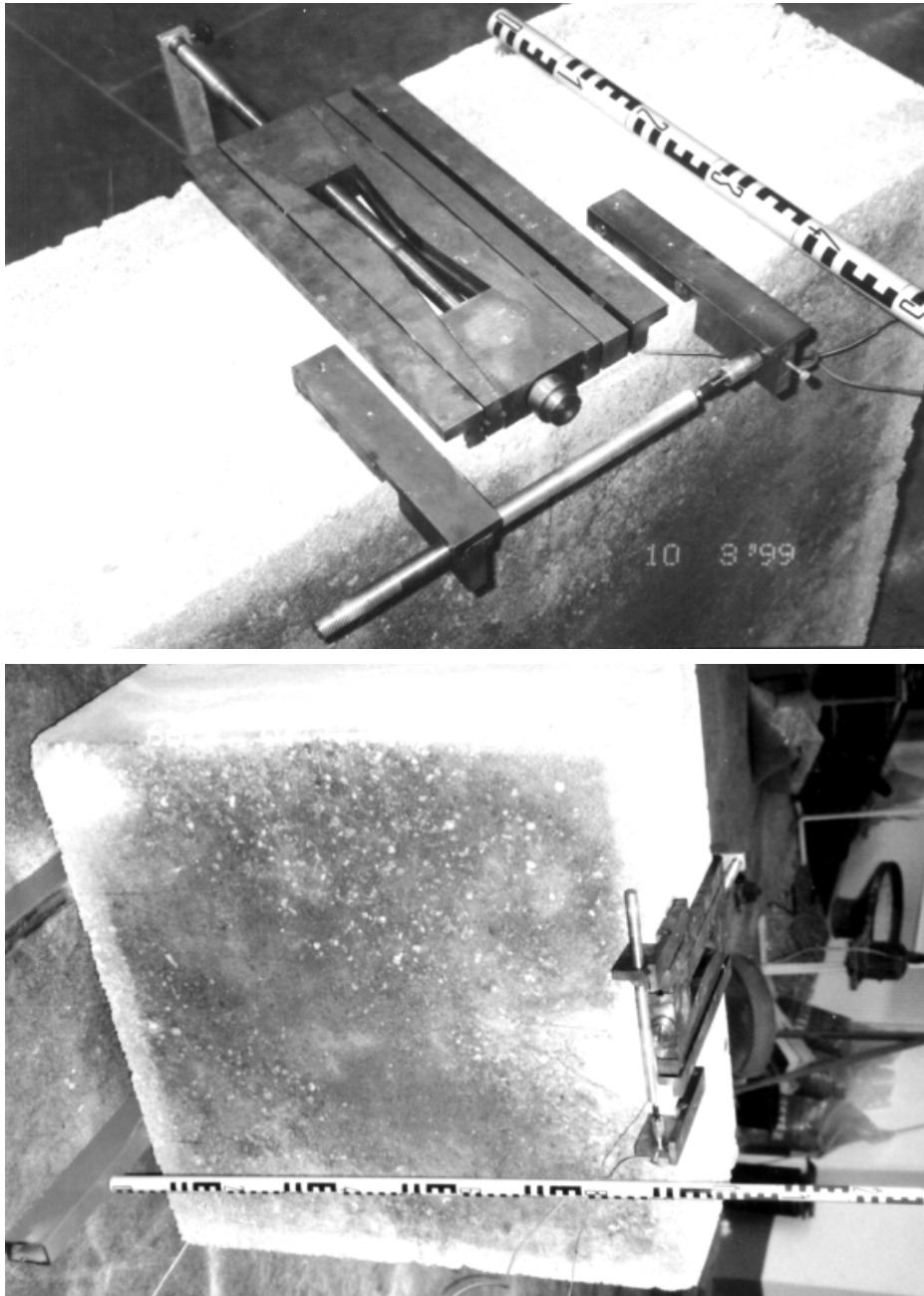


Figure 2. HWS-Test: Sample 900-900-400 mm with loading and CMOD- measuring device.

In order to ascertain the efficiency of the new testing method, comparative studies were carried out between the new method and the conventional wedge-splitting test on the basis of the same concrete and identical geometry. The sample dimensions were restricted to the testing equipment available for the WST-test.

A series of six specimens was prepared, and three out of the six were tested by the standard WST – method. The remaining three were tested by the new device for large WST specimens. Within these test series, concrete containing a maximum aggregate size of 60 mm and an amount of 285 kg of normal Portland cement per m^3 was fabricated. The w/c-factor was 0.6. For both tests, pre-notched ($a=h/3=133$ mm starter notch length) specimens of the same size and of almost the same geometry (length=400 mm, height=400 mm, thickness=160 mm) were prepared. The only difference was the size of the groove. For the WST specimen the groove

width was 40 mm, while for the HWST-specimen the groove width was 170 mm. The specimens with the 40 mm groove were tested by a standard WST -method with a vertical wedge action .The specimens with the 170 mm groove were tested by the new device (Fig. 1). The crack mouth opening displacement CMOD was measured with a LVDT device. The loading was performed via the crank drive by hand and because of this the process may be classified as quasi-CMOD controlled.

From among of three samples prepared for the HWST-procedure one completely failed and one was usable only for the determination of the fracture toughness. This was caused by a partly break-off of the groove walls during the removal of the moulds. The test results in the form of the horizontal splitting force versus the crack mouth opening displacement diagrams for both testing methods are summarized in Fig. 3 and in Table 1.

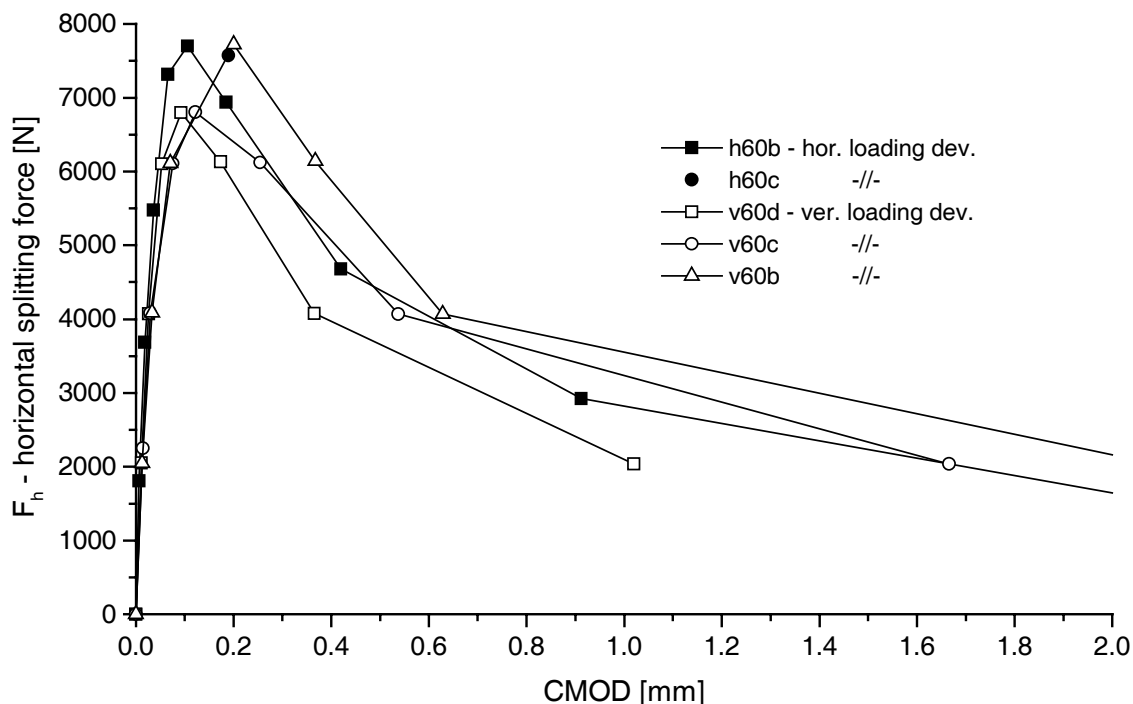


Figure 3. Standard (WST) versus new (HWST) loading device test results.

Table 1.: Test results

Fracture toughness K_C [MPa·m ^{1/2}]		Work of fracture W_f [Nm]*	
WST	HWST	WST	HWST
0.47	0.53	3.95	4.68
0.53	0.52	5.07	
0.47		4.58	

*analyzed for an intermediate phase (CMOD →1.0 mm) without normalization to the fracture area ($W_f/A_f \rightarrow G_f$)

As may be seen from the diagrams, the standard WST tests and the tests carried out with the horizontal wedge splitting test method HWST show similar results with mean value deviations of 7.1% and 3.3% for the fracture toughness and the work of fracture respectively.

This proves that the HWST-method is of universal application.

5 CONCLUSION

The demand for fracture mechanics materials testing of large samples, is especially given in the case of mass concrete as mainly used in dam engineering. Maximum aggregate sizes of mass concrete are within the range of 80 mm to 120 mm, therefore testing sample sizes of 1.0 m and more are necessary in order to gain realistic material values. Since the possibilities of testing such samples are limited by the usual laboratory equipment, a method has been developed for the fracture mechanics material testing of large samples. The method can be used in the laboratory and on a construction site because, aside from the crane capacity, there is no limitation regarding the sample size.

6 References

1. H.N. Linsbauer in Fracture Processes in Concrete, Rock and Ceramics (Eds.: J.G.M van Mier, J.G. Rots J.G. and A. Bakker), RILEM, E.&.N.Spon, 1991, p.779.
2. Sajna, A. Dissertation Vienna University of Technology, 1998
3. Šajna, H.N. Linsbauer in Fracture Mechanics of Concrete Structures (Eds.:H. Mihashi and K. Rokugo), Proc. FRAMCOS-3, AEDIFICATIO, 1998, Vol.1 p.101
4. RILEM Draft recommendation (50-FMC) Mater.Struct. 1985, 287-290
5. H.N. Linsbauer, E.K. Tschegg, Zement und Beton, 1986, 38-40
6. E.K. Tschegg, Materialprüfung 1991 338-342
7. Vervuurt, J.G.M. Van Mier in Fracture Mechanics of Concrete Structures (Ed.: F.H. Wittmann), Proc. FRAMCOS-2, AEDIFICATIO, 1995, p.295

A Near-Field Acoustic Sensor for Rheological Measurements in Both Liquids and Solids: Application to the Cement Setting

Ferrandis, JY., Cros B., Attal J.

Laboratoire d'Analyse des Interfaces et de Nanophysique, Université Montpellier 2, MONTPELLIER, FRANCE.

1 Introduction

The near-field acoustic sensor detects the density and the viscosity of liquids [1], and the emergence of elastic properties of evolving media [2]. During the processing of cement, strong variations of the rheological properties are involved in the paste. Because of these strong variations (from viscous fluid to solid), different devices must be used to characterize the processing. The near-field acoustic sensor both follows the alterations of the viscous paste and the emergence of the rigidity of the cement.

2 Near-field acoustic sensor

2.1 Technique

The near-field acoustic sensor uses the alterations of the resonance state of an acoustic horn to determine the properties of the medium in which the sensor tip is immersed. The viscosity η and the density ρ of liquid are measured [3]. The shape of the horn takes into account criteria such as amplification of acoustic waves and mechanical steadiness. A piezoelectric element serves as both the input and the output port. The input signal is a low frequency sinusoidal signal (50 kHz). It excites acoustic waves in the horn, which in turn load the electrodes. Because the tip is much smaller than the wavelength of the acoustic waves, the sensor operates in near field. The medium interacts with the sensor tip, loads the horn mechanically, and modifies the resonance. The response of the acoustic sensor is the impedance variation. 2 characteristics are detected by a frequency scanning: the resonance frequency f and the maximum of the real part of impedance Z .

2.2 Apparatus

The sensor is composed of two metallic parts, glued by epoxy to a PZ27 ceramics (Figure 1). The larger cylinder is terminated by a thin cylindrical tip immersed in the medium.

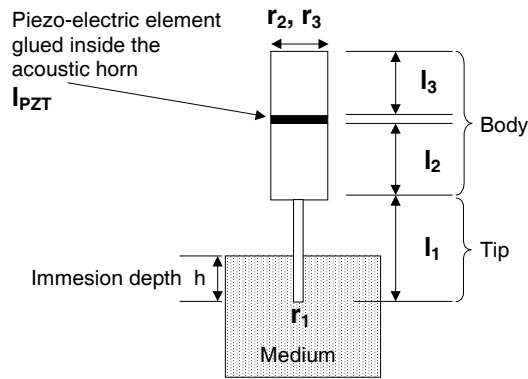


Figure 1. The acoustic sensor. A stepped horn is excited by a piezo-electric element. The tip is coupled with the body of the sensor.

The sensor has the following characteristics:

$$l_1 = 20 \text{ mm}, \quad r_1 = 0.6 \text{ mm}$$

$$l_2 = 24 \text{ mm}, \quad r_2 = 5 \text{ mm}$$

$$l_3 = 18 \text{ mm}, \quad r_3 = 5 \text{ mm}$$

$$l_{\text{PZT}} = 0.4 \text{ mm},$$

metal = invar (Fe-Ni alloy).

These dimensions result in the compromise of several requirements as a strong coupling between the large resonator and the tip and a great sensitivity to the fluid properties.

Invar has been chosen to reduce length sensitivity to temperature variations.

Excitation is supplied by a PZ27-piezoelectric disc. The synthesizer provides an electric signal whose amplitude is 1 V to limit the motions of the tip to 10 nm [3]. A lock'in amplifier measures the complex electrical impedance of the sensor.

2.3 Interaction probe-medium

By conception the acoustic sensor is just dipped in the medium to be tested. This is a major difference with many densitometer and viscosimeter, in which the piezo-electric element is totally immersed or where the liquid must fill the measurement cell.

The acoustic sensor interacts with the medium by 2 ways : through longitudinal waves (pressure) radiated in the medium by the flat end of the tip and through transverse waves (shear) also generated by the lateral surface in our design. The strengths exerted on the probe modify the resonance state and can be related to the properties of the sample.

For weak or mean loads (fluid sample), the resonance curve has 2 peaks (Figure 2). The stronger one (referred as peak 1) has a resonance frequency close to 46 kHz. It is to the resonance of the upper section of the sensor, coupled with the tip. The second peak (referred as peak 2) is about 52 kHz. It is the resonance of the tip immersed in the sample.

When the probe is free or immersed in a liquid medium, the horn operates like two coupled resonators. Neither of the two cylinders vibrates at its proper frequency, the vibration mode of each one being modified by the coupling with the other. When the load applied by the immersion medium increases, the dissipated energy increases. It lessens the energy stored in the horn. The resonance peaks of both cylinders decrease.

When the immersion medium becomes stiff, the probe is jammed and one resonance peak is detected. This resonance is equivalent to the resonance of the whole sensor, with one end fixed. The dissipation is weak and decreases when the stiffness of the medium increases. The

value of the resonance frequency becomes close to the natural frequency of the equivalent resonator.

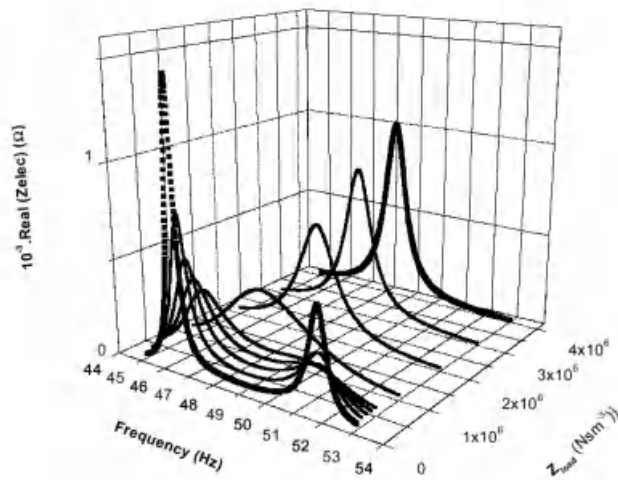


Figure 2. Alterations of the resonance curve of the acoustic sensor as a function of the acoustic load

3 Application to the cement setting

3.1 Material

The samples are mixtures of water and portland cement prepared with water/cement ratios between 0.4 and 0.6.

Cement is a hydraulic binder. Its mechanical strength is the result of the formation of strong bonds through chemical reaction with water. Cement setting takes place in several stages. The mixture with water first results in a repulsion between the grains. At this stage, the paste is fluid. The reaction between cement and water gives a colloidal gel constituted by hydrated compounds. Then the gel layers surrounding the grains connect together and make up bridges. The paste becomes strongly viscous and cannot be cast any more. Water does not easily diffuse through the gel whose formation is followed by a slowing down of the reaction.

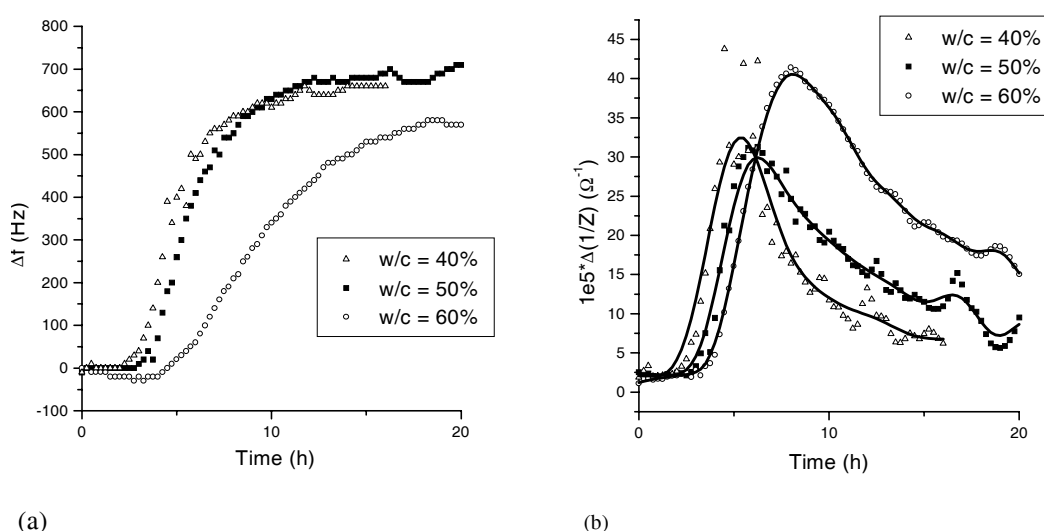
The emergence of the shear modulus takes place in the cement paste with the connectivity, i.e. when all grains are connected together by the hydrate-bridges (percolation threshold) [4]. The formed tridimensional network then fills the whole volume of the paste. The cement setting is still now characterized by the resistance to the penetration by the Vicat needle (ASTM C-191). The beginning and the end of the setting are defined by penetration depths empirically set. More recently, acoustic wave propagation has been used to follow the rheological and mechanical evolutions of the cement pastes [5, 6].

3.2 Results

The resonance curve was experimentally studied as a function of time for 3 water/cement mixtures. The difference of the resonance frequency in the medium and in air (Δf) and the alteration of the maximum of the impedance ($\Delta(1/Z)$) are the parameters which appeared to be the most convenient.

The experimental results showed that the horn operated according to two modes. The first one was involved when the sample was fluid and the second mode appeared with the coming out of the solid state. The change of the operating mode of the sonotrode corresponded to the cement setting and the emergence of the elastic properties.

This change could be accurately located. It began with the increase slope of the Δf curve (Figure 4a) and finished with the maximum of $\Delta(1/Z)$ of peak 1 (Figure 4b). The plotting of these 2 curves appeared to be a reliable method to characterize the shear threshold with a single sensor. The difference between the curves for the 3 ratios w/c confirmed that these 3 cement mixings had different rheological properties



(a) (b)
Figure 3. Alteration of the resonance of the peak 1 (a) Δf as a function of time (b) $\Delta(1/Z)$ as a function of time.

3.3 Discussion

The twofold operating of the horn is well adapted to show both the increase in viscosity and its vanishing with the emergence of an elastic behavior: a single sensor is used from liquid to solid state. The change of operating during setting points out the shear threshold. It corresponds to a sharp change of the resonance frequency of peak 1.

The setting can be described as the connection of the cement grains by the chemical compounds formed by reaction between the anhydrous clinker and water. These compounds display various types of morphology which give them different rheological behavior. The sensitivity of the ultrasonic techniques to the evolution of fluidity during the first ten minutes is still weak. Moreover, these techniques have not resulted yet in the development of a rheometer suitable for use on site. The other methods for checking the cement setting, like isothermal calorimetry and conductimetry only indirectly characterize the setting, because they follow the chemical evolution of the medium and not its mechanical properties. On the contrary, our method based on acoustic near field is very sensitive to all rheological changes and provides all the information on the fluidity (information on the viscoelastic medium) and later on the stiffness (information on the formation of an elastic medium) required to use hydraulic binders. This information still remains qualitative. The setting is characterized by the change of operating mode of the horn, pointed out by the maximum of the curve plotting $\Delta(1/Z)$ as a function of time. The experimental curves confirm that the rheological properties of the cement pastes and, mainly, the setting time, are related to the ratio w/c .

4 Conclusion

A sensor based on the acoustic near field technique has been designed and developed. Owing to the study of the changes of the resonance features of the horn, the evolution of the rheological properties of cement paste can be characterized without discontinuity. Thanks to its design, this sensor is sensitive enough to detect all stages of the evolution of cement paste, which bring about changes of the rheological properties. Information remains qualitative, but a standardization by materials with known rheological properties would provide more quantitative information. The method can be applied to other products whose processing requires the knowledge of the shear threshold, i.e. the time for which the stiffness of the product is sufficient for its handling : other hydraulic binders, glues, varnishes, paints and inks. More generally, mediums affected by strong changes of their rheological properties, like polymers involving a cross-linkage, can be characterized by this kind of sensor.

5 References

- [1] C. Prugne, J. van Est, B. Cros, G. Lévêque, J. Attal,, Meas. Sci. & Technol. 1998, 9, 1894-1898
- [2] B. Cros, J.Y. Ferrandis, M. Pauthe, La Revue de Métallurgie – Science et Génie des Matériaux, in press
- [3] J. Van Est, C. Prugne, B. Cros, J. Attal, B. Cretin,, Appl. Phys. 1998, A 66, S357-S360
- [4] D.P. Bentz, E.J. Garboczi,, Cement & Concrete Research 1991, 2, 325-344
- [5] F. de Larrard, C. Hu, T. Sedran, J.C. Szigtar, M. Joly, F. Claux, F. Derkx,, ACI Mater. J. 1997, 234-243
- [6] A. Boumiz, Adv. Cement Based Materials 1996, 3, 94-106

The Value of the SCB Test for Fracture Testing

Fedde Tolman, Adriaan J. den Herder

Netherlands Pavement Consultants b.v., Utrecht, The Netherlands

1 Introduction

Usual tests for determination of stress and strain properties of bound granular materials are the Uniaxial Tensile Test (UTT), the Indirect (splitting) Tensile Test (ITT), Wedge (splitting) Tensile Test (WTT) and Bending Tests in Three (TPB) or Four (FPB) point loading. An alternative for these tests is the Semicircular Bending Test (SCB). A semi-circle is loaded in three point loading. The advantage of the SCB test are the loading in compression and the ease of obtaining specimen from structures by coring, which is the least laborious and destructive way of obtaining specimens from existing structures for determining tensile or shear fracture properties. The advantage of the UTT is the approximately uniform stress and strain distribution. The disadvantages are the execution problems. Specimens have to be glued to platens, or clamped, which are laborious and disturb the uniformity. Excentricities lead to bending moments and thus also disturb the uniformity. The ITT is loaded in compression, so the problems of introducing the load as mentioned for the UTT are avoided. However the compression load may lead to local shear failure because the stresses and strains are only uniform over part of the potential fracture line. Also shear failure along the fracture line may happen. This failure type can hardly be discerned from tensile failure afterwards. Bending beams can be loaded in compression on the cost of introducing some shear and an unclear stress strain field. Furthermore specimens are relatively expensive especially when they have to be taken from existing structures, because beams have to be sawn instead of the much easier coring. The short bending beam is comparable to the SCB because the cut of corners of the semi-circle do hardly influence the stress and strain fields. The advantage of the SCB over the WTT is that a usual three point bending set without further accessories can be employed. The general disadvantage of the SCB is the short span, which leads to obscurance of the stress and strain fields. Fracture probably is of a combined shear bending type. The SCB test has been proposed in the BREU research program DuraCrete as a compliance test for concrete and is being investigated in The Netherlands for quality control of pavements.

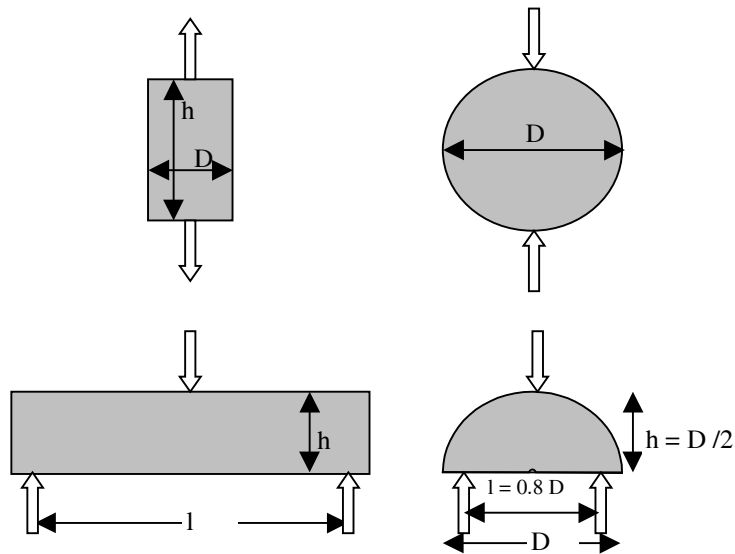


Figure 1: Schematic test set ups for the Uniaxial Tensile Test (UTT), the Indirect (splitting) Tensile Test (ITT), the Three or Four Point Bending Test (BT) and the Semicircular Bending Test (SCB)

Table 1: Overview of advantages and disadvantages of tensile tests

test	uniformity of stress and strain	load surfaces	stress near load surfaces	specimen
UTT	+	-	-	-
ITT	0	+	-	+
BT	0	+	+	-
SCB	-	+	+	+

The objectives of this paper are:

- to indicate the relation between the strength derived from the SCB and other types of tests
- to indicate the variation coefficient of these tests

2 Definitions

Usual definitions for strength and stiffness (at zero load) are indicated in Figure 2. In case of load control tests, failure develops almost instantaneously after reaching the maximum attainable load (strength). This also occurs in case of brittle failure in displacement controlled tests.

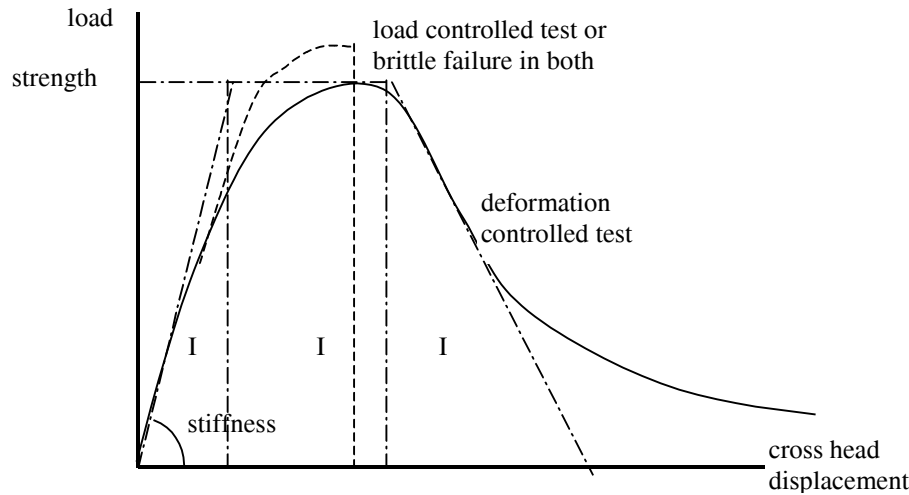


Figure 2: Schematized load deformation diagram

The strength in load controlled tests may occasionally be somewhat higher than in displacement controlled tests. Energy terms may be defined as indicated in Figure 2. Area I (below the load – deformation curve may be called the elastic work and area II the plastic – damage work. Area III and IV are the post peak damage work.

To arrive from these definitions at material parameters test-typical geometrical corrections have to be applied, in general

$$f = \alpha \frac{F}{bh} \quad (1)$$

f	material property (e.g. stiffness, strength)	MPa
F	load	N
b	thickness of the specimen	mm
h	width (beam height) of the specimen	mm
h_0	length of stress concentration notch	mm
α	test typical geometry factor (see Table 2)	

Table 2: Typical values of α for strength

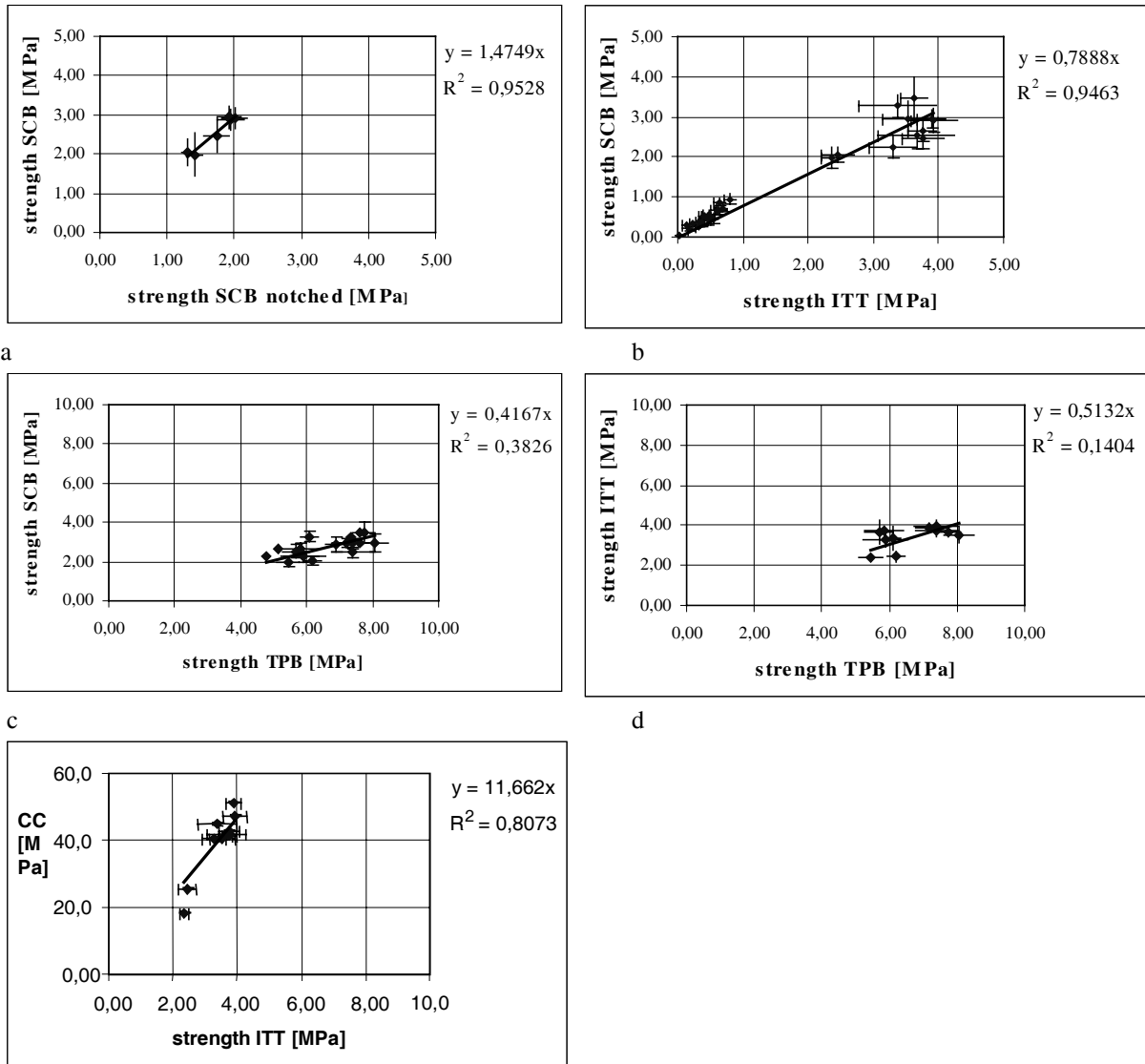
	value used	elastic (maximum value)	plastic (minimum value)
ITT	0.64 (= $2/\pi$)		
TPB (bending)	12 ($l/h = 8$)	1.5 l/h	l/h
TPB (shear)		0.75	0.5
SCB	1	2.4	1.6

Damage mechanisms, eventually resulting in failure, may be discerned in:

- fracture, growth of a crack
- yield, with cross section contraction and rise of local stress as consequences
- fatigue, defined as growth and accumulation of localized damage spots (abstained is also from understandings as time-dependency, though practically this will be an accompanying aspect, and cyclic load)

These mechanisms can not be discerned with the straightforward test methods as described, but may in a qualitative way help to explain results.

3 Results



e
Figure 3: test results

It is found that

$$\frac{(F / b(h - h_0))_{SCBnotched}}{(F / bh)_{SCB}} = 0,67$$

$$\frac{(F/bh)_{SCB}}{(F/bh)_{ITT}} = 0.5, \text{ when only the cement - bitumen emulsion is regarded } \frac{(F/bh)_{SCB}}{(F/bh)_{ITT}} = 0.76$$

$$\frac{(F/bh)_{SCB}}{(F/bh)_{TPB}} = 4.8$$

$$\frac{(F/bh)_{ITT}}{(F/bh)_{TPB}} = 9.6$$

Table 3: test program and results

Material	test type	test T [°C]	test speed [mm/s]	number of specimen	average coefficient of variation of the strength*
cement concrete (3 grades: C35, C45, C55, each in 2 humidities: wet and air dried)	CC	20		41	0.04
	ITT	20		72	0.10
	TPB**	20		83	0.07
	SCB	20		77	0.09
	notched SCB	20		123	0.12
asphalt concrete	SCB	0	0.085	4	0.11
cement bound asphalt granulate	SCB	10	0.085	15	0.13
	FPB	10	0.1	4	0.06
bitumen bound asphalt granulate	SCB	0	0.085	12	0.20
cement – bitumen emulsion (10 binder combinations, 10 stone – sand combinations)	ITT	5	0.85	69	0.15
	SCB	5	0.085	140	0.18

* the coefficient of variation is determined on series of 4 to 8 specimens; the values as presented are averages of these series

** both load and displacement controlled

4 Conclusions

Correlations are calculated between tests to determine tensile properties for a number of cement and bitumen bound materials. The coefficients for each class of materials may deviate rather a lot from the calculated coefficients for the complete set of materials.

The correlations between the tensile tests (ITT, TPB and SCB) are better than the correlation to the CC.

Typical values of the coefficients of variation for bound granular materials were found to be 0.05 to 0.20. The lower values are found for the CC and BT, intermediate values for SCB and ITT and the higher values for SCB tests on bound granulate and emulsion bound materials.

5 References

1. CEB FIP model code 1990
2. Lim, I.L.; Johnston, I.W.; Choi, S.K.; Boland, J.N.; Fracture testing of a soft rock with semi-circular specimens under three-point bending; Int. J. Rock Mech. Min. Sci. & Geomech. Abstr., vol 31, no. 3; 1994
3. Gehlen, C.; Ludwig, H; Tolman, F.; Compliance testing for probabilistic design purposes – evaluation report; BE95-1347 DuraCrete; 1998
4. Haar, J. ter; Tolman, F.; Compliance tests on fatigue of concrete (part 1 and 2); BE95-1347 DuraCrete; 1999
5. Tolman, F.; Duin, H. van; The SCB test on bound granular materials; ISAET 1999

IV Transport Phenomena and Durability

The Ion Mobility of Deteriorating Salts in Masonry Materials of Different Moisture Content

Anja Buchwald, Christian Kaps
Bauhaus-Universität Weimar, Professur Bauchemie

1 Introduction

The existence and movement of water and damaging salts are at the origin of numerous types of decay observed in masonry. Salt migration can be subdivided at least into two processes based totally on different mechanisms. Ions of dissolved salts can be transported with the migrating water. The second transport mechanism is the ion diffusion driven by a concentration gradient. In practice this mechanism comes into play to remove dissolved ions from salt containing masonry by application of a compress. For the calculation of the duration of such a desalination process the knowledge about salt diffusion coefficient is necessary. The diffusion coefficient of the ion pair of Na^+ and SO_4^{2-} in fully saturated brick material were recently presented [1]. Nevertheless in reality the water saturation is much less than 100 %. Therefore diffusion measurements were carried out to determine the influence of the degree of water saturation on the observed diffusion coefficient of salt ions in brick and mortar material. Additionally to this the impedance spectroscopy were used as an independent method to measure the ion mobility and therefore the diffusion coefficient of these and other materials also.

2 Determined Investigations

2.1 Three-Layer Diffusion Experiment

In order to measure the diffusivity of salt ions at different moisture levels, sandwich specimens have been prepared. These layered specimens consist of three plates, each of them of about 1,7 cm (brick) or 3 cm (mortar) thickness. The central layer was impregnated by a salt solution (Na_2SO_4). All three plates are equilibrated with the same moisture content by microwave impulse drying. Paper filters have been inserted between two adjacent plates in order to ensure a better contact at the interfacial zones. This sandwich construction is mechanically compressed in order to enhance the contact between the three layers. Immediately all the faces of the sandwich specimens are sealed with wax in order to prevent any moisture exchange between specimens and the surrounding atmosphere. At given duration's of diffusion, the three plates were disconnected and drilled down step by step up to defined depths in order to used the brick powder to analyze the water-soluble ion content of Na^+ and SO_4^{2-} . Assuming that no advection phenomenon and no chemical reaction can take place during the run, the transient transfer of the ions held in porewater of the porous system can be described by a diffusion equation given by the second Fick's law. The solution of this equation is done numerically and already proposed in [2]. To find the best ion diffusion coefficient, the computer

program [3] fits the calculated concentration profile to the experimental profile by minimizing the sum of squares.

2.2 Impedance Spectroscopy (IS)

Analogous prepared cylinder shaped samples with 18 mm in diameter and 5 to 35 mm thickness were used for impedance spectroscopy in a SI 1260 impedance analyzer. For best electrical contact between samples and electrode silver coated gum were used to avoid artifacts due to surface resistance [4]. If plotted in the complex impedance plane (Nyquist-plot), the IS-data form a depressed arc in the high-frequency zone which goes over in a straight line at lower frequencies. A typical curve of a salt and moisture penetrated sample is shown in **Figure 1**. The bulk resistance is then found as the interception of the high frequency-arc and the real axis using the indicated equivalent circuit for fitting the experimental data. The arc-depressing factor n of the CPE which symbolizes the distribution of relaxation time is related to pore size distribution [5,6]

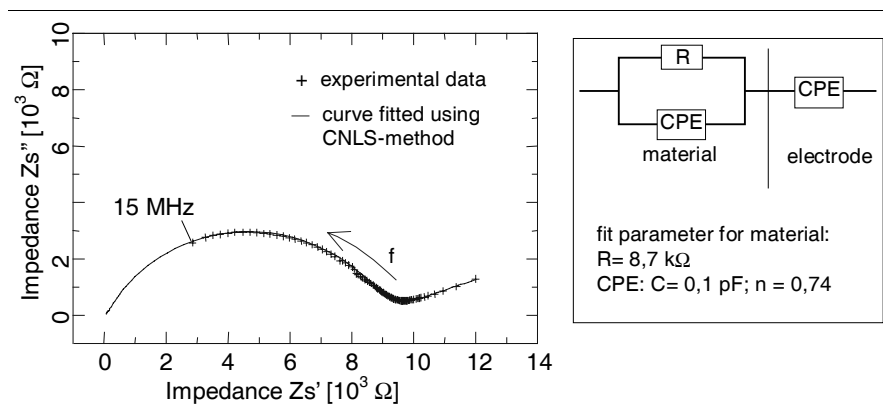


Figure 1. Nyquist plot and equivalent circuit of a typical sample (f-frequency; Circuit elements: R-resistance, CPE-constant phase element with C-capacity and n- arc-depressing factor).

The conductivity σ_{eff} of the material can then be determined using R and the geometry h (thickness of cylinder) and A (area of cylinder):

$$\sigma_{\text{eff}} = \frac{1}{R} \frac{h}{A} \quad (1)$$

Using Nernst-Einstein-relation, the diffusion coefficient D can be calculated from σ_{eff} and the salt concentration in the sample c_{salt} [7]:

$$D = \sigma_{\text{eff}} \frac{k \cdot T}{z^2 \cdot F \cdot e \cdot c_{\text{salt}}} \quad (2)$$

3 Materials

The investigated building materials include brick, mortar and sandstone. Beside these materials porous glass as a model material were include, which has a similar pore structure at different pore diameters. An overview about the porosity characteristics are given in Table 1. It can easily be seen, that the porous glass material represent a broad spectrum of porosity properties

where the building materials can be inserted. The pore structure of the sandstone and the porous glass materials are similar. The porosity of the brick material is formed by small gaps mainly orientated in extrusion direction. The mortar contains two different kind of porosity, ones the capillaries and as second the big air holes (compare the medium pore diameter measured by MIP).

Table 1. Porosity characteristics of the used materials

		bulk density [g/cm ³]	density [g/cm ³]	true porosity [vol.- %]	apparent porosity [vol.-%]	coefficient of water adsorp- tion [kg/m ² √h]	permeabil- ity to gases [10 ⁻¹⁴ m ²]	medium pore diameter [μm]
brick	Z1	1.81	2.81	36	34	19	0.45	2
lime mortar	M	1.80	2.65	32	31	6	6.8	2 / 200
sandstone 1	S1	2.15	2.63	18	17	1...4	1...3	0.5
sandstone 2	S2	2.07	2.69	23	22	9...20	8...14	50
porous glass 1	P1	1.35	2.39	43	39	-	11.6	100
porous glass 2	P2	1.27	2.33	45	43	-	11.2	80
porous glass 3	P3	1.70	2.33	27	23	-	5...8	22
porous glass 4	P4	1.69	2.31	27	24	-	6.5	10
porous glass 5	P5	1.68	2.28	26	24	-	0.25	0.9

4 Results

The absolute values of D for all materials at 100% water saturation measured by impedance spectroscopy are given in

Table 2. The influence of pore morphology on the diffusion coefficient has been already discussed in [8].

Table 2. Diffusion coefficient of Na₂SO₄ in fully saturated material by impedance spectroscopy

	Z1	M	S1	S2	P1	P2	P3	P4	P5
D [10 ⁻⁶ cm ² /s]	2.6	4.2	3.9	2.9	3.1	3.3	3.2	3.4	3.4

Figure 2 shows the diffusion coefficient of Na₂SO₄ in brick material (left side) and in the lime mortar (right side). The diffusion coefficient of the salt ions in the fully saturated materials are between 2×10^{-6} and about 4.5×10^{-6} cm²/s. The diffusion coefficient in the brick material measured by impedance spectroscopy seems to be higher than by diffusion experiment. There might be additional ions solvated by pore solution out of bulk brick material increase the measured conductivity and therefor affect the diffusion coefficient. The influence of the water saturation on the diffusion coefficient seems to be almost linear down to about 30%. Afterwards the diffusion coefficient decreases less rapidly and comes to almost zero. This behavior is similar to already described potential relation between R and S_w in sandstone [9] Other authors found exponential or linear relation between D and S_w in soils [10,11]

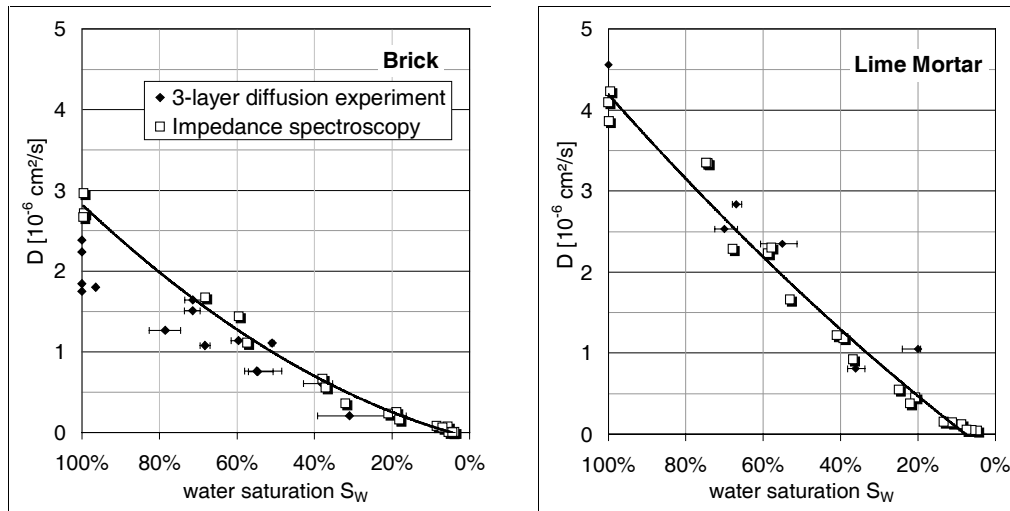


Figure 2. Comparison of diffusion coefficients of Na_2SO_4 determined in diffusion experiment as well as by impedance spectroscopy in relation to water saturation

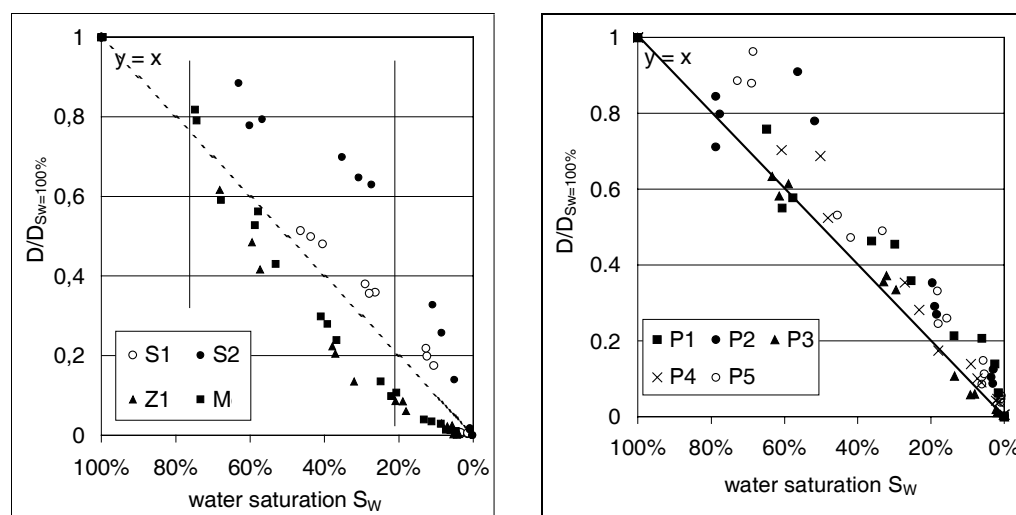
The values differ from each other significant especially in the diffusion experiment. That might first be caused by taking always new samples for each experiment and each moisture content and second by difficulties in contacting the three plates as well as unpleasant advective and convective water movement.

It can be said that the usage of both diffusion experiment and impedance spectroscopy result in the same diffusion coefficients in the relation to moisture content. The diffusion coefficients of the two involved methods are consistent. Each method contains advantages and disadvantages (Table 3). A combination of both increases not only the numbers of measurements and therefore the consistency of the assumption. Both methods complete each other in the light of minimizing the maximal error. For instance the Three-Layer Diffusion Experiment is difficult to manage at moisture saturation's smaller then 30 %. The Impedance spectroscopy consist of errors at high saturation's because of stray and cable inductance's.

If comparing the diffusion coefficient of all materials in relation to the moisture content in **Figure 3**, it can be seen that there are 2 typical groups of curves formed by the data. If coarsely looked, the diffusion coefficient decrease almost 1:1 to water saturation. But in detail the decreasing of D in brick (Z1) and mortar (M) is more rapidly then in sandstone S1 and all porous glasses and shows potential relation. The other extreme symbolized the sandstone S2 because D decreases more moderate at higher water saturation. In-between 20 % - 80 % water saturation the curves in **Figure 3** (left side) follow the sequence $S2 > S1 > M > Z1$.

Table 3. Comparison of the different methods to determine Diffusion coefficient in relation to moisture content (advantages and disadvantages)

	3-layer diffusion experiment	impedance spectroscopy
pros	<ul style="list-style-type: none"> concentration curve is visible (mistakes influence the curve shape, but it can be taken into account) 	<ul style="list-style-type: none"> quick and easy measurement all moisture degrees are measurable on only one sample
cons	<ul style="list-style-type: none"> different moisture content of the three plates leads to moisture transport and change the salt concentration the contact between the plates can limit the salt transport low moisture content are difficult to manage in experiment immense scope of sample preparing and analysis every moisture content needs new samples and an own diffusion experiment 	<ul style="list-style-type: none"> incorrect electrode contact leads to measurement artifacts if the electrical behavior of the material comes in the same order of magnitude then cable and stray immitance's which lead to measurement errors in the high frequency zone (high conducting materials)

**Figure 3.** Relative values of diffusion coefficients in relation to water saturation of different materials measured by impedance spectroscopy

This corresponds with the arc-depression factor n and therefore with distribution of relaxation time. The expected curve shape should theoretically follow an straight line up to a certain water saturation due to reducing of solution volume. Underneath the concentration of the pore solution increases rapidly which causes in non-proportional decreasing of material conductivity. This curve shape show all the porous glasses and the sandstone. But the potential relation between D and S_w of brick and mortar can't be explained by this hypothesis. Obviously there is an additional cause which decreases D . This might either due to pore morphology (connectivity of pores, pore size distribution) or to ion adsorption/desorption at inner surface. The two groups of materials with brick and mortar on one side and the sandstone's and the porous glasses on the other differ both in pore morphology and chemistry of inner surface. The argument that the pore morphology with the connectivity of the pores have a great influence on

the water distribution and so on the conductivity seems to be more plausible. Further investigation will verify this hypothesis.

This work was supported by the Deutsche Bundesstiftung Umwelt and by the Deutsche Forschungsgemeinschaft at the SFB 524 "Materials and constructions for the revitalization of buildings".

5 References:

1. Buchwald, Ch. Kaps, GDCh-Monographie 15, 1999, 46-51
2. H. Sadouki, A. Buchwald, F.H. Wittmann, Ch. Kaps, International Journal for Restoration of Building and Monuments, 1999, 5, 3-14
3. R. Kriegel, "Win_Diff – a diffusion simulation program", Weimar 1999
4. J.-H. Hwang, K.S. Kirkpatrick, T.O. Mason, E.J. Garboczi, Solid state ionics. 1997, 98, 93-104
5. P. Gu, P. Xie, Y. Fu, J.J. Beaudoin, Cement and Concrete Research, 1994, 24, 86-88
6. B.J. Christensen, T.O. Mason, H.M. Jennings, J. Am. Ceram. Soc. 1992, 75, 4, 939-945
7. T. Kudo, K. Fueki, Solid state ionics, VCH, Tokyo, 1990, p.62
8. Buchwald, Ch. Kaps: *Zum Ionentransport bauschädlicher Salze in feuchtebelasteten Bauwerkstoffen*. 5th International Colloquium -Materials Science and Restoration- 30.nov.-2.dec.1999, in progress
9. C.F. Rust, Petroleum Transactions, AIME, 1952, 195, 217-224
10. M.J.M. Romkens, R.R. Bruce, Soil Science, 1964, 98, 332-337
11. L.K. Porter, W.D. Kemper, R.D. Jackson, B.A. Stewart, Soil Sci. Soc. Proc. 1960, 24, 4, 460-463

A Percolation Model for Water Sorption in Porous Cementitious Materials

Bernhard Elsener, Dieter Flückiger and Hans Böhni

Institute of Materials Chemistry and Corrosion, Swiss Federal Institute of Technology ETH Hönggerberg, CH-8093 Zurich

1 Abstract

The highly disordered pore system of cement paste is described and numerically modelled as fractal structure. Water sorption experiments on cement paste with different porosity and numerical percolation experiments with Monte Carlo simulations are performed and have shown to be self similar, thus the percolation theory with the percolation threshold p_c describes the kinetics of water sorption at all porosities consistently. With the same percolation model (connectivity of pores) the deviation from the classical power law for water sorption at long times and low porosities, the drastic reduction of the effective diffusion coefficient and the sharp increase in resistivity with lower porosity and lower relative humidity can be explained.

2 Introduction

This microstructure of cement paste consists of solid and porous phases, and it is the spatial and topological arrangement of these phases that is ultimately responsible for the strength and transport properties of the paste. One key topological attribute is the *connectivity or percolation* of phases within this microstructure ([figure 1](#)): a percolating phase forms a three dimensional spanning cluster, while a phase that has not percolated consists of isolated clusters [1]. The durability or service life of cement-based materials is also directly influenced by phase percolation because the *transport properties* of such materials are determined to a large degree by the amount and connectivity of the capillary porosity within the microstructure. For water sorption in cement paste and for diffusion of degradative species, such as chloride ions, both the connectivity of the pore space and of the porous hydration products are critical: as the capillary porosity becomes disconnected at low w/c ratios or long hydration times, transport rates decrease markedly and become controlled by the gel porosity of the highly-connected calcium silicate hydrate phase [2].

The *kinetics of water sorption* of porous cement based materials as cement paste, mortar or concrete are generally described by the classical theory with the capillary or potential model resulting in the well known square root dependance of water uptake with time [3]. A lot of literature results, however, showed that this square root law does not fit the experimental data [4] at longer times and / or at low porosity. To explain these deviations, a new model based on the percolation theory has been proposed [5]. The structure of cement paste is described with a 3-d simple cubic lattice, the sites of the lattice being occupied with a probability p

(pores in the cement paste), the empty sites describe the cement matrix (probability $1-p$). The occupied sites (pores) form a cluster if they are neighbored.

In this work results of laboratory experiments on water sorption in cement paste and of numerical experiments (percolation) are performed, the transport processes are modelled by Monte-Carlo simulations. The results obtained are used to rationalize the marked influence of capillary porosity on the effective diffusion coefficient, on resistivity and on water sorption coefficient of porous cement based materials.

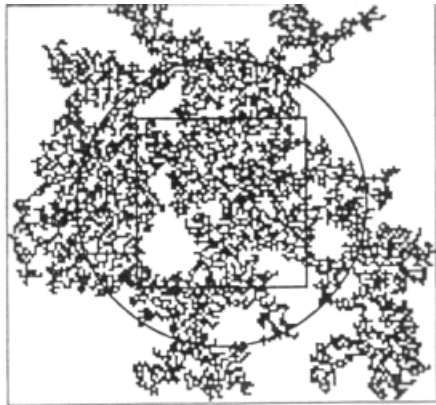


Figure 1: Finite cluster at the percolation threshold p_c (after [1])

3 Percolation Theory

Percolation theory [6] was developed to mathematically deal with disordered media, in which the disorder is defined by a random variation in the degree of connectivity[7]. The main concept of percolation theory is the existence of a percolation threshold, that value of probability p , usually denoted p_c , at which there exists an unbroken path from one side of the system to the other (figure 1). In other words, for p greater than p_c , there is always a spanning cluster, although some isolated, non-spanning clusters can still be present.

The percolation properties of the cement paste microstructural model can be computed on a digital-image-based model that has an underlying lattice structure [8] or simply by creating random 3d lattice that allow to determine the connectivity of the system for different porosities [5].

4 Experimental

To study the influence of porosity on water sorption both, experiments with cement paste and numerical experiments have been performed. More details in [5].

4.1 Cement paste

Cement paste samples of dimension 40 x 40 x 160 mm have been prepared. The mix design was adjusted such that a range of capillary (10 – 35%) and gel porosity (6 – 15%) could be obtained. In the low porosity range filler was added to the mix. The samples were hydrated for

7 to 28 days (degree of hydration 0.5 – 0.95) and then dried at 105 °C in order to evaporate all liquid water in the pore system.

4.2 Water sorption experiments

At least three parallel experiments were performed for every cement paste mix. The samples were immersed 3 mm into tap water. The sample weight was measured in logarithmic intervals (4 decades, from minutes to days) by removing the cement paste sample from the water bath, drying the lower surface with cleanex, measuring the weight and re-immersing the sample in the water bath. This operation took about 20 seconds.

4.3 Numerical experiments

The numerical experiments based on the percolation theory were performed with a simple 3d cubic lattice with site-percolation. The occupied sites, indicating the capillary pores, were assigned a probability p , the empty site (cement paste matrix) had the probability $1-p$. Random 3d structures of size $100 \times 100 \times 100$ (thus 1 Million of sites) were calculated by the computer model [5].

Transport processes (water sorption or diffusion) was modelled with Monte-Carlo simulations using a random walker algorithm. In each time step the walker randomly moves to the next (allowed) site. The distance is calculated as vector between the starting point and the point at time t in the lattice. To reach convergence of the algorithm each numerical experiment was calculated for 1000 random 3d structures and 1000 random starting points of the random walker in each 3d structure. This required a total calculation time of ca. 12 hours [5].

5 Results and discussion

5.1 Capillary water sorption on cement paste

The capillary water sorption (expressed in g/m^2) for different gel- and capillary porosities of cement paste is shown in [figure 2](#) both in the logarithmic (Fig. 2a) and square root representation (Fig. 2b). It can be observed that for low capillary porosity (13 and 16%) the square root law is fulfilled only at short times ($t < 20$ h) and the water uptake reaches a nearly limiting value after 500 hours. Contrary, for high porosities (32 % CP) a rapid water uptake is found (the constant value at longer times is due to the limitation of the sample height). The logarithmic diagram gives the same information but it is possible to determine the exponent of the power law (eq.) from the slope of the curves. It can be noted that the slope for high porosities is close to 0.5, indicating that for this case the square root law is correct. For lower porosities the slope of the curves are markedly increasing with time.

5.2 Monte Carlo simulations

The results of Monte-Carlo simulations (figure 3) for the same porosities as in the real cement paste samples show a similar trend: for high porosities (32% CP) a square root dependance (fig. 3b) is found. From the logarithmic graph (Fig. 3a) it can be seen that the slope is 0.5 only at low number of time steps. At low porosities (13 and 16% CP) the curves reach a nearly

limiting value with time (fig. 3b) and the slope of the logarithmic curves increase with time (fig. 3a). It has to be noted that - for reasons of the way of calculation - the numerical results are dimensionless on both the time and the distance axis. -

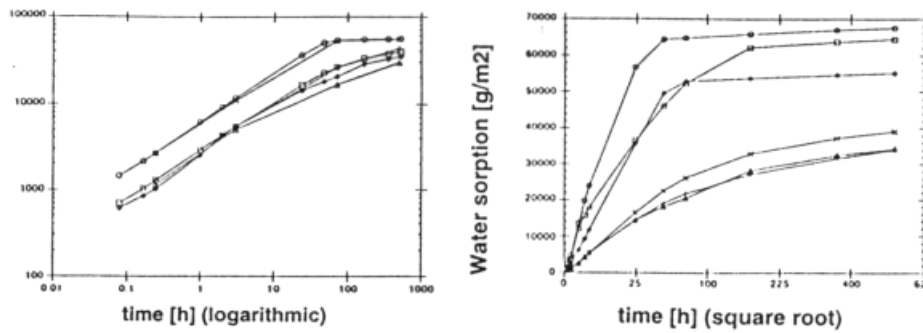


Figure 2: Results of water sorption on cement paste. Logarithmic scale (left) and square root scale (right). Capillary porosities for curves from top to bottom: 32%, 29%, 26%, 20%, 16%, 13%.

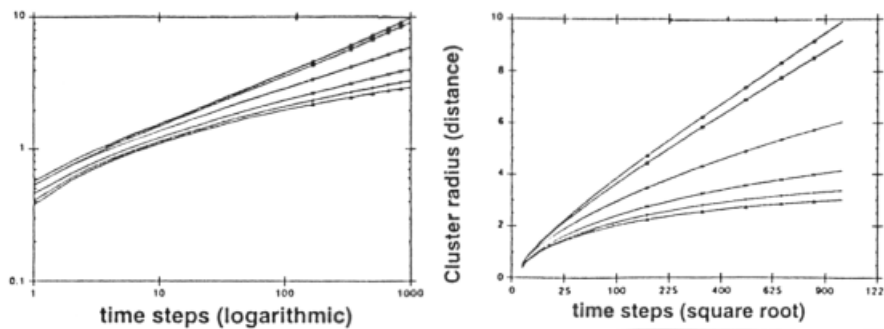


Figure 3: Results of numerical experiments (Monte Carlo simulations). Logarithmic scale (left) and square root scale (right). Capillary porosities for curves from top to bottom: 32%, 29%, 26%, 20%, 16%, 13%.

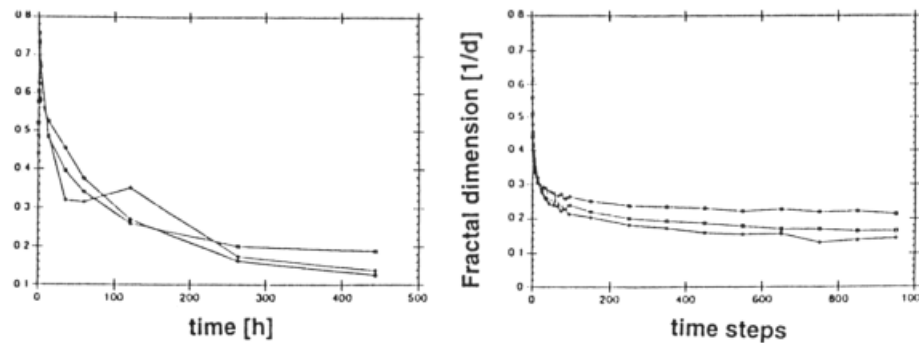


Figure 4: Fractal dimension (=slope of curves in 2a and 3a) for the cement paste (left) and numerical experiments (right). Capillary porosity 13, 16 and 20%. Note the asymptotic value at long times 0.17 ± 0.02 for both experiments.

5.3 Self similarity

The self similarity of numerical and cement paste sorption experiments can be checked when the slope of the distance time curves (fig. 2a and 3a) are determined and plotted versus time (figure 4). As it can be noted the value of the slope (equal to the reciprocal of the fractal dimension d of the lattice [5]) asymptotically reaches the same value of 0.17 ± 0.02 for both the cement paste (fig. 4a) and the numerical experiments (fig. 4b). This result demonstrates

that the two experiments are similar in terms of fractal dimension of the structure and in terms of the kinetic processes occurring.

Thus, modelling the influence of topological arrangement of the solid phases in the microstructure of cement paste with the approach of fractal structure and percolation threshold is correct. In the following some „engineering“ applications regarding diffusion coefficient, resistivity and the coefficient of water sorption are discussed.

5.3.1 Diffusion coefficient

Transport of ions in water saturated concrete frequently is described by the „effective diffusion coefficient“. This value is determined by the true diffusion coefficient of the ions in the pore solution of the cement paste and by a correction factor due to the topological arrangement of solid phase and pores. It has been shown [5, 9] that the influence of porosity on the effective diffusion coefficient can be predicted by percolation theory: figure 5 shows that the normalized diffusion coefficient ($D = 1$ for 100% porosity, thus solution) drastically decreases with decreasing porosity, describing very well the experimentally observed diffusion coefficient in OPC concrete [10] and values of the sorptivity measured for different porosity [11]. Thus the reduction of the effective diffusion coefficient is due to topological arrangement of the solid phase of cement paste and the reduction in connectivity of the pores.

5.3.2 Resistivity of cement paste

Based on the assumption of a fractal structure of cement paste (two phase system, conducting phase = pores, isolating phase = matrix) the resistivity ρ of cement based materials can be calculated by [12]

$$1/\rho = \sigma = \sigma_0 (p_0 - p_c)^\gamma \quad (1)$$

σ conductivity

σ_0 conductivity of pore solution

p_0 volume fraction of pore solution

p_c percolation threshold

γ percolation exponent

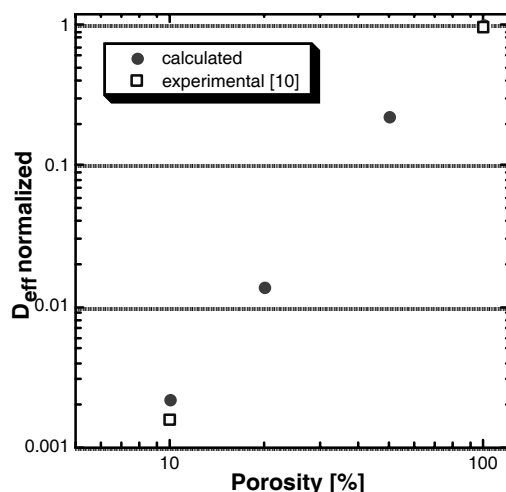


Figure 5: Normalized effective diffusion coefficient D_{eff} calculated from percolation theory. Comparison with experimental data from Collepari [10]

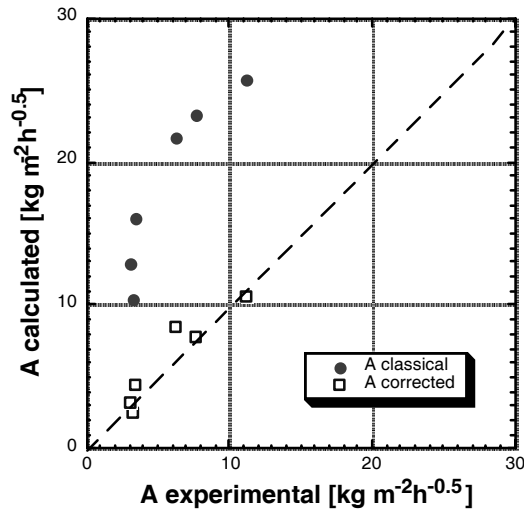


Figure 6: Classical A_{class} and corrected A_{corr} water sorption coefficient vs measured values A_{exp} of the cement pastes tested.

The resistivity of cement paste and mortars with different w/c ratios stored at RH 60 – 100% until reaching the equilibrium humidity could be described and predicted very accurately based on the percolation theory and eq. (1). Thus the increase in resistivity with lower RH observed for a given topological arrangement of the solid phase and pores (defined by w/c ratio) is determined by the degree of pore water connectivity in the pores.

5.3.3 Capillary water suction

The calculated „classical“ water sorption coefficients A_{class} (calculated with an effective pore radius) usually overestimate the measured values (figure 6). Based on the reduction of the effective diffusion coefficient (figure 5), a correction factor $\sqrt{D_{eff}}$ for the „classical“ water sorption coefficient can be calculated. In this way the calculated values for the coefficient $A_{corrected}$ are obtained that coincide well with the experimentally measured ones and allow correct prediction of the capillary water suction for cement based materials at long times. The experimental results obtained on cement paste can be predicted correctly [5].

6 Conclusions

The highly disordered pore system of cement paste is best described as fractal structure. This fractal structure implies a percolation threshold p_c of the porosity p where the transport properties (sorption, diffusion) become abnormal.

The percolation theory, thus purely „geometrical“ effects of topological arrangement of solid phase and pores, explains with one model

- the deviation from the classical power law for water sorption at long times and low porosity
- the drastic reduction of the effective diffusion coefficient D_{eff} and
- the increase in resistivity with lower porosity and lower relative humidity

7 References

- [1] J. Feder, Fractals, Plenum Press New York (1988)
- [2] D.N. Winslow, M.D. Cohen, D.P. Bentz, K.A. Snyder, and E.J. Garboczi, Cement and Concrete Research 24 (1994) 25-37.
- [3] DIN 52617, Bestimmung des Wasseraufnahmekoeffizienten von Baustoffen, Beut Verlag (1987)
- [4] C. Hall, Water Sorptivity of mortars and concrete – a review, Mag. of Concr. Res. 41 (1989) 51-61
- [5] D. Flückiger, Percolationsbetrachtungen zum Feuchtigkeitstransport in porösen Körpern, PhD Thesis No 10223, ETH Zürich (1993)
- [6] D. Stauffer, Introduction to Percolation Theory (Taylor and Francis, London, 1985)]
- [7] R. Zallen, The Physics of Amorphous Solids (J. Wiley and Sons, New York, 1983)
- [8] E.J. Garboczi and D.P. Bentz, J. of Materials Sci. 27 (1992) 2083-2092.
- [9] B. Elsener, Ionenmigration und elektrische Leitfähigkeit im Beton", SIA Doc.D065 Schweiz. Ingenieur- und Architektenverein, Zürich, 1990, p. 51 – 59
- [10] M. Collepardi, A. Marcialis and R. Turrizani, J. American Ceramic Society, 55 (1972) 534 - 53
- [11] Sorptivity (marchese)
- [12] D. Bürchler, B. Elsener and H. Böhni, Electrical resistivity and dielectric porperties of hardened cement paste and mortars, in „Electrically based Microstructural Characterization“, ed. R.A. Gerhardt, S.R. Taylor and E.J. Garboczi, Mat. Res. Soc. Symp. Proc. Vol. 411 (1996) 407

New Experimental Study Relating Cracking to Water Permeability of Normal Strength Concrete

Corina-Maria Aldea, Masoud Ghandehari, Surendra P. Shah, Alan Karr
National Science Foundation Center for Science and Technology of Advanced Cement Based Materials,
Northwestern University, Evanston, IL, U.S.A.

1 Abstract

The goal of the research presented here was to study the relationship between cracking and water permeability of normal strength concrete. The present study is an ongoing extension of previous work relating cracking to concrete permeability performed at ACBM, Northwestern University, and is novel in the crack generation and crack control. 50mm slices were sawn from precast cylinders and used for the tests. The factors chosen for the experimental design were the location of the slice within the cylinder and average crack mouth opening displacement (CMOD) of the induced cracks, ranging from 50 to 300 microns. Cracking was characterized by CMOD, crack length and crack area, and water permeability by permeability coefficient and average flow rate. A feedback-controlled wedge splitting test was used to generate width-controlled cracks and speckle interferometry was used to record the cracking history. Water permeability was evaluated by a low-pressure water permeability test for loaded specimens at the designed CMOD. The experimental results showed that water permeability of cracked material significantly increased with increasing crack width and flow was quite repeatable for the same cracking level. Crack parameters significantly affect water permeability and there is no location effect. Given the sample geometry the crack parameters are not linearly independent, there is no direct relationship between water flow and crack length, where as comparable relationships exist between either CMOD or crack area and flow characteristics.

2 Introduction

Although earlier work has shown that cracking affects permeability, the tests performed at ACBM Northwestern University used unloaded specimens [1, 2, 3]. As cracks in real structures are under load, the goal of the study presented here is to investigate the effect of cracks under load on water permeability. In addition to this, it is desirable to compare the experimental results with theoretical predictions. In order to quantify the permeability of cracked concrete, previous investigators [4, 5, 6, 7] attempted to determine a relationship between the experimentally-measured and calculated water flow rate. Theoretic flow was obtained using a model from rock mechanics based on laminar flow through a smooth parallel-sided slot. As this model requires knowledge of crack profile, a new test was designed in order to provide the information about both crack width and crack length. Feedback-controlled wedge-splitting tensile tests were used to induce cracks of specified

widths in concrete specimens and speckle interferometry was used to monitor the crack history throughout the test. Water permeability of cracked samples was then evaluated by a low pressure water permeability test of loaded samples. The experimental procedure, the research results and the comparison with the theoretical model as well as with the previous results are fully described in [8].

3 Experimental Program

3.1 Details About the Test Series

Normal strength concrete with a cement-to-sand-to aggregate ratio 1:2:2 and a water-to-cement ratio $w/c=0.45$ was used. Samples were precast in cylindrical molds 100x200mm (4x8in.) with mold inserts in order to provide the required specimen geometry (Figure 1). Precast cylinders were stored in a controlled chamber at 20° C and 100% RH until the age of 28 days and then cut into 50mm-thick (2in) slices. Sample preparation was performed at 56-days. Special aluminum loading brackets (Figure 1) were then attached to the samples using a high strength waterproof adhesive. Cracks were induced using a feedback-controlled wedge splitting test. The cracked samples were then vacuum saturated according to the procedure described in ASTM C 1202-94 and set up for the water permeability test (WPT). Two to four samples for each crack mouth displacement (CMOD) were tested.

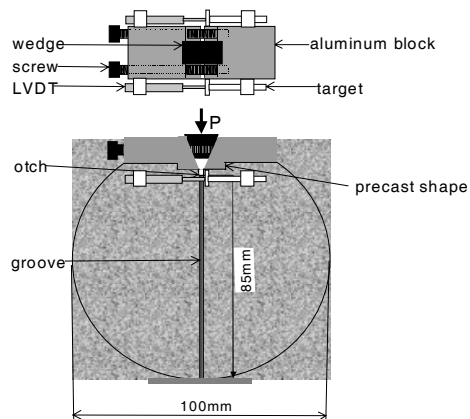


Figure 1. Sample geometry.

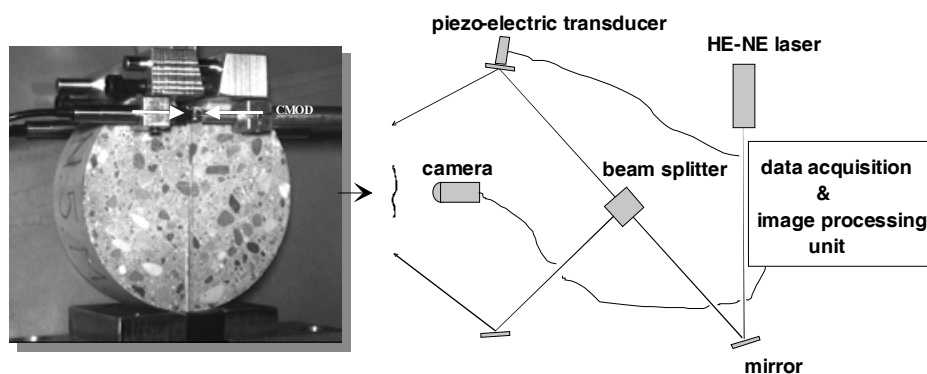


Figure 2. Wedge-splitting test setup and schematic of the interferometer.

3.2 Loading Device

A speckle pattern interferometry technique was used for accurate detection of crack propagation, while close loop feed back control loading was used to obtain stable post-peak fracture (Figure 2). The specimens were equipped with special loading brackets in order to sustain the prescribed crack mouth opening displacement (CMOD). Linear variable displacement transducers (LVDT) with a range of 0.5mm were used as feed-back sensors. The LVDTs were glued on each side of the specimen, normal to the loading direction at the level of the initial notch tip. The crack width at a given distance from the crack mouth will be referred to as crack opening displacement (COD), where as CMOD will be used for the crack width at the level of the initial notch tip. Average recorded displacement of the two LVDTs was used as a feedback control. Prescribed CMODs under loading were 50, 100, 200, and 300 microns. Once the desired CMOD was achieved, the screws on each side of the sample bracket were tightened in order to hold the target CMOD. The effectiveness of this procedure was verified. The CMOD was maintained over 24 hours giving excellent results. The optical device is fully described in [8].

3.3 Water Permeability Test

The water permeability test (WPT) is described by [1., 2]. The WPT test consisted of monitoring the water level in the pipette and then refilling it to the initial level with a syringe measuring only the inflow. The setup is based on axial water flow through the sample, given the low pressure of approximately 30-cm head. The change in head was recorded at regular intervals, depending on the average crack opening, and the time elapsed after the beginning of the test. The permeability coefficient was used to quantify water flow, and it was calculated assuming laminar flow through the cracked material, based on Darcy's law, and using the assumption of the continuity of flow [1, 2].

4 Results

Figure 3 presents typical crack profiles within the range of the induced CMOD. Polynomials of second degree are best-fit curves for the experimental data. Cracked area was integrated based on the measured crack profile (COD) and crack length. The crack length ranged from 64% to 95% of the specimen depth for target CMOD values ranging from 50 to 300 microns, although for target CMOD larger than 100 microns the crack propagated almost through the entire specimen depth.

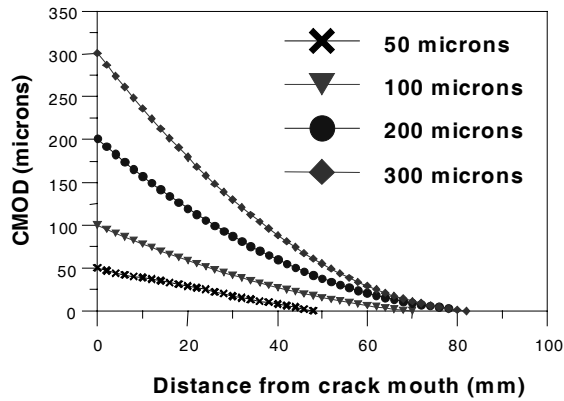


Figure 3. Typical crack profiles.

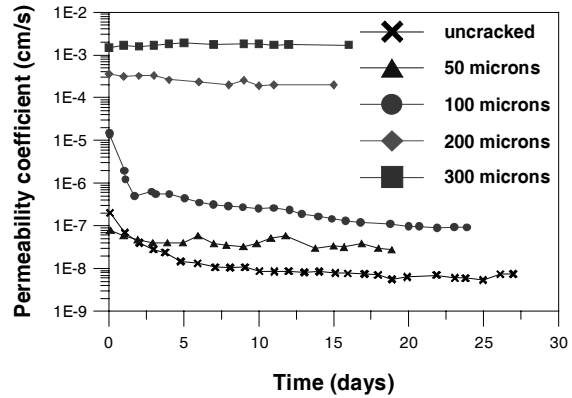
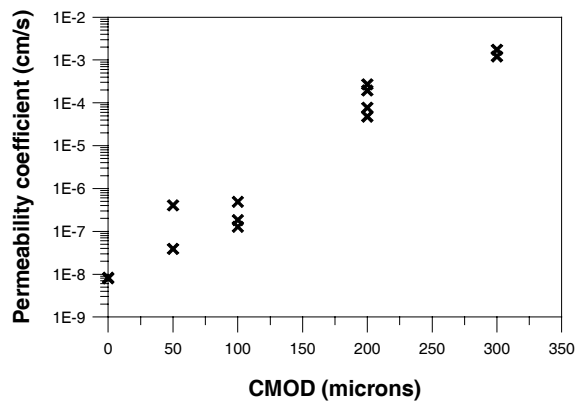


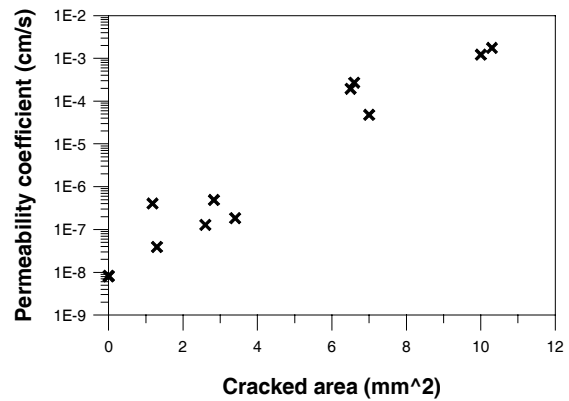
Figure 4. Typical permeability coefficients.

Water flow was monitored for about 30 days for most of the specimens tested. WPT tests for wider cracks (200 and 300microns) were stopped after about 15 days. For these samples flow was rapid and five to six measurements were taken every day using a stopwatch. Figure 4 presents typical changes in permeability coefficient with time. Each data point represents a permeability coefficient corresponding to two successive readings for the uncracked samples and the samples with CMODs of 50 and 100 microns, and the daily average of five to six values obtained for samples with 200 and 300 microns. Permeability coefficient increased with increasing crack width by several orders of magnitude. The decrease in permeability coefficient with time for the cracks below 100 microns is probably due to the completed saturation and crack healing of the cracks. In the case of the samples with larger cracks no change in permeability was observed, indicating the dominance of cracks to permeability. Insignificant healing is presumed for large crack openings.

It was observed that given the range in the specimen size, there is no clear relationship between permeability coefficient and crack length, whereas permeability coefficient increases with increasing CMOD and subsequently the cracked area. Figures 5 present the relationship between the crack parameters and permeability coefficient. Permeability coefficients were calculated as the average of the values corresponding to steady state flow [8]. The same trends are observed relating the permeability coefficient with both CMOD and cracked area. These suggest that given the geometry used, one parameter (i.e. CMOD) seems to be sufficient to define the relationship with water flow. Similar trends are obtained relating flow rate with cracking parameters.



a. CMOD vs. permeability coefficient.



b. Cracked area vs. permeability coefficient.

Figure 5. Relationship between crack parameters and flow.

5 Conclusions

- CMOD and crack length were monitored throughout the test and the WPT was carried out on loaded samples.
- The benefit of wedge-splitting test consists in providing accurate information about the induced crack geometry.
- Crack parameters determined in this study are not linearly independent. Given the sample geometry, there is no direct relationship between water flow and crack length, where as comparable relationships exist between either CMOD or crack area and flow characteristics. This suggests that for the sample geometry used in this study one parameter, i.e. crack width, is sufficient to characterize the relationship between cracking and water flow.

6 Acknowledgements

This research was carried out at the ACBM Center, Northwestern University. Support from the National Science Foundation (NSF) through grant DMS/9313013 to the National Institute of Statistical Sciences (NISS) is greatly appreciated. Steve Hall is acknowledged for help in sample preparation.

7 References

- [1] K. Wang, D. Jansen, S.P. Shah, A. Karr, *Cem. and Concr. Res.*, 1997, 27(3), 381-393.
- [2] C.M. Aldea, S.P. Shah, A. Karr, *Mat. and Struct.*, 1999, 32(219), 370-376.
- [3] C.M. Aldea, S.P. Shah, A. Karr, *ASCE J. of Mat. in Civ. Engg.* 1999, 11(3), 181-187.
- [4] M. Tsukamoto, J.D. Wörner, *Darmstadt Concr., Annual J. on Concr. and Concr. Struct.*, 1991, 6, 123-135.
- [5] M. Tsukamoto, *Darmstadt Concr., Annual J. on Concr. and Concr. Struct.*, 1990, 5, 215-225.
- [6] C. Edvardsen, *Concrete Precasting Plant and Technology*, 1996, 62(Nov.), 77-85.
- [7] B. Gérard., *Contribution des couplages mécanique-chimie-transfert dans la tenue à long terme des ouvrages de stockage de déchets radioactifs*, 1996, Ph.D. dissertation (in French), ENS Cachan , France, p. 290.
- [8] C.M. Aldea, M. Ghandehari, S.P. Shah, A. Karr, submitted to *ACI Mat. J.*, 1999.

Micro ice lens formation, artificial saturation and damage during freeze thaw attack

Max J. Setzer University of Essen, Institute of Building Physics and Materials Science - IBPM

Abstract

Frost damage is primarily caused by ice expansion and hydraulic pressure. It can only occur if a certain critical degree of saturation is reached at least locally. In normal concrete structures this condition is not fulfilled even after long isothermal capillary suction. During a freeze thaw cycle water is sucked in. The process is characterized by three conditions: 1) The matrix of hardened cement paste is not infinitely rigid. 2) Due to surface interaction, a remarkable amount of water in the gel pores remains unfrozen and triple point shifts. 3) This water is under increasing negative pressure of $\Delta p \approx 1.22 \text{ MPa}/(T - T_0)$. The micro ice lens model describes the process. During cooling the gel matrix shrinks and water is squeezed out, condensing at the micro ice lenses present. During heating, the gel matrix containing unfrozen water expands even if there is no melting of ice. Since the micro ice lenses are still frozen, the volume change can only be balanced by an uptake of water. Cyclic freeze-thaw testing is primarily the action of a micro pump increasing saturation. If a critical degree of saturation is reached by this effect, concrete is damaged within few cycles. Pore size distribution is decisive for the amount of unfrozen water, the transport capacity or density and the amount of pores, which are to be filled by the micro ice lens pump. It must be kept in mind for test procedures and the design of new, durable concretes.

Key words: Ice formation, frost damage, surface interaction, micro ice lens, frost suction, freeze thaw testing

1. Introduction

In this contribution only a coarse draft of the micro-ice-lens model is outlined. A more detailed description is found in [1-3].

The behavior of pore water below 0 °C is characterized by the depression of freezing *point in the gel pores*. The depression increases with decreasing pore size and reaches -60 °C. The unfrozen water comprises an appreciable amount of total water in hardened cement paste (approximately 30 % to 60 % at -20 °C). When it starts to freeze, hydraulic pressures are generated by the 9 % volume expansion of ice. Nevertheless, surface interaction between the matrix of hardened cement paste and pore water or pore ice, respectively, is the most relevant phenomenon to be considered in any case. Due to the surface interaction the behavior of both matrix and pore water deviates significantly from macroscopic behavior. It is the reason for the depression of freezing and melting point. Due to the

depression of freezing point pressure differences between gel pores and larger pores of 1.22 Mpa/K(depression of freezing point) are generated . There transport from small to larger pores has been claimed already in [4].

However, the fact that an uptake of water during a freeze thaw cycle is observed has not been adequately considered. Besides the pressure differences already noted, the transport of water to ice is enhanced by the gel matrix that is not infinitely rigid. The extreme pressures generated squeeze out the gel matrix like a sponge during freezing. During melting the gel expands and tries to suck in water. However, the macroscopic ice is still frozen. Water cannot be transported back to the gel in sufficient short time. However, if available it is sucked in from outside increasing the degree of saturation. This leads to a phenomenon, „micro ice lens formation“ and after a freeze thaw cycle a „micro ice lens pump.“ This can explain the artificial water uptake and saturation by freeze-thaw cycles. The mechanism shall be described in this article.

This artificial freeze-thaw saturation has serious consequences for durability against freeze thaw attack and therefore, both for the mix design and the testing of durability against this attack. In testing freeze thaw cycles are necessary since only in this way an artificial saturation by the micro ice lens pump is possible [5]. Experiments (e.g. [6]) prove that after a critical degree is reached the concrete is damaged in few cycles. The cycles are not necessary to overcome the strength and ductility of concrete. A more detailed description of the micro-ice lens model is found in [2,3].

2. Thermodynamic basis

For an - at least semiquantitative - description thermodynamics are used as found in [4] and more details on the thermodynamics of the micro-ice-lens formation in [2,3]. A first point is that the criteria for both mechanical and chemical equilibrium differ in a porous medium from bulk systems since surface effects are dominant. In contrast to other authors who use as a rule the free enthalpy or Gibbs potential the Ω -potential is adopted here in a modified form for surfaces.

$$\begin{aligned}\Omega &= U - ST - n\mu = F - n\mu \\ d\Omega &= -SdT - pdV + \gamma dA - nd\mu\end{aligned}\tag{1}$$

with the internal energy U , the entropy S , the temperature T , the volume V , the pressure p , the surface free energy γ , the number of moles n and the chemical potential μ . The mechanical potential depends only on the volume and surface area as extensive thermodynamic parameters, the temperature, the pressure and the chemical potential are intensive. It can be proved [8] that this potential is given by:

$$\Omega = -V \cdot p + \gamma \cdot A\tag{2}$$

In a more detailed discussion the volume has to be replaced by the sum of all partial volumes as well as the surface by the sum of all surfaces. The potential proves to be a powerful tool to deduce the most essential relations for phase transitions and stability in porous media. It is outlined in more detail in [2,3].

With it the stability criteria can be formulated in a simple and universal way. Under equilibrium conditions at constant temperature $dT=0$ and chemical potential $d\mu_k=0$ the condition for mechanical stability for i phases and j interfaces is found from equation (1):

$$\sum_i p_i dV_i = \sum_j \gamma_j dA_j \quad (3)$$

For two phases in contact with constant total volume $V=V_1+V_2$ equation (3) gives

$$\Delta p_{12} := p_1 - p_2 = \sum_j \gamma_j \left(\frac{\partial A_j}{\partial V_1} \right)_{T, \mu, j \neq 1} \quad (4)$$

If a phase 2 (ice or vapor) proceeds into a liquid filled pore equation (4) reduces to

$$\Delta p_{12} = p_1 - p_2 = \frac{\gamma_{ml} - \gamma_{m2}}{R_H} \quad (5)$$

with the surface free energies of the interface matrix - liquid γ_{ml} and matrix - phase 2 γ_{m2} . The hydraulic radius R_H is the ratio of the cross section area of the pore at the proceeding phase by the rim i.e. the line where the phases meet. Due to mechanical stability between the surface energies it is

$$\Delta \gamma_{12} := \gamma_{ml} - \gamma_{m2} = -\gamma_{l2} \cos \vartheta \quad (6)$$

with the surface energy between liquid and phase 2 γ_{l2} and the contact angel ϑ . Taking into account the correlation between curvature and hydraulic radius

$$\kappa_c := \left(\frac{1}{r_{c1}} + \frac{1}{r_{c2}} \right) = \frac{\cos \vartheta}{R_H} \quad (7)$$

the pressure difference becomes with this:

$$\Delta p_{12} = -\Delta \gamma_{12} \kappa_{12} \quad (8)$$

Before percolation sets in this mean curvature κ increases until the critical value for percolation is reached.

The depression of both freezing and melting point can be deduced. For cylindrically shaped pores it is a good approximation, for melting

$$\Delta T \approx \frac{v_l \gamma_{li}}{(s_l - s_i) r_i} \approx \frac{32 \text{ nm} \cdot \text{K}}{r_p - t} \quad (9)$$

and for freezing (primarily applicable for percolation and only restricted for heterogeneous nucleation in the pores)

$$\Delta T \approx \frac{v_l \gamma_{li} \cos \vartheta}{(s_l - s_i) R_H} \approx \frac{64 \text{ nm} \cdot \text{K}}{r_p - t} \quad (10)$$

where r_i is the radius of the melting ice nucleus, r_p the radius of the pore and t the thickness of the adsorbed film as mentioned above.

To understand the mechanism of micro ice lens pumping it must be understood that the triple point condition, i.e. the equilibrium among liquid water, vapor and ice shifts with

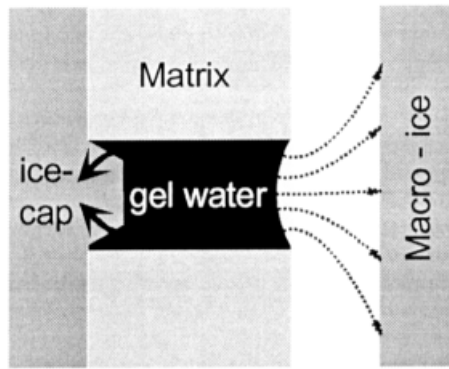


Figure 3. Triple point change of pore liquid

temperature in a porous medium. Figure 3 shows the coexistence of 3 phases. If temperature is diminished the triple point of liquid pore water, ice and vapor shifts. This is possible since, following Defay [10], the variance w of capillary systems with curved interfaces is given by

$$w = 1 + (c - r') - (\psi - s) \quad (11)$$

with s types of surfaces, φ number of bulk phases, c number of

components, r' number of reactions and ψ number of surface phases. It is apparent that w does not depend on the number of phases. With $c=1$, $r'=0$, $s=\psi=1$ the variance w becomes 2.

At the interfaces between the different phases - pore water, ice, and vapor mechanical and chemical equilibrium must be established. Since at the triple point the chemical potentials μ_k for all phases k and components must be equal (Gibb's phase rule) and to preserve equilibrium any changes in chemical potentials $\partial\mu_k$ must also be equal [10] it follows:

$$(s_l - s_i) \left(1 - \frac{v_l - v_i}{v_v - v_i} \frac{s_v - s_i}{s_l - s_i} \right) dT = v_l (dp_l - dp_i) - \frac{v_v (v_l - v_i)}{v_v - v_i} (dp_v - dp_i) \quad (12)$$

since $v_v \approx 10^3 v_l \approx 10^3 v_i \ll v_l, v_i$ the condition for triple point becomes

$$(s_l - s_i) dT = v_l dp_l - v_i dp_i - (v_l - v_i) dp_v \quad (13)$$

Following the variance rule of Defay two parameters can be selected freely. One is the temperature, the second a pressure or equivalently one of the curvatures. Ice forms first in larger pores. The curvature of the ice vapor interface κ_{iv} can be used as the second parameter. If the specimen is sufficiently water saturated the first ice particles formed are macroscopic. (To clarify what macroscopic means in the sense used here: The depression of freezing point of ice crystals near $1 \mu\text{m}$ is below 0.13 K and the pressure difference between liquid and ice below 0.15 MPa. Therefore at $-10 \text{ }^\circ\text{C}$ the effect is below 1%.) The curvature of the ice vapor interface $\kappa_{iv} \approx 0$. The vapor pressure is the saturation pressure over a plain ice surface and the second term on the right hand of equation (8) becomes zero.

Inserting usual values of water it is found with $\vartheta = T - T_0$:

$$\Delta s_{li} = 22.026 \left(1 + 0.00641 \cdot \vartheta - 3.71e - 5 \cdot \vartheta^2 \right) \frac{\text{J}}{\text{mol} \cdot \text{K}} \quad (14)$$

and for the pressure in the pore liquid at shifted triple point with the external pressure P_0 :

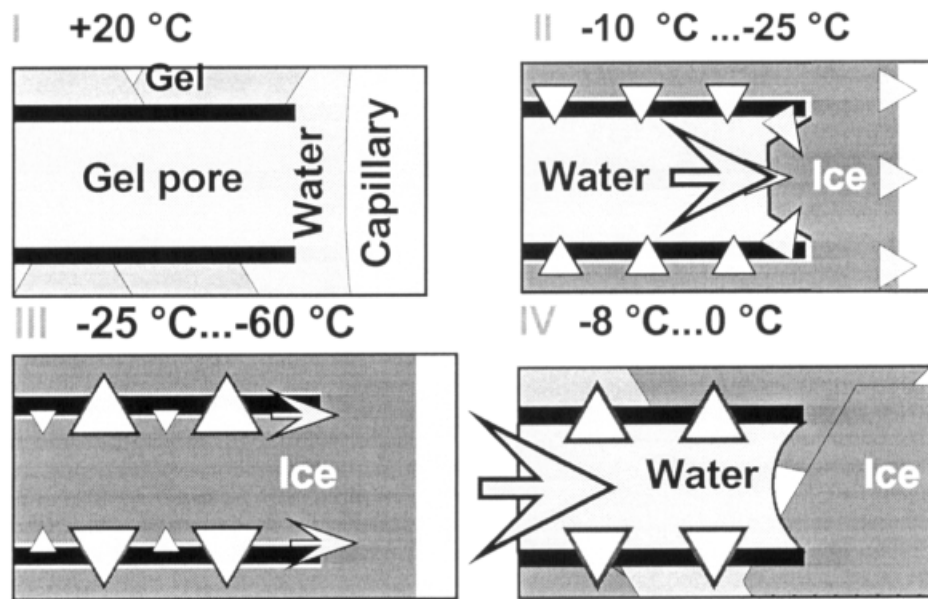


Figure 4. Schematic plot of the micro ice lens model. I) Shows a gel pore and the rim of a capillary which is partially saturated at 20 °C. II) Is the cooling part where water is sucked out of the gel and transported to the macroscopic ice. The gel is shrinking. III) Is the freezing in the gel pores. IV) Is the heating part. The pressure is reduced and the gel expands. Since the micro ice lens is still frozen water can only be sucked in from external sources. Cooling and heating below -23 °C is discussed elsewhere.

$$\Delta p_l := p_l - p_0 = 1.2225 \cdot \vartheta \left(1 + 3.25 \cdot 10^{-3} \vartheta - 1.6 \cdot 10^{-5} \vartheta^2 \right) \quad \text{MPa} \quad (15)$$

3. Model of Micro ice lens formation and micro pumping [1-3]

There are two essential points that must be kept in mind:

1. Following the thermodynamic considerations, water is transported to the larger ice crystals either directly or by evaporation from the liquid and freezing on the ice. Following equation (15) the pressure in the liquid that generates this transport, depends only on the temperature.
2. The matrix is not infinitely rigid.
Therefore, during temperature changes the following processes take place:
 - A. On **cooling** (number II in figure 4) the pressure difference in the water filled gel pores increases - equation (15). The gel filled with unfrozen water shrinks and water is squeezed out comparable to a sponge. It is trapped at the bulk ice i.e. the micro ice lenses.
 - B. On **heating** (number IV in figure 4) the pressure difference in the water filled gel pores decreases - equation (15). The gel expands. However, water can only be sucked in from external sources since the micro ice lenses still remain frozen.
3. If external sources are available a **freeze thaw cycle** acts as a micro pump artificially increasing the degree of saturation.

Since in real situations both the frost front and the melting front are progressing from one surface, the effect of the micro-pump is enhanced. The same is valid for the freeze thaw hysteresis - equations (9) and (10) - which increases the temperature range where water can be transported to the micro ice lenses. The minimum temperature increases the effect - and speeds up the test - as long as it is not below a critical value where gel water freezes.

5. Experimental results

It is seen in figure 5 (by Stockhausen [11,12]) that the expected expansion of ice is not seen. Apparently the coarser pores are not completely water saturated in this specimen although it has been stored at 100 % r.h. prior to freezing. Both effects deviating from bulk behavior can be observed: During cooling the specimen contracts (in figure 5a -II) during heating it expands (IV). It is also worth to note, that the contraction takes only place

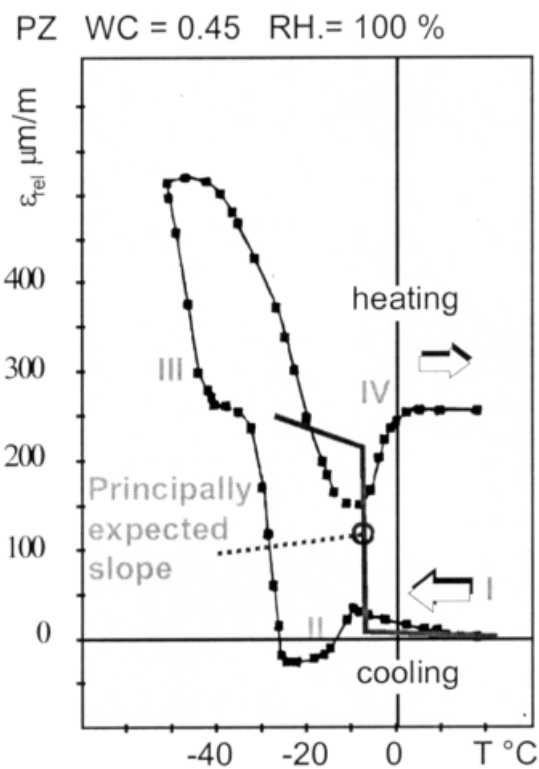


Figure 5. Thermal expansion of sealed hardened cement paste [12]. The relative expansion ϵ_{rel} is the difference between the expansion of the wet specimen ϵ_{wet} and of a dry reference ϵ_{dry} i.e. $\epsilon_{rel} = \epsilon_{wet} - \epsilon_{dry}$. A dry specimen would give a straight line. The principally expected slope of the freezing of bulk water with some supercooling is plotted for comparison.

if ice is formed i.e. it is due to triple point shift. Nevertheless, an expansion is superimposed - visible by the irreversible expansion after a freeze thaw cycle.

In freeze thaw testing several freeze thaw cycles are applied. In contrast to the most commonly used models the cycles are not necessary to overcome the strength and ductility of concrete. They are essential to reach a certain critical degree of saturation where damage starts immediately and needs only very few cycles to destroy the concrete. In the CIF freeze thaw test procedure both saturation micro ice lens pumping over the isothermal saturation and the damage after a critical degree is reached can be observed. The supersaturation is shown in fig. 6. The nick point characterizes the start of damage as shown in [13].

5. Conclusions

Frost action consists of two basic mechanisms:

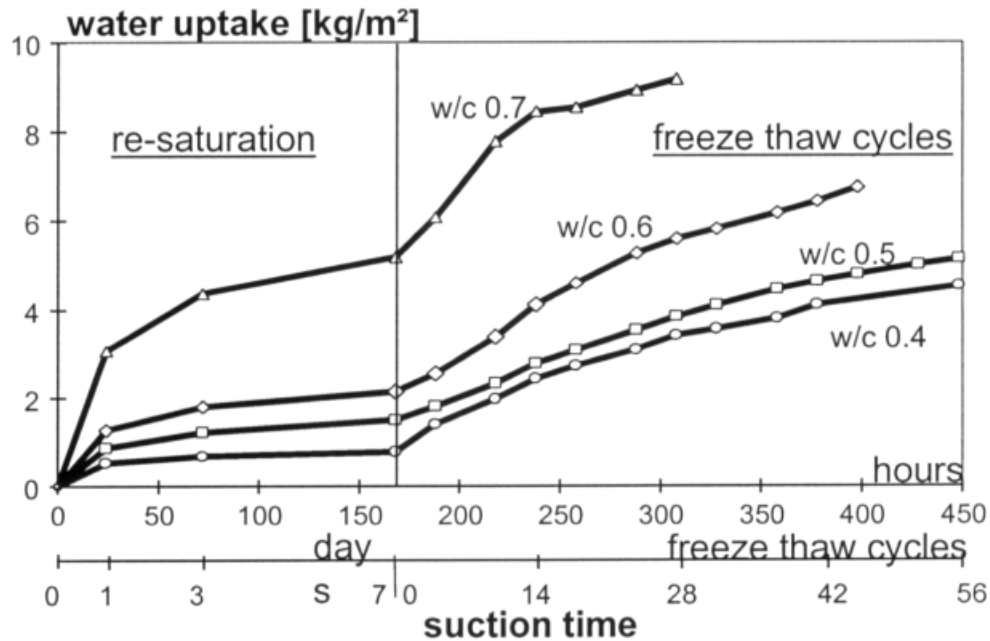


Figure 6. Water uptake during CIF test. The suction time is in hours - upper scale. The second scale shows the time in days for isothermal capillary suction - left part - and the number of freeze thaw cycles (2 per day) - right part. (Reprint from [5])

1. The expansion of ice: It creates hydraulic pressures. Water is squeezed out and the matrix is damaged. However, this type of damage is only relevant if a critical degree of saturation is reached.
2. This effect is preceded by an artificial saturation during a freeze thaw cycle caused by surface interaction of the pore water with the matrix. Extremely high negative pressures are generated in the unfrozen pore water. It is squeezed out. It is trapped at the ice particles that are called micro ice lenses. Additionally, the matrix is not infinitely rigid. Therefore, micro ice lenses act as a micro pump.
3. If a critical degree of saturation is reached damage occurs within a few cycles.

Therefore, cyclic freezing is most important for the saturation process. This must be taken into account in freeze thaw testing as already done e.g. in CDF / CIF test [14,15].

The effect of dissolved salts is superimposed linearly. If the concentration is moderate the effect will modify the results to a minor degree. The model of the micro ice lens pumping still works - as is seen from experimental findings. Nevertheless, the model must be refined. This must include the change of surface interaction. Analysis of experimental results [5,13] suggest that by this changed interaction heterogeneous nucleation in the pores is suppressed and percolation, therefore favored. Due to this the author would like to suggest the term pagophilicity for ice-attracting and pagophobicity for ice-repelling according to hydrophilicity and hydrophobicity (Pagos is the Greek name of ice). These surface effects strongly affect the mechanism leading to ice formation - heterogeneous nucleation and percolation. Dissolved salts change pagophobicity. On the other hand with dissolved salts chemical reactions occur changing the matrix.

6. Acknowledgement

The support of DFG - German research foundation - is acknowledged.

7. References

1. Setzer, M.J.: Micro Ice Lens Formation. In: Pore solution in hardened cement paste (Wittmann, Setzer, Adolphs eds.) Proceedings of the 3rd Int. Bolomey workshop. AEDIFICATIO, Zurich 1999
2. Setzer, M.J. (1999) Micro ice lens formation and frost damage. Minneapolis Workshop on Frost Damage in Concrete, edited by D.J. Janssen, M.J. Setzer, and M.B. Snyder, RILEM, pp. 1-15.
3. Setzer, M.J.: Micro Ice Lens Model, Freeze thaw saturation and testing. Int. Journal for restoration of buildings. 1999
4. Setzer, M. J. (1977): Einfluß des Wassergehaltes auf die Eigenschaften des erhärteten Betons. Schriftenreihe DASTb. Heft 280, 43-117
5. Auberg, R.; Setzer, M.J.: Influence of water uptake during freezing and thawing. In [21] p. 232-245
6. Setzer, M.J.: Basis of testing the freeze thaw resistance: surface and internal deterioration. in [21] p 157
7. Setzer, M.J.; Auberg, R. eds.: Frost Resistance of Concrete RILEM Proc. 34. Spon, London 1997.
8. Setzer, M.J.; Auberg, R.; Palecki, S.: Non-destructive testing of internal damage of concrete caused by frost attack. This proceedings
9. Landau, L.D.; Lifshitz, E.M: Lehrbuch der theoretischen Physik - Vol.: V Statistische Physik. Akademie. Berlin 1966
10. Defay, R.; Prigogine, I.; Bellemans, A.; Everett, D. H. (transl.): Surface tension and adsorption. Longmans, London. 1966
11. Stockhausen, N., Setzer, M.J. (1980): Anomalien der thermischen Ausdehnung und Gefriervorgänge in Zementstein. Tonindustrie Zeitung **104/2**, p. 83-88
12. Stockhausen, N.: Die Dilatation hochporöser Festkörper bei Wasseraufnahme und Eisbildung. Dis. TU München 1981
13. Auberg, R.: Zuverlässige Prüfung des Frost- und Frost-Tausalz-Widerstands mit dem CDF- und CIF-Test. (Reliable testing of frost and frost-deicing salt resistance by CDF and CIF test). Ph.D. thesis, University of Essen, Shaker publ. Aachen (1998)
14. RILEM Recommendation, RILEM TC 117 FDC: (1996) CDF Test- Test Method for the Freeze-Thaw Resistance of concrete with sodium chloride solution. Materials and Structures Vol. 29, p. 523-528
15. Setzer, M.J.; Auberg, R.: CIF-Test - Method for Testing the Resistance of Concrete against frost. (Capillary suction, Internal damage and Freeze thaw test). Betonwerk und Fertigerteiltechnik - Concr. Precast. Plant, 4 (1998) 94-106, and this workshop.

Chemical Deterioration of Concrete Constructions in Riga

Silvija Igaune, Yanina Setina, Inta Vitina, Uldis Cielens
Riga Technical University, Institute of Silicate Materials, Latvia

1 Introduction

Most of all bridges and by-passes in Riga are constructed after World War II and they are made from prefabricated reinforced concrete elements.

Roads and bridges are treated with rock salt or salt solutions as a de-icing measure in frosty weather in the winter in Latvia. The amount of salt used for by-passes depends on the severity of the winter and varies from 6-7 kg/m² all season.

In many buildings and reinforced constructions (bridges, by-passes, tunnels) everybody can see cracks, white or brown salt run off, carbonation of concrete and steel corrosion. To prevent these phenomena it is necessary to carry out investigations to solve the problems of corrosion, and conservation and restoration of concrete and reinforced concrete.

As it is known deterioration of concrete dependence on many factors: aggressive substances, including water, which penetrate through the surface and accumulate in the outer concrete layer and penetrate further into the bulk of the concrete /1-4/.

There are really three basic mechanisms to consider:

1. Physical deterioration, e. g., freeze thaw action including de-icing salts and the restraining effects of thermal gradients, cracking, abrasion and wear, or salt scaling due to recrystallization of salts in the pores where the expansion pressure of crystal growth leads to surface scaling of concrete and reducing the quality and strength.
2. Chemical deterioration, i. e. concrete reacting with the surrounding media causing either expansion of the concrete leading to cracking and spalling (alkali-silica reaction or sulphate attack) or dissolution and disintegration of the cement paste which binds the fine and coarse aggregates together.
3. Electro-chemical deterioration, i. e. corrosion of steel reinforcement having been de-passivated either by carbonation or chloride contamination of the both /5-7/.

In order to investigate the corrosion of concrete and reinforced constructions about forty samples of 3 Riga bridges were taken as cores from different places and analysed.

As the most interesting object from corrosion aspect we chose the viaduct across Daugavgrivas street. The viaduct is an extension of Vanshu bridge across the river Daugava and is located on the left side of the river.

It is built in 1981 and is made from prefabricated reinforced concrete elements, the surface is overlaid with rolled asphalt. In this viaduct everybody can see all corrosion processes of reinforced concrete.

In fact the main reasons for deterioration of concrete in service life are water, salt solutions and change of temperature.

For investigations of these processes samples of various substances were taken in different places:

- water from pits in asphalt,

- salts run down from the surface of pile and cross beam,
- white and brown stalactites,
- disintegrated concrete from beam,
- cores of concrete from the end of beam,
- cores from the driving part of the viaduct .

Cores were taken with 57 mm diameter with a diamond coring rig near the joints for determining of water soluble salts and carbonation.

2 Methods

Water soluble salts were analyzed by the following wet chemical method /8/:

- Na⁺, K⁺ by flame photometric method,
- Cl⁻ by volumetric titration with AgNO₃, indicator K₂Cr₂O₄,
- SO₄²⁻ by gravimetric method with BaCl₂,
- CO₂ by Dietrich- Frieling method,
- Fe₂O₃ by colorimetric method, dissolving the sample in HCl.

Average value standard deviation for all determinations is $\pm(0,01 \div 0,05 \text{ weight}\%)$.

3 Results and discussion

3.1. Results of chemical analyses of polluted water

It was established that the surface of rolled asphalt was covered with a network of cracks that had developed near the joints.

The water probes were taken in March at thaw time from pits ($\approx 200 \times 200$ mm and 30-60 mm in depth) in asphalt near the joints.

From the table 1 it is seen very high content of sodium chloride (6-8 g/l) in de-icing water which causes corrosion of concrete.

Table 1. Results of chemical analyses of de-icing water

Number of probes	K ⁺ , weight %	Na ⁺ , weight %	NaCl, weight %	NaCl, g/l
1	0,010	0,278	0,73	7,3
2	0,015	0,300	0,79	7,9
3	0,011	0,245	0,64	6,4
4	0,006	0,300	0,79	7,9

3.2 Chemical analyses of run down salts and stalactites

Chemical analyses show that run down salts and stalactites contain mainly CaCO₃ with small Na⁺ (0,06-0,18 weight %), K⁺ (0,02-0,04 weight %) and Cl⁻ (0,18-0,31 weight %) amount, but the brown stalactite samples contain 39,5 % Fe₂O₃.

It is suggested that poorly sealed joints allow water and salts to penetrate into the concrete and therefore are essential factor which promotes deterioration of the concrete.

Over a period of time cracking develops probably due to a number of causes including traffic stresses, thermal expansion and frost action.

Water then penetrates into these cracks, mostly during the winter simultaneously carrying de-icing salt in.

CaCO₃ is formed on the surface of concrete as the result of water migration by washed of Ca(OH)₂ from concrete which reacts with CO₂ in the air.

Reducing pH from 11-12 to 8 causes concrete carbonation which leads to the steel corrosion, and it is confirmed by the presence of a great content of Fe₂O₃ (39,5 %) in stalactites.

When the concrete surface has been covered with thick and dense carbonation layer, the risk of reinforcement corrosion is minimized /9/.

On the other hand, if dry concrete is carbonated by the ingress of CO₂, the passivation layer on the reinforcement can be destroyed and corrosion increases

Chemical analyses of concrete

3.3 Chemical analyses of disintegrated concrete from the cross beam

Concrete of the cross beam is cracked, covered with white and brown salts. Pieces of concrete easily separate from the beam exposing the corroded reinforcing steel and therefore they are danger for the pedestrians.

The results of chemical analyses of samples 14, 15, 16 in table 2 and figure 1 show very high content of sodium chloride (Cl⁻ 0,5÷0,7 %) and CO₂ (6÷18 %).

The found out amounts of chlorides and carbonation above the critical limit cause total de-integration of reinforcement.

Table 2. Results of chemical analyses of concrete

Nr	Na ₂ O eq. %	Cl, w. %	NaCl, w. %	CO ₂ , w. %	[SO ₄] ²⁻ , w. %	pH	Depth mm
14	1,047	0,50	1,19	18,57	0,36	9,24	0-10
15	0,396	0,55	0,91	10,12	0,76	8,88	10-20
16	0,455	0,72	0,82	10,12	0,57	10,08	20-40

Chloride based salts provide a serious risk of local pit corrosion of the bars when chlorides in sufficient quantities reach the reinforcement. If the salt contains alkali- metal ions, it enters the concrete and thereby increases the total alkali content with added risks of alkali-aggregate reactions if the concrete contains reactive aggregates /9/.

As a de-icing agent, salt causes a freezing shock to the surface layers when the ice is forced to thaw. The results may be temperature induced scaling, delamination and crumbling of the concrete surface.

These structures that are subjected to de-icing salt applications after a certain period of exposure to exhibit signs of distress due to ingress of chlorides and the corrosion of the reinforcing steel. This becomes apparent with the formation of cracks, frequently accompanied by rust staining and spalling of concrete.

All major deterioration mechanisms require sufficient amounts of water. Chloride based salts are some of the most harmful chemicals to which concrete can be exposed. Chlorides may lead to serious pit corrosion wherever they reach the reinforcement in sufficient quantities. De-icing salts cause freeze shocks of the exposed frozen concrete surfaces, which may damage the concrete.

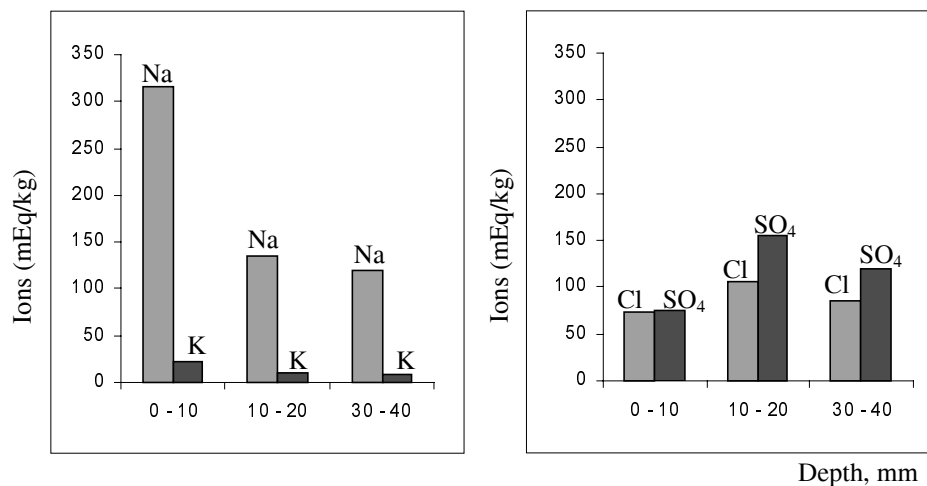


Figure 1. Content of Na^+ , K^+ and Cl^- , SO_4^{2-} ions in disintegrated concrete samples from cross beam.

3.3.2 Analyses of concrete cores from the end of cross beam

Concrete cores are taken from the end of the cross beam at 40 mm depth.

Concrete is crumbly because coarse aggregate easily separates from concrete. In our opinion it is the case of physical deterioration. The de-icing salt solution causes a freezing shock due to recrystallization of salt in the pores.

Table 3 Results of chemical analyses of concrete from the end of the cross beam

Nr	Na_2O eq. %	Cl^- , w. %	NaCl , w. %	CO_2 , w. %	$[\text{SO}_4]^{2-}$, w. %	pH	Depth mm
17	0,068	0,36	0,59	6,42	0,26	11,19	0-40
18	0,086	0,13	0,21	4,05	0,23	11,49	0-40
19	0,091	0,17	0,28	5,28	0,32	11,57	0-40
20	0,013	0,21	0,34	6,69	0,320,	11,40	0-40

As the result the expansion pressure of crystal growth increases which leads to concrete damage. Nevertheless as these places are under the rain the Cl^- ions have been washed away and its concentration is not so dramatically high in these places.

3.3.3 Chemical analyses of concrete cores from the driving part

The concrete cores were taken from the driving part of the viaduct at full 280 mm depth through the concrete slab after the asphalt layer was taken off.

Concrete is hard, reinforcing steel is in a good condition.

Table 4. Results of chemical analyses of concrete cores from driving part

Nr	Na ₂ O eq. %	Cl ⁻ , w. %	NaCl, w. %	CO ₂ , w. %	[SO ₄] ²⁻ , w. %	pH	Depth mm
21.1	0,101	0,08	0,23	2,64	0,23	11,32	0-30
21.2	0,099	0,06	0,18	3,78	0,24	11,32	30-60
21.3	0,121	0,05	0,15	3,43	0,33	11,79	200-250
...
22.1	0,106	0,07	0,20	4,22	0,29	11,70	0-30
22.2	0,095	0,10	0,29	3,08	0,26	11,84	30-60
22.3	0,134	0,21	0,61	4,49	0,29	11,70	250-280

Content of sulphates comprises SO₃ from cement.

Results of analyses table 4 and figure 2 show that there are no expressed indications of corrosion except at the bottom of the cores (exactly over the street) where increased amount of sulphates (due to polluted air from transport exhausts) and chlorides (due to run down water) are observed.

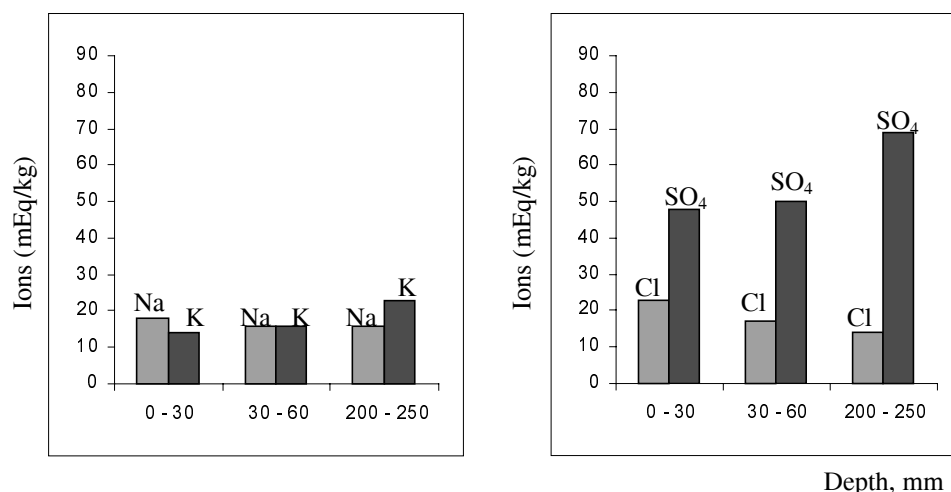


Figure 2. Content of Na⁺, K⁺ and Cl⁻, SO₄²⁻ ions in concrete samples from driving part.

4 Summary

Investigations show that degradation of concrete and reinforced concrete of the viaduct of Vanshu bridge in Riga is the result of sodium chloride attack (Cl⁻ 0,5-0,7 weight %) and carbonation (CO₂ 6-18%) and decrease of pH from 12 to 8,8. This deterioration includes traffic stress, thermal expansion and frost action. The service life of the construction depends on aggressive substances - water and salt solution which penetrate and accumulate in the concrete, causing further corrosion of steel.

5 References

1. S. Diamond, 9. Int. conf. on alkali-aggregate reaction, Kyoto, 1989, 83-94.
2. A. Poole, Pr.11. Int. conf .on alkali-aggregate reaction, London, 1992, 9-15.
3. G. West , Alkali-aggregate reaction in concrete roads and bridges. , London, 1996, p. 157..
4. W. Breit, Concrete Precasting Plant, 1998, 37-45.
5. J.M.Obrecht, R., R. Galli, P. Zimmermann, Intern. J. for Restauration of Buildings and Monuments, 1997, 3, 457-467.
6. W.J. Carter, H. Ezirim, M. Emerson, Magazine of Concrete Research, 1992,.44, 31-37.
7. St. Rostam, Construction and Building Materials, 1996, 10, 407-421.
8. European Standard EN 196, Part 2.
9. P. Lunk, Intern. J. for Rest. of Buildings and Monuments, 1998, 4, 399-422.

Influence of interfacial effects on the determination of dielectric properties of cement paste

Maricruz Alonso*, Carmen Andrade*, Michel Keddam**, X. Ramón Nóvoa, Hisasi Takenouti**

Universidade de Vigo. E.T.S.E.I.M., Lagoas-Marcosende, 9, 36280 Vigo, Spain. (rnovoa@uvigo.es)

* Institute of Construction Sciences "Eduardo Torroja". CSIC. Apdo. 19002, Madrid, Spain.

** Université Pierre et Marie Curie, UPR15 CNRS, 75252 Paris Cedex 05, France.

1 ABSTRACT

The present study analyses the impedance of cement paste specimens previously oven-dried or conditioned at 50% and 100% RH, in order to calculate their dielectric constant, ϵ . The results show that when oven-dried the cement paste has an almost perfect capacitive behaviour with reasonably low ϵ values. However, when the cement paste contains a certain amount of moisture, the shape of the Impedance Spectroscopy, IS, diagram changes significantly and, according to the literature, abnormally high ϵ values are obtained. These changes are interpreted in terms of some bulk and interfacial phenomenon. Appropriate electrical insulation of the electrode/paste interface by means of polyester sheets allows obtaining reasonable ϵ values for moisten specimens and to advance in the identification of the phenomenon defining the shape of the obtained IS diagrams.

Keywords: Dielectric Properties, Cement Paste, Concrete, Impedance Spectroscopy.

2 INTRODUCTION

The study of the electrical properties of concrete is recently attracting interest. Thus, several authors [1-3] indicate that some features of concrete microstructure, as porosity, may be studied by means of AC techniques as Electrochemical Impedance Spectroscopy (EIS). However, the moisture content [4, 5] and degree of hydration [6, 7] have been studied in the past by means of single high frequency perturbation. These studies tried to calculate the dielectric constant of the concrete in order to correlate this parameter with the amount of free water in pores. Frequencies in the range 10^9 to 10^{12} Hz were used in these studies.

For years no more attention has been paid to AC techniques, perhaps due to the complexity of the equipment needed for testing. Only scientists working in the field of rebar corrosion [8-10] identified some kind of response in the high frequency range (beyond 10 kHz) which was attributed either to the concrete/steel interface or to the concrete itself.

As recently mentioned, some other authors [1-3] have published results claiming for the possibility to characterise the concrete/steel interface by means of modelling the high frequency response in the impedance spectrum. These authors find abnormally high dielectric constants for concrete that is attributed to tortuosity effects [11] or to a fractal geometry [12]. The fractal geometry is also used to explain the depletion of the capacitive arc observed at

frequencies above 100 kHz [13]. Nevertheless, the identification of the amount of voids in a solid material by means of IS seems very unlikely. This electrical method is based in its ability to polarise the charged particles or species, not to identify the degree or type of porosity of solid materials [14], unless they are filled with a conducting fluid. Only porous metallic materials give an identifiable response when studied by IS [15]. What seems more reasonable is the old attempt of characterising water content in the pores, as water induces a dramatic change in the dielectric constant of insulating materials [6]. In a recent paper by the authors [16] it has been shown that the abnormally high dielectric constants found, appear to be due to the use of an unsuitable electrical analogue model to interpret the experimental Impedance Spectra. Thus, single R-RC randles circuits are used to fit results that, in fact, show more than one time constant. In the present paper more results are presented that confirm previous findings, and some hypothesis are advanced to physically describe the more likely processes inducing the observed type of behaviour.

3 EXPERIMENTAL

3.1 Specimens

Cement paste of w/c ratio equal to 0.4 was cast in moulds of 4x4x16 cm and cured in atmosphere having RH>95% during 24 hours. Afterwards the specimens were held in plastic bags until testing, in order to avoid premature drying. Before testing the specimens were cut in slices of 1 cm thick. They were then abraded until obtaining perfect plain parallel specimens down to 0.35 cm thick. The specimens were then conditioned at different ambient humidity. However, due to the aim of the present paper, only the results at relative humidity $\approx 100\%$, $\approx 50\%$ and $\approx 0\%$ will be discussed. These testing conditions correspond respectively to damp, dried at room temperature, and one-hour oven drying at 150°C. The specimens were pressed between the two graphite plates in order to avoid air gaps at the specimen/graphite interface. The electric field was applied between these flexible graphite plates. In order to avoid any interfacial phenomena, some trials have been performed introducing in the specimen/graphite interface polyethylene sheets of 100 μm thick, as shown in figure 1.

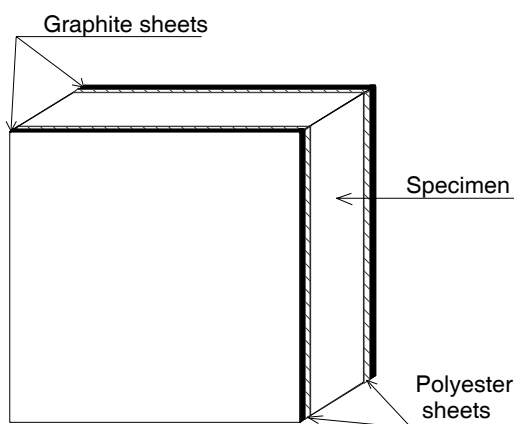


Figure 1. Schematic representation of the Electrode arrangement employed for impedance measurements. Polyester sheets are removed in some experiments.

3.2 Technique and Equipment

Impedance measurements were performed using the two-electrode arrangement depicted in figure 1. This measuring cell was directly wired to a HP-4194A Impedance/Gain-Phase Analyzer. This apparatus allows measuring capacitance in the range of 10^{-14} F to 0.1 F having a maximum resolution of 10^{-16} F.

3.3 Data Processing

As a first approach, the impedance data have been modelled using the impedance function, Z , defined in equation 1 that corresponds to the circuit in figure 2:

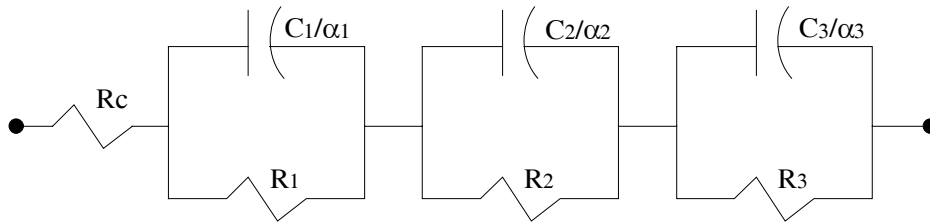


Figure 2. Equivalent circuit used to fit the different experimental impedance data. α_i characterises the dispersion of the R_iC_i time constant.

$$Z = R_c + \sum_{i=1}^3 \frac{R_i}{1 + (j\omega R_i C_i)^{\alpha_i}} \quad (1)$$

In equation 1 R_c accounts for the contact resistance, $j = \sqrt{-1}$, $\omega = 2\pi f$ and α_i is the degree of dispersion of the time constant R_iC_i [16]. $0 \leq \alpha_i \leq 1$. Obviously, the number of time constants R_iC_i chosen to fit the impedance data depends on the corresponding shape of the Nyquist or Bode plots. The fitting procedure employed was described elsewhere [17].

4 RESULTS

Figure 3 shows the impedance spectra of the oven-dried specimens (1h at 150 °C) with and without polyester sheets in Nyquist and Bode plots. It may be noticed that the use of the polyester sheets does not modify the response. This confirms the need of moisture to develop the kind of interfacial phenomena previously reported [16]. Only at frequencies higher than 10^7 Hz, it may be noticed the appearance of another time constant when no polyester sheet is introduced (see Bode plot) that perhaps may be linked to small amounts of water not removed by the oven treatment. The fitting of an R_0 - R_1C_1 electrical model into these results gives the values shown in Table 1. The ϵ value obtained from the data in Table 1 seems reasonable for a ceramic material. It is close to 7.3, the ϵ value found in [16].

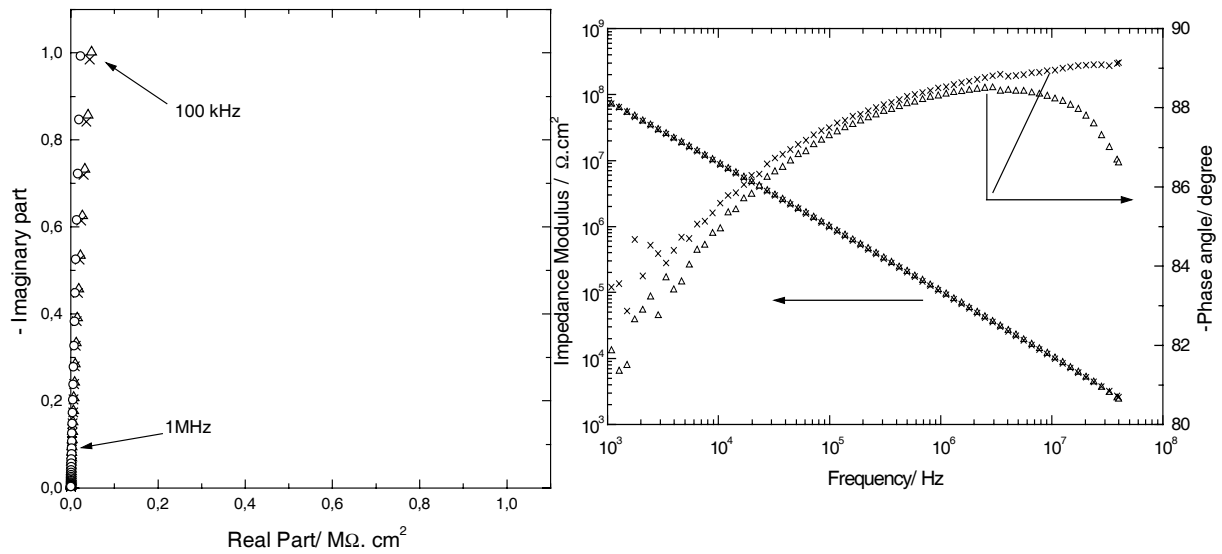


Figure 3. Nyquist (3a) and Bode (3b) plots corresponding to the impedance spectra obtained from the oven-dried specimen using two different experimental set-ups: Δ : using a direct contact between graphite electrodes and cement paste. x : including a polyester sheet between the graphite electrodes and the cement paste. The contribution of the series impedance corresponding to the polyester sheets has been mathematically eliminated. In figure (3a) the points (\bullet) correspond to the fitting of data (x) using parameters in Table 1.

Table 1. Best fitting parameters for the impedance spectrum (x) in figures 3 and 4 according to equation 1. From the C_1 value and the dimensions of the test specimen, it results $\epsilon = 9.1$, 75.9, and 93.3, respectively for data in figures 3, 4 and 5.

	R_0 ($\Omega.cm^2$)	R_1 ($\Omega.cm^2$)	C_1 (pF/cm^2)	α_1	R_2 ($\Omega.cm^2$)	C_2 (nF/cm^2)	α_2
Figure 3	0.5	1.10^{25} (fixed)	2.3	0.986	–	–	–
Figure 4	0.1	4185	19.2	0.718	1.10^{25} (fixed)	61.6	0.877
Figure 5	54	1531	23	0.756	1.10^{25} (fixed)	39.2	0.90

Figure 4 shows the same specimen as in figure 3 but after some hours at ambient RH, that is with a certain small amount of moisture. Again, the impedance spectra are obtained with and without polyester sheets. In the case of direct contact between metal and paste, it can be observed in the Bode plot the clear existence of several time constants, which however reduce to only two when the interface is isolated by the polyester sheets. The time constant at the lowest frequencies is attributed to the capacitance of the double layer on graphite electrodes when no polyester sheets are used.

The fitting of an $R_0 - R_1C_1 - C_2$ electrical model to the response with polyester sheets gives the parameters in Table 1. To fit the impedance spectrum without polyester sheets (data (Δ) in figure 4), three time constants have been used in equation 1. The results are similar to those in Table 1, but including the third time constant with C_3 values in the μF range. Again, the ϵ value obtained from C_1 seems reasonable thinking that now moisture partially fills the pores of the paste.

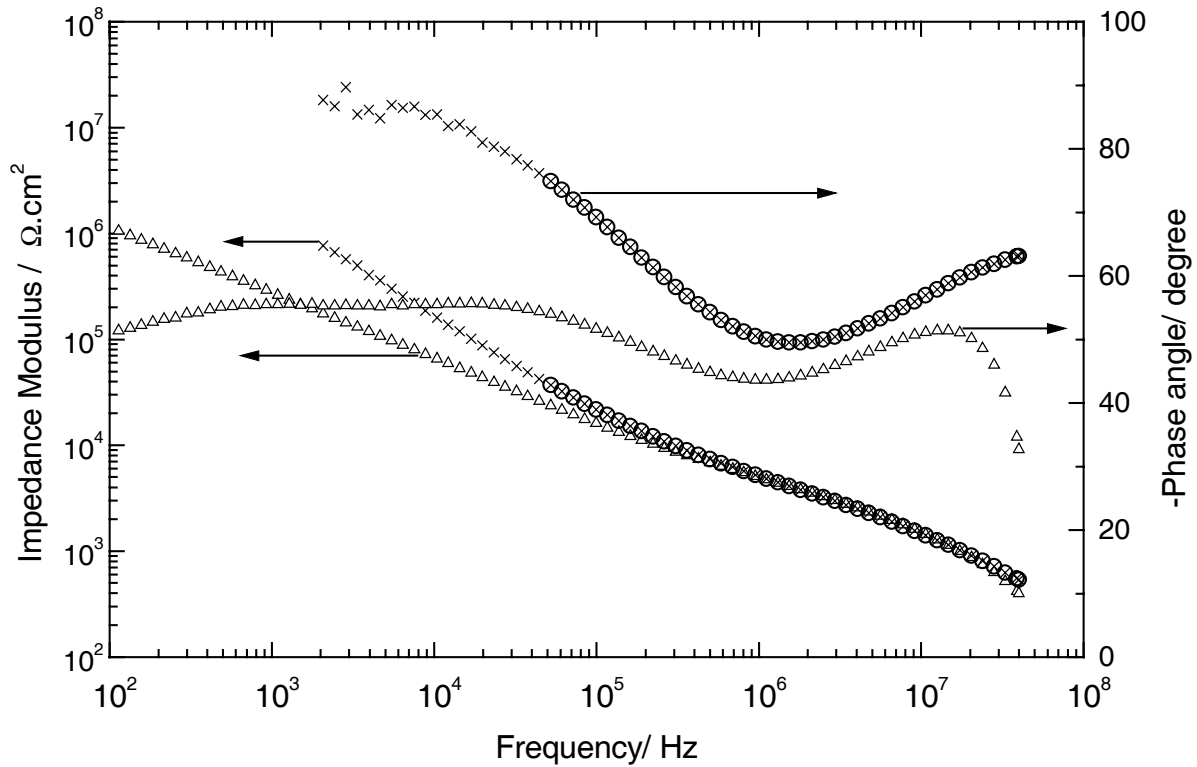


Figure 4. Bode plot corresponding to the impedance spectra obtained from the specimen exposed to ambient RH using the same experimental set-ups and symbols as in figure 3. The points (o) correspond to the fitting of data (x) using the parameters in table 1.

Figure 5 shows the results of the water-saturated specimen with and without polyester sheets between graphite electrodes. Now, the change is dramatic, and an apparently single depressed semicircle appears when the graphite is in direct contact with the moist paste, whereas this loop almost disappears remaining only the part at the highest frequencies when the interface is isolated by the mylar sheets. It seems then clear that some interfacial phenomena develop when a polarizable metal contacts the paste. These phenomena are more pronounced as higher is the moisture content. The fitting of an electrical analogue $R_0 - R_1C_1 - R_2C_2$ to the water saturated specimen isolated with polyester sheets gives the values in table 1. ϵ increases again due the higher moisture content in the specimen but remains in the range of reasonable values, three orders of magnitude lower than the values obtained using C_2 as the dielectric capacitance of the system. If no polyester sheets are used to isolate the interface then errors of interpretation can arise when considering the high frequency loop in figure 5 as only one dispersed time constant giving a capacitance value close to C_2 in table 1.

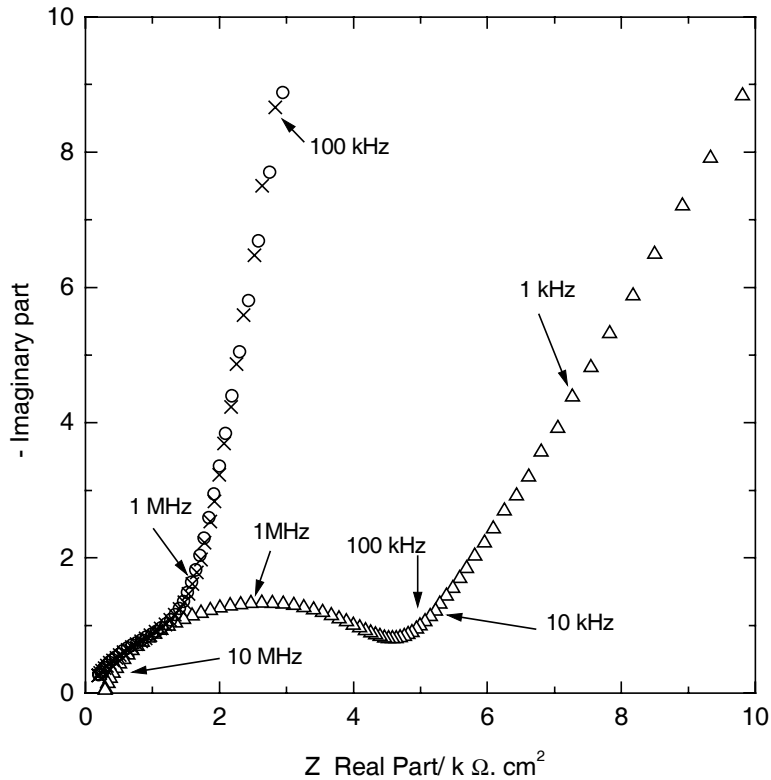


Figure 5. Nyquist plot corresponding to the impedance spectra obtained from the damp specimen using the same experimental set-ups and symbols as in figure 3. The points (o) correspond to the fitting of data (x) using the parameters in Table 1. The points (o) correspond to the fitting of data (x) using the parameters in table 1.

5 Discussion

The present results confirm the identification of three time constants in the scanned range of frequency: One in the region of beyond 1 MHz, with capacitances (C_1) in the range of pF/cm^2 that are associated to the dielectric behaviour of the cement phases. Another in the region of 1 MHz -100 kHz, with capacitances (C_2) in the range of nF/cm^2 that are attributed to the mobile carriers generated by the moisture increasingly filling the pores, as it will be discussed later, or more unlikely, to some screen charge/hopping charge effects. The last time constant found in the range of kHz, with capacitances in the range of $\mu\text{F}/\text{cm}^2$, typical of double layers (on the graphite electrodes).

The phenomena associated to the existence of mobile carriers, with or without screen effects towards the electrode are well described in the literature [19] although scarcely experimentally studied, due to the complexity of fitting reliable models to the results obtained. In the present case, the ionic content of pore water seems to be the most sensible assumption to justify them.

5.1 Behaviour without polyester sheets

The aspect of the Nyquist plot changes dramatically when water starts to wet the system. Other authors [1-3] have usually found this pattern. If a single R-RC circuit is used to fit the high frequency region, then the dielectric constant calculated results abnormally high.

However, if the observed depression is attributed to the existence of several relaxation time constants (in fact two time constants), then the calculated values of the dielectric constants become reasonable for a wet dielectric material.

Therefore, the depleted pattern of the Nyquist diagram in the present case has been attributed to the overlapping of three phenomena aiming in the three time constants aforementioned: the cement phases, the mobile carriers in the pore solution and the double layer of the metallic electrode. The intercalation of polyester sheets reduces double layer effects.

5.2 Behaviour with polyester sheets

Once minimised the interface with the metallic electrode, the shape of the diagram changes and only two time constants are observed for moisten specimens. The appearance of a semicircle in the Nyquist diagram when the moisture is increasingly filling the pores may be associated to a higher total conduction of the specimen. This behaviour may be modelled, following the Maxwell-Wagner theory on a conductive material encased in a dielectric one, as an electrical analogue of two Randles circuits. One of the circuits would correspond to the pores and the other, the cement phases.

When the specimen is perfectly dry it behaves as a quasi-perfect dielectric. However, as soon as the moisture fills the pores, a dielectric loss appears (the conduction through pores increases). The pattern of the graph will depend therefore on the ratio R_1/R_2 [18] that is on the total amount of free carriers moving in the pores with respect of those in the solid phases. In addition to this trend, it can be observed that the Nyquist plot is very distorted or depleted (α values lower than 1), suggesting a certain deviation from pure Debye model. Whether this deviation is due to the existence of multiple relaxation time constants caused by some additional screen effects of the electrodes or simply it comes from the aforementioned particular R_1/R_2 ratios needs further clarification.

5.3 Ionic conduction

The hydrated cement paste, in addition to the calcium silicate hydrate gel and other solid phases, contains a variety of voids that exert an important influence on the cement properties. Concerning the electrical properties, the water filling this voids or pores can dissolve ionic species (mainly Ca^{2+} and OH^-) from the solid phases resulting in some ionic conduction through the interconnected capillary pores. However, the ability of water to dissolve ions will depend largely on its "state" inside the pores. Water in larger pores (grater than 50 nm) may be considered as "free" water [20] and the chemistry in this phase will be different to that corresponding to water in smaller capillaries (5 to 50 nm) where water is held by surface forces of the paste particles ("adsorbed" water). Part of the water held between the surfaces of certain planes of the $\text{CaO} \cdot \text{SiO}_2 \cdot \text{H}_2\text{O}$ structure by hydrogen bonding and called "interlayer" water, will have also a different chemistry, and different to that corresponding to the "linked" water which is chemically bonded to form the cement hydration products. The differences in water activities leads to the existence of ionic concentration gradients between pore wall and pore inside acting as the main driving force for diffusion of ions between the bulk and pore wall. Under this assumption, the model describing the AC behaviour of the tested specimen should include, in addition to the R_1C_1 time constant corresponding to the dielectric characteristics of the system, the diffusion impedance due to the ionic displacements between bulk and pore wall. Equation 2 accounts for such model. The diffusion impedance, Z_D ,

considers that the ionic carriers are blocked at the interfaces [19], in this case pore walls and polyester sheets. R_D corresponds to the diffusion resistance and τ_D is the average time constant of the diffusion processes. The quality of the fitting of data in figures 4 and 5 is similar using equation 1 or equation 2. The results using equation 2 are given in table 2.

$$Z = R_0 + \frac{R_1}{1 + (j\omega R_1 C_1)^{\alpha_1} + (R_1/Z_D)} \text{ being } Z_D = R_D \frac{\coth \sqrt{(j\omega\tau_D)^{\alpha_D}}}{\sqrt{(j\omega\tau_D)^{\alpha_D}}} \quad (2)$$

Table 2. Parameters fitting the impedance spectra in figures 4 (ambient RH) and 5 (damp) according to equation 2 From the C_1 value and the dimensions of the test specimen, it results $\varepsilon = 26.5$ and 45.9 , respectively for ambient RH and damp conditions.

Condition	R_0 ($\Omega \cdot \text{cm}^2$)	R_1 ($\Omega \cdot \text{cm}^2$)	C_1 (pF/cm^2)	α_1	R_D ($\text{k}\Omega \cdot \text{cm}^2$)	τ_D (μs)	α_D
Ambient	40	1013	6.7	0.867	12.3	0.68	0.856
Damp	99	424	11.6	1.0	3.5	0.55	0.888

Even “reasonable”, the ε values given in table 1 for humidified specimens can be considered high for a system that is not 100% water. The ε values obtained now from C_1 data in table 2 seem to be more consistent with a porous structure in which pores (totally filled with water in damp specimens) represent 28% of the total volume of the hydrated paste [21]. However, the difference is purely formal. It comes from the fact that equation 1 considers a series arrangement of C_1 and C_2 while in equation 2 C_1 is in parallel with Z_D .

Using the τ_D values given in table 4 and assuming an average diffusion coefficient, D , of $10^{-5} \text{ cm}^2 \text{ s}^{-1}$, the characteristic length of diffusion, δ , can be obtained: $\delta = \sqrt{\tau_D D} = 23$ to 26 nm . These values fall in the domain of the capillary voids for hydrated cement paste [20].

6 Conclusions

The results above discussed permit to conclude that: A) The oven dried cement paste presents an almost perfect dielectric behaviour with a single time constant. The capacitance found is typically in the pF/cm^2 range. B) The moisture filling the pores behaves as mobile carriers that induce a second time constant with a capacitance in the nF/cm^2 range. C) When the electrode is in direct contact to the moistened cement paste, a third time constant appears in the range of $\mu\text{F}/\text{cm}^2$. D) If a single Randles circuit is used to fit the experimental results, abnormally high values of the dielectric constant are calculated. However, when the results are modelled using of two or three time constants, reasonable results are obtained for the capacitance values.

7 References

- [1] B.J.Christensen, R. T. Coverdale, R.A. Olson, S.J. Ford, E.J. Garboczi, H.M. Jennings, T.O. Mason, J. Am. Ceram. Soc., 1994, 77, 2789-2804.
- [2] P. Gu, Z. Xu, P. Xie, J.J. Beaudoin, Cem. Concr. Res., 1993, 23, 531-535.

- [3] Z. Xu, M. Tang, J.J. Beaudoin, *Adv. Cem. Res.*, 1993, 5, 171-176.
- [4] P. Gu, P. Xie, Y. Fu, J.J. Beaudoin, *Cem. Concr. Res.*, 1994, 24, p. 92-94.
- [5] W.J. McCarter, S. Garvin, *J. Phys. D., App. Phys.* 22 (1989), 1773-1776.
- [6] F.H. Wittmann, F. Schlude, *Cem. Concr. Res.*, 1975, 5, 63-68.
- [7] K. Goner, M. K. Smit, F.H. Wittman, *Cem. Concr. Res.*, 1982, 12, 447-453.
- [8] D.E. John, P.C. Searson, J.L. Dawson, *Br. Corros. J.*, 1981, 16, 102-108.
- [9] C. Andrade, V. Castelo, C. Alonso, J. A. González, *ASTM STP 906*, ASTM, N. Y., 1986, p. 43.
- [10] A. Sagüés, *NACE-Corrosion '87*, paper #. 118, 1987.
- [11] B.J. Christensen, T.O. Mason, H.M. Jennings, *J. Am. Ceram. Soc.* 1992, 75, 939-945.
- [12] W.J. McCarter, *Adv. Cem. Res.*, 1994, 6, 147-152.
- [13] D. Buerchler, B. Elsener, H. Boehni, *Mat. Res. Soc. Symp. Proc.* 1996, 411, 407-412.
- [14] J. R. Macdonald, "Impedance Spectroscopy", Ed. J. Wiley, 1987, p. 201.
- [15] H. Keiser, K.D. Beccu, M.A. Gutjahr, *Electrochim. Acta*, 1976, 21, 539-545.
- [16] M. Keddám, H. Takenouti, X.R. Nóvoa, C. Andrade, C. Alonso, *Cem. Concr. Res.* 1997, 27, 1191-1201.
- [17] C.M. Abreu, M. Izquierdo, M. Keddám, X.R. Nóvoa, H. Takenouti, *Electrochim. Acta*, 1996, 41, 2405-2415.
- [18] J.M. Albella, J.M. Martínez, "Física de Dieléctricos", Ed. Marcombo, Barcelona, 1984, p. 118.
- [19] J. R. Macdonald, *Op. Cit.*, p. 56.
- [20] N.P. Mailvaganam, R.T. Hemmings, "Science of Concrete and Polymeric Building Materials". In "Repair and Protection of Concrete Structures". N.P. Mailvaganam Ed., CRC Press, 1992, p. 12.
- [21] F.M. Lea "The Chemistry of Cement and Concrete" Ed. Arnold, 1970, p. 27.

Exploitation of Marble Residues through Material Compound in a Polymer Matrix

Corpas Iglesias, Francisco Antonio [1], Codina Sánchez, Simón[1, Ruiz Román, José Manuel [2], García Cambronero, Luis Enrique [2], Ruiz Prieto, José Manuel [2], Alonso, Cristina [2].
[1]. Departamento de Ingeniería Química, Ambiental y de los Materiales. E.U.P Linares. Universidad de Jaén.
[2]. Departamento de Ingeniería de Materiales. E.T.S de Ingenieros de Minas. Universidad Politécnica de Madrid.

1 Abstract

In this work, we put forward the use of the marble residues, as the extraction process residues as the manufacture ones, through the material compound from a determined marble granulation over a polymer matrix.

With this propose, we have several epoxidic, acrylic resins and specific products of different manufacturers. These materials have been distinguished mechanical and microstructurally to compare them in a functional way.

KEY WORDS: Marble, Re-use, marble residues, compound materials

2 Introduction [1,2]

The residues coming from marble cut during its extraction and manufacture generate environmental impacts, which involves social and financial problems, too. From a chemical point of view, these residues are without toxic and harmful elements, being its main problem the suitable store. Only in the cut operation over 170 Kg of dry residue per cubic metre are produced in the marble.

The residues proceeding from marble production and Calcium Carbonate (CaCO_3) basically have the same utility, to use it as a dissolvent in order to the process for the re-use the lead in batteries, as a inert material in prefabricated materials in building, for paint making (where over a 30 % without changes in the viscosity, its possible to getting an improvement in the density and stiffness although the mechanical characteristic get worse.

The contents in MgO and SO^{-2} ions limit the potential use of marble in the concrete industry, dued the humidity's rate of the residues, so increases the energetic consumption, being necessary an evaporation through an previous and strong dried. Finally, the marble is used to reduce the emission of SO in the thermal centrals with a bedrock fluid, combustion system.

We want start an investigation line in order to increase the application range of this marble residues, particularly the decoration and building materials; and this way, we contribute to the production of environmental with impact and create its use.

3 Experimental Procedure

The following polymers are using to form the matrix of the white common marble compound (Macael white marble):

A	Bisphenol A Diglycidylether	Liquid
B	Epolam 2001	Liquid
C	Condufast	Solid
D	Specifast (Acrylic hot mounting resing)	Solid
E	Isofast (Dialyphtaete hot)	Solid

Firstable, we have prepared the white pulverising marble in a mechanical way, after a first sieved, and then, the mechanical pulverizing has been accelerated through a ball-mill. The material obtained in this way is classified in two granulations:

- Among 0.63 mm and 0.4 mm
- Less of 0.4 mm

Independently of experimented percentages of the polymer, in contradiction with the marble; we have made over 24 gr. of mixtures. These mixtures have been introduced into a 35-mm cylinder, using a thermal bore in the punch to get the control of the polymer temperature.

The temperature has been increased in a graded form using an external resistance until 50°C in the A and B polymers and until 130°C in the C, D and E polymers. Simultaneously, we have prepared the hydraulic material, make a pressure of 33 Mpa and consequently, we must readjust during the heating process in the marble and polymer readaptation.

Samples weighted (as are obtained with enviromental`s humidity) P_{amb} are introduced in a 110°C furnace to weigh them in a dry P and are weighted again after shortly introducing them into a water P_s . Finally, the samples are put into a tray during 56h. to be weigh again in water P_h . In this way, the apparent specific weigh, absorption coefficient and the absolute absorption are obtained.

Samples` machinery has been subjectively analysed by the sawed with metallic arc; the obtained sections have been filled away and polished to carry out the Knoop duress test trials over the surfaces of faces and rifling sections.

4 Results and Discussion

Polymers A and B are shown a liquid state onto two components, resin and stiffer, while the polymers C, D and E are shown with a determinated granulation in a solid state. It`s observed several problems in the polymers A and B in order to get some homogeneous mixtures, for heterogeneous areas have obtained in the proofs, else during the pressure in the progressive increment of temperature, a part of the resin fluid, through the punch and the base of the matrix, where, there`s no a good mixture between the resin and the marble. An increment of resin percentage has reduced the problem, but a larger amount of resin is wasted as a disadvantage, during the compaction phase.

Polymers C, D and E have got a best mixture than liquid polymers A and B, giving homogeneous mixtures in all used percentages, as well as there aren't loss of resin problems, during the compaction.

As a consequence of polymers A and B in a 56h water permanence, there were material losses (marble bad fixed in the polymer chains), which is a reason to put aside these resins at the moment. It's no possible the temperatures increment during the compression dued some limitations in the set of compaction with C and E resins.

We only have obtained compact samples with D resin, without some loss marble problems after the period of permanence under water.

4.1 Water absorption

Using the two granulation and with some different proportions, we have made 10 samples of D polymer (Acrylic) and we have obtained a small decrease of weigh after the furnace drying-up (110°C), from a 0.07 % of weigh, and a weigh gaining after a period of 2.62% of water. In the following table, values of an apparent specific weigh absorption coefficient (%) and water absorption (%), are shown:

Samples	Pa	Gs	Ga	Gh	p.e.a	coef. Abs. %	Absorption %
D4 10% - 0,4 %	23,504	23,493	25,112	25,28	139,839	7,607	10,637
D3 13% - 0,4 %	23,393	23,369	25,121	25,747	37,331	10,176	3,799
D 15% - 0,4 %	23,731	23,703	24,407	24,757	67,723	4,447	3,011
D2 17% - 0,4 %	23,735	23,712	24,458	24,84	62,073	4,757	2,953
D5 20% - 0,4 %	23,731	23,713	23,821	24,034	111,329	1,354	1,507
D8 23% - 0,4 %	23,57	23,558	23,588	23,823	100,247	1,125	1,128
D1 15% - 0,63 %	23,604	23,586	24,012	24,191	131,765	2,565	3,38
D6 17% - 0,63 %	23,364	23,347	23,752	23,887	172,941	2,313	4
D7 20% - 0,63 %	23,84	23,838	23,995	24,141	163,274	1,271	2,075
D9 23% - 0,63 %	23,844	23,829	23,896	24,06	145,299	0,969	1,409

4.2 Knoop hardness test

We used the UNE (22-188), for ornamental marbles and limestones, using a 100gr charge into the pyramidal deeper, with a 30 seconds performance period. We must consider the following things: the external surfaces of samples exposed to the matrix hot metal, show a larger proportionality of the resin polymer, in contradiction with the marble presence, and with a general homogeneous section of polymer/marble in samples. These considerations are widely noted when the resin and lower granulation samples (lower 0.4mm) increase.

In general terms, dates show smaller values than the pure polymer, after the test of the marble hard (DK = 57 Mpa) and the pure polymer (DK = 9 Mpa), because the density obtained is different in the polymer chains.

In the next table and graphic is observed the superficial duress where is shown that samples with a lower to 0.63mm and upper to 0.4mm granulation and with lower percentages to 15% have a clear lack of cohesion which is presented in the absence of superficial polymer and a impossibility of polish to make the microhardness test.

Samples	130°C	\bar{x}	σ	DK Mpa
D4	10% 0.4	1.560	0.1751	5,7304
D3	13% 0.4	1.406	0.0527	7,0544
D	15% 0.4	1.304	0.1829	8,2012
D2	17% 0.4	1.240	0.0848	9,0696
D5	20% 0.4	1.276	0.1241	8,565
8	23% 0.4	1,327	0,0883	7,9193
D1	15% 0.63	1.159	0.1252	10,3816
D6	17% 0.63	1.326	0.1262	7,9313
D7	20% 0.63	1.263	0.1372	8,7423
D9	23% 0.63	1,283	0,1188	8,4718

Along the section, the hardness shows a remarkable homogeneity in all samples. It's perfectly appreciated marble grains in opposition to the polymer with 57 Mpa marble duress and a superficial duress, for larger granulation samples (<0.63 and >0.4). In samples with a smaller granulation (0.4<), this effect is less appreciated, so when the deeper falls upon partially on the resin and as well as on marble grains, because there's a slightly increase of duress or there's no variation at the respect of the surface, having in account the deeper incidence.

5 Conclusions

In order to get compacted and homogeneous samples, liquid assayed polymers Bysphenol A Diglycidylether and Epolam 2001 don't show good attitudes, studying later the production conditions change to prove their applicability.

C and D polymers (Codufast and Isofast) must get a polymer under stricter conditions than used ones, as a consequence of obtained results under some possible pressures and temperatures of the polymer, with the set used in tests.

D polymer, named Specifast (acrylic hot mounting resin) in commercial terms, show good characteristics of use, noting a larger granulation (<0.63 and >0.4) and needing larger percentages of the polymer in order to keep the cohesion, with good results upper to 20% in comparison with good results upper to 15% in samples with a granulation lower to 0.4mm. It's observed a bad merchantability using lower percentages.

A superficial effect of a larger polymer is observed in a close dependence in used percentages, while these effects disappeared into the samples. Into these ones, some grains of marble are observed in the polymer matrix, with different microhardness with larger granulation samples and almost equal microhardness with lower granulation.

6 Bibliography

1. Ornamental Stones Manual. Severa Authors. E.T.S.I.I. of Mines. Madrid.
2. Llopis, L. Et. Al. "The Natural Stone and its Normalisation" VIII National Congress of Engineering Projects. Madrid, October 7-9
3. Rules UNE 22-182 and UNE 22-188
4. Products Catalogue.

Permeability of Bound Granular Covers

Fedde Tolman

Netherlands Pavement Consultants, Utrecht, the Netherlands

Lucas Jan Ebels

UWP Engineers, Umtata, South Africa

1 Introduction

Civil engineering structural elements have the primary functions of carrying loads or separating environments. In case of the separation function two environments, of either gaseous, liquid or solid nature, and a separating layer may be discerned. Separating layers may encompass a large range of dimensions and materials, e.g. paints and coatings, concrete covers on reinforcement, claddings, outdoor walls, dikes and dams. Typical civil engineering materials used for the separation function are cement or bitumen bound mineral aggregates and cohesive soils.

Fluids (liquids or gases among which vapors) or ions may enter the separation layer due to exposition to the environment and are then stored or passed through. This may result in a change in mechanical or transport properties of the materials constituting the separation layer or pollution of the receiving environment. The problem therefore may be thought to exist of three parts:

1. *transport* of fluids (gas or liquid), which is assumed to be a result of two mechanisms [1]:
 - convection (driving forces according to [1]: pressure gradient, capillary action and friction of in pores);
 - diffusion (driving force: concentration gradient).
2. *reactions* between the fluid and the solid which are assumed to be physical processes, a matter of precipitation and dissolving, or chemical-physical: reaction products precipitating or dissolving
3. *mechanical effects* which may be:
 - expansion and shrinkage possibly resulting in clogging of pores or creation of pores and cracks;
 - weakening and softening with effects on structural load carrying capacity or abrasion resistance.

Due to the mix of inter-dependending mechanisms of different nature a rather complex problem results.

The penetration of fluids or ions in or through separation layers can be characterized as a durability problem. The processes usually last long compared to human memory, transport processes are important and the damage is gradual but hard to reverse. The problems are increasingly important because of the ever increasing scale of the built environment. In this article this wide scope is limited to a theoretical formulation of the topics mentioned and a description of a test method on bitumen bound granular materials in layers of approximately 40 mm under small fluid pressures. These cases are especially relevant for floors as protection against soil pollution or as protection of the concrete structure below a pavement. Discussed

will be the physical modeling of the mentioned processes, the propagated test method and some considerations on structural application.

2 Theory

2.1 Transport

General

Civil engineering materials may be regarded to exist of:

- mineral particles, which are highly resistant to fluid transport;
- binder and interface layers between aggregate and binder layer, which are transporting or storing fluid depending on the materials involved;
- pores and cracks, through which usually most of the transport occurs;

The material moving in or through the separating layer will be called fluid and the material constituting the separation layer solid. Capillaries and cracks will be imagined as tubes in the solid. Closed voids and vacancies are considered to act as the solid.

Both the convection and the diffusion model are based on the balance equations for conservation of mass completed by constitutive equations and respectively the balance equation for momentum and a gradient equation. The general balance equation is:

$$\frac{\Delta r}{\Delta t} dx dy dz = -\frac{\partial F}{\partial x} dx dy dz + S \rightarrow \frac{\partial r}{\partial t} = -\nabla F + s \quad (1)$$

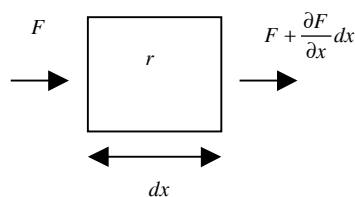


Figure 1. Uni-directional balance equation (Euler), F: flux, S:source, ∇ : $[\partial/\partial x, \partial/\partial y, \partial/\partial z]^T$

To solve the emerging differential equations boundary conditions (BC) have to be imposed. In this article two extreme BC will be discussed:

- absorption, i.e. no emission through the lower boundary;
- permeation, i.e. transmission through the separating layer without storage.

The first BC may be more easy to test in case of low permeability materials, while the second is often the most critical practical case. Independent of the convection or the diffusion model (or a combination of both), test results on one BC gives sufficient information for solving problems with other BC's.

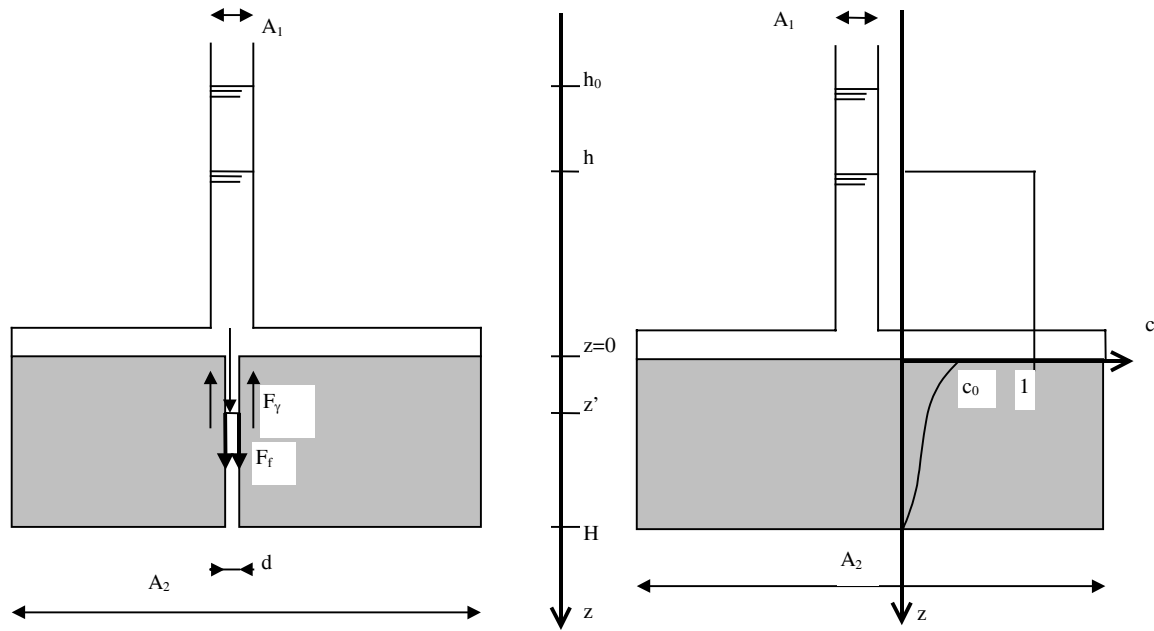


Figure 2. Schematization of possible test set ups for the convection and the diffusion model

Convection

Unidirectional flow due to capillary action (F_γ), gravity (F_g), and friction (F_f) results in an ordinary first order differential equation.

$$\alpha\gamma\pi d + \rho g \frac{1}{4} \pi d^2 (z' + h) - 8\pi\eta z' u' = 0 \quad (2)$$

With γ surface energy of the contact area between solid and fluid [J/m^2], d equivalent void diameter [m], ρ density [kg/m^3], g gravity acceleration [m/s^2], η viscosity [$\text{Pa}\cdot\text{s}$], h_0 level in gauge at $t=0$ [m], $h' = h_0 - h$, z' depth of fluid penetration [m], u' fluid velocity in the pore.

In case of *absorption* emission does not occur so $u' = dh/dt$, $\alpha = 1$ and (2) results in

$$h' \frac{dh'}{dt} - Ah' - B = 0 \quad (3)$$

$$A = \frac{\rho g (1 - k) k d^2}{32\eta} \quad (4)$$

$$B = \frac{4\alpha\gamma k^2 d}{32\eta} + \frac{\rho g k^2 d^2 h_0}{32\eta} \quad (5)$$

By definition $k = \pi d^2 / 4 A_2$. h' can not be written explicitly, but approximations for small and large times with the initial condition $h = h_0$ can be found

$$t = \frac{B}{A^2} \left(\frac{A}{B} h' - \ln \left(\frac{A}{B} h' + 1 \right) \right) \quad (6)$$

$$h'(t) = \sqrt{2B} \cdot t^{1/2} \quad (7)$$

$$h'(t) = A \cdot t \quad (8)$$

In case of *permeation* $k = A_1 / A_2$, $z = H$ and $\alpha = 0$ in case of outflow in fluid, or $\alpha = -1$ in case of outflow in air (more precisely in vacuum), resulting in

$$h' = \left(h_0 + \frac{B}{A}\right) (1 - \exp(-At)) \quad (9)$$

$$A = \frac{\rho g k d^2}{32 \eta H} \quad (10)$$

$$B = \frac{4 \alpha \gamma d + \rho g k d^2 H}{32 \eta H} \quad (11)$$

Diffusion

From the equations for concentration c of continuity $\frac{\partial c}{\partial t} = -\frac{\partial F}{\partial z}$ and transport according to Fick $F = -D \frac{\partial c}{\partial z}$ the diffusion equation with diffusion coefficient D (m^2/s), a second order partial differential equation of the parabolic type, results

$$\frac{\partial c}{\partial t} - D \frac{\partial^2 c}{\partial x^2} = 0 \quad (12)$$

In case of a constant concentration on one surface and no transport through the other surface (*absorption*) the boundary conditions may be formulated as $c = c_0$ and $F = -D \partial c / \partial x = 0$, resulting in [4]

$$c(t) = \frac{2}{H} \sum_{n=1}^{\infty} \frac{(2n+1)(-1)^n \pi D}{2H} \exp\left(-\frac{(2n+1)^2 \pi^2 Dt}{4H^2}\right) \cos\left(\frac{(2n+1)\pi(H-z)}{2H}\right) \int_0^t (c_0(t)) \exp\left(\frac{(2n+1)^2 \pi^2 Dt}{4H^2}\right) dt \quad (13)$$

h can be derived by integrating c over the volume. The first term ($n = 0$) and constant c_0 is approximately

$$h' = -\frac{8 c_0 H}{\pi^2 k} \left(1 - \exp\left(-\frac{\pi^2 Dt}{4H^2}\right)\right) \quad (14)$$

In case the concentration at one surface is constant and the flux is constant (*permeation*), the boundary conditions are $c = c_0$ and constant flux $F = -D \partial c / \partial x$, which results in

$$h' = \frac{D c_0}{k H} t \quad (15)$$

The diffusion model may especially be relevant in case the solid also has fluid-like properties, like visco-elastic materials (asphalt) or materials with pores that are filled with fluid.

2.2 Reactions

Examples of reactions from civil engineering materials are:

- reaction between carbondioxide from the air and carbonates in the concrete, resulting in lowering of the concrete pH
- alkali aggregate reactions and ettringite, which may result in cracking due to unequal expansion and restrains, and thaumasite reactions in concrete
- chloride diffusing and binding to the concrete pore-walls
- softening of the bituminous binder in asphalt due to diffusion of carbonhydroxides like gas and petrol and in laboratories methylene chloride or toluene

In the last case the possibility of dissolution of carbonhydroxides in each other is of importance, which is indicated by the Hildebrand parameter δ^*

$$\delta^* = \left(\frac{\gamma}{V^{1/3}} \right) \quad (16)$$

With V a measure for the molecular volume and γ the surface energy. An optimum in solubility is found in case of equal values of δ^* for both participating materials. δ^* gives no indication on the speed of the process, which depends among others on temperature, size of the exposed surfaces and of abrasion of reaction products. Consequencies may be

- clogging or erosion of the pores
- dissolving of the materials constituting the layer (salt in water) or softening of the binder (bitumen + oil)
- abrasion of the layer (mechanical)
- cracking of the layer, what may result in large fluid flow but is not in the scope of this paper.

3 Tests

3.1 Conditioning

In order to determine the values of the material parameters when exposed to the environment in their application, the specimens have to be conditioned. For the resistance of bitumen bound material against carbon hydroxide agents a simple method is found to place the specimen on a porous support, e.g. a sieve, and place the sieve in a basin, filled with the agent up to a level that it reaches the surface of the specimen. This set up has been used for conditioning asphalt specimen by submerging 10 mm of the specimen. The basin has to be covered to obtain a vapor equilibrium above the liquid surface.

3.2 Transport

The Uniaxial Absorption Test (UAT) been developed to monitor the ingress of several fluids into specimen of different kinds of asphalt mixtures. Investigated are the influence of the type of solid, the type of fluid and the pressure height. As test fluid for bitumen bound materials ethanol is preferred, as it does not react with bitumen and due to the favorable viscosity and surface energy, processes develop comparatively quickly. Presentation of the preliminary quantified results is outside the scope of this paper.

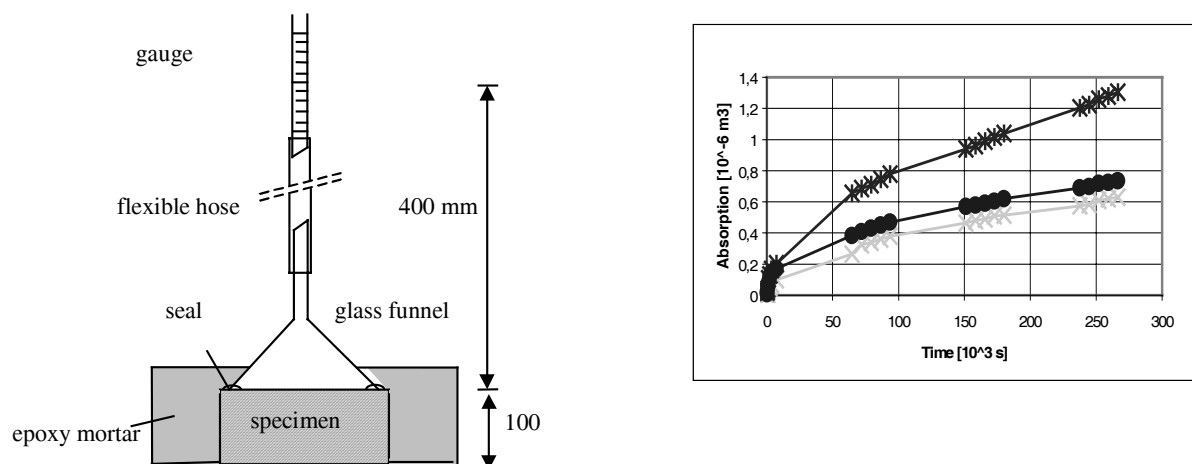


Figure 3. Set up for capillary absorption test and the typical development of absorption of ethanol in Dense Asphalt Concrete 0/11 (pressure head of 0.004 MPa)

3.3 Abrasion

As abrasion test brushing of one flat surface of a specimen has been chosen as the result on a reference and experimental investigation of test procedures. The forces exerted by the brush have to be controllable. In case low forces are desired a long haired copper brush may be used to eliminate the pressure differences depending on machine or operator. Brushing should be proceeded until no further abrasion is apparent. Reference data are not yet available.

4 Structural applications

In principle the tests as described in combination with data available in literature deliver the material parameters needed to make calculations of structures in the same way as for load bearing structures by separating the description of geometry, the balance of forces and the constitutive equations. As cracks and joints transport more fluid than is permeated through the solid itself, and on the other hand the surface of the solid is in structures in good condition larger than the surface of cracks and joints much depends on a good schematization of the actual situation. The processes under consideration are usually long lasting and the values of the material parameters may change largely in that period, resulting in non-linear processes. Furthermore the prediction of the processes and the values of the parameters, which can practically only be determined at small time periods or under accelerated test conditions, are therefore usually subjected to rather large uncertainties. Both the physical durability models and the stochastic of the variables and their action in the models demand enlarged attention.

Pressure heads may range from almost zero (e.g. predominantly capillary driven absorption of water on concrete elements exposed to air) via millimeters (e.g. pavements with spilled oil) and decimeters (emergency reservoirs) to decameters (basin wall protection, dams).

5 Conclusions

The absorption test has been presented as a test to measure parameters for transport processes in bound granular covers for both environmental protection and protection against environmental agents. Theoretical model have been described and test methods for similar objectives have been compared to the Unidirectional Absorption Test (UAT). It has been concluded from experiments that the UAT is discriminating between differences in fluids and solids, fluids and solids being not to strictly defined by name according to the codes.

Accelerating the absorption processes within the possibilities of the model can be done by varying the pressure and the test fluid.

From visual inspections of specimens exposed to test fluids with a fluorescent tracer it became clear that the mechanisms may be described similarly on macro scale but may differ a lot on micro scale.

The large gain of the combination of the UAT and physical modeling is that structural calculations are possible next to comparing materials. This enables to take into account properly the effect of structural details (joints) and to estimate a life time.

By durability considerations and probabilistic calculations a better insight is gained in life time calculations and reliabilities. Furthermore maintenance and inspection programs can be planned on reasonable basis. Durability processes are generally subject to more uncertainty than momentous resistance mechanisms for two reasons:

- the process is an extrapolation of mechanisms which can be determined in short periods; these processes often exceed human memory, because their effect may only be noticeable after decades to centuries;
- the processes are time non-linear due to changing material properties

As these processes are highly uncertain, for the reason of both the type of mechanisms and the duration of the processes, a probabilistic approach is favorable.

6 References

1. CEB FIP Model code 1990 (final draft july 1991)
2. Tolman, F.; Ebels, L.J.; Impermeability of bituminous materials; CUR report 99-3; NPC 988270; 1999
3. Wegen, G.J.L. van der; Fluid ingress in concrete; CUR – CROW - PBV report 98-2; 1998
4. Carslaw, H.S.; Jaeger, J.C.; Conduction of heat in solids; 2nd edition 1959

Gas Permeability, Porosity and Carbonation of Modern Conservation Lime Mortar Mix

Jan Válek, John Hughes and Peter Bartos

Advanced Concrete and Masonry Centre, University of Paisley, Scotland

Email: jan.valek@paisley.ac.uk

Abstract

The paper attempts to connect practical problems arising from the use of lime mortars in conservation and the latest scientific research in transport phenomena and durability of porous materials. It identifies specific requirements and current issues, which need to be clarified from conservation practice. It also examines the scope of the problems by carrying out simple experiments on lime mortar specimens. Characteristics like gas permeability, porosity and gain of weight were determined after six months of curing. These characteristics were related to the carbonation process. Two hypotheses are suggested. First, the gas permeability of lime mortars is influenced more by surface finish than the amount of water added to the mix. Second, the carbonation process of lime mortars depends on the surface gas permeability rather than the internal gas permeability. The surface permeability is possibly the rate-determining factor.

1 Introduction

On assessing the masonry of ancient monuments it is possible to find many examples of historic lime mortars surviving 500 years and more in very good condition. Successful mortar mixes are being analyzed and attempts being made at reproduction for conservation and restoration work. However, during the past, there have been also many failures of the mortars and sometimes even the same mortar mix on one part of the structure survived and on another part deteriorated. It is clearly not only composition or mechanical strength of the mortar mix but also the aging process, which determined the successful and the most durable mix.

In modern building design the strength of material is valued as the most important characteristic. This approach was applied also in masonry conservation, where cement based mortars superseded the traditionally used lime mortars. However, at the moment, after an era of using cement, lime based mortars are again recommended for use in conservation works carried out on stone masonry. It has been suggested that in conservation works carried out on traditional stone masonry, the strength of the mortar is very often not important [1]. What is more important is how the mortar performs and whether it complies with the purpose of conservation work. Durability is required, but the mortar could be also used as a sacrificial layer to protect the original masonry. In any case, the mortar should be compatible with the original adjacent masonry. That means, the mortar should not cause or accelerate any harm to the original masonry and preferably it should also protect it. Additionally, the manner in which the weather-

ing process changes the appearance of the mortar can be very important in the conservation of stone masonry.

The use of lime mortars for the conservation of historic structures is often in the hands of craftsmen, and a traditional approach is applied. However, a better scientific understanding is necessary. The transport processes of water and gas related to masonry materials, which relate to practical conservation problems should be examined and practical methods of measurement urgently developed.

Four main areas, where the moisture or gas transport mechanisms are of a crucial importance are:

- Cement based mortars used for repointing historic masonry are often suggested as a cause of damage to adjacent masonry due to having lower permeability than the stone. Moisture evaporation occurs through the original stone instead of the mortar and the damage mechanisms due to the salt crystallization or frost attack occurs. [2]
- Damage due to frost or salt attack is well known. There is a relation between the moisture and its transport through the material and the damage processes. [3] The application of the knowledge of transport mechanisms to the mortar and its relation to the pore structure is important for the prediction of its durability[4]
- Weathering processes control the appearance of masonry. Materials used for a repair, which weather in a different way to the original material are not acceptable. The form of weathering is controlled by the moisture and gas transport mechanisms.
- Carbonation of the lime mortars is the most valuable process when the soluble $\text{Ca}(\text{OH})_2$ is changed to less soluble CaCO_3 , which provides durability. The rate of carbonation depends on the gas permeability of the mortar and presence of moisture. [5]

2 Methods, Materials etc

The process of mortar production from mixing to fully hardened matured mortar was assessed from the point of view of how its porosity is formed and developed. In order to study these processes, simple experiments were carried out to examine the basic relations between individual characteristics like porosity, permeability, carbonation and water content of fresh mortar mix.

A lime mortar mix, commonly used in conservation for repointing, was used to cast twenty-four 50mm cubes. The mix was in proportion 1:3 of non-hydraulic lime putty (Shapfell) and sand (Gowrie). The cubes were cured under uncontrolled indoors conditions with temperature around 20°C and relative humidity 55% for the first month, then half of the cubes were placed outdoors at an exposure site with an average temperature range of 8-14 °C and relative humidity range of 60-85% for next five months. After that period, the porosity, carbonation depth and permeability were determined. Changes of weight of the cubes were monitored throughout the whole maturing period.

3 Moisture Content and Porosity

The amount of water in a mortar mix, which evaporates with drying, controls the eventual porosity of the mortar. The water content of the mix is also directly related to the workability, which consequently has an influence on the quality of compaction of the mortar.

Normally, when mortar is made out of lime putty no water is added. There is enough water from the lime putty itself. In the case of this experiment water was intentionally added to the mix to provide different mortar quality. The first six cubes, marked o1, were made without the addition of water. The amount of water was increased gradually with the number of the cube (100ml per number) but only cubes o6, o11 and o14 were cast and used further in this experiment. The actual content of the water present in the fresh mix was determined by drying the mortar in an oven at temperature $105\pm 5^{\circ}\text{C}$. The moisture content is the mass of water in a sample over the mass of dry sample. The values are presented in figure 1. The moisture content of the sample o1 with no added water was higher than that of the sample o6 with added water. This was probably caused by evaporation of the water during mixing in combination with an error of the method.

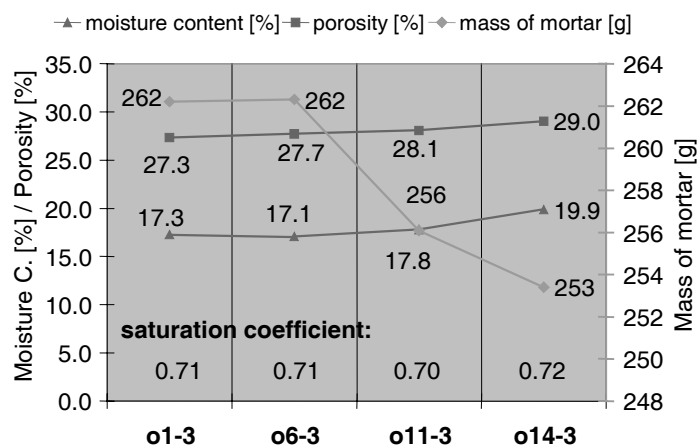


Figure 1. Comparison of the Moisture Content, Porosity and Mass of mortar specimens.

The mortar cubes were de-molded after two days and the initial weight was measured. The more water was added into the mix, the lighter samples were obtained. This can be related to the amount of water evaporated from the sample, but also to a degree of compaction. The wetter samples were stickier and more difficult to compact and placed into the mould.

The relation between porosity of the matured samples and the influence of composition of the fresh mortar is presented in figure 1. The porosity of the specimens was determined by immersing the specimens into water under vacuum for four hours. The mass of water absorbed in specimen was a difference of the oven dried mass (at $105\pm 5^{\circ}\text{C}$) and the vacuum saturated mass. More precisely the porosity is here defined as a percentage of a volume of a mortar's pore space in total volume of the mortar. The porosity was accompanied with a saturation coefficient. It is a measure of the extent to which the pores are filled when the mortar is exposed and allowed to absorb water. The sample was immersed into water for 24 hours. The average value of this coefficient was 0.71. These simple methods are recommended for assessment of durability of building stones. [5]

4 Carbonation

The most common way to determine the depth of carbonation of mortars in practice is by a Phenolphthalein pH indicator. Carbonation reduces the pH value of 12.5 of Calcium Hydroxide ($\text{Ca}(\text{OH})_2$) to pH values below 9 of Calcium Carbonate (CaCO_3). When the sample is sprayed with the pH indicator it changes its color from colorless to magenta in a region where the pH value is higher than 9. According to [7, 8] the method does not recognize a partially carbonated mortar, only fully carbonated mortar can be determined. The advantage of the use of Phenolphthalein indicator is that it offers a non-destructive and very efficient measurement.

Weight changes of the specimens were monitored throughout the whole curing period. Their development with time is shown in figure 2. This is for cubes stored indoors, in constant curing conditions. The weight changes of the specimens placed outdoors were dependent more on the weather conditions. The lime mortar cubes dried rapidly during first six days the next ten days stayed on a similar level and after a 17 days of age, the weight started to gain. The weight gain is interpreted as being related to the carbonation process. This was in accordance with Parrot's observations on the carbonation of concrete [5], where he suggested that the kinetics of the carbonation process could be assessed from the gain of weight with time.

Lime mortar carbonation is controlled by gas permeability through surface layer, pore structure and environmental conditions during carbonation. From analogue studies on concrete [5] more pores mixes are suggested to carbonate more rapidly. The cubes, both stored indoors and outdoors were fractured and the carbonation depth was determined by the Phenolphthalein indicator. The cubes stored indoors were fully carbonated only on the surface, the cubes stored outdoors were fully carbonated up to 12.5mm depth. All cubes stored under one condition had the same response to the indicator regardless of the porosity. This was also compared to the measurement of gains of mass, which as was suggested above was related to the carbonation process (see table 1). Cubes stored outdoors had gained more weight than the cubes stored indoors. Cubes with higher porosity had not gained more weight, the results were scattered.

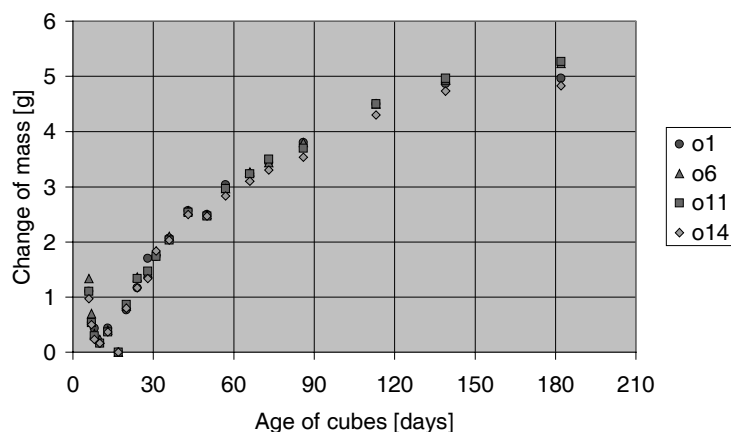


Figure 2. Change of mass of lime mortar with age in constant indoor conditions.

The pattern of the reaction or speed of colour change when sprayed by the indicator was observed in detail. For cubes stored indoors there were identified three different regions, one which was fully carbonated and the color stayed colorless, the second one which changed color immediately and a third one in between where the color gradually changed over one to two minutes in the direction from un-carbonated towards carbonated. The third region was

from 1 to 20mm deep. Such a region was not observed for cubes cured outdoors. A hypothesis can be offered that the third region was a partially carbonated zone. Such a zone would be expected and especially in indoors conditions where the pores were not blocked with moisture therefore a free passage for CO₂. Studies on concrete [8] showed that the partially carbonated zone is much wider for material cured in indoors conditions than of that cured outdoors.

Table 1. Changes of weight of the specimens and its difference between indoors and outdoors.

Cubes, i- indoors, o-outdoors	o1i	o1o	o6i	o6o	o11i	o11o	o14i	o14o
Overall weight gained [g]	3.6	4.3	3.4	4.1	3.6	5.1	2.9	4.0
Weight gained after separation [g]	1.7	2.6	2.0	2.4	2.1	2.3	1.5	2.3

The difference between the weight of cubes gained when cured indoors and outdoors was around 30 per cent, see table 1. In other words, if the gain of weight during curing is considered solely due to the carbonation, than it can be suggested that the cubes cured indoors are only 30% less carbonated. However, the depth of carbonation indicated by Phenolphthalein was 0-1mm and 12.5mm for indoor and outdoor exposure respectively.

5 Permeability

A key factor, related to decay processes and aging of mortars, is the presence of moisture and its movement throughout the material. Another important factor for durability of lime mortars is the carbonation process. To assess these key factors the gas permeability of the mortars was used and examined. The gas permeability describes the ease of the penetration of gas into the material which can be related to the carbonation process of lime mortars. [5]

A portable, steady state gas permeameter was used to measure the gas permeability. This equipment was developed and is commonly used in petroleum engineering for measuring sandstone outcrops. Its application on masonry materials and trial experiments were first described in literature [9]. The main advantages of this method over other methods are that it is non-destructive, applicable in in-situ measurements and relatively fast. The use of this equipment in laboratory on modern mortars was a part of the evaluation of its use for measuring conservation mortar mixes.

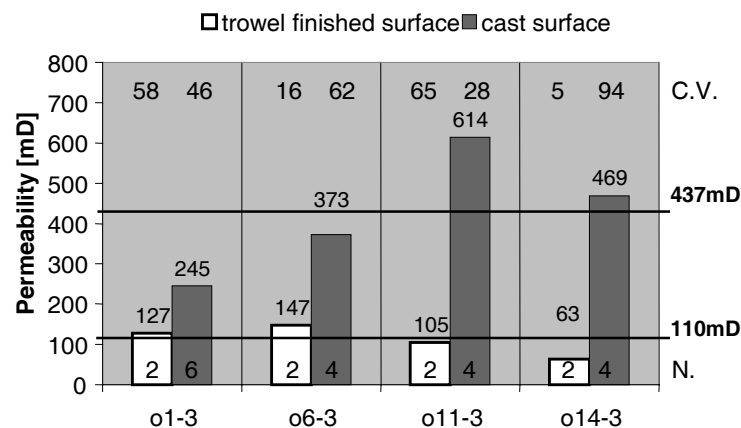


Figure 3. Gas permeability of lime mortar cubes, C.V.– Coefficient of Variability, N- number of measurements.

The gas permeability of the cubes matured indoors was measured on the top surface, which was finished and smoothed by trowel when cast and on the lateral surfaces, which was just created by a vertical side of a steel mould when cast. The top surface was found less permeable than the lateral surface. In the case of the cubes used for the porosity measurement, there seems to be a general increase of permeability with increase of moisture of the mix measured on the lateral side. However, the gas permeability of the top surface decreases with the increase of the moisture of the mix. These results are presented in figure 3. The common disadvantage of the permeability measurements is their high variability caused by the natural variation of pores. A coefficient of variability (C.V.) for the measurement was very high and the measurement was repeated for all indoor cubes to obtain a more accurate value. This showed, that the gas permeability measured on the lateral surface and top surface was in average the same for all cubes, it was 437mD and 110mD respectively.

The different amount of moisture added to mortar mix did not have any distinctive influence on the surface gas permeability measured. The surface finish was far more important to the gas permeability than the internal porosity. From the differences between top and lateral surface is obvious that the surface finish has major influence on the surface gas permeability.

6 Discussion

The lime mortar specimens were prepared with different amounts of water in order to obtain different porosity of the hardened mortar specimens. The added water had an influence on a compaction and weight of the specimens and also the porosity increased with the amount of water added.

Lime mortar specimens were cured in two indoors and outdoors conditions and these conditions influenced their carbonation process. This was measured using a pH indicator and a relationship with weight changes was also suggested. There was no obvious relationship between the carbonation and the measured porosity. This can be related to the surface gas permeability. The gas permeability was more influenced by the surface finish than the amount of water added into the mix. The in average similar level of the surface gas permeability is suggested to be related to the similar depth of the carbonation. The measurement of carbonation pointed out a need for more precise method of determination. More detailed research should explore the relation between the weight gain, depth of neutralization by Phenolphthalein and the gradient of carbonation the partially carbonated zone.

7 Conclusions

The carbonation process of lime mortars is important to building conservation and requires better scientific explanation. In order to carry out applied research in detail the initial experiments have been undertaken to understand the limitations and to suggest objectives for further research.

- Amount of water added to the mix had an influence on the porosity but not on the surface gas permeability or carbonation depth.

- The gas permeability of the surface of the mortar cubes varied with the surface finish. The surface permeability had a greater effect on the carbonation than the porosity of the cubes.
- Carbonation cannot be measured quantitatively by Phenolphthalein pH indicator; it can only determine the complete neutralization depth. Other, more precise methods, which would be non-destructive, are needed.

8 References

1. Maxwell, The use of lime mortars in the context of dry stone build, Proceedings of the international RILEM workshop, Historic mortars: characteristics and tests, University of Paisley, May 1999.
2. S. Holmes, M. Wingate, Building with lime, a practical introduction, Intermediate Technology Publications 1997, p. 62
3. P. K. Larsen, Desalination of painted brick vaults Denmark Technical University DTU, Lyngby 1999
4. B. Meng, Calculation of moisture transport coefficients on the basis of relevant pore structure parameters, Materials and Structures, 27, 1994, pp.125-134.
5. L. J. Parrot, Carbonation, moisture and empty pores, Advances in Cement Research, vol. 4, No.15, 1991/92, pp. 111-118
6. K. Ross, R. N. Butlin, Durability tests for building stone, Building Research Establishment, BRE Report BR 141, Garston CRC, 1989
7. S. Ohgishi, H. Ono, Study to estimate the depth of neutralisation on concrete members, Cement Association Japan Review, 1993, pp.168-170
8. L. J. Parrot, D. C. Killoh, Carbonation in a 36 year old, in-situ concrete, Cement and concrete research, vol. 19, 1989, pp. 649-656
9. J. Valek, J. J. Hughes and P. M. J. Bartos, Portable probe gas permeametry in the testing of historic masonry and mortars, Proceedings of the international RILEM workshop, Historic mortars: characteristics and tests, University of Paisley, May 1999.

Author Index*

- Aldea, C.-M. 170
Alonso, M. 189
Alonso,, C. 198
Andrade, C. 189
Attal, J. 144
- Barragán, B. 72
Bartos, P. 209
Beaupr, D. 8
Böhni, H. 163
Buchwald, A. 157
- Camanho, P.P. 41
Cambronero, L.E.G. 57
Campiono, G. 86
Carol, I. 48
Carpinteri, A: 132
Chacón, I. 57
Chiaia, B. 132
Cielens, U. 183
Codina Sánchez,, S. 198
Cornetti, P. 132
Corpas Iglesias,, F.A. 198
Cros, B. 144
- de Fatima Zalochi, R. 72
den Herder, A.J. 149
- Ebels, L.J. 202
Elsener, B. 163
- Fernandes, A.A. 41
Fernandes, M. C. 41
Ferrandis, J.Y. 144
Ferreira, A.J. M. 41
Figueiredo, M. A. V. 41
Flückinger, D. 163
Fuchs, K. 138
- Garcia Cambronero, L.E. 198
Gettu, R. 48, 72
Ghandehari, M. 170
- Haller, P. 66
Hammer, T. A. 18
Helland, S. 18
Holand, I. 18
Hughes, J. 209
- Igaune, S. 183
- Jolin, M. 8
- Kaps, C. 157
Karihaloo, B.L. 95
Karr, A. 170
Keddam, M. 189
- Linsbauer, H.N. 138
Linsel, St. 23
- Maage, M. 18
MartIn, M. A. 48, 72
Mayrhofer, C. 78
Mechtcherine, V. 119
Mijnsbergen, J. P. G. 18
Mindess, S. 8, 86
Moraño, A.J. 57
Müller, H. S. 23
Müller, H.S. 119
- Popovics, J.S. 112
- Ramón Nóvoa, X. 189
Roncero, J. 48
Ruiz Prieto,, J.M. 198
Ruiz Roman, J.M. 57
Ruiz Román,, J.M. 198
- Šajina, A. 138
Schlumpf, J. 3
Schwesinger, P. 28
Setina, Y. 183
Setzer, M.J. 175
Shah, S. P. 35
Shah, S.P. 112, 170
Shi, C. 125

* The page numbers refer to the first page of the respecting article

Sickert, G. 28
Sluys, B. 125
Subramaniam, K.V. 112
Sveinsdóttir, E. L. 18

Takenouti, H. 189
Tolman, F. 149, 202

Válek, J. 209
van Breugel, K. 18
van Dam, A.G. 125
van Mier, J.G.M. 125
Vitina, I. 183

Wang, J. 95
Wehsener, J. 66
Weiss, W. J. 35
Yang, W. 35

Subject Index*

A

Acoustic sensor 144
Admixtures, chemical 48
Artificial saturation 175

B

Biaxial compression-Tension 112
Bitumen bound granular material 202
Bound granular covers 202

C

Carbonation 209
Cement 57
Cementitious composites 95
Cementitious layer 28
Cementitious material 3, 163
Cement paste 189
Cement setting 144
Chemical admixtures 48
Chemical deterioration 183
CMOD 170
Cohesive damage model 132
Composites, cement 57
– fiber reinforced 95
Compound materials 198
Compression 86
Concentric load 86
Concrete 18, 48, 72, 78, 125, 170
– damage model 132
– drying shrinkage 48
– fibre reinforced 86
– fracture mechanical behaviour 119
– lightweight 23
– polymer 41
– self compacting 3
– shrinkage-reduced 28
– special 41
– structural lightweight aggregate 18
Concrete constructions 183
Construction 18
Cracking 170
Crack interaction 125
Crack mouth opening displacement 170
Crack propagation 112

D

Damage model 132
Densified wood 66
Design, economic 18
Deteriorating salts 157
Deterioration, chemical 183
Dielectric properties, cement 189
Drying shrinkage 48
Ductility 72
Dynamic loading 78

E

Eccentric load 86
Economic design 18

F

Fatigue 112
Fiber 78
Fiber-reinforced cementitious composites 95
Fibers, fibre 57
Flexural resistance 57
Fluid transport 202
Fractal band 132
Fracture mechanical behaviour 119
Fracture mechanics 138
Fracture testing 149
Freeze thaw testing 175
Fresh shotcrete 8
Frost damage 175
Frost suction 175

G

Gas permeability 209

H

High performance concrete 28
– lightweight 23
– shrinkage-reduced 28
High strength fibre reinforced concrete 86
Horizontal wedge splitting test 138
HPC 28
HWST 138

* The page numbers refer to the first page of the respecting article

I

Ice formation 175
Impact resistance 57
Impedance spectroscopy 157
Interfacial effects 189
Ion mobility 157

J

Joints, timber 66

L

Lightweight concrete 23
Lime mortar mix 209
LWAC 23

M

Marble residues 198
Materials, cementitious 3
– compound 198
– masonry 157
– porous 163
Material toughness, concrete 72
Matrix, polymer 198
Microcracks 95
Micro ice lens 175
Micromechanics 95
Moisture content 157
Mortar 209

N

Normal strength concrete 170
Normal weight concrete 23
NWC 23

P

Percolation model 163
Polymer 198
Polymer concrete 41
Porosity 209
Porous cementitious materials 163
Portland cement concrete 112
Precast special concrete 41

R

Reinforced cement 57
Reinforced composites 95

Rheological measurements 144
Rings, shrinkage cracking 35

S

Salts, deteriorating 157
Saturation, artificial 175
SCB 149
SCC 3
Self compacting concrete 3
Semicircular bending test 149
Sensor, acoustic 144
Separation layers 202
Shotcrete 8
Shrinkage reducing admixtures 48
Shrinkage, drying 48
Shrinkage cracking 35
Shrinkage reduction 3
SIFCON 78
Slurry infiltrated fiber concrete 78
Special concrete 41
Specimen size/geometry 35
SRA 48
Steel fibers 72
Structural lightweight aggregate concrete 18
Surface interaction 175

T

Taguchi method 41
Technical textiles 66
Tensile tests 125
Textiles, technical 66
Timber joints 66
Timber-steel compounds 66

U

Uniaxial tensile tests 125

W

Water permeability 170
Water sorption 163
Wedge splitting 138
Wood, densified 66